



Exploiting over-actuation for improved active safety of autonomous electric vehicles

WENLIANG ZHANG

Doctoral Thesis
Stockholm, Sweden, 2022

TRITA-SCI-FOU 2022:15
ISBN 978-91-8040-219-4

KTH Royal Institute of Technology
School of Engineering Sciences
Department of Engineering Mechanics
SE-100 44 Stockholm
Sweden

Akademisk avhandling som med tillstånd av Kungl Tekniska högskolan framlägges till offentlig granskning för avläggande av teknologie doktorexamen i farkostteknik måndag den 13 juni 2022 klockan 13.00 i Sal E3, Osquars backe 14, KTH, Stockholm.

© Wenliang Zhang, 2022

Tryck: Universitetsservice US AB

Abstract

The increasing demand for road vehicles has led to challenging road safety and environmental issues. The deployment of active safety systems and autonomous vehicles can contribute to safer roads by assisting or replacing human drivers in the task of maintaining vehicle control in critical conditions: e.g., an obstacle-avoidance manoeuvre. Road vehicle electrification can bring about environmental benefits and at the same time enable the development of over-actuated vehicle platforms. Over-actuation can be explored together with active safety and automated driving systems in order to enhance vehicle safety. On the other hand, to achieve their best possible performance, such safety and automated systems require the knowledge of vehicle states such as sideslip angle as well as reliable trajectories. However, measuring such crucial states can be overly expensive on production vehicles.

The studies presented in this thesis aim to explore how over-actuation can improve path-following and yaw-stability performance of autonomous electric vehicles in critical manoeuvres and investigate the associated state estimation and trajectory planning problems.

To achieve these goals, this thesis focuses on five aspects. First, it explores vehicle dynamics modelling by introducing vehicle and tyre models of various levels of complexity. In particular, the camber effect on lateral tyre forces was modelled using a simple, yet effective, component, which allows for individual camber control of each wheel. Second, it addresses the state estimation problem by designing and evaluating three moving horizon estimation (MHE) based estimators and an unscented Kalman filter. The evaluation in three critical manoeuvres showed that the estimator MHE outperformed the other algorithms, with improved convergence rate, accuracy and response to external disturbances and modelling errors, due to its consideration of a sequence of most recent measurements and process noises. Third, trajectory planning is studied through optimal control formulations and by examining the effect of model complexity in critical driving scenarios. It was shown that the advanced double-track planner with load transfer and the Magic Formula tyre model was desired to achieve more consistent trajectory planning and tracking performance as well as smaller peak yaw rate and sideslip angle. Fourth, the path following and yaw stability problem is tackled in the model predictive control framework and by exploring various over-actuation configurations – active front steering (AFS), torque vectoring (TV) and active camber (AC). The results in safety-critical conditions showed that AFS + TV improved yaw stability, path following and passing velocity compared to AFS, and AFS + AC performed better than AFS + TV. The integrated control of AFS + TV + AC further enhanced vehicle safety and was more robust to reference trajectory variations, as a result of its more effective actuator and tyre utilisation. Finally, this work details the framework for optimal control implementation, which facilitates efficient computing, smooth parameter tuning and results analysis, as well as sustainable code development.

The research presented in this thesis has contributed to the modelling, formulation and control of autonomous electric vehicles by exploiting over-actuation for enhanced vehicle safety. It has been shown that over-actuation control strategies can be a promising solution for improving active safety, and thus they contribute to a safer and more sustainable future transport.

Sammanfattning

Den ökande efterfrågan på vägfordon har orsakat utmanande trafiksäkerhets- och miljöutmaningar. Introduktionen av aktiva säkerhetssystem och autonoma fordon kan bidra till säkrare vägar genom att hjälpa eller ersätta mänskliga förare med att köra fordonet i kritiska situationer, t.ex. en undanmanöver. Dessutom kan elektrifieringen av vägfordon ge miljövinster och samtidigt möjliggöra utvecklingen av överaktuerade fordonsplattformar. Med tillgång till ett ökande antal aktuatorer ger det fler frihetsgrader för att styra fordonet. Detta kan utforskas tillsammans med aktiv säkerhet och autonoma fordon för att öka säkerheten. Men för att upprvisa sin bästa möjliga prestanda, kräver dessa säkerhets- och automatiserade system kunskap om fordonstillstånd och tillförlitliga fordonstrajektorier. Däremot kan kritiska fordonstillstånd som exempelvis fordonets avdriftsvinkel oftast inte mätas i produktionsfordon eftersom sensorerna är väldigt kostsamma.

Studierna som presenteras i denna avhandling syftar till att utnyttja överaktuering för att förbättra trajektorieföljning och girstabilitet hos autonoma elfordon i kritiska manövrar. Dessutom undersöks tillhörande problem med tillståndsuppskattning och trajektorieplanering.

För att nå dessa mål så handlar arbetet i denna avhandling om följande fem huvudområden. Första området handlar om fordonsdynamikmodellering och både fordons- och däckmodeller med varierande grad av komplexitet utforskas och valideras. Specifict modelleras effekten av camber på de laterala däckkrafterna med en enkel men dock effektiv komponent som möjliggör individuell reglering av camberinviklarna för varje hjul. Det andra området belyser parameterskattning där tre MHE baserade algoritmer och en UKF baserad algoritm tas fram och utvärderas. Studien visade för tre olika kritiska körfall att standardformuleringen av MHE fungerade bättre än de andra algoritmerna och gav mer korrekta och feltoleranta skattningar med snabbare konvergering. I det tredje området så formuleras trajektorieplanering som ett optimalt reglerproblem och effekten av modellkomplexitet på trajektorieplaneringsförmågan i kritiska körfall studeras. Här visades det att planeraren med de mest avancerade modellerna presterade bättre än de andra genom högre fordonshastighet samt mindre girvinkelhastighet och avdriftsvinkel i testerna. Fjärde området handlar om trajektorieföljning och girstabilitet i ett modellprediktivt reglerramverk. Här utvärderas flera kombinationer av överaktuering, nämligen aktiv styrning (AFS), vridmomentsvektorisering (TV) och aktiv camber (AC) samt kombinationer av dem. Resultaten visar att AFS tillsammans med TV förbättrar girstabilitet, trajektorieföljning och dynamiska prestandan i testerna och att AFS i kombination med AC kunde ytterligare förbättra prestandan. Den integrerade regleringen av AFS tillsammans med TV och AC hade generellt sett den bästa prestandan, som ett resultat av mer effektivt utnyttjande av aktuatorer och däckgrepp. Slutliga området handlar om implementering av ett ramverk för regleroptimeringen som möjliggör effektiva beräkningar, underlättar parameterjusteringar och resultatanalys samt bidrar till hållbar kodutveckling.

Forskningen har bidragit till modellering, formulering och reglering av autonoma elektriska fordon genom att dra nytta av överaktuering för förbättrad fordonssäkerhet. Det har visats att reglerstrategier för överaktuering kan vara en lovande lösning för förbättrad aktiv säkerhet och därmed bidra till säkrare och miljövänligare transporter.

Acknowledgement

I received a great deal of support and assistance throughout my PhD journey at KTH Vehicle Dynamics in the Department of Engineering Mechanics at KTH Royal Institute of Technology in Stockholm, Sweden.

First and foremost, I would like to thank my supervisors Lars Drugge and Mikael Nybacka for their patient guidance, dedicated support and generous encouragement during my entire work. Their rich experience and unique perspectives have always inspired me to see, analyse and solve difficult problems from novel angles, and their assistance was always there whenever I needed it. I also wish to thank Professor Zhenpo Wang at the Beijing Institute of Technology in China for opening the door to my research and for supporting me in pursuing my studies at KTH. Thank you all for the help. I would not have completed this thesis without it.

I would like to express my appreciation to fellow and former colleagues at KTH Vehicle Dynamics, Annika Stensson Trigell, Malte Rothhämel, Georgios Papaioannou, Mohammad Mehdi Davari, İlhan Yunus, Henrik Hvittfeldt and Lisa Ydrefors. I am grateful for the constructive suggestions from Jenny Jerrelind and the stimulating discussions from Mats Jonasson. I extend special thanks to Peikun Sun, Jukka Hyttinen and Lin Zhao for the intriguing ideas and joyful times spent together.

Advice given by Changfu Zou from Chalmers University of Technology has been a great help in state estimation and academic writing. The help from Xin Li and Kiartan Wikfeldt is also appreciated – the training given by them at the KTH Centre for High Performance Computing (PDC) broadened my knowledge on scientific computing and sustainable software development.

I was fortunate to be part of the PhD Affiliation Programme at KTH Integrated Transport Research Lab (ITRL). The talented minds and insightful seminars led me into broader transport topics, and the valuable discussions with Masoumeh Parseh and Lars Svensson inspired my trajectory planning studies.

The help from free and open-source software communities is greatly appreciated. Many thanks to Michael J. Risbeck and Joris Gillis for the precious discussions on moving horizon estimation and optimisation problem implementation. Special thanks to [Obsidian](#), plug-in developers and community members for making my ideas, tasks and projects on research and life manageable.

I wish to acknowledge all the support I received from the Swedish Electromobility Centre (SEC). The Doctoral Student Network, seminars and activities across

Sweden were great sources of information for electric mobility and left me with happy memories.

The support and assistance provided by Modelon AB are also gratefully acknowledged. My special thanks are extended to Johan Andreasson for building the collaboration, Mathias Strandberg for help with training and model development and Fredrik Magnusson for introducing me to optimisation implementation and scientific Python.

In addition, I would like to thank my friends for their encouragement, shared meals and sports activities, as well as for sharing the highs and lows of my PhD process.

Finally, I wish to express my profound gratitude to my parents for their unconditional love and unfailing support throughout the years of my research and life. Without you being always there for me, none of this would have happened.

Wenliang Zhang
Stockholm, February 2022

Dissertation

This thesis consists of two parts. The first part presents an overview of the relevant research field and a summary of the present work. The second part includes the following appended scientific publications.

Appended papers

- A *Advanced vehicle state monitoring: Evaluating moving horizon estimators and unscented Kalman filter,*

Wenliang Zhang, Zhenpo Wang, Changfu Zou, Lars Drugge and Mikael Nybacka,

IEEE Transactions on Vehicular Technology, vol. 68, no. 6, 2019.

Authors' contributions: Zhang performed the studies, completed the analyses, and wrote the paper. Wang, Zou, Drugge and Nybacka supervised the work, provided useful ideas, and proofread the paper.

- B *Active camber for enhancing path following and yaw stability of over-actuated autonomous electric vehicles,*

Wenliang Zhang, Lars Drugge, Mikael Nybacka and Zhenpo Wang,

Vehicle System Dynamics, vol. 59, no. 5, 2020.

Authors' contributions: Zhang performed the studies, completed the analyses, and wrote the paper. Drugge, Nybacka and Wang supervised the work, provided useful ideas, and proofread the paper.

- C *Evaluating model predictive path following and yaw stability controllers for over-actuated autonomous electric vehicles,*

Wenliang Zhang, Zhenpo Wang, Lars Drugge and Mikael Nybacka,

IEEE Transactions on Vehicular Technology, vol. 69, no. 11, 2020.

Authors' contributions: Zhang performed the studies, completed the analyses, and wrote the paper. Wang, Drugge and Nybacka supervised the work, provided useful ideas, and proofread the paper.

D *Exploring model complexity for trajectory planning of autonomous vehicles in critical driving scenarios,*

Wenliang Zhang, Lars Drugge, Mikael Nybacka, Jenny Jerrelind, Zhenpo Wang and Junjun Zhu,

Advances in Dynamics of Vehicles on Roads and Tracks (IAVSD 2021), 2021.

Authors' contributions: Zhang performed the studies, completed the analyses, and wrote the paper. Drugge, Nybacka, Jerrelind, Wang and Zhu supervised the work, provided useful ideas, and proofread the paper.

E *Integrated control of motion actuators for enhancing path following and yaw stability of autonomous electric vehicles,*

Wenliang Zhang, Lars Drugge, Mikael Nybacka, Jenny Jerrelind and Zhenpo Wang,

Submitted for publication, 2022.

Authors' contributions: Zhang performed the studies, completed the analyses, and wrote the paper. Drugge, Nybacka, Jerrelind and Wang supervised the work, provided useful ideas, and proofread the paper.

Papers not appended

F *State and parameter estimation based on a modified particle filter for an in-wheel-motor-drive electric vehicle,*

Junjun Zhu, Zhenpo Wang, Lei Zhang and Wenliang Zhang,

Mechanism and Machine Theory, vol. 133, 2019.

G *Exploring active camber for path following and yaw stability of autonomous vehicles,*

Wenliang Zhang, Lars Drugge, Mikael Nybacka and Zhenpo Wang,

Advances in Dynamics of Vehicles on Roads and Tracks (IAVSD 2019, Lecture Notes in Mechanical Engineering), 2020.

H *Study of different steering feedback models influence during remote driving,*

Lin Zhao, Mikael Nybacka, Lars Drugge, Jonas Mårtensson, Saurabh Vyas, Chirag Savant, Wenliang Zhang and Robin Palmberg,

Advances in Dynamics of Vehicles on Roads and Tracks (IAVSD 2021), 2021.

Nomenclature and acronyms

General symbols

\mathcal{A}	A set in which the elements denote the front left, front right, rear left and rear right wheels, respectively, $= \{fl, fr, rl, rr\}$.
\mathcal{B}	A set in which the elements denote the front and rear axles, respectively, $= \{f, r\}$.
XOY	Earth frame; for Global Positioning System.
x_{b0y_b}	Vehicle body frame; for inertial measurement unit.
x_{oy}	Vehicle frame; for describing vehicle motion.
x_{t0y_t}	Wheel frame; for describing wheel motion.
$f_c(\cdot), h_c(\cdot)$	Continuous-time state, output equation.
$f(\cdot), h(\cdot)$	Discrete-time state, output equation.
$g_t(\cdot)$	State constraint equation for trajectory planner.
$\mathcal{H}_p(\cdot)$	State constraint equation for path following and yaw stability controller.

Model variables

x, u, y	System state, input, output vector.
v_x, v_y	Longitudinal, lateral velocity at CoG in frame xoy (m/s).
v	Combined velocity at CoG in frame xoy (m/s), $= \sqrt{v_x^2 + v_y^2}$.
ω_z	Yaw rate around CoG in frame xoy (rad/s).
ψ	Yaw angle in frame XOY (rad).
X, Y	Longitudinal, lateral position in frame XOY (m).

ω_i	Angular velocity of the wheel in frame $x_t o y_t$ (rad/s) ($i \in \mathcal{A}$).
β	Sideslip angle (rad), $= \arctan v_y/v_x \approx v_y/v_x$.
a_x, a_y	Longitudinal, lateral acceleration in frame $x_b o y_b$ (m/s ²).
v_{cx_i}, v_{cy_i}	Longitudinal, lateral velocity at the wheel centre in frame $x_t o y_t$ (m/s) ($i \in \mathcal{A}$).
v_{cx_j}, v_{cy_j}	Longitudinal, lateral velocity at the wheel centre in frame $x_t o y_t$ (m/s) ($j \in \mathcal{B}$).
α_i	Tyre slip angle in frame $x_t o y_t$ (rad) ($i \in \mathcal{A}$).
α_j	Tyre slip angle in frame $x_t o y_t$ (rad) ($j \in \mathcal{B}$).
κ_i	Tyre slip ratio in frame $x_t o y_t$ ($i \in \mathcal{A}$).
γ_i	Tyre camber angle in frame $x_t o y_t$ (rad) ($i \in \mathcal{A}$).
δ_f	Steering angle, mean of two front wheels in frame $x o y$ (rad).
T_i	Drive/braking torque on the wheel in frame $x_t o y_t$ (Nm) ($i \in \mathcal{A}$).
F_{xi}, F_{yi}	Longitudinal, lateral tyre force in frame $x_t o y_t$ (N) ($i \in \mathcal{A}$).
$F_{y\gamma i}$	Lateral tyre force caused by wheel camber in frame $x_t o y_t$ (N) ($i \in \mathcal{A}$).
F_{xj}, F_{yj}	Longitudinal, lateral axle force in frame $x_t o y_t$ (N) ($j \in \mathcal{B}$).
F_{zi}	Vertical tyre force in frame $x_t o y_t$ (N) ($i \in \mathcal{A}$).
F_{xy}	Total force applied to CoG (N).
M_{zd}	Required yaw moment (from the contribution of longitudinal tyre forces) for the yaw movement of the vehicle (Nm).
M_z	Required yaw moment (from the contribution of both longitudinal and lateral tyre forces) for the yaw movement of the vehicle (Nm).
Y_M	Output variable of the MF tyre model, e.g., F_{xi} or F_{yi} ($i \in \mathcal{A}$).
X_M	Input variable of the MF tyre model, e.g., κ_i or $\tan \alpha_i$ ($i \in \mathcal{A}$).

Model parameters

$C_{\alpha i}$	Tyre cornering stiffness (N/rad) ($i \in \mathcal{A}$).
$C_{\alpha j}$	Axle cornering stiffness (N/rad) ($j \in \mathcal{B}$).
$C_{\kappa i}$	Tyre longitudinal stiffness (N) ($i \in \mathcal{A}$).

$C_{\gamma i}$	Tyre camber stiffness (N/rad) ($i \in \mathcal{A}$).
$C_{\gamma 0i}$	Tyre camber stiffness when with zero slip angle (N/rad) ($i \in \mathcal{A}$).
$C_{\gamma fi}$	Tyre camber stiffness when slip angle reaches α_{lim} (N/rad) ($i \in \mathcal{A}$).
$C_{\gamma \alpha i}$	Variation in tyre camber stiffness with respect to slip angle (N/rad ²) ($i \in \mathcal{A}$).
α_{lim}	Limiting value for determining tyre camber stiffness (rad).
I_{wi}	Wheel rotational inertia (kg · m ²) ($i \in \mathcal{A}$).
r_e	Tyre radius (m).
B, C, E	Stiffness, shape, curvature factor of the MF tyre model.
D	Peak value of the MF tyre model.
S_H, S_V	Horizontal, vertical shift of the MF tyre model.
m	Vehicle mass (kg).
I_z	Vehicle yaw inertia (kg · m ²).
B_f, B_r	Front, rear track width (m).
l_f, l_r	Distance from CoG to front, rear axle (m).
h_g	Height of CoG (m).
μ	Road friction coefficient.
g	Gravitational acceleration (m/s ²).
C_d	Air drag coefficient.
A_f	Frontal area (m ²).
D_a	Air density (kg/m ³).

Estimator variables

$w(\cdot), v(\cdot)$	Vector for process, measurement noise.
$\mathbf{x}_h, \mathbf{w}_h, \mathbf{v}_h$	Sequence of vectors for state, process noise, measurement noise.
$x_{i k}$	A state estimate obtained with measurements up until time step k .
$x_{k-N_h k-N_h-1}$	The <i>a priori</i> state estimate at time step $k - N_h$.
$x_{k-N_h k-N_h}$	The <i>a posteriori</i> state estimate at time step $k - N_h$.

$x_{k-N_h|k}$ Smoothed state estimate at time step k .

Estimator parameters

Q_k, R_k Covariance matrix for process, measurement noise.

N_h Horizon length of MHE.

$P_{k-N_h|k-N_h-1}$ The error covariance matrix corresponding to $x_{k-N_h|k-N_h-1}$.

$P_{k-N_h|k-N_h}$ The error covariance matrix corresponding to $x_{k-N_h|k-N_h}$.

K_{k-N_h} Kalman gain for EKF around $x_{k-N_h|k}$.

$A_{k-N_h|k}$ Jacobian matrix for EKF around $x_{k-N_h|k}$.

$C_{k-N_h|k}$ Jacobian matrix for EKF around $x_{k-N_h|k}$.

y_{k-N_h} Measured signals at time step $k - N_h$.

u_{k-N_h} Input signals at time step $k - N_h$.

Planner variables

x_0, x_f Initial, terminal state vector.

u_0 Initial control vector.

v_0, v_f Initial, terminal longitudinal velocity at CoG in frame xoy (m/s).

Δu_i Variation of control vector.

Planner parameters

N_t Horizon length of trajectory planner.

\tilde{x}_0, \tilde{x}_f Initial, final value for state vector.

\tilde{u}_0 Initial value for control vector.

u_{min}, u_{max} Lower, upper boundary on control vector.

$\Delta u_{min}, \Delta u_{max}$ Lower, upper boundary on variation of control vector.

β_{min}, β_{max} Lower, upper boundary on sideslip angle.

$\omega_{zmin}, \omega_{zmax}$ Lower, upper boundary on yaw rate.

Controller variables

s Slack vector.

\mathbf{x}_p, \mathbf{s} Sequence of state, slack vectors.

$\boldsymbol{u}_p, \Delta\boldsymbol{u}_p$ Sequence of control, variation of control vectors.

Controller parameters

N_p Prediction horizon of MPC.

Q_y, Q_{yf} Weight matrix for penalising stage, terminal output tracking.

R_u, R_{du} Weight matrix for penalising control and variation of control.

Q_s, Q_{sf} Weight matrix for penalising stage, terminal slack.

$y^{ref}(\cdot)$ Reference trajectory vector from trajectory planner.

$\Delta\gamma$ Variation of camber angle.

\boldsymbol{u}^* Solution sequence from MPC.

$u_{k|k}^*$ Final solution from MPC.

Miscellaneous

t_{cvg} Time to converge (s).

Acronyms

AC	Active camber
ACM	Autonomous corner module
AEV	Autonomous electric vehicle
AFS	Active front steering
AV	Autonomous vehicle
CO₂	Carbon dioxide
CoG	Centre of gravity of vehicle
DC	Direct collocation
DLC	Double-lane change
DMS	Direct multiple shooting
DoF	Degree of freedom
DSS	Direct single shooting
DTB	Double-track dynamic vehicle model with Dugoff tyre model
DTMIlt	Double-track dynamic vehicle model with load transfer and MF tyre model
EKF	Extended Kalman filter
EM	Electric motor
ESC	Electronic stability control
EV	Electric vehicle
FIE	Full information estimation
FMU	Functional mock-up unit
GDP	Gross domestic product
GHG	Greenhouse gas
GPS	Global Positioning System
ICE	Internal combustion engine
IDE	Integrated development environment
IMU	Inertial measurement unit
IPM	Interior point method
ITF	International Transport Forum
ITRL	Integrated Transport Research Lab
KF	Kalman filter
LQR	Linear quadratic regulator
MF	Magic Formula
MHE	Moving horizon estimation

mMHE	Modified MHE
MPC	Model predictive control
NLP	Nonlinear programming problem
OCP	Optimal control problem
OICA	International Organization of Motor Vehicle Manufacturers
OLEA	One-level controller with equal torque allocation
OLTV	One-level controller with torque vectoring
PDC	Centre for High Performance Computing
PF	Particle filter
PID	Proportional–integral–derivative
RCV	Research concept vehicle
RLS-MHE	Recursive-least-squares MHE
RMS	Root-mean-square
RQ	Research question
SEC	Swedish Electromobility Centre
SI	International System of Units
SLC	Single-lane change
SMC	Sliding-mode control
SMO	Sliding-mode observer
STD	Single-track dynamic vehicle model with a simplified MF tyre model
STDL	Single-track dynamic vehicle model with a linear tyre model
STK	Single-track kinematic model
TLOA	Two-level controller with optimisation-based torque allocation
TLRA	Two-level controller with rule-based torque allocation
TV	Torque vectoring
UKF	Unscented Kalman filter
VCS	Version control system

Contents

Dissertation	v
Nomenclature and acronyms	vii
List of figures and tables	xvii
1 Introduction	1
1.1 Background	1
1.1.1 Road safety and automation	2
1.1.2 Electrification and over-actuation	3
1.2 Research objective and questions	5
1.3 Limitations	6
1.4 Research approach	6
2 Vehicle dynamics modelling	9
2.1 Vehicle modelling	9
2.1.1 Single-track kinematic model	9
2.1.2 Single-track dynamic model	10
2.1.3 Double-track dynamic model	11
2.2 Tyre modelling	12
2.2.1 Linear tyre model	13
2.2.2 Dugoff tyre model	13
2.2.3 Dugoff tyre model with camber effect	14
2.2.4 Magic Formula tyre model	15
2.3 Model summary	16
2.4 Vehicle plant modelling	17
3 State estimation	19
3.1 Background	19
3.2 Estimation algorithms	20
3.2.1 Kalman filter	20
3.2.2 Extended Kalman filter	20
3.2.3 Unscented Kalman filter	21

3.3	Moving horizon estimation	21
3.4	Results and discussion	23
4	Trajectory planning	25
4.1	Background	25
4.2	Planner formulation	26
4.3	Results and discussion	27
5	Path following and yaw stability control	31
5.1	Background	31
5.2	Controller formulation	33
5.3	Results and discussion	34
5.3.1	Torque vectoring	35
5.3.2	Active camber	37
5.3.3	Integrated control	39
6	Optimal control implementation	43
6.1	Background	43
6.2	Implementation	44
6.2.1	Framework	44
6.2.2	Optimal control problem	45
6.2.3	Parameter tuning	46
6.2.4	Optimisation techniques	48
7	Summary of appended papers	49
8	Scientific contributions	55
9	Conclusions and future directions	59
9.1	Conclusions	59
9.2	Recommendations for future work	61
Bibliography		63
Appended papers		73
Paper A: Advanced vehicle state monitoring: Evaluating moving horizon estimators and unscented Kalman filter	75	
Paper B: Active camber for enhancing path following and yaw stability of over-actuated autonomous electric vehicles	91	
Paper C: Evaluating model predictive path following and yaw stability controllers for over-actuated autonomous electric vehicles	115	
Paper D: Exploring model complexity for trajectory planning of autonomous vehicles in critical driving scenarios	133	
Paper E: Integrated control of motion actuators for enhancing path following and yaw stability of autonomous electric vehicles	145	

List of figures and tables

List of figures

1.1	Annual person-kilometres for road passenger vehicles [1].	2
1.2	Process map for the research presented in this thesis, including modelling, strategies and resulting publications.	7
2.1	Kinematic vehicle model.	10
2.2	Single-track dynamic vehicle model.	10
2.3	Double-track dynamic vehicle model.	11
2.4	Wheel frame and velocities.	13
2.5	Tyre camber stiffness variation with respect to slip angle.	14
2.6	Verification of the Dugoff tyre model with camber effect (Paper B).	14
2.7	Dymola vehicle plant model.	16
2.8	Algorithm evaluation illustration.	17
3.1	Comparison of four estimation algorithms in the modified DLC manoeuvre (Paper A).	23
4.1	Comparison of trajectory planning of planners with various levels of model complexity in the evasive DLC manoeuvre (Paper D).	28
4.2	Comparison of trajectory tracking of planners with various levels of model complexity in the evasive DLC manoeuvre (Paper D).	29
5.1	Tracking performance and tyre behaviour without yaw stability control in medium-friction conditions ($\mu = 0.6$) with a reference velocity of 76 km/h (Paper C).	35
5.2	Tracking performance and control actions of Controllers OLTV, OLEA, TLOA and TLRA in high-friction condition ($\mu = 1$) with reference velocity 85 km/h (Paper C).	36
5.3	Tracking performance and control actions from the camber controller with road friction $\mu = 0.6$ (Paper B)	38
5.4	Comparison of trajectory tracking of the four combinations of overactuation with the initial velocity being 76 km/h (Paper E)	40

6.1	Main framework for implementing the studies presented in this dissertation.	45
6.2	OCP implementation of state estimation, trajectory planning and path following and yaw stability control strategies.	46
6.3	Effect of the optimisation techniques and horizon length in the circular manoeuvre (Paper A).	47

List of tables

3.1	State estimates in the modified DLC manoeuvre (Paper A).	23
5.1	Comparison of the four controllers at various reference velocities in high-friction condition ($\mu = 1$) (Paper C).	36
5.2	Results obtained with ($\Delta\gamma = 15-60^\circ/\text{s}$) and without (–) camber control in high-friction ($\mu = 1$) condition (Paper B).	37
5.3	Trajectory tracking errors of the four over-actuation configurations (Paper E).	39

Chapter 1

Introduction

This chapter discusses the challenges of improving road safety and reducing greenhouse gas emissions associated with the popularity of road vehicles. It also presents potential measures for addressing these issues by harnessing active safety, automation, electrification and over-actuated vehicle technologies. It then poses the research objective and questions and introduces the approach used to address them.

1.1 Background

Road vehicles provide freedom of mobility, facilitate social and professional interactions, and promote economic development. With access to private vehicles, people nowadays travel more often and further than before [2], especially in richer countries, where people travel five times further on a daily basis than they did 60 years ago [3]. Moreover, annual person-kilometres for road passenger vehicles¹ have increased considerably in the past two decades [1], as shown in Fig. 1.1. As a result of the increased demand in mobility, global vehicle production, sales and use have grown significantly over the last two decades, according to the statistics from OICA² [1, 4, 5].

When looking to the future, both the passenger and freight transport activities are expected to increase more than two-fold by 2050 compared to 2015 under current government policies, even when considering the impact caused by the COVID-19 global pandemic [6]. The continuously growing demand for road vehicle usage, which is a result of economic development, population growth and improvements in quality of life, has been causing various issues that need to be addressed, including road accidents, carbon dioxide (CO₂) emissions, energy waste, congestion, etc.

¹Road passenger vehicles here include passenger cars, buses and coaches.

²International Organization of Motor Vehicle Manufacturers.

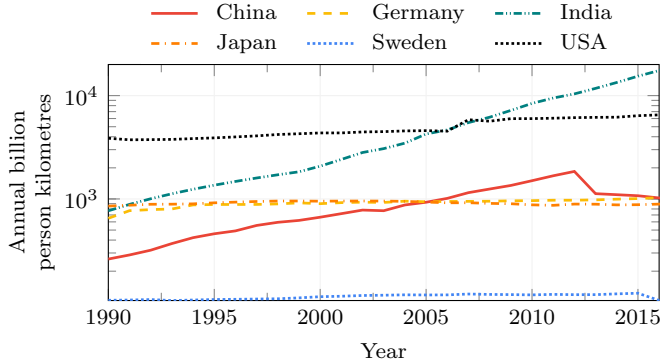


Figure 1.1: Annual person-kilometres for road passenger vehicles [1].

1.1.1 Road safety and automation

Traffic accidents cause approximately 1.3 million fatalities around the world every year, and injuries from traffic accidents are the leading cause of death among young people ages 5 to 29 [7]. Moreover, road accident injuries result in significant economic losses totalling approximately 3% of most countries' gross domestic product (GDP), due to the cost of treatment and reduced productivity [8]. On the other hand, the total number of vehicle occupant deaths decreased by 14% in the 42 ITF³ member countries in 2018 compared with 2010. This reduction is attributed to safer roads, active safety systems such as electronic stability control (ESC) [9] and passive safety devices such as airbags and seat belts [10].

While devices such as airbags mitigate impacts after a crash, ESC protects occupants by preventing the vehicle from skidding and losing control, which can occur in emergency conditions such as obstacle-avoidance manoeuvres. In such cases, ESC helps the driver control the vehicle by generating the desired yaw motion correction so that the vehicle can recover from over- or under-steering. ESC has been shown to be effective in reducing fatalities and serious injuries during single vehicle crashes and roll over accidents [11–13]. For instance, in the United States ESC is estimated to have saved the lives of more than 7,000 occupants in passenger vehicle crashes from 2011 to 2015 [14].

Human errors are critical reasons for road accidents. Examples of such human mistakes include distractions such as using mobile phones while driving and violating traffic laws such as speeding and driving while intoxicated. Specifically, speeding and alcohol-impaired driving were associated with 25% to 65% of fatal road crashes in the ITF countries in 2018 [10]. Of the 36,096 fatalities caused by road vehicle crashes in the United States during 2019, 38.6% were attributed to alcohol-impaired, distracted and drowsy driving [15]. These studies indicate that human drivers are prone to errors that can lead to fatal crashes or serious

³International Transport Forum.

injuries. Therefore, introducing automation into the driving process may help alleviate this issue. While ESC provides a certain degree of assistance to the human driver, autonomous vehicles (AVs) are able to complete all driving tasks without human input [16]. Consequently, human's error-prone driving behaviour can be eliminated and most road accidents avoided, given that AVs perform better than human drivers.

The last two decades have seen rapid development in AVs. Traditional car manufacturers such as General Motors, Ford, Volvo, Audi and Volkswagen, as well as technology companies such as Waymo, Baidu, Cruise, Motional, Zoox and Didi Chuxing, are all developing autonomous driving solutions. Considering the gradual deployment of different levels of automated driving systems and mixed-road participants, e.g., e-scooter riders, cyclists and pedestrians, the driving environment is becoming increasingly complicated. Therefore, in order for AVs to drive safely in such mixed traffic conditions, it is crucial that they be able to follow safe and reliable reference signals from a trajectory planner. This is especially important in critical driving conditions such as obstacle-avoidance manoeuvres where the vehicle enters the region of nonlinear dynamics and the tyres tend to saturate.

While active safety and automated driving systems play a crucial role in saving lives, such systems often rely on the knowledge of critical vehicle states to optimise performance. For instance, to determine when to assist human drivers, ESC might compare the actual state of the vehicle with its reference value and act when the deviation exceeds a certain threshold. However, measuring crucial states such as sideslip angle can be difficult to achieve on production vehicles, due to the high cost of sensors. Therefore, such states need to be obtained by using cost-effective sensors and state estimation techniques.

1.1.2 Electrification and over-actuation

The transport sector⁴ accounted for 27% of global CO₂ emissions through direct fuel consumption⁵ in 2019 [17], among which passenger and freight road vehicles accounted for around 44% and 30% of transport emissions, respectively [18]. Moreover, CO₂ emissions from the transport sector have been increasing steadily over the past 30 years, and they are predicted to continue growing in the near future. Furthermore, increasing demand on passenger and freight transport and the fact that transport has the highest reliance on fossil fuels among all end-use sectors make it difficult to decarbonise [6]. Nonetheless, various measures can be taken to achieve more sustainable transport. Specifically, such measures include reducing unnecessary transport activities, adopting more sustainable transport modes, improving fuel technologies and energy efficiency, and rapidly promoting the use of electric vehicles (EVs) [6, 19].

⁴The calculation allocates the CO₂ emissions during electricity and heat generations to final usage sectors, including Transport, Industry, Buildings and Others.

⁵Emissions from fuel production, vehicle manufacturing, infrastructure building, etc., are excluded from the calculation.

In the past decade, there has been a rapid increase in EV sales. Until 2020, there were more than 10 million EVs in use around the world. In 2020 alone, EV sales reached 3 million, a 40% increase compared with 2019, although global car sales decreased by 16% during the same period as a result of the COVID-19 pandemic [20]. Further, it was predicted that EV sales in 2021 would reach 6.4 million [21]. One fact worth noting is that governmental incentives were a critical factor promoting the purchase of EVs in the past. However, the ratio of governmental subsidies to total customer spending on EVs has decreased in the past five years, indicating that EVs are becoming more and more popular among vehicle owners. To further promote EV usage, more than 20 countries have announced electrification goals, internal combustion engine (ICE) bans or net-zero pledges, with the target years ranging from 2025 to 2050. Based on current governmental policies and goals, it is projected that the global EV stock would increase steadily to a share of 7% of total road vehicles in 2030. Such an EV fleet would contribute to a reduction in greenhouse gas (GHG) emissions of more than 30% compared to a corresponding number of ICE vehicles [20].

As vehicles are becoming more electrified, an increasing number of onboard motion actuators are available. For instance, the BYD Han [22] has one electric motor (EM) installed on each axle, and the Polestar 1 [23] is configured with one ICE in the front axle plus two EMs in the rear. The Tesla Model S Plaid [24] and Audi e-tron S [25] have three EMs in total, one in the front axle and two in the rear. The motion actuator configurations above provide these production cars with enhanced handling and traction performance. When the number of motion actuators exceeds the degrees of freedom (DoFs) to be controlled, the vehicle becomes over-actuated. Zoox [26] has developed a vehicle platform that has the capability of individual traction, all wheel steering and active suspension. This makes the vehicle over-actuated, as the motion actuators outnumber the three directions to be controlled: i.e., longitudinal, lateral and yaw movements. The concept of the autonomous corner module (ACM) [27] was invented in 1998; this technology enables the control of each wheel in its longitudinal, lateral and vertical directions through individual torque, camber, steering and vertical load actuators [28]. Based on ACM, a research concept vehicle (RCV) was developed by KTH Royal Institute of Technology [29] with the capability to individually steer, camber and drive each wheel.

By exploiting such highly over-actuated wheel modules, the vehicle can be controlled more freely [30]. For instance, studies have been carried out using over-actuation to improve energy efficiency [31] of vehicles by reducing tyre energy loss [32] and controlling vehicle power loss [33]. Moreover, over-actuation can contribute to improving road safety through active safety and automated driving systems. When a conventional ICE vehicle performs an obstacle-avoidance manoeuvre, the ESC system can assist the driver in manoeuvring the vehicle by braking the wheels on one side to allow the vehicle recover to the desired trajectory. In contrast, when an over-actuated vehicle with individual wheel traction operates in the same condition, the vehicle can be controlled to brake the wheels on one side but

drive the wheels on the other side. This provides more effective vehicle dynamics control and thus additional safety in analogous dangerous manoeuvres, e.g., during failure conditions [34]. As another example, over-actuation has been studied as a way to improve vehicle path tracking performance [35], which is a crucial task in autonomous driving scenarios.

1.2 Research objective and questions

The need for improved road safety and the trend toward road vehicle electrification and automation are the motivations for the main objectives of this thesis. Specifically, the studies presented in this work aim to investigate the potential of using different means of over-actuation and their combinations to improve the path following and yaw stability performance of AVs in critical driving conditions and to develop state estimation and trajectory planning strategies that are suitable for use in such conditions.

However, from the literature review that is detailed in the following chapters, it can be seen that existing studies are insufficient to achieve the goals of this work in the following aspects. Firstly, previous studies usually address path following and yaw stability separately, which may undermine the overall control performance. Secondly, reliable vehicle state estimation, e.g., in presence of initialisation errors, disturbances and model mismatch, in critical conditions needs to be further studied. Finally, simple vehicle and tyre models may not be suitable for trajectory planning in critical conditions.

Considering the issues identified above and the potential of over-actuation to improve vehicle safety, the research questions (RQs) of the thesis are formulated as follows:

- State estimation for active safety applications
 - How to achieve state estimation in critical manoeuvres? (**RQ 1.1**)
 - How to enable reliable estimation of crucial vehicle states? (**RQ 1.2**)
- Trajectory planning for active safety applications
 - How to achieve yaw stability when planning trajectories in critical conditions? (**RQ 2.1**)
 - How would model complexity affect trajectory planning performance? (**RQ 2.2**)
- Path following and yaw stability control strategies using over-actuation
 - How can path following and yaw stability performance be improved in critical conditions? (**RQ 3.1**)
 - How would different means of over-actuation and their combinations influence path following and yaw stability performance? (**RQ 3.2**)

1.3 Limitations

The intention was to verify the developed algorithms using the KTH RCV platform, but the vehicle was not operational at the time of algorithm assessment. Instead, the algorithms have been assessed by using a sufficiently detailed vehicle plant model which is described in **Paper C**. This vehicle plant was built in Dymola [36] and then exported as a functional mock-up unit (FMU) [37]. Consequently, the FMU model consists of 44 continuous states and 57,330 variables, which is significantly more advanced than the models used to develop those algorithms. Considering this, the FMU vehicle model is a suitable choice for assessing the algorithms developed in the appended studies.

1.4 Research approach

Fig. 1.2 presents a process map that visualises the methods for addressing the research questions identified in Section 1.2, the connections among the methods and the publications that are appended in this thesis. The relationships among the research questions, the corresponding methods, the related thesis chapters and the resulting papers will be further discussed below.

This thesis starts with the modelling of vehicle dynamics, which is a crucial component of the studies covered in the thesis, since model-based methods are used in all these studies: state estimation, trajectory planning, as well as path following and yaw stability control. Both single- and double-track models are used for modelling vehicle behaviour, with different levels of details considered in each type of model. Similarly, the tyre property is mimicked by using both linear and nonlinear models. In particular, the camber effect of the tyre is modelled using a simple, yet effective, component so that the active camber study can be carried out by individually controlling the inclination of each wheel (see **Paper B**). The modelling of vehicle and tyre behaviour is detailed in Chapter 2 and in the appended papers.

The research questions RQs 1.1–1.2 are posed due to the need for reliable state estimation in critical conditions. To address these questions, a double-track vehicle model and a nonlinear tyre model are incorporated into the moving horizon estimation (MHE) [38] algorithm. Specifically, it was found through a literature review that, compared with a Kalman filter (KF) [39] and its altered algorithms, MHE can potentially better deal with model mismatch and external disturbances in state estimation applications. The MHE state estimator that was developed is compared with various other estimators, and all are evaluated in three critical driving manoeuvres in terms of convergence rate, accuracy, as well as robustness to initialisation errors, model mismatch and external disturbances (see **Paper A** and Chapter 3).

The trajectory planning problem – research questions RQs 2.1-2.2 – is presented with the aim of generating proper reference signals for concurrent path following

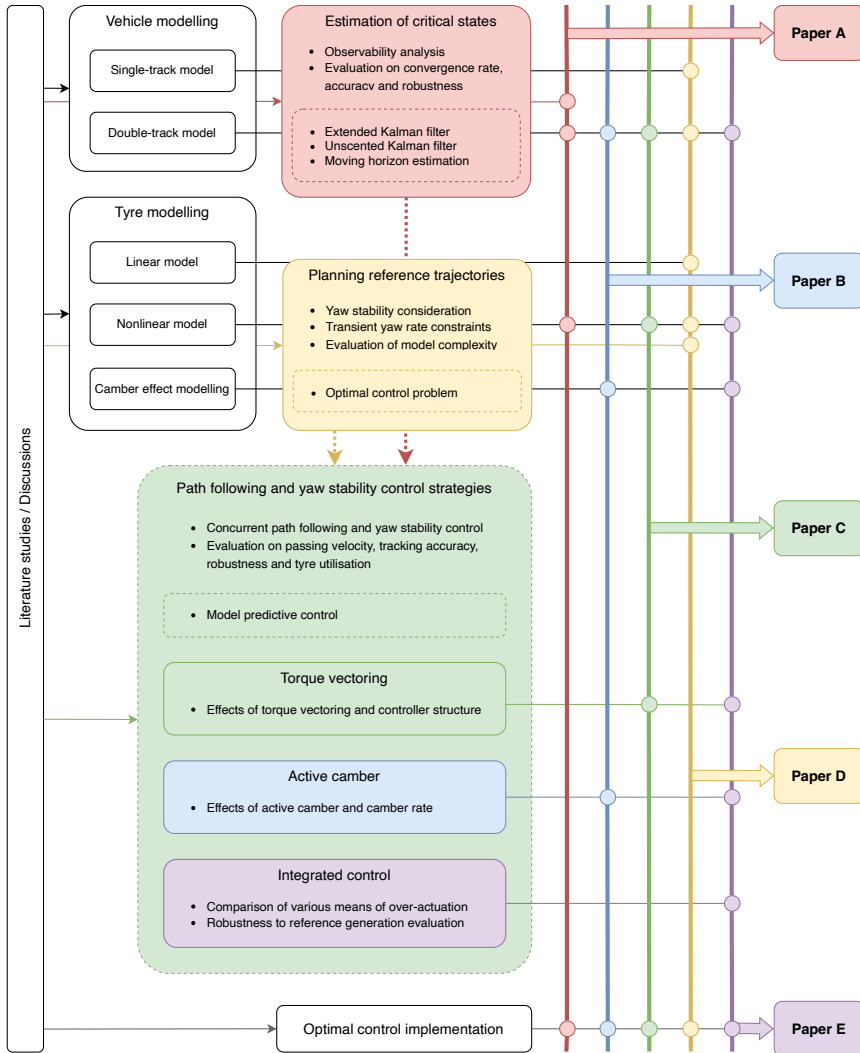


Figure 1.2: Process map for the research presented in this thesis, including modelling, strategies and resulting publications. The blocks on the left part of the map correspond to the thesis chapters, of which the three coloured blocks directly lead to the five papers shown in the rightmost column. The dots along the five vertical lines represent the combinations of methods used in each paper.

and yaw stability control. This issue is addressed by explicitly considering yaw stability in the planner formulation and by analysing the effect of model complexity on the planner performance. To formulate yaw stability in the planner, sideslip angle and yaw rate are planned simultaneously with the path, and constraints concerning these two states are explicitly considered. In addition, transient terms

regarding variation in the sideslip angle are taken into account in the yaw rate constraints for improved dynamic performance. Combining all these with various combinations of vehicle and tyre models of different levels of complexity, trajectory planning is formulated as optimal control problems (OCPs). Planners of various levels of complexity are evaluated in two critical driving manoeuvres at various initial velocities (see **Paper D** and Chapter 4).

Path following and yaw stability control, corresponding to research questions RQs 3.1–3.2, is studied for improved performance by exploiting over-actuation. These questions are approached by exploring the potential of different over-actuation configurations in various critical driving conditions. For better combined performance, path following and yaw stability are controlled simultaneously by coupling a double-track vehicle model and a nonlinear tyre model with the model predictive control (MPC) [40] framework, where constraints concerning yaw stability and actuator limits are considered. Based on this formulation of the problem, the effects of torque vectoring (TV) and controller structure (see **Paper C** and Section 5.3.1) as well as active camber and camber rate (see **Paper B** and Section 5.3.2) on path following and yaw stability performance are analysed and discussed with regard to passing velocity, tracking accuracy, robustness and tyre utilisation. Building on these results, the effects of various combinations of over-actuation are examined in **Paper E** and Section 5.3.3. Additionally, the robustness to trajectory generation of the studied over-actuation cases is investigated in **Paper E** by utilising the trajectory planning results obtained in **Paper D**.

Optimisation-based methods – MHE, OCP and MPC – are adopted to formulate the problems for the research detailed above. Therefore, various aspects of optimal control implementation are covered in Chapter 6, ranging from framework and optimal control problem to parameter tuning and optimisation techniques.

Chapter 2

Vehicle dynamics modelling

The movement of a planar vehicle can be described using its two principal subsystems: the vehicle body and tyre. This chapter describes vehicle and tyre modelling for use in the design of vehicle state estimators, trajectory planners and path following and yaw stability controllers. Additionally, the vehicle plant for evaluating these algorithms is introduced.

2.1 Vehicle modelling

Depending on the specific application at hand, various types of models can be used to simulate vehicle behaviour. While simpler models are easy to implement, more advanced models provide additional details which can better represent the actual vehicle response, especially in critical driving conditions. For instance, the effect of model complexity on trajectory planning performance is studied in **Paper D**.

2.1.1 Single-track kinematic model

By assuming that the front and rear wheels travel in the same directions as the corresponding steering directions [41], a single-track kinematic model can be built (see Fig. 2.1). This model is developed without considering tyre forces that influence vehicle motion but including the additional force of air drag. To represent the transformations among state variables, three frames are used, namely the earth frame XOY , the vehicle body frame x_{boy_b} , and the vehicle frame xoy . Specifically, this model can be represented as

$$m\dot{v} = F_{xy} - C_d A_f \frac{D_a v_x^2}{2} \quad (2.1)$$

$$\dot{\psi} = \frac{v \cos \beta}{l_f + l_r} \tan \delta_f \quad (2.2)$$

$$\dot{X} = v \cos(\psi + \beta) \quad (2.3)$$

$$\dot{Y} = v \sin(\psi + \beta) \quad (2.4)$$

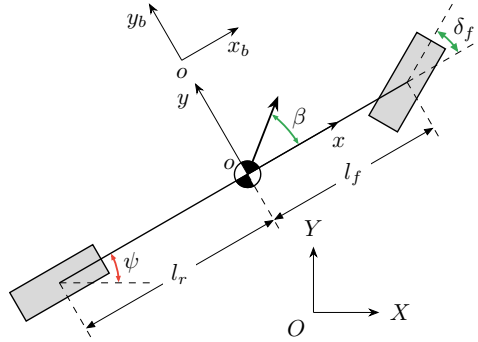


Figure 2.1: Kinematic vehicle model.

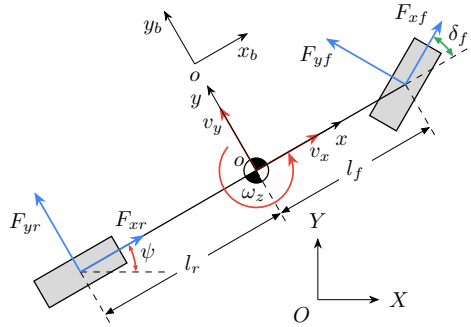


Figure 2.2: Single-track dynamic vehicle model.

where v_x and v_y denote the longitudinal and lateral velocities at the centre of gravity (CoG), respectively; $v = \sqrt{v_x^2 + v_y^2}$ is the combined velocity at CoG; and $\beta = \arctan v_y/v_x \approx v_y/v_x$ (valid for a small angle) is the sideslip angle. ψ represents the yaw angle, X the longitudinal position, and Y the lateral position. δ_f is the steering angle at the front wheels, and F_{xy} the combined actuator force. m signifies the vehicle mass, and l_f and l_r the distance from CoG to the front and rear axles, respectively. C_d , A_f and D_a stand for the drag coefficient, frontal area and air density, respectively. The single-track kinematic model is used in **Paper D**.

2.1.2 Single-track dynamic model

In contrast to the kinematic model described in Section 2.1.1, the vehicle model introduced in Fig. 2.2 takes the tyre forces on the front and rear axles into account and, accordingly, it models the longitudinal, lateral and yaw movements of the vehicle in a dynamic manner. This model is developed by adopting a wheel frame x_toyt [see Fig. 2.4(a)], in addition to the three frames described earlier. This

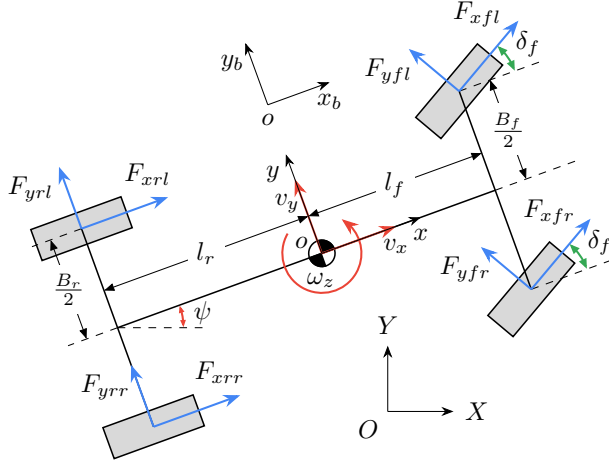


Figure 2.3: Double-track dynamic vehicle model.

model [42] is governed by the following equations:

$$mv_x = F_{xf} \cos \delta_f + F_{xr} - F_{yf} \sin \delta_f + mv_y \omega_z - C_d A_f \frac{D_a v_x^2}{2} \quad (2.5)$$

$$mv_y = F_{xf} \sin \delta_f + F_{yf} \cos \delta_f + F_{yr} - mv_x \omega_z \quad (2.6)$$

$$I_z \dot{\omega}_z = l_f (F_{xf} \sin \delta_f + F_{yf} \cos \delta_f) - l_r F_{yr} \quad (2.7)$$

$$\dot{\psi} = \omega_z \quad (2.8)$$

$$\dot{X} = v_x \cos \psi - v_y \sin \psi \quad (2.9)$$

$$\dot{Y} = v_x \sin \psi + v_y \cos \psi \quad (2.10)$$

where F_{xj} and F_{yj} ($j \in \mathcal{B}$) represent the longitudinal and lateral axle forces in frame $x_t o y_t$, respectively, in which $\mathcal{B} = \{f, r\}$ is a set denoting the front and rear axles. ω_z is the yaw rate around CoG in frame xoy , and I_z the vehicle yaw inertia. The single-track dynamic model is also used in **Paper D**.

2.1.3 Double-track dynamic model

As an extension of the single-track dynamic model given in Section 2.1.3, the double-track dynamic model shown in Fig. 2.3 considers each corner of the vehicle individually. As a result, this model has seven degrees of freedom (DoFs) in total, including longitudinal, lateral and yaw movements of the vehicle body and the rotational dynamics of the four wheels. Moreover, with this model, load transfer along the longitudinal and lateral directions of vehicle frame xoy can be taken into account, and the longitudinal and lateral tyre forces can be determined for each wheel. This provides a more detailed way to simulate vehicle behaviour. This model is given as

follows [41, 43]:

$$m\dot{v}_x = mv_y\omega_z - (F_{yfl} + F_{yfr}) \sin \delta_f + (F_{xfl} + F_{xfr}) \cos \delta_f + F_{xrl} + F_{xrr} \quad (2.11)$$

$$m\dot{v}_y = -mv_x\omega_z + (F_{yfl} + F_{yfr}) \cos \delta_f + F_{yrl} + F_{yrr} + (F_{xfl} + F_{xfr}) \sin \delta_f \quad (2.12)$$

$$\begin{aligned} I_z\dot{\omega}_z &= l_f(F_{yfl} + F_{yfr}) \cos \delta_f - l_r(F_{yrl} + F_{yrr}) + \frac{B_f}{2}(F_{xfr} - F_{xfl}) \cos \delta_f \\ &\quad + \frac{B_r}{2}(F_{xrr} - F_{xrl}) \end{aligned} \quad (2.13)$$

$$\dot{X} = v_x \cos \psi - v_y \sin \psi \quad (2.14)$$

$$\dot{Y} = v_x \sin \psi + v_y \cos \psi \quad (2.15)$$

$$\dot{\psi} = \omega_z \quad (2.16)$$

$$I_{wi}\dot{\omega}_i = T_i - r_e F_{xi} \quad (2.17)$$

where ω_i ($i \in \mathcal{A}$) is the angular velocity of the wheel in frame $x_t o y_t$, in which $\mathcal{A} = \{fl, fr, rl, rr\}$ is a set denoting the front left, front right, rear left and rear right wheels. T_i represents the drive/braking torque on the wheel, and F_{xi} and F_{yi} the longitudinal and lateral tyre forces, respectively. B_f and B_r are the front and rear track width, respectively; I_{wi} the wheel rotational inertia; and r_e the tyre radius. Double-track dynamic models are used in **Papers A–E**.

In order to calculate the longitudinal and lateral tyre forces, the wheel vertical load is required. By considering steady-state conditions and ignoring the effect of suspension and the coupling between the roll and pitch movements, the vertical load equations are derived as [42]

$$F_{zfl} = \frac{l_r mg}{2(l_f + l_r)} - \frac{h_g m a_x}{2(l_f + l_r)} - \frac{l_r h_g m a_y}{B_f(l_f + l_r)} \quad (2.18a)$$

$$F_{zfr} = \frac{l_r mg}{2(l_f + l_r)} - \frac{h_g m a_x}{2(l_f + l_r)} + \frac{l_r h_g m a_y}{B_f(l_f + l_r)} \quad (2.18b)$$

$$F_{zrl} = \frac{l_f mg}{2(l_f + l_r)} + \frac{h_g m a_x}{2(l_f + l_r)} - \frac{l_f h_g m a_y}{B_r(l_f + l_r)} \quad (2.18c)$$

$$F_{zrr} = \frac{l_f mg}{2(l_f + l_r)} + \frac{h_g m a_x}{2(l_f + l_r)} + \frac{l_f h_g m a_y}{B_r(l_f + l_r)} \quad (2.18d)$$

where a_x and a_y are the longitudinal and lateral accelerations in frame $x_b o y_b$, respectively; and F_{zi} ($i \in \mathcal{A}$) is the vertical tyre force in frame $x_t o y_t$. h_g is the height of CoG, and g the gravitational acceleration.

2.2 Tyre modelling

While the vehicle models detailed in Section 2.1 mimic vehicle behaviour as a whole, tyre models depict the interaction between the vehicle body and the road and provide input for vehicle modelling. The tyre models detailed in this section are developed in steady-state conditions, which are commonly used in vehicle dynamics control applications. Various types of non-steady-state tyre models were introduced by Pacejka [44].

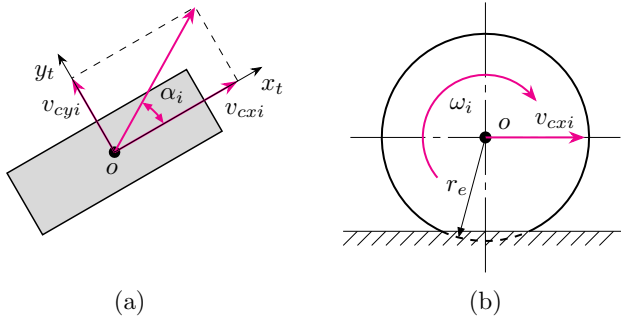


Figure 2.4: Wheel frame and velocities.

2.2.1 Linear tyre model

By ignoring the coupling effect between longitudinal and lateral tyre forces, the lateral tyre force can be represented in a linear relationship to the tyre slip angle as follows:

$$F_{yj} = C_{\alpha j} \alpha_j \quad (2.19)$$

where $\alpha_j = \arctan \frac{v_{cyj}}{v_{cxj}}$ ($j \in \mathcal{B}$) is the tyre slip angle in frame $x_t o y_t$ [see Fig. 2.4(a)], in which v_{cxj} and v_{cyj} are the longitudinal and lateral velocities at the wheel centre, respectively. $C_{\alpha j}$ denotes the axle cornering stiffness.

As can be seen, with this model the tyre force would reach an unreasonable value if the slip angle becomes too large. Therefore, this tyre model is valid within a small range of slip angles. This model is used in **Paper D**.

2.2.2 Dugoff tyre model

To extend the capability of the linear tyre model given in Section 2.2.1, the Dugoff tyre model [45] can be used in combined slip conditions and works for an extended range of slip angles. The Dugoff model derives from the assumption of uniform vertical load distribution across the tyre-road contact area. This model is beneficial in terms of independent longitudinal and lateral tyre stiffness values and the inclusion of a simple road friction coefficient [41]. Specifically, this model is given by

$$F_{xi} = C_{\kappa i} \frac{\kappa_i}{1 + \kappa_i} f(\lambda_i) \quad (2.20a)$$

$$F_{yi} = C_{\alpha i} \frac{\tan \alpha_i}{1 + \kappa_i} f(\lambda_i) \quad (2.20b)$$

$$\lambda_i = \frac{\mu F_{zi}(1 + \kappa_i)}{2((C_{\kappa i} \kappa_i)^2 + (C_{\alpha i} \tan \alpha_i)^2)^{1/2}} \quad (2.20c)$$

$$f(\lambda_i) = \begin{cases} (2 - \lambda_i)\lambda_i, & \text{if } \lambda_i < 1 \\ 1, & \text{if } \lambda_i \geq 1 \end{cases} \quad (2.20d)$$

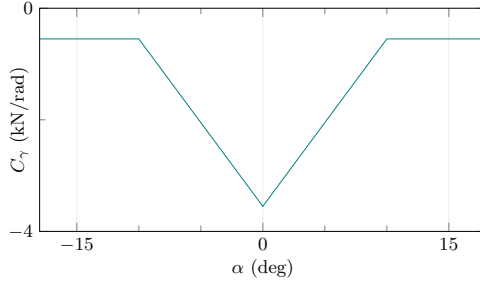


Figure 2.5: Tyre camber stiffness variation with respect to slip angle.

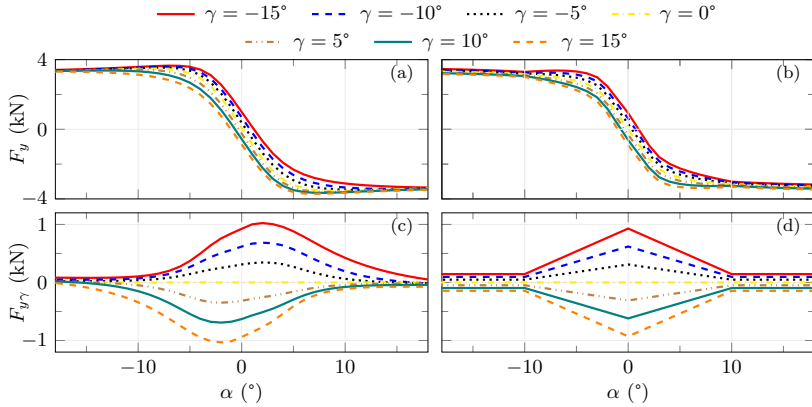


Figure 2.6: Verification of the Dugoff tyre model with camber effect (**Paper B**). (a) and (c) show the lateral tyre force and the gain due to camber, respectively, from the MF tyre equations [44, Eqs. (4.E1)–(4.E78)], and (b) and (d) show the corresponding tyre forces from the Dugoff tyre model with camber effect as described in Section 2.2.3.

where $\kappa_i = \frac{\omega_i r_e - v_{cxi}}{v_{cxi}}$ and $\alpha_i = \arctan \frac{v_{cyi}}{v_{cxi}}$ ($i \in \mathcal{A}$) are the tyre slip ratio and slip angle in frame x_{t0y_t} , respectively (see Fig. 2.4). $C_{\kappa i}$ and $C_{\alpha i}$ are the tyre cornering and longitudinal stiffness, respectively; and μ denotes the road friction coefficient. This model is used in **Papers C, D and E**.

2.2.3 Dugoff tyre model with camber effect

Both the linear model introduced in Section 2.2.1 and the Dugoff model described in Section 2.2.2 are commonly used tyre models for controller design, where the tyre forces are mainly functions of the tyre slip angle and/or slip ratio. Additionally, to represent the influence of wheel camber on the lateral tyre forces, a simple, yet effective, linear component is developed in **Paper B**, which allows for individually controlling the inclination angle of each wheel. Specifically, in addition to Eq. (2.20), the extra camber tyre force in the Dugoff tyre model with camber effect is

given by

$$F_{y\gamma i} = C_{\gamma i} \gamma_i \quad (2.21a)$$

$$C_{\gamma i} = \begin{cases} C_{\gamma 0i} + C_{\gamma \alpha i} |\alpha_i|, & \text{if } |\alpha_i| < \alpha_{lim} \\ C_{\gamma fi}, & \text{if } |\alpha_i| \geq \alpha_{lim} \end{cases} \quad (2.21b)$$

where $F_{y\gamma i}$ ($i \in \mathcal{A}$) denotes the extra lateral tyre force due to camber effect in frame $x_{toy t}$, γ_i the camber angle, and $C_{\gamma i}$ the camber stiffness. $C_{\gamma 0i}$ and $C_{\gamma fi}$ represent the camber stiffness when with zero tyre slip angle and when the slip angle reaches α_{lim} , respectively, in which α_{lim} is a saturation value that depends on tyre property; and $C_{\gamma \alpha i}$ denotes the variation in camber stiffness with regard to the tyre slip angle. This model is used in **Papers B and E**.

Note that the wheel camber angle γ_i here is defined as the angle between the wheel plane and the plane vertical to the ground [44]. Moreover, the camber angle is defined as positive if it results in a negative camber tyre force, to be consistent with the sign definition of tyre slip angle.

The camber stiffness variation, as defined in Eq. (2.21b), with respect to tyre slip angle can be seen in Fig. 2.5. As a result, the verification of the Dugoff tyre model with camber effect is shown in Fig. 2.6. As can be seen, the extra camber tyre force given by Eq. (2.21) does a good job of imitating the camber property of the more sophisticated Magic Formula (MF) tyre model, which is described in Section 2.2.4. For instance, camber stiffness reduces with tyre slip angle and saturates after reaching a certain slip angle value. Moreover, the overall behaviour of the camber tyre model does a good job of capturing the characteristics of the MF tyre model.

2.2.4 Magic Formula tyre model

Despite the simplicity of the tyre models described in Sections 2.2.1–2.2.3, they may lack the considerations of non-uniform pressure distribution, friction coefficient adjustment, inflation pressure, etc. To this end, the semi-empirical tyre model Magic Formula is introduced to determine tyre forces and moments. The simplified representation of the MF tyre model can be given as [44]

$$y_M = D \sin[C \arctan\{Bx_M - E(Bx_M - \arctan Bx_M)\}] \quad (2.22a)$$

$$Y_M(X_M) = y_M(x_M) + S_V \quad (2.22b)$$

$$x_M = X_M + S_H \quad (2.22c)$$

where X_M is the input variable, e.g., κ_i or $\tan \alpha_i$, and Y_M the output, e.g., F_{xi} or F_{yi} ($i \in \mathcal{A}$). B , C and E denote the stiffness, shape and curvature factors, respectively; D the peak value; and S_H and S_V the horizontal and vertical shift, respectively. The full set of equations have been derived by Pacejka [44, Eqs. (4.E1)–(4.E78)].

The lateral tyre force that this model yields is shown in Fig. 2.6(a). This model is commonly used in high-fidelity applications: e.g., software for vehicle dynamics simulations, due to its inclusion of extensive modelling details. In **Papers A–E**,

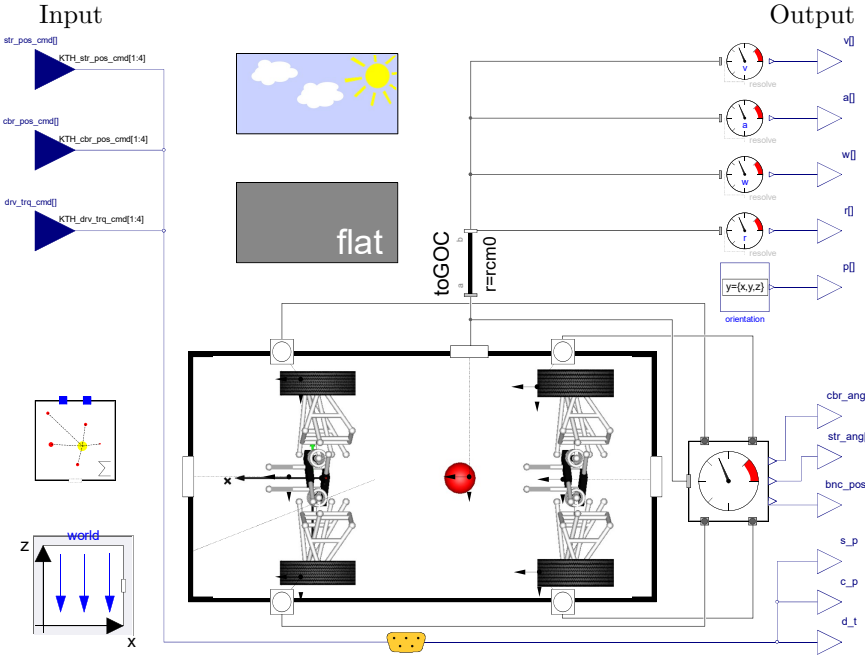


Figure 2.7: Dymola vehicle plant model.

this model is adopted to develop the vehicle plant model for algorithm assessment, which is described in Section 2.4.

2.3 Model summary

Combining the vehicle and tyre models described in Sections 2.1 and 2.2, the system dynamics can be represented in the following continuous-time form:

$$\dot{x} = f_c(x, u) \quad (2.23a)$$

$$y = h_c(x, u) \quad (2.23b)$$

where x , u and y are the state, input and output vectors, respectively.

By using proper numerical techniques, which will be detailed in Chapter 6, the continuous-time system defined by Eq. (2.23) can be re-written in the following discrete-time form:

$$x_{k+1} = f(x_k, u_k) \quad (2.24a)$$

$$y_k = h(x_k, u_k). \quad (2.24b)$$

In the following chapters, this system representation will be used in the design of the estimators, planners and controllers.

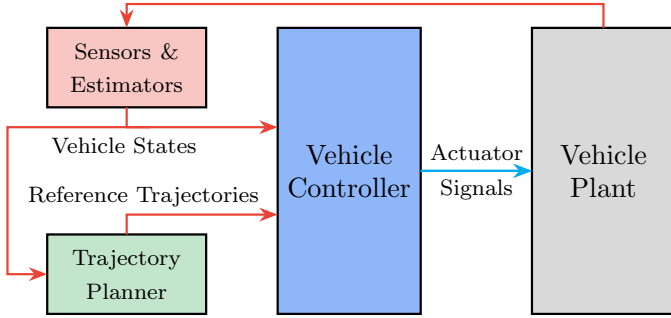


Figure 2.8: Algorithm evaluation illustration.

2.4 Vehicle plant modelling

The vehicle plant model features the KTH RCV [29] with the functionalities of four-wheel steering, drive and camber. The plant model is developed in **Dymola** [36] by using the physical modelling language **Modelica** and the Vehicle Dynamics Library. Specifically, the main components of the vehicle plant include double-wishbone suspensions, wheels with the complete MF tyre model [44], an aerodynamics component, as well as the steering, drive and camber actuators. This vehicle plant is illustrated in Fig. 2.7 and is also detailed in **Paper C**.

The Dymola vehicle plant is exported as an FMU [37] with 44 continuous states and 57,330 variables, which is significantly more advanced than the models derived in Sections 2.1–2.3. Consequently, this FMU plant is used to assess the algorithms developed in the following chapters. The algorithm assessment framework by using this vehicle plant is illustrated in Fig. 2.8 and further detailed in Chapter 6.

Chapter 3

State estimation

Having introduced the models in Chapter 2, this chapter now describes various algorithms for vehicle state estimation. Three moving horizon estimation based algorithms and the unscented Kalman filter are presented in more detail, and the results for these algorithms are discussed.

3.1 Background

It is essential to have knowledge of vehicle states in order for the vehicles' active safety systems to function. While signals like yaw rate can be obtained by using low-cost inertial measurement unit (IMU) devices, critical states like sideslip angle can be difficult to measure, especially with the cost-effective sensors installed on production vehicles. Therefore, state estimators/observers are required to obtain such states.

State estimators can be designed by incorporating a system model with an estimation algorithm. There are two main categories of models used for vehicle state estimation: kinematics-based and dynamics-based models. Kinematics-based estimators do not rely on specific vehicle or tyre models/parameters and usually yield state estimates – e.g., sideslip angle – by considering the mathematical relationships among signals gauged by Global Positioning System (GPS) and IMU devices [46–48]. However, these methods may suffer from sensor bias and faults, potential loss of GPS signals and the low update frequency of GPS devices (or their high cost) [49], although they are simple to implement.

On the other hand, dynamics-based estimators, which involve vehicle and tyre models such as those described in Chapter 2, have been proposed as a way to overcome the deficiencies of the kinematics-based methods. For instance, Anderson and Bevly [50] estimated vehicle sideslip angle and yaw rate by modelling the system with a single-track dynamic vehicle model coupled with a linear tyre model, using Kalman filter (KF) [39] as the estimation algorithm. With a similar system model, sideslip and roll angles were detected in by using a KF with the measurements from

tyre force sensors [51]. To extend the application of state estimators to nonlinear vehicle operation conditions, studies have adopted double-track dynamic vehicle models and nonlinear tyre models, combining them with algorithms such as sliding-mode observer (SMO) [52], extended Kalman filters (EKFs) [42, 53] and unscented Kalman filters (UKFs) [54, 55]. Previous studies have also adopted particle filter (PF) [56], deep neural network (DNN) [57] and moving horizon estimation (MHE) [58–60] for estimating vehicle states and parameters.

In **Paper A**, MHE is used for monitoring crucial vehicle states in critical driving conditions, due to its potential benefits in addressing model mismatch and external disturbances and its natural way of handling nonlinear system models. Specifically, a nonlinear system model is incorporated into three MHE-type estimators and a UKF for state estimation. These estimators are evaluated in various critical driving scenarios to assess their effectiveness in reliable state estimation.

3.2 Estimation algorithms

3.2.1 Kalman filter

At each time step, KF yields a state estimate through two phases. It first propagates the state estimate and the corresponding error covariance using the system model, which is called the time update. Subsequently, it updates the state estimate and its error covariance using the measured signals with a measurement update step [39]. This updated state estimate can then be used to determine the desired state to be estimated. In the context of vehicle state estimation, KF is a popular option to use with linear system models.

3.2.2 Extended Kalman filter

Building upon Eq. (2.24), a nonlinear system for estimator design can be denoted by

$$x_{k+1} = f(x_k, u_k) + w_k \quad (3.1a)$$

$$y_k = h(x_k, u_k) + v_k \quad (3.1b)$$

where the process and measurement noise vectors w_k and v_k satisfy

$$w_k \sim N(0, Q_k) \quad (3.2a)$$

$$v_k \sim N(0, R_k). \quad (3.2b)$$

In Eq. 3.2, Q_k and R_k are the covariance matrices for the process and measurement noises, respectively. As can be seen, the process and measurement noises are assumed to be Gaussian, zero mean and uncorrelated and are known.

In the case of a nonlinear system denoted by Eq. (3.1), the original KF formulation can no longer be used directly for state estimation; instead, EKF [61] can be

used. EKF linearizes the nonlinear system around the KF estimate, which yields the desired Jacobian matrices to represent the corresponding linear system at each sampling step. Subsequently, like the case of KF, time and measurement update phases are performed to propagate and update the state estimate and corresponding error covariance. EKF is used in **Paper A** to update the arrival cost of the MHE, which will be detailed in Section 3.3.

3.2.3 Unscented Kalman filter

Similar to other KF-type estimators, UKF [62] also relies on time and measurement updates to obtain the state estimate and corresponding error covariance. Moreover, like EKF, UKF was developed to work with nonlinear systems such as Eq. (3.1). However, unlike EKF, which relies on calculating Jacobian matrices from the nonlinear system, UKF instead uses unscented transformation with the original system to complete the time and measurement update steps. As a result, UKF has a higher order of accuracy than EKF – three versus one – and can be more computationally efficient than EKF, especially for highly nonlinear systems. **Paper A** adopts UKF with [63, Eqs. (14.56)–(14.67)].

3.3 Moving horizon estimation

While EKF and UKF use different techniques to approximate the original nonlinear system and/or state estimate, MHE [38, 64, 65] is able to naturally deal with nonlinearities in the problem formulation. Moreover, MHE adopts a fixed size for most recent measured signals, instead of merely using measurements at the current time step for state estimation. Therefore, MHE tends to be more accurate in state evolution and more robust in handling modelling mismatch, external disturbances, etc. One fact worth noting is that MHE with the horizon length being 1 is similar to the one-step filters EKF and UKF [66]. **Paper A** uses MHE for vehicle state estimation.

Essentially, MHE can be defined as an optimisation problem, as follows [67]:

$$\begin{aligned} \min_{\mathbf{x}_h, \mathbf{w}_h, \mathbf{v}_h} & \left\| \mathbf{x}_{k-N_h} - \mathbf{x}_{k-N_h|k-N_h-1} \right\|_{P_{k-N_h|k-N_h-1}^{-1}}^2 \\ & + \sum_{i=k-N_h}^{k-1} \|\mathbf{w}_i\|_{Q_k^{-1}}^2 + \sum_{i=k-N_h}^k \|\mathbf{v}_i\|_{R_k^{-1}}^2 \end{aligned} \quad (3.3a)$$

$$\text{s. t. } \mathbf{x}_{i+1} = f(\mathbf{x}_i, \mathbf{u}_i) + \mathbf{w}_i \quad (3.3b)$$

$$\mathbf{y}_i = h(\mathbf{x}_i, \mathbf{u}_i) + \mathbf{v}_i \quad (3.3c)$$

where $\mathbf{x}_h = [x_{k-N_h}, \dots, x_k]$, $\mathbf{w}_h = [w_{k-N_h}, \dots, w_{k-1}]$ and $\mathbf{v}_h = [v_{k-N_h}, \dots, v_k]$ are sequences of vectors for state, process noise and measurement noise, respectively, and N_h is the horizon length of the MHE estimator.

For a state estimate with the subscript $i|k$, e.g., $x_{i|k}$, it is defined as an estimate obtained with measurements up until sampling step k . With this notation,

$x_{k-N_h|k-N_h-1}$ is called the *a priori* state estimate at time step $k - N_h$, as this state estimate has yet not been updated by using the measured signals at this time instant, and $P_{k-N_h|k-N_h-1}$ is the corresponding error covariance matrix. Similarly, $x_{k-N_h|k-N_h}$ is the *a posteriori* state estimate at $k - N_h$, as it has already been updated with the latest measurements at this time step, and $P_{k-N_h|k-N_h}$ denotes the corresponding error covariance matrix.

As can be seen from Eq. (3.3a), the MHE cost function consists of three terms of L2-norm. For instance, $\|w_i\|_{Q_k^{-1}}^2$ can be further expressed as $w_i^T Q_k^{-1} w_i$. The three terms account for arrival cost, model mismatch and measurement errors, respectively. As with the cases for EKF and UKF, Q_k and R_k denote the error covariance matrices for the process and measurement noises, respectively. If there are relatively large process noises/modelling errors – i.e., Q_k has relatively large components – then it means that low trust should be put in the model. This is why the inverse matrix Q_k^{-1} is applied as the weight matrix corresponding to the process noise term in Eq. (3.3a), as this relatively small weight would allow for relatively large modelling errors. For a similar reason, inverse matrices $P_{k-N_h|k-N_h-1}^{-1}$ and R_k^{-1} are used for the arrival cost and measurement noise terms in the MHE cost function. On the other hand, if the model is more trustworthy than the measurements, then a relatively small Q_k , compared with R_k , should be used, and vice versa.

To ensure the best possible performance with respect to stability and optimality, all past measurements can be used for state estimation; this constitutes the so-called full information estimation (FIE) [66]. However, this would obviously entail a computationally unbearable burden as time evolves. To tackle this issue, a fixed size rather than an increasing size of past measurements – $N_h + 1$ sequences of most recent measurements – can be considered in the estimation formulation. This results in the MHE problem as formulated in Eq. (3.3). To compensate for the loss of past information from the MHE formulation, the arrival cost – the first term in Eq. (3.3a) – is adopted. Commonly used approaches for determining the arrival cost include EKF-based [64] and UKF-based [68] methods; smoothing or filtering updating strategies [66].

For simplicity, **Paper A** adopts the standard EKF formulation [63] for arrival cost calculation:

$$\begin{aligned} K_{k-N_h} &= P_{k-N_h|k-N_h-1} C_{k-N_h|k}^T (R_k \\ &\quad + C_{k-N_h|k} P_{k-N_h|k-N_h-1} C_{k-N_h|k}^T)^{-1} \end{aligned} \quad (3.4a)$$

$$\begin{aligned} x_{k-N_h|k-N_h} &= x_{k-N_h|k-N_h-1} + K_{k-N_h} (y_{k-N_h} \\ &\quad - h(x_{k-N_h|k}, u_{k-N_h})) \end{aligned} \quad (3.4b)$$

$$P_{k-N_h|k-N_h} = (I - K_{k-N_h} C_{k-N_h|k}) P_{k-N_h|k-N_h-1} \quad (3.4c)$$

$$x_{k-N_h+1|k-N_h} = f(x_{k-N_h|k}, u_{k-N_h}) \quad (3.4d)$$

$$P_{k-N_h+1|k-N_h} = A_{k-N_h|k} P_{k-N_h|k-N_h} A_{k-N_h|k}^T + Q_k \quad (3.4e)$$

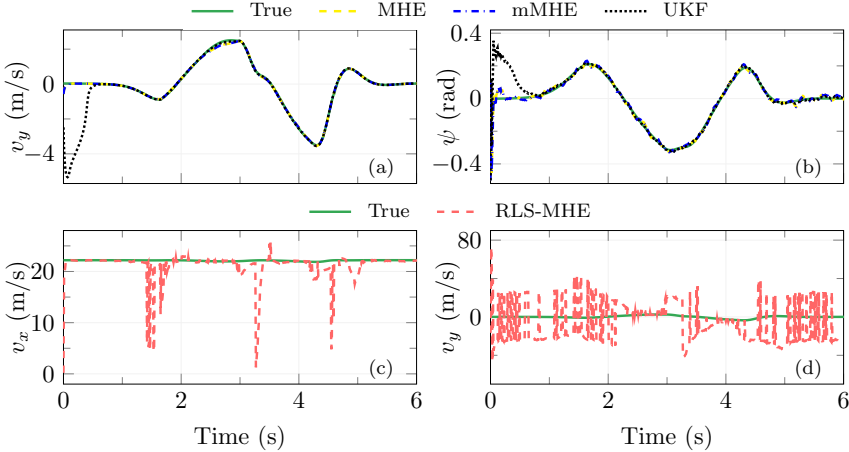


Figure 3.1: Comparison of four estimation algorithms in the modified DLC manoeuvre (**Paper A**). (a) and (b) show a comparison without the RLS-MHE estimator. (c) and (d) present the velocity estimates from the RLS-MHE.

Table 3.1: State estimates in the modified DLC manoeuvre (**Paper A**).

Estimator	v_x (m/s)		v_y (m/s)		ψ (rad)		t_{cvg} (s)
	e_{max}	e_{rms}	e_{max}	e_{rms}	e_{max}	e_{rms}	
MHE	0.137	0.049	0.606	0.064	0.500	0.034	0.21
mMHE	0.137	0.049	0.606	0.063	0.500	0.034	0.21
RLS-MHE	22.00	2.994	72.66	22.30	55.60	7.813	> 6
UKF	3.864	0.345	5.368	1.033	0.500	0.067	0.58

^a The time to converge, t_{cvg} , is calculated in such a way that all the estimated states converged within a tolerance to the true vehicle states.

where K_{k-N_h} is the Kalman gain, and u_{k-N_h} and y_{k-N_h} are the input and measurement signals at time step $k - N_h$, respectively. The Jacobian matrices $A_{k-N_h|k}$ and $C_{k-N_h|k}$ are calculated around the smoothed state estimate $x_{k-N_h|k}$ as

$$A_{k-N_h|k} = \frac{\partial f}{\partial x} \Big|_{x_{k-N_h|k}} \quad C_{k-N_h|k} = \frac{\partial h}{\partial x} \Big|_{x_{k-N_h|k}}. \quad (3.5)$$

3.4 Results and discussion

Besides UKF and MHE presented previously, this section discusses two MHE variants, a modified MHE (mMHE) [69] and a recursive-least-squares MHE (RLS-MHE). While mMHE discards the process noise term from the MHE formulation, RLS-MHE further drops the arrival cost term. These simplifications are made in

the hope of reducing the computational burden associated with MHE, which will be further discussed in Chapter 6. All these are also detailed in **Paper A**.

Paper A contributes to the topic of vehicle state estimation by synthesising a double-track dynamic vehicle model and a simplified MF tyre model for state estimation and by showing the local observability of this nonlinear system model. The three MHE-type estimators and UKF are incorporated with the system model for state estimation, and they are evaluated in three critical driving manoeuvres in terms of convergence rate, accuracy, as well as robustness to initialisation errors, model mismatch and external disturbances.

Fig. 3.1 and Table 3.1 show the comparison of the four algorithms for vehicle state estimation in the modified double-lane change (DLC) [43] manoeuvre. As can be seen, when the initial guesses are unsatisfactory, MHE converges to the true values faster than UKF and RLS-MHE. Moreover, unlike the case of UKF, where the v_y and ψ estimates deviate sharply after initialisation, the corresponding state estimates from MHE converge to the reference values immediately after the initial time step. mMHE performs comparably to MHE due to the relatively high accuracy of the system model in this manoeuvre. RLS-MHE performs much worse than MHE and UKF. Specifically, the state estimates from RLS-MHE frequently deviate heavily from the true values. This is mainly due to the fact, unlike MHE or mMHE, neither past information nor process noise are considered in the RLS-MHE formulation.

Chapter 4

Trajectory planning

This chapter introduces the design of trajectory planners used in critical driving scenarios. Planners of various levels of complexity are developed using different combinations of the vehicle and tyre models described in Chapter 2, and examples of results are presented and discussed.

4.1 Background

With the gradual deployment of different levels of automated driving systems and mixed-road participants, e.g., e-scooter riders and pedestrians, the driving environment is becoming more challenging, requiring AVs to drive safely in any condition. For AVs to operate safely, especially in critical driving scenarios – e.g., in an obstacle-avoidance manoeuvre – the generation of reliable and accurate trajectories from the planner is crucial.

In previous trajectory planning studies, various types of models have been adopted, including the point-mass model [70], single-track kinematic model [71] and single-track dynamic vehicle models [72–74]. While planners using these models are simple to implement, the underlining assumptions for developing these models may not hold in critical conditions such as an obstacle-avoidance manoeuvre. Specifically, lateral tyre forces may not have a linear relationship with the tyre slip angle any more. Furthermore, longitudinal and lateral tyre forces tend to be coupled in such conditions. This may result in unrealistic/inaccurate reference trajectories, such as under- or over-estimated sideslip angle. Moreover, states considering yaw stability – i.e., yaw rate and sideslip – are usually planned separately from the path in previous studies. If such reference signals are used in lower-level vehicle controllers to achieve active safety – e.g., in the path following and yaw stability controller – control performance and vehicle safety may be compromised.

To address the issues identified above, the yaw stability states are planned together with the path in **Paper D**, in order to potentially achieve improved path following and yaw stability performance. In addition, the effect of modelling accu-

racy on trajectory planning and control performance in critical driving scenarios is studied to determine the proper model for use in such conditions.

4.2 Planner formulation

Commonly used planning algorithms are mainly developed based on graph search, sampling, interpolation curve and numerical optimisation. A detailed review of these algorithms can be found in an earlier work by Gonzalez et al. [75]. For trajectory planning in critical driving conditions, obstacles should be avoided without losing yaw stability. Therefore, various types of constraints need to be considered, such as those concerning yaw stability, obstacle and actuator physical limits. For this, a numerical optimisation-based planner is used in **Paper D**, due to its natural way of handling constraints in problem formulation.

With the aim of planning trajectories through an evasive DLC manoeuvre [76] and inspiration from Fors et al. [77], the trajectory planner can be formulated as the following optimisation problem:

$$\min_{v_0, v_f} -0.05v_0 - 0.05v_f \quad (4.1a)$$

$$\text{s. t. } x_{i+1} = f(x_i, u_i), i \in \{0, 1, \dots, N_t - 1\} \quad (4.1b)$$

$$g_t(x_i) \leq 0 \quad (4.1c)$$

$$x_0 = \tilde{x}_0 \quad x_f = \tilde{x}_f \quad (4.1d)$$

$$u_0 = \tilde{u}_0 \quad (4.1e)$$

$$u_{min} \leq u_i \leq u_{max} \quad (4.1f)$$

$$\Delta u_{min} \leq \Delta u_i \leq \Delta u_{max} \quad (4.1g)$$

where v_0 and v_f denote the initial and final velocities, respectively, and Δu the variation of the control vector. $g_t(\cdot)$ is the state constraint equation, and N_t the horizon length of the planner. $x_{0/f}$ and u_0 represent the initial/final state and control vectors, respectively, and $\tilde{x}_{0/f}$ and \tilde{u}_0 the corresponding initial/final values. $u_{min/max}$, $\Delta u_{min/max}$, $\beta_{min/max}$ and $\omega_{zmin/max}$ are the boundaries for the corresponding control and state variables.

As indicated by the cost function denoted in Eq. (4.1a), one of the goals is to maximise both the entry and exit velocities. Moreover, this optimisation problem includes the constraints applied to the state and control variables, as can be seen in Eq. (4.1c)–(4.1g). Specifically, constraints are applied to sideslip angle and yaw rate to achieve yaw stability. For sideslip angle, the following constraints are applied [41]:

$$\beta_{max} = \arctan(0.02\mu g) \quad (4.2a)$$

$$\beta_{min} = -\arctan(0.02\mu g). \quad (4.2b)$$

For the yaw rate constraints, a commonly used method neglects the second and third terms of the right-hand side of the following equation, as derived by

Rajamani [41]:

$$\omega_{zmax} = \frac{\mu g}{v_x} - \tan(\beta) \frac{\dot{v}_x}{v_x} - \frac{\dot{\beta}}{\sqrt{1 + \tan^2 \beta}}. \quad (4.3)$$

During the test manoeuvre, longitudinal velocity can have a relatively small variation but relatively large magnitude. Moreover, the sideslip angle is usually rather small. This means that the second term can be neglected, and $\tan^2 \beta$ can be treated as zero. Nevertheless, the variation in sideslip angle may not be omitted from Eq. (4.3). Therefore, the yaw rate constraints used in the planner formulation are given as follows:

$$\omega_{zmax} = \frac{\mu g}{v_x} - \dot{\beta} \quad (4.4a)$$

$$\omega_{zmin} = -\frac{\mu g}{v_x} - \dot{\beta}. \quad (4.4b)$$

When these yaw rate constraints are applied, the dynamic performance of the vehicle would not be overly limited when planning trajectories through the test manoeuvre. More detailed discussions on the influence of these constraints can be found in **Paper B**.

4.3 Results and discussion

Using the planner formulation Eq. (4.1), this section discusses five trajectory planners with different levels of model complexity which has been detailed in Chapter 2. The three single-track planners include Planners STK, STDL and STD, which are designed by using a single-track kinematic model, a single-track dynamic vehicle model with a linear tyre model and a single-track dynamic vehicle model with a simplified MF tyre model, respectively. The two double-track planners DTB and DTMLt are formulated using a double-track dynamic vehicle model with the Dugoff tyre model, and a double-track dynamic vehicle model with load transfer and the MF tyre model, respectively.

The five trajectory planners are evaluated by examining their trajectory generation and tracking performance. Specifically, the one-level controller with torque vectoring (OLTV), which is detailed in Section 5.3.1, is used to track the trajectories from the planners, and the generated actuator signals are used to control the vehicle plant as described in Section 2.4. Subsequently, the resulting vehicle responses from the five planners are analysed.

The evaluation of the effect of model complexity on AVs' trajectory planning performance has also been carried out in **Paper D** by considering two critical manoeuvres and various initial velocities. **Paper D** contributes to the development of a trajectory planning framework that plans states considering yaw stability – yaw rate and sideslip angle – together with the path, where explicit constraints are imposed to achieve yaw stability. Moreover, path and transient yaw rate constraints,

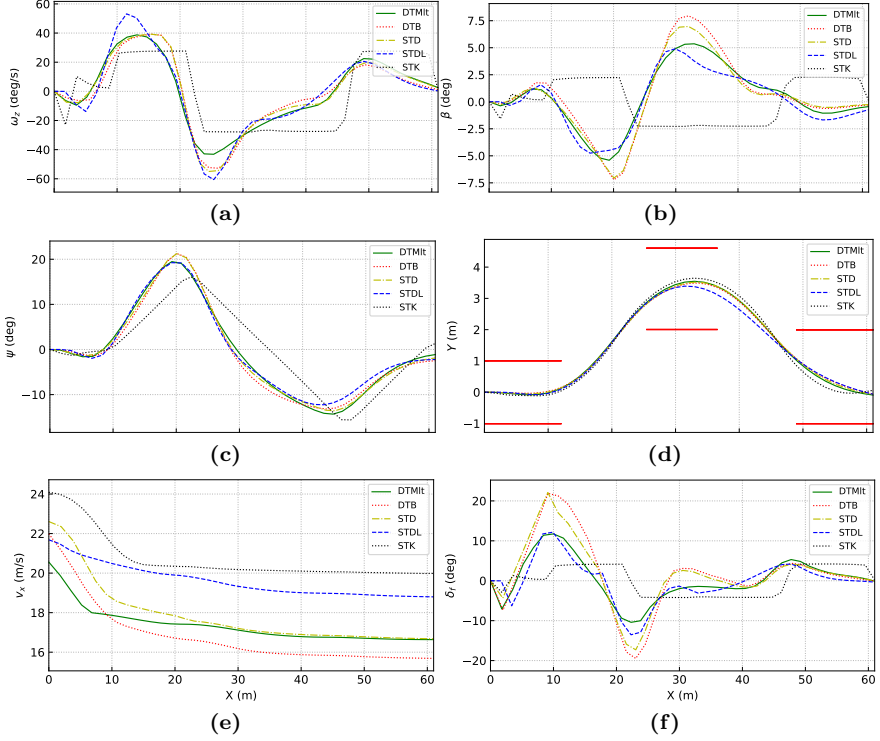


Figure 4.1: Comparison of trajectory planning of planners with various levels of model complexity in the evasive DLC manoeuvre (**Paper D**). (a)–(f) show the planned yaw rate (ω_z), sideslip angle (β), yaw angle (ψ), lateral position (Y), longitudinal velocity (v_x) and steering angle (δ_f), respectively. In (d), the solid red lines denote the cones for the DLC track.

in addition to physical limits on actuators, are taken into account in the planner formulation, in order to obtain practical reference trajectories with extended dynamic performance.

It should be noted that the trajectories from the planners described above are not updated per sampling step in the trajectory tracking evaluation. This is mainly due to the fact that no dynamic obstacles are considered in the test manoeuvres and the fact that this setup can be adequate to analyse the effect of model complexity on trajectory planning performance. Moreover, the term with $\dot{\beta}$ is discarded from the yaw rate constraints Eq. (4.4) for Planner STK because including this term may induce additional errors, considering that STK would generate a sideslip angle of the opposite sign compared to other planners. This point is discussed in detail in **Paper D**.

Fig. 4.1 shows the planned trajectories in the evasive DLC manoeuvre. As can be seen, all five planners successfully generate trajectories through this manoeu-

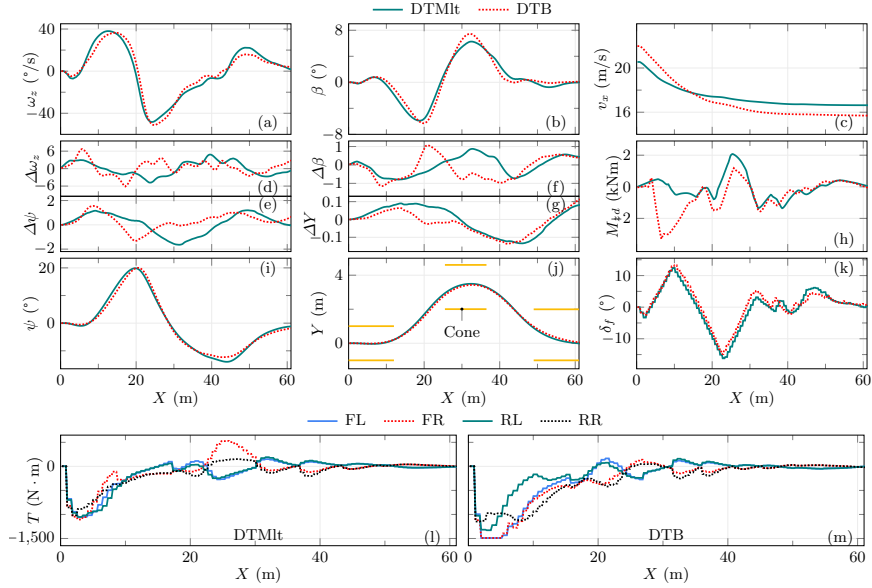


Figure 4.2: Comparison of trajectory tracking of planners with various levels of model complexity in the evasive DLC manoeuvre (**Paper D**). (a)–(c) and (i)–(j) show the yaw rate (ω_z), sideslip angle (β), longitudinal velocity (v_x), and lateral position (Y), respectively. (d)–(g) give the trajectory tracking errors corresponding to the yaw rate, yaw angle, sideslip angle, and lateral position, respectively. (k) presents the commanded steering angle at the front wheels, and (l) and (m) display the commanded drive/braking torques at the wheels. In (h), M_{zd} denotes the required yaw moment (from the contribution of longitudinal tyre forces) for the yaw movement of the vehicle [see Eq. (2.13)]. In (j), “Cone” denotes the cones for the DLC track.

vre. Nevertheless, the planners yield considerably different trajectories through the manoeuvre, especially in terms of yaw rate and sideslip angle.

Accordingly, Fig. 4.2 presents the trajectory tracking results using the reference trajectories from the respective planners. With the trajectories from Planners STK, STDL and STD, the vehicle is not able to pass the evasive DLC manoeuvre without hitting any cone. (This is why these planners are not shown in Fig. 4.2.) This observation for these three planners is contrary to what the corresponding trajectory planning results indicate. On the other hand, with the trajectories from Planners DTB and DTMLt, the vehicle is able to successfully execute the manoeuvre. Moreover, Planner DTB results in larger peak sideslip angle and yaw rate during trajectory tracking than Planner DTMLt.

The failed trajectory tracking in Planners STK, STDL and STD can be attributed to these planners’ unrealistic reference trajectories, e.g., overly large longitudinal velocity and/or sideslip angle, which may be the result of using overly simple models for trajectory planning in this critical driving manoeuvre.

Chapter 5

Path following and yaw stability control

Having obtained knowledge of the desired states and trajectories using state estimation and trajectory planning, as described in Chapters 3 and 4, this chapter details path following and yaw stability control. Controllers designed based on various means of over-actuation are presented and discussed.

5.1 Background

In critical driving conditions such as an obstacle-avoidance manoeuvre at high speed, vehicles may spin or drift out if not controlled properly. To avoid this, vehicle yaw stability control systems may need to act. Yaw stability can be achieved by generating a supplemental yaw moment that assists the vehicle in recovering the desired trajectory.

For conventional ICE vehicles or EVs with a single drive unit, yaw stability control is commonly achieved through differential braking: i.e., applying different amounts of braking forces on the left and right sides of the vehicle [9]. However, such yaw stability systems may not be sufficiently effective in critical driving scenarios and may deteriorate ride comfort.

An over-actuated EV has more actuators, including individual steering, traction and camber actuators, than the DoFs to be controlled, which are the longitudinal, lateral and yaw movements of the vehicle. This provides an increased degree of controllability, and thus the vehicle performance may be improved by exploiting such over-actuation.

Properly regulating the output torques of individual in-wheel/hub motors can correct the yaw movement of the vehicle by braking the wheels on one side while driving the wheels on the other side. This means that the desired yaw moment can potentially be generated more efficiently than in a conventional vehicle. Moreover, the vehicle can manoeuvre through the dangerous condition without decelerating

sharply, and thus ride comfort can be improved. Research has explored regulating individual wheel torques for improved yaw stability through, for example, control allocation and nonlinear optimisation [78], by using lateral tyre force sensors [79], as well as with a three-level controller [80].

Besides in-wheel/hub motors, camber actuators can also be controlled to achieve yaw stability, due to the potential to produce additional lateral tyre forces by controlling wheel inclination. Specifically, wheel camber can contribute to as much as 25% of the total lateral tyre force, as can be seen in Fig. 2.6. Studies have been carried out using camber control to improve vehicle safety [81], enhance trajectory tracking [82] and increase cornering margins [83].

Yaw stability controllers have been designed using various types of algorithms. These algorithms usually first attempt to approach the desired yaw rate and/or sideslip angle and then determine the final actuator behaviour accordingly. For instance, the yaw stability controller introduced by Rajamani [41] has a two-layer structure. The upper-level controller is designed using sliding-mode control (SMC) [84–87] and a double-track dynamic vehicle model combined with the Dugoff tyre model. This layer obtains a virtual yaw moment, where a single-track dynamic vehicle model is used to determine the desired sideslip angle and yaw rate. Based on the obtained yaw moment, the lower-level controller calculates the braking pressure on each wheel by using a rule-based method. Besides SMC, algorithms such as linear quadratic regulator (LQR) [88] and fuzzy proportional–integral–derivative (PID) [89] have been used in the upper-level controller to determine the virtual yaw moment. On the other hand, optimisation-based methods with various purposes have also been used in the lower level to allocate individual wheel torques in over-actuated EVs [90–92].

Apart from yaw stability, another significant objective for the safe driving of AVs is to follow the given path by the planner. Model predictive control (MPC) has been a popular option to accomplish this, due to its advantages in predicting future trajectories and handling constraints [93]. Research on employing MPC for path following in AVs has been carried by, for example, Falcone and colleagues [43, 94, 95] and Gallep et al. [96].

Previous studies usually address path following and yaw stability separately, which may undermine overall control performance. In contrast, **Papers B, C and E** use MPC to achieve these two objectives simultaneously in a combined framework for improved performance. In addition, explicit constraints are applied to yaw rate and sideslip angle, as can be seen in Eq. (5.2), which helps not only achieve yaw stability but also avoid tracking overshoot. This is often not tackled effectively in existing studies. Moreover, four controllers with different structures are designed and evaluated in **Paper C**, to study the effect of torque vectoring and controller structure on control performance. The influence of wheel inclination on lateral tyre forces is modelled in **Paper B**, which then evaluates the effects of active camber and camber rate on the control performance. Finally, the performance of various over-actuation configurations is assessed in **Paper E**.

5.2 Controller formulation

Unlike methods such as SMC and PID, where control actions are determined by considering a single time step, MPC yields control efforts by taking a fixed length of future horizon into account. Considering this, and with the aim of following the desired path and maintaining yaw stability, the MPC [66] problem can be formulated as

$$\begin{aligned} \min_{\mathbf{x}_p, \mathbf{u}_p, \Delta \mathbf{u}_p, \mathbf{s}} & \underbrace{\sum_{i=0}^{N_p-1} \|y_{k+i|k} - y_{k+i|k}^{ref}\|_{Q_y}^2}_{\text{tracking error}} + \underbrace{\sum_{i=0}^{N_p-1} \|u_{k+i|k}\|_{R_u}^2}_{\text{control action}} + \underbrace{\sum_{i=0}^{N_p-1} \|\Delta u_{k+i|k}\|_{R_{du}}^2}_{\text{change of control action}} \\ & + \underbrace{\|y_{k+N_p|k} - y_{k+N_p|k}\|_{Q_{yf}}^2}_{\text{terminal cost of tracking error}} + \underbrace{\sum_{i=0}^{N_p-1} \|s_{k+i|k}\|_{Q_s}^2}_{\text{slack term}} + \underbrace{\|s_{k+N_p|k}\|_{Q_{sf}}^2}_{\text{terminal cost of slack variable}} \end{aligned} \quad (5.1a)$$

$$\text{s. t. } x_{k+i+1|k} = f(x_{k+i|k}, u_{k+i|k}) \quad (5.1b)$$

$$y_{k+i|k} = h(x_{k+i|k}), i \in \{0, 1, \dots, N_p\} \quad (5.1c)$$

$$\Delta u_{k+i|k} = \begin{cases} u_{k+i|k} - u_{k+i-1|k}, & \text{if } i \geq 1 \\ u_{k|k} - u_{k-1|k-1}, & \text{if } i = 0 \end{cases} \quad (5.1d)$$

$$u_{min} \leq u_{k+i|k} \leq u_{max} \quad \Delta u_{min} \leq \Delta u_{k+i|k} \leq \Delta u_{max} \quad (5.1e)$$

$$\mathcal{H}_p(x_{k+i|k}, u_{k+i|k}, s_{k+i|k}) \leq 0 \quad (5.1f)$$

$$s_{k+i|k} \geq 0 \quad (5.1g)$$

where $\mathbf{x}_p = [x_{k+1|k}, \dots, x_{k+N_p|k}]$ and $\mathbf{s} = [s_{k|k}, \dots, s_{k+N_p|k}]$ are sequences of vectors for state and slack variables over the prediction horizon, N_p , respectively. $\mathbf{u}_p = [u_{k|k}, \dots, u_{k+N_p-1|k}]$ and $\Delta \mathbf{u}_p = [\Delta u_{k|k}, \dots, \Delta u_{k+N_p-1|k}]$ are sequences of vectors for control actions and change of control actions, respectively.

As can be seen from Eq. (5.1a), the cost function consists of three types of L2-norm terms, which penalise tracking errors between the actual and reference trajectories, control efforts, and the variation of control efforts, respectively. By considering these terms, the controller intends to approach as close as possible to the reference signals, minimise control efforts, and avoid excessive oscillations in the vehicle actuators. The method for tuning the corresponding weight matrices Q_y , R_u , R_{du} , Q_{yf} , Q_s and Q_{sf} used in the cost function is detailed in Section 6.2.3 and **Paper C**.

The reference trajectories, which consist of a sequence of reference trajectory vectors, i.e., $y_{k+i|k}^{ref} = [v_{x,k+i|k}^{ref} \psi_{k+i|k}^{ref} Y_{k+i|k}^{ref} \omega_{z,k+i|k}^{ref} \beta_{k+i|k}^{ref}]^T$ (corresponding to the output vector $y = [v_x \psi Y \omega \beta]^T$) over the prediction horizon, can be obtained from the trajectory planner, which is detailed in Chapter 4. By tracking these reference trajectories, the vehicle attempts to travel along the desired path and yaw angle with the desired yaw rate, sideslip angle and velocity.

Merely tracking the reference trajectories cannot avoid possible tracking overshoot, although it may try to make the vehicle follow the desired trajectories. To resolve this issue, explicit constraints are applied to the yaw rate and sideslip angle to achieve yaw stability. In fact, this is another advantage of MPC compared with commonly used methods such as SMC and PID. Specifically, the state constraint equation $\mathcal{H}_p(\cdot)$, which is used in Eq. (5.1f), can be further expressed as

$$\mathcal{H}_p(x_{k+p|k}, u_{k+p|k}, s_{k+p|k}) = \begin{bmatrix} \omega_{zmin} - \omega_{z,k+1|k} - s(1)_{k+p|k} \\ \beta_{min} - \beta_{k+1|k} - s(2)_{k+p|k} \\ \omega_{z,k+1|k} - \omega_{zmax} - s(1)_{k+p|k} \\ \beta_{k+1|k} - \beta_{max} - s(2)_{k+p|k} \end{bmatrix} \quad (5.2)$$

where the slack vector $s(\cdot)$ is used mainly to circumvent possible infeasibility issues when solving the resulting optimisation problems.

At each time step, signals from vehicle sensors and state estimator are accumulated as $x_{k|k}$ which forms a starting point for the MPC problem. Subsequently, the optimisation problem defined by Eq. (5.1) is solved, which results in the solution sequence $\mathbf{u}^* = [u_{k|k}^*, \dots, u_{k+N-1|k}^*]$. The first component of this sequence, $u_{k|k}^*$, is then treated as the final solution and applied to the corresponding actuators to control the vehicle.

5.3 Results and discussion

Combining the MPC formulation denoted by Eq. (5.1) with double-track vehicle models and various tyre models as detailed in Chapter 2, this section assesses the potential of using various means of over-actuation to achieve path following and yaw stability in critical driving conditions. Specifically, the over-actuation configurations examined include active front steering (AFS), AFS + torque vectoring (TV), AFS + active camber (AC) and AFS + TV + AC. In these investigations, the generated actuator signals are used to control the vehicle plant as described in Section 2.4, and the resulting vehicle responses are discussed.

The assessment on the vehicle configurations above has also been conducted in **Papers B, C and E**. These studies contribute by developing a framework for concurrent path following and yaw stability control in critical conditions. In this framework, constraints for yaw rate and sideslip angle are explicitly applied to achieve yaw stability and avoid tracking overshoot. Moreover, terms considering variation in the sideslip angle are included in the yaw rate constraints to extend dynamic performance.

Prior to discussing the performance when using different means of over-actuation, the results for the case of merely path following (without yaw stability control) are shown in Fig. 5.1. As can be seen, without yaw stability regulation, the vehicle cannot successfully complete the severe DLC manoeuvre [97]. Specifically, the vehicle runs into the cones and has a sideslip angle that is beyond the safety margin.

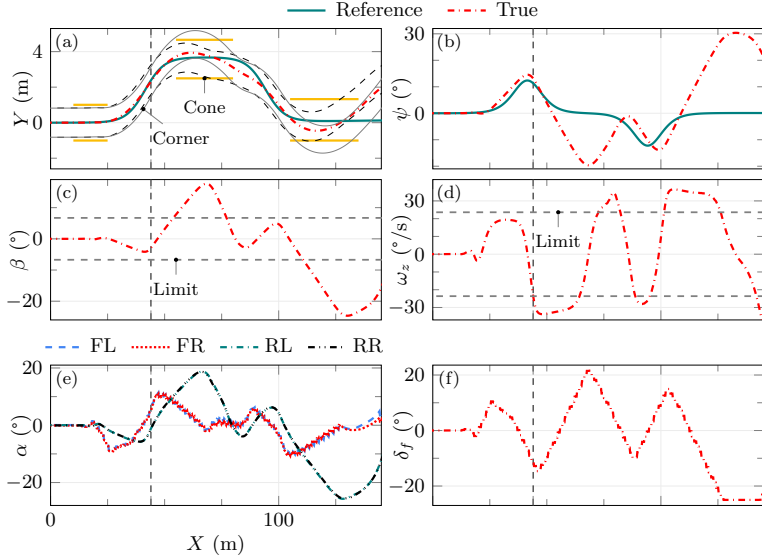


Figure 5.1: Tracking performance and tyre behaviour without yaw stability control in medium-friction conditions ($\mu = 0.6$) with a reference velocity of 76 km/h (**Paper C**). (a), (b), (c) and (d) present the lateral position, yaw angle, sideslip angle and yaw rate, respectively, and (e) and (f) show the tyre slip angle and front steering angle, respectively. In (a), “Cone” shows the position of the cones defining the boundary of the severe DLC track, and “Corner” indicates the trajectory of vehicle corners (black dashed lines represent front corners and grey solid lines rear corners). The “Limit” in (c) and (d) represent the constraints for the sideslip angle and yaw rate, respectively.

This indicates that path following alone cannot ensure safe driving of the vehicle, and thus yaw stability should be considered as well.

5.3.1 Torque vectoring

Besides the potential of torque vectoring, this section investigates the effect of controller structure on the path following and yaw stability performance in the severe DLC manoeuvre. Specifically, four controllers with different structures are evaluated: OLT_V (one-level with torque vectoring), OLEA (one-level with equal torque allocation), TLOA (two-level with optimisation-based torque allocation), and TLRA (two-level with rule-based torque allocation). These controllers are designed in the MPC framework denoted by Eq. (5.1) with a double-track dynamic vehicle model and the Dugoff tyre model, as detailed in Chapter 2. The four controllers are also extensively assessed in **Paper C**, with regard to tracking accuracy, tyre utilisation, robustness in the face of changes in road friction, as well as the effect of horizon length on tracking accuracy and computational efficiency.

With a one-level structure, Controller OLT_V determines directly a steering command to the two front wheels and torque requests to the individual wheels by ex-

Table 5.1: Comparison of the four controllers at various reference velocities in high-friction condition ($\mu = 1$) (**Paper C**).

v_x^{ref} (km/h)	Controller	ω_z (°/s)		β (°)		ψ (°)		Y (m)	
		e_{rms}	e_{max}	e_{rms}	e_{max}	e_{rms}	e_{max}	e_{rms}	e_{max}
85	OLTV	4.1	8.4	1.3	3.1	1.2	2.4	0.08	0.18
	OLEA	4.6	9.5	1.5	3.3	1.4	2.9	0.10	0.18
	TLOA	4.4	9.7	1.4	3.3	1.3	3.0	0.10	0.17
	TLRA	4.6	10.0	1.5	3.3	1.4	3.1	0.10	0.17
86	OLTV	4.3	8.2	1.3	3.2	1.3	2.6	0.08	0.18
	OLEA	4.8	10.4	1.6	3.6	1.5	3.1	0.10	0.19
91	OLTV	5.2	9.0	1.6	3.7	1.6	3.2	0.11	0.22

^a The colour blue indicates the lowest value of each column at the same reference velocity.

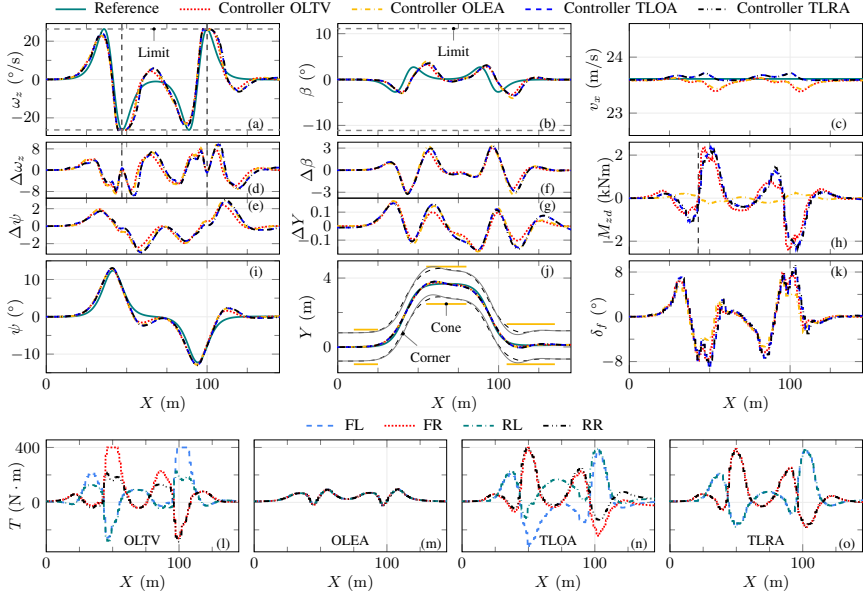


Figure 5.2: Tracking performance and control actions of Controllers OLT, OLEA, TLOA and TLRA in high-friction condition ($\mu = 1$) with reference velocity 85 km/h (**Paper C**). (a)–(c) and (i)–(j) show the yaw rate, sideslip angle, longitudinal velocity, yaw angle and position, respectively, (d)–(g) display the tracking errors, (k) presents the commanded front steering, and (l)–(o) display the commanded drive/braking torques of Controllers OLT, OLEA, TLOA and TLRA, respectively. The “Limit” in (a) and (b) denote the constraints for the yaw rate and sideslip angle, respectively. In (h), M_{zd} denotes the required yaw moment (from the contribution of longitudinal tyre forces) for the yaw movement of the vehicle [see Eq. (2.13)].

ploiting torque vectoring. With a similar one-level structure to OLT, OLEA allocates equally the individual wheel torques without exploring torque vectoring. The

Table 5.2: Results obtained with ($\Delta\gamma = 15 - 60^\circ/\text{s}$) and without (–) camber control in high-friction ($\mu = 1$) condition (**Paper B**).

v_x^{ref} (km/h)	$\Delta\gamma$ (°/s)	ω_z (°/s)		β (°)		ψ (°)		Y (m)	
		e_{rms}	e_{max}	e_{rms}	e_{max}	e_{rms}	e_{max}	e_{rms}	e_{max}
84	–	3.64	7.28	1.67	3.52	1.16	2.30	0.09	0.17
91	15	3.47	7.13	1.65	3.62	1.11	2.11	0.11	0.21
	30	3.68	10.20	1.58	3.44	1.09	1.78	0.13	0.27
99	45	3.03	9.64	1.25	2.51	0.88	1.52	0.12	0.27
	60	2.95	9.35	1.17	2.36	0.83	1.33	0.12	0.27

two-level controllers, TLOA and TLRA, both considering torque vectoring, work in a two-step procedure. They first yield a steering angle and virtual forces/moment in the upper level and then allocates the torques to individual wheels in the lower-level by using optimisation- and rule-based methods, respectively. Further details on the working principles of these controllers can be found in **Paper C**.

As can be seen from Table 5.1, without torque vectoring, Controller OLEA yields apparently larger root-mean-square (RMS) and maximum tracking errors and lower passing velocities than OLT. In contrast, by exploiting torque vectoring and adopting a one-level structure, OLT achieves a passing velocity that is 5 km/h higher than OLEA and 6 km/h higher than TLOA and TLRA. Moreover, Controller OLT generally produces smaller tracking errors than the other three controllers at the same velocities.

Controller TLOA performs slightly better than TLRA, as shown in Table 5.1 and Fig. 5.2. This is mainly due to the fact, in the tested scenario, the induced total longitudinal force and yaw moment (calculated using longitudinal tyre forces) for these two controllers are rather similar. Still, with an optimisation-based torque allocation strategy, TLOA has more DoFs than TLRA in terms of designing the cost function terms and tuning the weight matrices.

5.3.2 Active camber

By considering the influence of wheel camber via tyre modelling – i.e., Eq. (2.21) – this section investigates active camber as a means to achieve path following and yaw stability in the severe DLC manoeuvre. Specifically, to evaluate the performance of active camber, its results are compared with those from a controller of the same structure but without camber control. Moreover, controllers with various camber rates, $\Delta\gamma$, are discussed in order to assess the effect of camber rate on the performance of active camber. The effect of camber rate on the path following and yaw stability performance and the robustness in varying road friction conditions

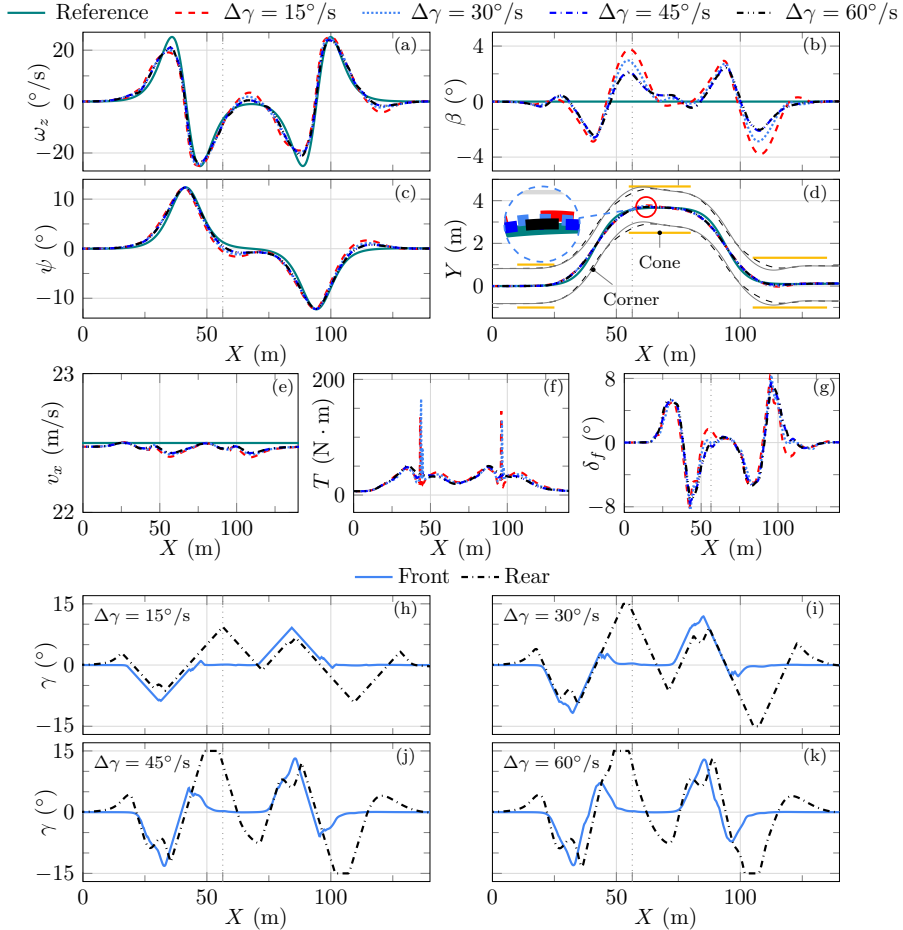


Figure 5.3: Tracking performance and control actions from the camber controller with road friction $\mu = 0.6$ (**Paper B**). (a)–(e) show the yaw rate, sideslip angle, yaw angle, position and longitudinal velocity, respectively; (f) and (g) present the commanded torque and steering, respectively; and (h)–(k) denote the commanded camber. In (d), “Corner” indicates the trajectory of the vehicle corners for $\Delta\gamma = 15^\circ/\text{s}$. “Front” and “Rear” denote the camber of the two front and the two rear wheels, respectively.

are examined in greater detail in **Paper B**, in terms of passing velocity, tracking accuracy and tyre utilisation.

The results for the cases with and without active camber are shown in Table 5.2 and Fig. 5.3. As can be seen, by exploiting active camber ($\Delta\gamma = 15^\circ/\text{s}$), the vehicle is able to complete the severe DLC manoeuvre at a velocity which is 8.3% higher than the case without camber control, 91 km/h versus 84 km/h. Further, the velocity gain becomes 17.9% when the camber rate increases to $\Delta\gamma = 30^\circ/\text{s}$.

Table 5.3: Trajectory tracking errors of the four over-actuation configurations (**Paper E**).

v_{xi} (km/h)	Controller	ω_z (°/s)		β (°)		ψ (°)	
		e_{rms}	e_{max}	e_{rms}	e_{max}	e_{rms}	e_{max}
73	S	3.2	7.7	0.6	1.0	0.9	1.9
	ST	2.9	7.7	0.5	0.9	0.8	1.7
	SC	2.0	6.0	0.3	0.7	0.6	1.5
	STC	2.0	6.9	0.2	0.4	0.5	1.2
76	ST	3.6	11.4	0.6	1.3	0.9	2.1
	SC	2.5	9.2	0.4	1.3	0.6	1.3
	STC	2.6	8.6	0.2	0.6	0.6	1.5
79	STC	3.3	9.6	0.5	1.2	0.8	2.5

^a The colour red indicates the highest value (at the same initial velocity) for each column, whilst the colour blue indicates the lowest value.

In general, active camber results in smaller tracking errors than the case without camber control. This is even true when comparing the former case at 91 km/h with the latter at 84 km/h.

The velocity gain and improved tracking accuracy that result from active camber can be attributed to the fact that wheel camber increases lateral tyre forces and additional yaw moment is generated by requesting different camber angles from the front and rear wheels. The first point has been shown in Fig. 2.6 and discussed in Section 2.2.3. The second point can be seen by examining Fig. 5.3(h). For instance, when the camber angles of the front and rear wheels are 0.11° and 9.36° at the position of $X = 56.41$ m, respectively, a positive yaw moment is generated, considering the fact that a positive camber angle yields a negative lateral tyre force.

5.3.3 Integrated control

While Sections 5.3.1 and 5.3.2 explore the effects of torque vectoring and active camber separately, this section evaluates various over-actuation configurations for path following and yaw stability control. Specifically, the performance of an integrated controller is compared against that of steering control, torque vectoring and active camber in the SLC manoeuvre through Controllers S (AFS), ST (AFS and TV), SC (AFS and AC), and STC (AFS, TV and AC). In this evaluation, reference trajectories from the planner which is elaborated in Chapter 4 is used. These over-actuation configurations are also assessed in **Paper E**, with respect to passing velocity, tracking accuracy, safety distance, as well as their robustness to varying velocities and reference trajectories.

As can be seen from Table 5.3, out of the four controllers, Controller S generally

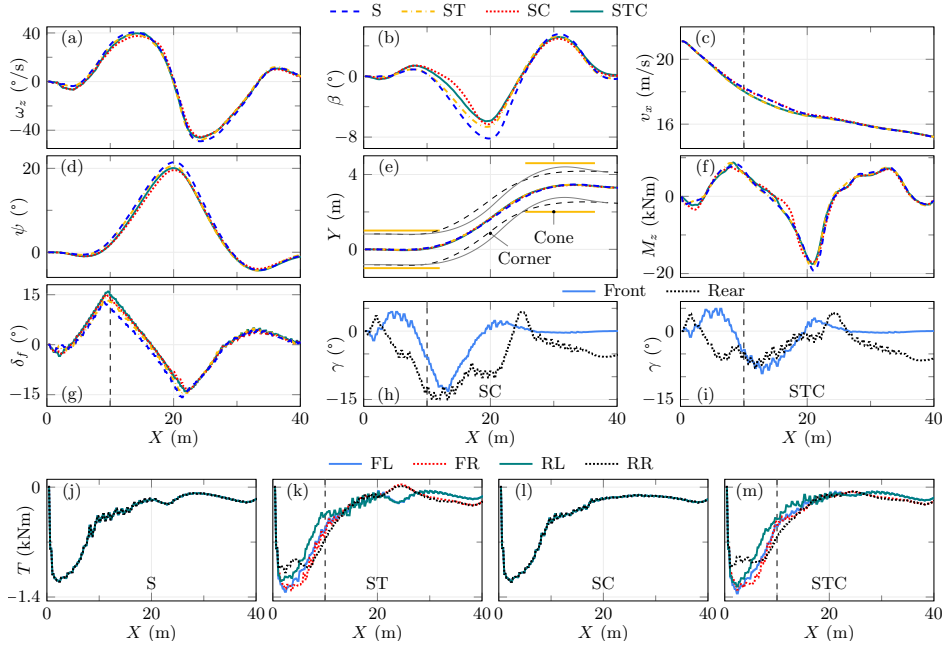


Figure 5.4: Comparison of trajectory tracking of the four combinations of over-actuation with the initial velocity being 76 km/h (**Paper E**). (a)–(e) show the yaw rate (ω_z), sideslip angle (β), longitudinal velocity (v_x), yaw angle (ψ), and lateral position (Y), respectively. In (f), M_z denotes the required yaw moment (from the contribution of both longitudinal and lateral tyre forces) for the yaw movement of the vehicle [see Eq. (2.13)]. (g) presents the commanded steering angle at the front wheels, (h) and (i) give the commanded camber angle of the front and rear wheels, and (j)–(m) display the commanded drive/braking torques at the wheels. In (e), “Corner” indicates the vehicle boundaries corresponding to Controller S.

results in the largest tracking errors corresponding to yaw rate, sideslip angle and yaw angle when the initial velocity is 73 km/h. This is because Controller S is not able to exploit torque vectoring or camber control, which is consistent with the observation for Controller OLEA, as discussed in Section 5.3.1. In contrast, Controller SC, in general, yields the smallest tracking errors for yaw rate, sideslip angle, yaw angle and lateral position when compared to the other three controllers because it was able to exploit torque vectoring and active camber in a combined manner and thus utilise the tyres more effectively.

Controller SC results in smaller tracking errors than ST at the same initial velocity, as shown in Table 5.3. This can be attributed to the fact that active camber can be more effective than torque vectoring in generating the required corrective yaw moment, as it was able to control the lateral tyre forces of larger magnitude than the longitudinal forces and request different magnitudes of camber angles/forces on the front and rear wheels. A similar observation can also be found in Section 5.3.2.

With regard to velocity, Controller STC yields the highest passing velocity among all four controllers (6 km/h higher than Controller S), as shown in Table 5.3. It should be noted that, with Controller S at the initial velocity 76 km/h, the front left corner of the vehicle in fact collides with the cone at around $X = 12$ m, as shown in Fig. 5.4(e), although the results for Controller S are shown in the figure for the purpose of controller comparison.

Chapter 6

Optimal control implementation

While the previous chapters focus on modelling and methods related to path following and yaw stability control, this chapter presents the implementation of those methods. Techniques for handling continuous-time optimal control problems are introduced. Frameworks and tools for implementing those methods are then presented. Further, the tuning of a few key parameters and the effect of optimisation techniques on the performance of two state estimators are discussed.

6.1 Background

As mentioned in Chapter 2, summarising the vehicle and tyre models results in the continuous-time system dynamics as stated in Eq. (2.23). With the system Eq. (2.23), the problems of state estimation, trajectory planning, as well as path following and yaw stability control, which are described in Chapters 3, 4 and 5, respectively, can be formulated as continuous-time OCPs because optimisation-based approaches are adopted.

From a practical point of view, a discrete-time system is often required when implementing algorithms for state estimation, trajectory planning, as well as path following and yaw stability control, as these types of algorithms are usually realized on digital devices. To discretise a continuous-time system, commonly used approaches include explicit methods such as the forward Euler and Runge–Kutta 4, and implicit techniques such as the backward Euler and collocation methods. For instance, the forward Euler method is used in **Paper A** to obtain the discrete-time system as given in Eq. (2.24), with which EKF, UKF and MHE are implemented. On the other hand, collocation methods are used in **Papers B–E** to discretise the systems for implementing the controllers and planners.

With proper methods for discretising continuous-time systems and techniques for handling optimisation problems, the original continuous-time OCPs can be solved numerically and efficiently by using direct approaches and structure-exploiting solvers [98]. Popular direct approaches for handling continuous-time OCPs include

direct single shooting (DSS) [99], direct multiple shooting (DMS) [100] and direct collocation (DC) [101]. DSS approximates the continuous-time control function by using piecewise polynomials and eliminates the state variables on the discretised time grids by using the state equation. On the other hand, DMS treats both the control and state variables as optimisation variables and the corresponding state equation as equality constraints. Compared with DMS, DC further divides each of the time grids into various sub-intervals, where a polynomial is used to connect the collocation states along the sub-intervals.

From the discussions above, it can be seen that DMS yields more optimisation variables and equality constraints than DSS. Nevertheless, the OCP that results from DMS is sparser than that from DSS, as each of the containing functions of the OCP from DMS is only related to a few of the corresponding variables. In the case of DC, the resulting OCP is even sparser than that from DMS. Fortunately, the structure of such large but sparse OCPs can be exploited by optimisation tools that use nonlinear interior point methods (IPMs), e.g., IPOPT [102], which can then solve the OCPs efficiently. More discussions regarding techniques for numerically solving OCPs are given by Diehl et al. [98].

In **Papers B–E**, the DC technique combined with IPOPT is used to solve the resulting OCPs. In **Paper A**, DMS is adopted and its computational performance is compared with that of DSS. Besides, **Paper A** contributes by studying the effects of horizon length on the accuracy and computational efficiency of the MHE-type state estimators. Similarly, **Paper C** discusses the influence of horizon length on the performance of two MPC-type path following and yaw stability controllers.

6.2 Implementation

When implementing the estimators, planners and controllers, factors of various aspects need to be considered, including the framework for generating and analysing the results, the tools for obtaining solutions to those problems, as well as the methods for better defining the problems and yielding the solutions.

6.2.1 Framework

The main framework for carrying out the studies presented in this dissertation is shown in Fig. 6.1. As can be seen, this framework mainly consists of three parts: “Preprocessing”, “Processing” and “Postprocessing”. Preprocessing defines parameters and test scenarios, which are then treated as inputs to the processing, then performs tests to ensure that the framework runs properly, and specifies requirements for the main tools and packages involved in the framework. Processing includes modules for defining models, designing estimators, controllers and planners and executing simulations. By integrating the vehicle plant in the form of an FMU into the framework, co-simulations can be executed conveniently and reliably. A few main packages used in this part include MPCTools [103], `rockit` [104],

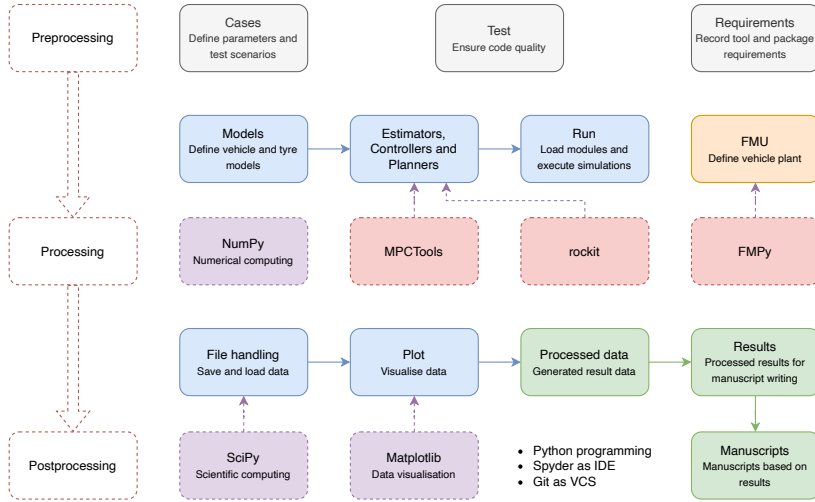


Figure 6.1: Main framework for implementing the studies presented in this dissertation.

FMPy [105] and NumPy [106]. Using the data generated from the processing, post-processing mainly involves saving/loading, visualising and processing the results, with the main packages being SciPy [107] and Matplotlib [108].

The entire framework uses Python [109] as the main programming language, Spyder [110] as the integrated development environment (IDE) and Git [111] as the version control system (VCS). With this setup and the structure explained in the last paragraph, this framework offers the following benefits in the presented studies. Firstly, computational efficiency can be significantly improved. For instance, the time required to perform one co-simulation in the case of a path following and yaw stability controller, as detailed in **Paper C**, is reduced by 20 times, compared with the implementation in MATLAB/Simulink. In fact, this is why this framework was initially developed. Secondly, it allows a smooth process for defining parameters, running simulations and generating results, which facilitates a positive loop for analysing results and tuning parameters. Thirdly, by adopting a modular structure, using VCS, performing tests, and recording requirements for tools and packages, etc., it enables the development of sustainable code.

6.2.2 Optimal control problem

Fig. 6.2 illustrates the main tools involved for solving the optimisation-based state estimation, trajectory planning, as well as path following and yaw stability control problems. As explained in Section 6.1, these problems can essentially be formulated as continuous-time OCPs and can then be implemented using MPCTools and rockit, which are interfaces to CasADi [112]. By using these tools and taking proper direct approaches – e.g., DMS and DC – the continuous-time OCPs can be

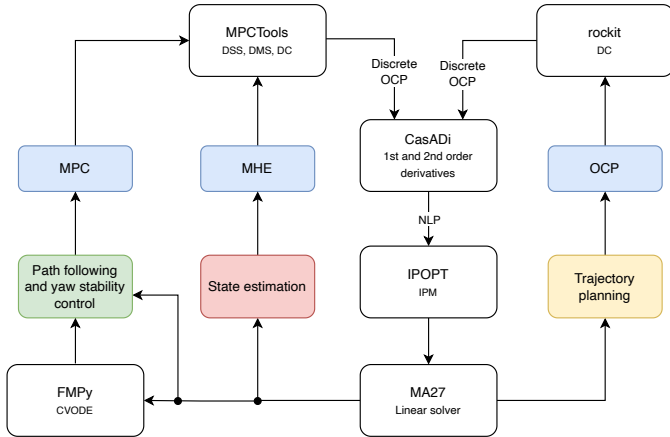


Figure 6.2: OCP implementation of state estimation, trajectory planning and path following and yaw stability control strategies.

converted into discrete OCPs. Subsequently, the OCPs can be transformed into nonlinear programming problems (NLPs), with the first and second order derivatives being given by CasADi. By exploiting their sparsity structure, IPOPT [102] finally solves the resulting NLPs with the help of solvers such as MA27 [113]. In the case of path following and yaw stability control, these solutions can then be passed on to the FMU vehicle plant (with CVODE [114] being the built-in solver), which is handled using FMPy. The updated vehicle states can then be used to control the vehicle in the next time step, thus forming a closed-loop control system.

6.2.3 Parameter tuning

When implementing the estimators, planners and controllers, parameters such as weight matrices and horizon length should be tuned properly so that they yield reasonable OCPs that satisfy the design objectives and do not cause additional obstacles to the solvers. Take the path following and yaw stability control case as an example, as can be seen from Eq. (5.1a), its cost function includes four main terms that take effect along the prediction horizon – terms for penalising tracking errors, magnitude of control actions, magnitude of variations of control actions, as well as a slack term – with the corresponding weight matrices being Q_y , R_u , R_{du} and Q_s , respectively. These weight matrices are specifically defined for Controller

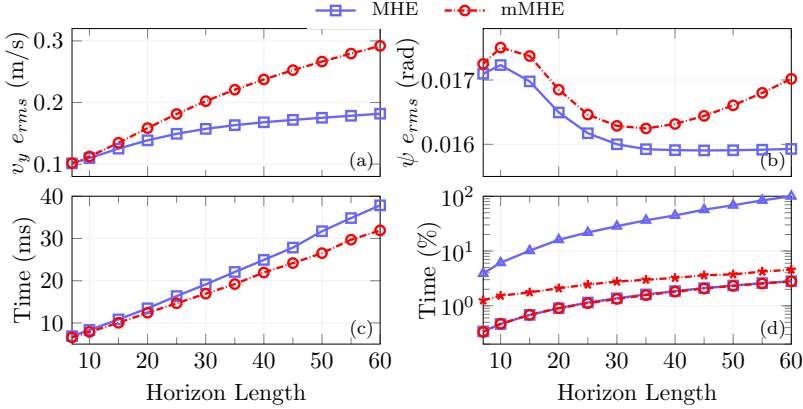


Figure 6.3: Effect of the optimisation techniques and horizon length in the circular manoeuvre (**Paper A**). (a) and (b) show the RMS estimation errors with DMS. (c) shows the computation time per optimisation step with DMS. (d) compares the computation time per optimisation step between DSS and DMS (the y tick value has been scaled with respect to the maximum time). In (d), the blue line with triangles denotes the results for the MHE with DSS, while the red line with stars denotes the results for mMHE with DSS.

OLTV in **Paper C**, as follows:

$$R_u = \text{diag} \left(\begin{bmatrix} 10 & 5 \cdot 10^{-6} & 5 \cdot 10^{-6} & 5 \cdot 10^{-6} & 5 \cdot 10^{-6} \end{bmatrix} \right) \quad (6.1a)$$

$$R_{du} = \text{diag} \left(\begin{bmatrix} 10 & 5 \cdot 10^{-6} & 5 \cdot 10^{-6} & 5 \cdot 10^{-6} & 5 \cdot 10^{-6} \end{bmatrix} \right) \quad (6.1b)$$

$$Q_y = \text{diag} \left(\begin{bmatrix} 120 & 30 & 30 & 100 & 10 \end{bmatrix} \right) \quad (6.1c)$$

$$Q_s = \text{diag} \left(\begin{bmatrix} 10^6 & 10^6 \end{bmatrix} \right). \quad (6.1d)$$

Because SI (International System of Units) units are used, the overall magnitude of the tracking errors is significantly less than that of the control actions in the test scenarios. Therefore, to emphasise the objective of trajectory tracking, a Q_y matrix with relatively large elements compared to R_u , should be used, so that the cost function term corresponding to the tracking errors has a relatively large weight. Similarly, the weight matrices R_{du} and Q_s can be determined. As far as determining the elements within each weight matrix, both the units and importance of the corresponding variables should be taken into account. Methods for tuning the weight matrices are also discussed in **Paper C**.

It should be noted that the main reason for having a notably large Q_s matrix is to avoid violating the corresponding state constraints as much as possible. As explained in Section 5.2, the slack variables/constraints are introduced mainly to address the possible infeasibility issue. In addition, it is preferable if the corresponding constraints are met, and thus a large Q_s is used to penalise the possible violation of these constraints. Moreover, the selected weight matrices should ensure

that the overall magnitude of the cost function should be close to the magnitude of 1 so that it can be more efficient for the solvers to find the solutions. This point is also discussed in **Paper D**.

In **Paper A**, the horizon length of the MHE-type estimators is chosen as 10, to achieve a good balance between estimation accuracy and computational efficiency. As can be seen from Fig. 6.3(a)–(b), the estimation errors of MHE do not obviously decrease as the horizon length increases. One reason for this could be that relatively large modelling errors exist in this test manoeuvre which compromise the advantage of using more measurements for estimation. On the other hand, mMHE has a similar tendency as the MHE when the horizon length increases, but with larger errors. This is because neglecting model mismatch in its formulation makes mMHE unable to handle the relatively large modelling errors in this manoeuvre. Moreover, a larger horizon length results in a considerably increased computational time for both MHE and mMHE, as shown in Fig. 6.3(c). On the other hand, the computational efficiency of MHE is not that different from that of mMHE due to the use of the DMS technique and the structure-exploiting optimisation package IPOPT.

6.2.4 Optimisation techniques

This section further discusses the effects of optimisation techniques – DSS versus DMS – on the computational efficiency of MHE and mMHE. In the following discussions, the MHE and mMHE problems are solved using DSS and DMS techniques combined with the optimisation package IPOPT and the linear solver MA27.

As can be seen from Fig. 6.3(d), DMS is substantially more efficient than DSS for both MHE and mMHE. Moreover, with DSS, the computational time difference between MHE and mMHE is significantly larger than that with DMS, although DMS results in more optimisation variables and equality constraints than DSS. The advantages of DMS over DSS can be mainly attributed to the simultaneous integration on each time grid, the initialisation strategy for state trajectory, the improved convergence rate – especially for nonlinear and unstable systems [66] – and the use of the structure-exploiting IPM optimisation package IPOPT. More discussions on this can be found in **Paper A**.

Chapter 7

Summary of appended papers

Paper A: Advanced vehicle state monitoring: Evaluating moving horizon estimators and unscented Kalman filter

The presented studies aim to achieve a reliable estimation of crucial vehicle states in critical driving conditions. In such circumstances, the performance of a state estimator may be jeopardised by model mismatches and external disturbances, in addition to measurement noises. To address these issues, moving horizon estimation (MHE) has been chosen as the algorithm for monitoring critical vehicle states, due to its advantages in handling non-linearities and uncertainties over traditional Kalman filter-type algorithms.

As a comparison, two MHE variants, modified MHE (mMHE) and recursive-least-squares (RLS) MHE, together with an unscented Kalman filter (UKF), have been designed to estimate these vehicle states. All these estimation algorithms are incorporated into a nonlinear vehicle system model whose observability is analysed. These estimators are evaluated with measurements from three critical manoeuvres and are discussed in terms of convergence rate, accuracy and robustness. For the MHE-type estimators, the effects of horizon length and optimisation techniques on their accuracy and computational efficiency are also discussed.

The results show that mMHE and MHE performed similarly with regard to convergence rate and accuracy, and they were both superior to the other two estimators, RLS-MHE and UKF, in all the three manoeuvres. On the other hand, RLS-MHE suffered from frequent estimation oscillations which made it unsuitable for use in the test scenarios. In the robustness tests, mMHE performed comparably to MHE in terms of handling initialisation deviations and modelling errors but performed worse in response to external disturbances. In addition, MHE outperformed UKF in the robustness tests. When the horizon size increased in the case with relatively large modelling errors, mMHE degraded more obviously than MHE, due to its lack of consideration for process noise in its formulation. Finally, MHE was computationally as efficient as mMHE when using the direct multiple shooting (DMS) technique and exploiting the sparsity structure of the resulting optimisation

problems, compared to using direct single shooting (DSS).

The results indicate that, by considering a sequence of past measurements and process noises in the problem formulation, MHE was a better option than the other three estimators for vehicle state estimation in the test scenarios, and it can be sufficiently efficient in computation.

Paper B: Active camber for enhancing path following and yaw stability of over-actuated autonomous electric vehicles

This paper presents an investigation of employing active camber for concurrent path following and yaw stability of over-actuated autonomous electric vehicles (AEVs) in critical driving scenarios. In such conditions, conventional active safety systems that mainly rely on braking intervention may not yield the desired performance, as tyre forces may saturate. Therefore, this paper explores active camber as a means to address this issue, due to its potential to generate and control lateral tyre forces, and thus the desired corrective yaw moment.

The camber effect on lateral tyre forces is modelled by using a simple, yet effective, component, in addition to the Dugoff tyre model, allowing for individual wheel inclination regulation. This modified Dugoff tyre model that considers the camber effect is combined with a double-track vehicle model, and together they are incorporated into the model predictive control (MPC) formulation to accomplish active camber, where constraints related to both yaw stability and actuator limits are considered. Active camber performance is evaluated in the severe double-lane change (DLC) manoeuvre at various camber rates and road conditions with respect to path following, yaw stability and passing velocity.

The results show that, with the desired camber rates, active camber was able to improve passing velocity by 15, 7 and 5 km/h in the high-, medium- and low-friction road conditions, respectively. Active camber was also able to improve the path following and yaw stability performance in these conditions. Moreover, the required peak power for the camber actuators were significantly lower than that from the drive motors, and the consumed energy could be neglected in the scenarios studied. The studies on camber actuation indicate that $45^{\circ}/s$ was the preferred camber rate at the high- and medium-road friction levels, as a relatively fast camber rate is needed in these highly dynamic driving scenarios to rapidly reach the desired wheel inclination. On the other hand, a lower camber rate, $30^{\circ}/s$, was sufficient in the low-friction condition, where the overly narrow effective camber region makes camber control not as effective and larger camber rates not as beneficial as in high- and medium-friction conditions.

Paper C: Evaluating model predictive path following and yaw stability controllers for over-actuated autonomous electric vehicles

While **Paper B** focuses on using active camber to achieve path following and yaw stability of AEVs in critical conditions, this paper pursues a detailed investiga-

tion that applies another means of over-actuation, torque vectoring, for a similar purpose. Besides, this paper evaluates the effect of controller structure on control performance by using MPC. Specifically, it presents two one-level controllers, OLTВ (torque vectoring) and OLEA (equal torque allocation), and two two-level controllers, TLOA (optimisation-based torque allocation) and TLRA (rule-based torque allocation). The four controllers are assessed in the severe DLC manoeuvre in terms of passing velocity, tracking accuracy, tyre utilisation and robustness to road friction variation. OLTВ and TLOA are also discussed with respect to the effect of horizon length on their accuracy and computational efficiency.

It was found that Controller OLTВ produced higher tracking accuracy and passing velocity (by up to 5 km/h) than OLEA. This indicates that torque vectoring was able to improve path following and yaw stability performance in the test scenarios. The studies on controller structure revealed that the one-level OLTВ had the highest passing velocity among the four controllers at all three road friction levels. On the other hand, OLTВ showed degraded tracking accuracy for yaw rate as the road friction changed, while the two-level controllers TLOA and TLRA yielded more consistent yaw rate tracking in these varying conditions. Furthermore, OLTВ, although producing much larger optimisation problems, had computational efficiency comparable to TLOA, by using the direct collocation (DC) method and sparsity-exploiting tool IPOPT. When analysing the two-level controllers, the rule-based TLRA had tracking accuracy and passing velocity comparable to the optimisation-based TLOA but was simpler to implement. Nevertheless, TLOA provided more degrees of freedom in designing its cost function, and thus offering potential performance improvement and the consideration of additional design objectives.

The tracking accuracy of OLTВ and TLOA improved considerably as the horizon length increased to a certain threshold and degraded after exceeding that value. This is a reasonable observation in this highly dynamic manoeuvre, as the preview distance of MPC, which is determined by the horizon length, would highly influence the obtained control actions and thus the tracking performance.

Paper D: Exploring model complexity for trajectory planning of autonomous vehicles in critical driving scenarios

This paper presents an evaluation of trajectory planning in critical driving manoeuvres. In such situations, using overly simple models for trajectory planning may yield unrealistic reference signals, which may not be suitable for use in active safety system applications. To handle this issue, trajectory planning is formulated as optimal control problems (OCPs) that considers yaw stability, obstacle avoidance and actuator physical limits in its formulation. Additionally, transient terms related to variation in sideslip angle are included in the yaw rate constraints to better reflect the dynamic behaviour of the vehicle.

To evaluate the influence of model complexity on planner performance, five trajectory planners of different levels of complexity are designed: STK (single-track kinematic model), STDL (single-track dynamic vehicle model with linear tyre

model), STD (single-track dynamic vehicle model with simplified Magic Formula tyre model), DTB (double-track dynamic vehicle model with Dugoff tyre model) and DTMLt (double-track dynamic vehicle model with load transfer and Magic Formula tyre model). These planners are evaluated in two critical driving manoeuvres at various initial velocities.

The results indicate that, firstly, by tracking the reference trajectories from the double-track planners DTMLt and DTB, the vehicle successfully executed the evasive DLC manoeuvre. With the trajectories from the simpler single-track planners, STD, STDL and STK, however, the vehicle failed to follow the evasive DLC track, which was contrary to the corresponding trajectory planning results. Secondly, in the single-lane change (SLC) manoeuvre, the two double-track planners produced consistently high passing velocity during trajectory planning and tracking. In contrast, in trajectory planning the three single-track planners over-estimated the passing velocity by 5, 19, and 17 km/h, respectively, compared to trajectory tracking. Finally, the more advanced planner DTMLt yielded a smaller peak yaw rate and sideslip angle than DTB in both the evasive DLC and SLC manoeuvres.

In summary, the more advanced double-track planners are needed to produce consistent trajectory planning and tracking performance in the safety-critical SLC and DLC manoeuvres. In contrast, the three single-track planners were not suitable candidates for trajectory planning in the tested manoeuvres due to their unsatisfactory performance.

Paper E: Integrated control of motion actuators for enhancing path following and yaw stability of autonomous electric vehicles

Based on the findings of **Papers B** and **C**, this paper presents an investigation of various motion actuator configurations for path following and yaw stability of AEVs in critical driving scenarios. The results from **Paper D** are used to test the robustness of the over-actuation configurations to reference trajectory generation. Specifically, four types of motion actuator integrations are evaluated, including active front steering (AFS), AFS + torque vectoring (TV), AFS + active camber (AC), as well as the integrated control of AFS + TV + AC. These over-actuation configurations are implemented in the MPC framework based on a double-track vehicle model, together with the camber tyre model developed in **Paper B** and the Dugoff tyre model. They are examined in the SLC manoeuvre at various initial velocities, comparing their passing velocity, tracking accuracy, safety distance and robustness to reference trajectories.

The results show that the integrated control of AFS + TV + AC outperformed the others when using both the advanced and simplified trajectories, with higher passing velocities, lower peak values and tracking errors for critical vehicle states such as sideslip angle, as well as a larger safety distance in the most critical position. In contrast, AFS performed the worst out of the four configurations, due to its lack of access to over-actuation. Moreover, AFS + AC was superior to AFS + TV with improved passing velocity, tracking accuracy and safety distance, as active camber

was able to more effectively utilise the tyres and generate the desired yaw moment by regulating the lateral tyre forces of front and rear wheels. Finally, AFS and AFS + TV were not as robust in response to trajectory variations as the other two means of over-actuation.

Chapter 8

Scientific contributions

This chapter summarises the main scientific contributions made in the studies carried out for this thesis work.

1. Moving horizon estimation (MHE), and its variants modified MHE (mMHE) and recursive-least-squares MHE, as well as unscented Kalman filter, have been incorporated with a nonlinear system model for vehicle state estimation. This system model consists of a double-track vehicle model and a simplified Magic Formula (MF) tyre model and has been verified to be locally observable and thus suitable for state estimation applications. The four estimators are evaluated in three critical manoeuvres, with MHE showing improved convergence rate, accuracy and response to external disturbances and modelling errors (**Paper A**).
2. The camber effect on lateral tyre forces has been modelled by using a simple, yet effective, component, in addition to the Dugoff tyre model. This camber tyre model allows for individually controlling the inclination angle of each wheel and has shown its effectiveness in the presented active camber studies (**Paper B**).
3. To achieve concurrent path following and yaw stability control of autonomous electric vehicles in critical conditions, a framework has been proposed that incorporates model predictive control (MPC) with double-track vehicle models and combined-slip tyre models. Constraints for yaw rate and sideslip angle are considered in this framework, which helps achieve yaw stability and avoid tracking overshoot for these two states. Moreover, terms considering variation in sideslip angle are included in the yaw rate constraints to achieve higher dynamic performance. Physical limits on vehicle actuators are explicitly considered in order to yield realistic control actions without compromising control performance. This framework has been utilised in the extensive path following and yaw stability studies (**Papers B, C and E**).

4. The effects of camber actuators on the control performance have been examined. Specifically, they are discussed at various camber rates, with different levels of improvement in path following, yaw stability and passing velocities. Moreover, the required peak power and consumed energy for the camber actuators are found to be considerably less than those corresponding to the drive motors (**Paper B**).
5. Controllers of various structures have been designed, including two one-level controllers, i.e., OLTV (torque vectoring) and OLEA (equal torque allocation), and two two-level ones, i.e., TLOA (optimisation-based torque allocation) and TLRA (rule-based torque allocation), to evaluate the effects of torque vectoring and controller structure on the path following and yaw stability performance. The results have shown that torque vectoring improved path following, yaw stability and passing velocity in the severe double-lane change manoeuvre. In addition, the one-level OLTV produced higher passing velocity than the other controllers in varying road friction conditions while the two-level TLOA and TLRA yielded more consistent tracking accuracy for yaw rate in these conditions (**Paper C**).
6. Various over-actuation configurations have been studied as a way to enhance path following and yaw stability in critical conditions. Specifically, AFS (active front steering) + TV (torque vectoring) and AFS + AC (active camber) have been evaluated in **Paper C** and **Paper B**, respectively, and these two configurations are further compared with AFS and AFS + TV + AC in **Paper E**. The evaluations have shown improved performance of the integrated control of AFS + TV + AC over the others, with higher passing velocities, lower peak values and tracking errors for sideslip angle, larger safety distance in the most critical position, as well as more consistent performance in response to varying reference trajectories.
7. To evaluate the effect of model complexity on planning performance, a trajectory planning framework for critical driving scenarios has been developed using optimal control problem (OCP) formulations. Specifically, states associated with yaw stability – yaw rate and sideslip angle – are planned together with the path, with constraints imposed to achieve yaw stability. Obstacles, transient yaw rate constraints and physical limits on actuators, are taken into account to obtain practical reference trajectories with extended dynamic performance. This framework has been demonstrated to be effective in the presented trajectory planning studies (**Paper D**).
8. Various combinations of vehicle and tyre models of different levels of complexity have been incorporated into the trajectory planning framework and studied in terms of their influence on planning performance. They are assessed in the evasive single- and double-lane change manoeuvres at various initial velocities, in which the most advanced double-track planner with load

transfer and MF tyre model outperformed the others with more consistent trajectory planning and tracking performance as well as smaller peak yaw rate and sideslip angle (**Paper D**).

9. The influence of estimator and controller parameters on accuracy and computational efficiency has been investigated. Specifically, the effects of horizon length on the two MHE-based estimators, MHE and mMHE, and the two MPC-based controllers, OLTv and TLOA, have been analysed and the desired horizon length has been determined accordingly (**Papers A** and **C**).
10. The impact of various types of optimisation techniques on estimator and controller performance has been discussed. Direct single and multiple shooting techniques are examined in the context of MHE and mMHE in **Paper A**, with multiple shooting being more computationally efficient when exploiting the sparsity structure of the resulting optimisation problems. Direct collocation is utilised in **Papers B–E** to efficiently handle the continuous-time OCPs and thus obtain the solutions.

In addition to the scientific contributions described above, an integrated framework for “Preprocessing”, “Processing” and “Postprocessing” has been developed in the studies presented in this work. This framework facilitates efficient computing, smooth parameter tuning and results analysis, as well as sustainable code development (Chapter 6).

Chapter 9

Conclusions and future directions

This chapter concludes the research presented in this thesis and provides suggestions for future work in this field.

9.1 Conclusions

The studies presented in this thesis aim to improve the active safety of autonomous electric vehicles by exploiting the potential of over-actuation. In particular, the work focuses on enhancing path following and yaw stability performance of autonomous vehicles by using over-actuation, as well as establishing vehicle state estimation and trajectory planning strategies in critical driving scenarios.

To model the vehicle dynamics that are needed for developing the strategies for state estimation, trajectory planning as well as path following and yaw stability control, vehicle and tyre models of various levels of complexity have been introduced. They include single-track kinematic and dynamic vehicle models, double-track dynamic vehicle models, a linear tyre model, the Dugoff tyre model, a camber tyre model, as well as the Magic Formula (MF) tyre model. Specifically, the camber effect on lateral tyre forces was modelled by using a simple, yet effective, component. This way of modelling the camber effect, together with the Dugoff tyre model, allows for individual control of wheel inclination, which enables effective active camber and thus improved path following and yaw stability performance.

To address RQs 1.1–1.2, which are associated with reliable state estimation in critical driving scenarios, an extensive evaluation has been carried out on four state estimators. The estimators, including moving horizon estimation (MHE), modified MHE (mMHE), recursive-least-squares (RLS) MHE and unscented Kalman filter (UKF), were designed based on a nonlinear system model that was verified to be locally observable. These estimators were evaluated in three critical manoeuvres. It was found that MHE outperformed RLS-MHE and UKF in terms of convergence rate, estimation accuracy, as well as their response to modelling errors and external disturbances. Moreover, mMHE performed comparably to MHE with respect to

convergence and accuracy but was not as robust in handling external disturbances and relatively large modelling errors in the circular manoeuvre.

To achieve trajectory planning in critical conditions, i.e., RQs 2.1–2.2, five planners with various combinations of vehicle and tyre models of different levels of complexity have been evaluated. The planners were designed by simultaneously considering path and yaw stability-related states – yaw rate and sideslip angle – in the problem formulation. In addition, constraints for achieving obstacle avoidance, yaw stability and feasible control actions were explicitly included in the formulation. Moreover, variation in sideslip angle was taken into account in the yaw rate constraints, yielding extended dynamic performance. Combining all these, the trajectory planning problems were formulated as optimal control problems (OCPs), and the planners were examined in two safety-critical manoeuvres. The evaluation regarding model complexity showed that the more advanced double-track planner with load transfer and the MF tyre model performed better than the one with the Dugoff tyre model in terms of passing velocity as well as peak yaw rate and sideslip angle. The three simpler single-track planners were not suitable for use in these critical driving scenarios due to their over- or under-estimated trajectories.

To improve path following and yaw stability performance in critical manoeuvres by exploiting over-actuation, i.e., RQs 3.1–3.2, various means and combinations of motion actuation have been studied, with regard to passing velocity, tracking accuracy, safety distance, and robustness under variations in road condition and reference trajectory. Double-track vehicle models, combined with the Dugoff tyre model and its altered version with camber effect, were used to model vehicle dynamics for designing the path following and yaw stability controllers. These controllers were formulated as model predictive control (MPC) problems, with path following and yaw stability being considered concurrently. Specifically, explicit constraints were applied to yaw rate and sideslip angle in order to achieve yaw stability and avoid tracking overshoot. Additionally, physical limits on vehicle actuators were considered, resulting in feasible control actions without compromising control performance. With these MPC formulations, the effects of torque vectoring (TV), active camber (AC) and the integrated control of motion actuators have been evaluated comprehensively in various safety-critical driving scenarios.

- Exploiting torque vectoring improved passing velocity and tracking accuracy. With the one-level controller structure, torque vectoring yielded the highest passing velocity at all three road friction levels, but its tracking accuracy for yaw rate degraded when road friction varied. With the two-level structure, the rule-based torque allocation algorithm had the same passing velocity as the optimisation-based algorithm and comparable tracking accuracy while being simpler to implement; on the other hand, the optimisation-based method had more degrees of freedom in designing and tuning its cost function terms. Furthermore, the tracking accuracy of the one-level controller with torque vectoring and the two-level controller with optimisation-based torque allocation improved significantly as the horizon size increased to a certain threshold,

but their performance degraded thereafter.

- Active camber was able to improve the path following and yaw stability performance with higher passing velocities at all three road friction levels. For better combined performance, $\Delta\gamma = 45^\circ/\text{s}$ was the preferred camber rate in the high- and medium-friction conditions, and $\Delta\gamma = 30^\circ/\text{s}$ was sufficient in the low-friction condition due to the narrow effective camber region in this case. Moreover, the required peak power and consumed energy for the camber actuators were considerably lower than that for the wheel motors in the tested scenarios.
- In the research concerning integrated motion actuators, four over-actuation configurations have been evaluated in the single-lane change manoeuvre at various initial velocities, including active front steering (AFS), AFS + TV, AFS + AC and AFS + TV + AC. The results show that the integrated control of AFS + TV + AC outperformed the others with higher passing velocities, lower peak values and tracking errors for sideslip angle, a larger safety distance in the most critical location, and more robust response to reference trajectory variations. Moreover, AFS + AC was superior to AFS + TV due to the more effective tyre utilisation of active camber over torque vectoring. AFS performed the worst among the four configurations, and AFS and AFS + TV were not as robust in dealing with trajectory variations as the other two configurations.

An integrated framework has been developed to implement the MHE, OCP and MPC problems arising from the state estimation, trajectory planning as well as path following and yaw stability control studies. The framework covers the definition of parameters and test scenarios, the formulation and solving of problems, and the generation and analysis of results. By building this framework in an integrated manner, it was able to achieve an appropriate definition of test conditions, improved computational efficiency, smooth parameter tuning and results analysis, and sustainable code development.

In summary, the research presented here has contributed to the modelling, formulation and control of autonomous electric vehicles by exploiting over-actuation for enhanced vehicle safety, as well as the associated state estimation and trajectory planning problems. These studies have shown that over-actuation control strategies can be a promising solution for improving active safety, and thus they contribute to a safer and more sustainable future transport.

9.2 Recommendations for future work

The camber tyre model presented in this thesis provides a simple, yet effective, way of representing the effect of wheel inclination on lateral tyre forces, which is suitable for control design applications. In the future, it is recommended to consider the

effect of camber on longitudinal tyre forces so that the influence of wheel camber on tyre forces can be modelled more accurately. Additionally, it would be valuable to study the effect of camber on tyre wear, as camber control can alter the tyre contact patch with the road. This could then provide insights for future tyre design for active camber applications. Moreover, it is suggested to improve the smoothness of the tyre model to potentially enhance the computational efficiency of the resulting optimisation problems.

The vehicle and tyre models developed here, with different levels of complexity and various means of over-actuation, have demonstrated their effectiveness in the state estimation, trajectory planning as well as path following and yaw stability control studies. In the future, more vehicle components could be modelled, and more means of over-actuation (such as individual active suspension) could be explored. This could potentially further improve modelling accuracy, enhance vehicle performance, and facilitate the inclusion of indicators such as comfort in the design objectives.

The proposed state estimators have been analysed with regard to different tuning parameters and operation conditions. It would be valuable to further examine the algorithms concerning these factors in terms of theoretical aspects. Moreover, the state estimation studies presented here mainly focused on estimating critical vehicle states in flat road conditions. In the future, it would be interesting to estimate states and parameters such as roll angle, road friction level and bank angle, as they are also crucial to vehicle safety.

The trajectory planning studies mainly aimed to generate reliable and realistic reference trajectories in critical manoeuvres. The trajectories were not updated at each sampling step in the corresponding trajectory tracking assessment. Future trajectory planning and tracking studies could be conducted in a combined manner to achieve improved performance. For instance, the influence of over-actuation configurations on the combined performance could be investigated. Further, trajectory planning could be carried out in environments with moving obstacles to facilitate vehicle safety in more critical scenarios.

The formulated estimation, planning and control problems were resolved using numerical solvers that give locally optimal solutions. It is also worth addressing these problems using global optimisation algorithms such as dynamic programming [115] and evaluating the performance difference. It is also suggested to employ techniques such as real-time iteration and code generation [66, 98, 116] on the developed algorithms. Based on these techniques, it is recommended to deploy the algorithms for more experimental studies.

Bibliography

- [1] OICA, “World vehicles sales statistics,” accessed on 2022-01-25. [Online]. Available: <https://www.oica.net/category/sales-statistics/>
- [2] D. Banister, “The climate crisis and transport,” *Transport Reviews*, vol. 39, no. 5, pp. 565–568, Jul. 2019.
- [3] ——, *Inequality in transport*. Marcham, Oxfordshire: Alexandrine Press, 2018.
- [4] OICA, “World vehicles production statistics,” accessed on 2022-01-25. [Online]. Available: <https://www.oica.net/production-statistics/>
- [5] ——, “World vehicles in use,” accessed on 2022-01-25. [Online]. Available: <https://www.oica.net/category/vehicles-in-use/>
- [6] ITF, “ITF transport outlook 2021,” ITF, Paris, techreport, 2021.
- [7] WHO, *Global Status Report on Road Safety 2018*. Geneva: World Health Organization, 2019.
- [8] ——, “Road traffic injuries,” Jan. 2022, accessed on 2022-01-25. [Online]. Available: <https://www.who.int/news-room/fact-sheets/detail/road-traffic-injuries>
- [9] E. K. Liebemann, K. Meder, J. Schuh, and G. Nenninger, “Safety and performance enhancement: The Bosch electronic stability control (ESP),” in *Proc. SAE Convergence*, 2004, pp. 1–8.
- [10] ITF, “Road safety annual report 2020,” ITF, Paris, techreport, 2020. [Online]. Available: <https://www.itf-oecd.org/road-safety-annual-report-2020>
- [11] A. Erke, “Effects of electronic stability control (esc) on accidents: A review of empirical evidence,” *Accident Analysis & Prevention*, vol. 40, no. 1, pp. 167–173, Jan. 2008.
- [12] A. Høye, “The effects of electronic stability control (ESC) on crashes—an update,” *Accident Analysis & Prevention*, vol. 43, no. 3, pp. 1148–1159, May 2011.

- [13] L. Riexinger, R. Sherony, and H. Gabler, “Has electronic stability control reduced rollover crashes?” in *SAE Technical Paper Series*. SAE International, Apr. 2019.
- [14] C. N. Webb, “Estimating lives saved by electronic stability control, 2011-2015,” NHTSA, U.S. Dept. of Transportation, Washington, DC, Traffic Safety Facts Research Note DOT HS 812 391, Mar. 2017.
- [15] N. C. for Statistics and Analysis., “Overview of motor vehicle crashes in 2019,” NHTSA, U.S. Dept. of Transportation, Washington, DC, Traffic Safety Facts Research Note DOT HS 813 060, Dec. 2020.
- [16] SAE, *Taxonomy and Definitions for Terms Related to Driving Automation Systems for On-Road Motor Vehicles*, SAE Std., 2021.
- [17] IEA, “Greenhouse gas emissions from energy – data explorer,” IEA, Paris, accessed on 2022-01-27. [Online]. Available: <https://www.iea.org/articles/greenhouse-gas-emissions-from-energy-data-explorer>
- [18] ——, “Transport sector CO₂ emissions by mode in the sustainable development scenario, 2000-2030,” IEA, Paris, accessed on 2022-01-27. [Online]. Available: <https://www.iea.org/data-and-statistics/charts/transport-sector-co2-emissions-by-mode-in-the-sustainable-development-scenario-2000-2030>
- [19] ——, “World energy outlook 2021,” IEA, Paris, resreport, 2021. [Online]. Available: <https://www.iea.org/reports/world-energy-outlook-2021>
- [20] ——, “Global EV outlook 2021,” IEA, Paris, techreport, 2021. [Online]. Available: <https://www.iea.org/reports/global-ev-outlook-2021>
- [21] EV-Volumes, “Global EV sales for 2021 H1,” accessed on 2022-01-27. [Online]. Available: <https://www.ev-volumes.com/>
- [22] BYD, “Han EV,” accessed on 2022-01-27. [Online]. Available: <https://en.byd.com/auto/>
- [23] Polestar, “Polestar 1,” accessed on 2022-01-27. [Online]. Available: <https://www.polestar.com/se/polestar-1/>
- [24] Tesla, “Model S Plaid,” accessed on 2022-01-27. [Online]. Available: <https://www.tesla.com/models>
- [25] Audi, “Audi e-tron S,” Jan. 2022, accessed on 2022-01-27. [Online]. Available: <https://www.audi.com/en.html>
- [26] Zoox, “Safety,” accessed on 2022-01-27. [Online]. Available: <https://zoox.com/safety/>

- [27] S. Zetterström, “Vehicle wheel suspension arrangement,” USA Patent US6 386 553B2, 1998.
- [28] M. Jonasson and J. Andreasson, “Exploiting autonomous corner modules to resolve force constraints in the tyre contact patch,” *Vehicle System Dynamics*, vol. 46, no. 7, pp. 553–573, May 2008.
- [29] O. Wallmark, M. Nybacka, D. Malmquist *et al.*, “Design and implementation of an experimental research and concept demonstration vehicle,” in *2014 IEEE Vehicle Power and Propulsion Conf.*, 2014, pp. 1–6.
- [30] M. Jonasson, “Exploiting individual wheel actuators to enhance vehicle dynamics and safety in electric vehicles,” Ph.D. dissertation, KTH, Vehicle Dynamics, 2009, qC 20100722.
- [31] J. Rauh and D. Ammon, “System dynamics of electrified vehicles: some facts, thoughts, and challenges,” *Vehicle System Dynamics*, vol. 49, no. 7, pp. 1005–1020, Jul. 2011.
- [32] M. M. Davari, “Exploiting over-actuation to reduce tyre energy losses in vehicle manoeuvres,” Ph.D. dissertation, KTH, Vehicle Dynamics, 2017, qC 20170524.
- [33] P. Sun, “Improving energy-efficiency of electric vehicles by over-actuation,” Ph.D. dissertation, KTH, Vehicle Dynamics, Stockholm, 2020.
- [34] D. Wanner, “Controlling over-actuated road vehicles during failure conditions,” Ph.D. dissertation, KTH, Vehicle Dynamics, 2015, qC 20150520.
- [35] J. Edrén, “Motion modelling and control strategies of over-actuated vehicles,” Ph.D. dissertation, KTH, Vehicle Dynamics, 2014, finansierat av SHC, Swedish Hybrid Vehicle Centre. QC 20141114.
- [36] D. Systèmes. (2016) Dymola 2017. [Online]. Available: <https://www.3ds.com/products-services/catia/products/dymola>
- [37] M. Association. (2014) Functional mockup interface for model exchange and co-simulation, version 2.0. [Online]. Available: fmi-standard.org
- [38] D. Robertson and J. Lee, “A least squares formulation for state estimation,” *Journal of Process Control*, vol. 5, no. 4, pp. 291–299, Aug. 1995.
- [39] R. E. Kalman, “A new approach to linear filtering and prediction problems,” *Journal of Basic Engineering*, vol. 82, no. 1, pp. 35–45, Mar. 1960.
- [40] H. Michalska and D. Mayne, “Robust receding horizon control of constrained nonlinear systems,” *IEEE Transactions on Automatic Control*, vol. 38, no. 11, pp. 1623–1633, 1993.

- [41] R. Rajamani, *Vehicle Dynamics and Control*, 2nd ed. New York, NY, USA: Springer, 2012.
- [42] M. Doumiati, A. Charara, and A. Victorino, *Vehicle Dynamics Estimation Using Kalman Filtering: Experimental Validation*, 1st ed. London, UK: ISTE Ltd, 2012.
- [43] P. Falcone, F. Borrelli, J. Asgari *et al.*, “Predictive active steering control for autonomous vehicle systems,” *IEEE Trans. Control Syst. Technol.*, vol. 15, no. 3, pp. 566–580, May 2007.
- [44] H. Pacejka, *Tire and Vehicle Dynamics*, 3rd ed. Oxford, UK: Elsevier, 2012.
- [45] H. Dugoff, P. S. Fancher, and L. Segel, “Tire performance characteristics affecting vehicle response to steering and braking control inputs,” U.S. National Bureau of Standards, Washington, DC, Tech. Rep. Contract CST-460, Aug. 1969.
- [46] D. M. Bevly, J. C. Gerdes, and C. Wilson, “The use of GPS based velocity measurements for measurement of sideslip and wheel slip,” *Veh. Syst. Dyn.*, vol. 38, no. 2, pp. 127–147, 2002.
- [47] D. M. Bevly, J. Ryu, and J. C. Gerdes, “Integrating INS sensors with GPS measurements for continuous estimation of vehicle sideslip, roll, and tire cornering stiffness,” *IEEE Trans. Intell. Transp. Syst.*, vol. 7, no. 4, pp. 483–493, Dec. 2006.
- [48] D. Selmanaj, M. Corno, G. Panzani, and S. M. Savaresi, “Vehicle sideslip estimation: A kinematic based approach,” *Control Eng. Pract.*, vol. 67, pp. 1–12, Oct. 2017.
- [49] K. T. Leung, J. F. Whidborne, D. Purdy, and A. Dunoyer, “A review of ground vehicle dynamic state estimations utilising GPS/INS,” *Veh. Syst. Dyn.*, vol. 49, no. 1-2, pp. 29–58, 2011.
- [50] R. Anderson and D. M. Bevly, “Using GPS with a model-based estimator to estimate critical vehicle states,” *Veh. Syst. Dyn.*, vol. 48, no. 12, pp. 1413–1438, 2010.
- [51] K. Nam, S. Oh, H. Fujimoto, and Y. Hori, “Estimation of sideslip and roll angles of electric vehicles using lateral tire force sensors through RLS and Kalman filter approaches,” *IEEE Trans. Ind. Electron.*, vol. 60, no. 3, pp. 988–1000, Mar. 2013.
- [52] Y. Chen, Y. Ji, and K. Guo, “A reduced-order nonlinear sliding mode observer for vehicle slip angle and tyre forces,” *Veh. Syst. Dyn.*, vol. 52, no. 12, pp. 1716–1728, 2014.

- [53] H. Guo, H. Chen, F. Xu *et al.*, “Implementation of EKF for vehicle velocities estimation on FPGA,” *IEEE Trans. Ind. Electron.*, vol. 60, no. 9, pp. 3823–3835, Sep. 2013.
- [54] S. Antonov, A. Fehn, and A. Kugi, “Unscented Kalman filter for vehicle state estimation,” *Veh. Syst. Dyn.*, vol. 49, no. 9, pp. 1497–1520, Sep. 2011.
- [55] A. Katriniok and D. Abel, “Adaptive EKF-based vehicle state estimation with online assessment of local observability,” *IEEE Trans. Control Syst. Technol.*, vol. 24, no. 4, pp. 1368–1381, Jul. 2016.
- [56] K. Berntorp, “Joint wheel-slip and vehicle-motion estimation based on inertial, GPS, and wheel-speed sensors,” *IEEE Trans. Control Syst. Technol.*, vol. 24, no. 3, pp. 1020–1027, May 2016.
- [57] Y. Liang, S. Müller, D. Rolle *et al.*, “Vehicle side-slip angle estimation with deep neural network and sensor data fusion,” in *Proceedings*. Springer Fachmedien Wiesbaden, Nov. 2019, pp. 159–178.
- [58] M. Canale, L. Fagiano, and C. Novara, “A direct moving horizon approach to vehicle side-slip angle estimation,” in *49th IEEE Conf. Decision Control*, 2010, pp. 2898–2903.
- [59] M. Zanon, J. Frasch, and M. Diehl, “Nonlinear moving horizon estimation for combined state and friction coefficient estimation in autonomous driving,” in *2013 European Control Conf.*, 2013, pp. 4130–4135.
- [60] J. Frasch, T. Kraus, W. Saeys, and M. Diehl, “Moving horizon observation for autonomous operation of agricultural vehicles,” in *2013 European Control Conf.*, 2013, pp. 4148–4153.
- [61] J. F. Bellantoni and K. W. Dodge, “A square root formulation of the Kalman-schmidt filter.” *AIAA Journal*, vol. 5, no. 7, pp. 1309–1314, Jul. 1967.
- [62] S. J. Julier and J. K. Uhlmann, “New extension of the Kalman filter to nonlinear systems,” in *AeroSense '97*, I. Kadar, Ed. SPIE, Jul. 1997.
- [63] Simon, *Optimal State Estimation: Kalman, H Infinity, and Nonlinear Approaches*. Wiley-Interscience, Jun. 2006.
- [64] D. G. Robertson, J. H. Lee, and J. B. Rawlings, “A moving horizon-based approach for least-squares estimation,” *AIChE J.*, vol. 42, no. 8, pp. 2209–2224, Aug. 1996.
- [65] C. Rao, J. Rawlings, and D. Mayne, “Constrained state estimation for non-linear discrete-time systems: stability and moving horizon approximations,” *IEEE Transactions on Automatic Control*, vol. 48, no. 2, pp. 246–258, Feb. 2003.

- [66] J. B. Rawlings, D. Q. Mayne, and M. M. Diehl, *Model Predictive Control: Theory, Computation, and Design*, 2nd ed. Madison, WI, USA: Nob Hill Publishing, 2017.
- [67] C. V. Rao and J. B. Rawlings, “Constrained process monitoring: Moving-horizon approach,” *AICHE J.*, vol. 48, no. 1, pp. 97–109, Jan. 2002.
- [68] C. C. Qu and J. Hahn, “Computation of arrival cost for moving horizon estimation via unscented Kalman filtering,” *J. Process Control*, vol. 19, no. 2, pp. 358–363, Feb. 2009.
- [69] R. Xiong and M. A. Grover, “A modified moving horizon estimator for in situ sensing of a chemical vapor deposition process,” *IEEE Trans. Control Syst. Technol.*, vol. 17, no. 5, pp. 1228–1235, Sep. 2009.
- [70] V. Delsart, T. Fraichard, and L. Martinez, “Real-time trajectory generation for car-like vehicles navigating dynamic environments,” in *2009 IEEE International Conference on Robotics and Automation*. IEEE, May 2009.
- [71] P. F. Lima, “Optimization-based motion planning and model predictive control for autonomous driving : With experimental evaluation on a heavy-duty construction truck,” Ph.D. dissertation, KTH, Automatic Control, Stockholm, Sweden, 2018, qC 20180824.
- [72] U. Rosolia, S. D. Bruyne, and A. G. Alleyne, “Autonomous vehicle control: A nonconvex approach for obstacle avoidance,” *IEEE Transactions on Control Systems Technology*, vol. 25, no. 2, pp. 469–484, Mar. 2017.
- [73] Y. Rasekhipour, A. Khajepour, S.-K. Chen, and B. Litkouhi, “A potential field-based model predictive path-planning controller for autonomous road vehicles,” *IEEE Transactions on Intelligent Transportation Systems*, vol. 18, no. 5, pp. 1255–1267, May 2017.
- [74] C. Rathgeber, F. Winkler, X. Kang, and S. Müller, “Optimal trajectories for highly automated driving,” 2015.
- [75] D. Gonzalez, J. Perez, V. Milanes, and F. Nashashibi, “A review of motion planning techniques for automated vehicles,” *IEEE Transactions on Intelligent Transportation Systems*, vol. 17, no. 4, pp. 1135–1145, Apr. 2016.
- [76] ISO, *Road vehicles - Passenger cars - Test track for a severe lane-change manoeuvre - Part 2: Obstacle avoidance*, ISO Std. 3888-2: 2011, IDT, 2011.
- [77] V. Fors, B. Olofsson, and L. Nielsen, “Formulation and interpretation of optimal braking and steering patterns towards autonomous safety-critical manoeuvres,” *Vehicle System Dynamics*, vol. 57, no. 8, pp. 1206–1223, Nov. 2018.

- [78] M. Jonasson, J. Andreasson, S. Solyom *et al.*, “Utilization of actuators to improve vehicle stability at the limit: From hydraulic brakes toward electric propulsion,” *Journal of Dynamic Systems, Measurement, and Control*, vol. 133, no. 5, p. 051003, 2011.
- [79] K. Nam, H. Fujimoto, and Y. Hori, “Lateral stability control of in-wheel-motor-driven electric vehicles based on sideslip angle estimation using lateral tire force sensors,” *IEEE Trans. Veh. Technol.*, vol. 61, no. 5, pp. 1972–1985, Jun. 2012.
- [80] H. Alipour, M. Sabahi, and M. B. B. Sharifian, “Lateral stabilization of a four wheel independent drive electric vehicle on slippery roads,” *Mechatronics*, vol. 30, pp. 275–285, Sep. 2015.
- [81] J. Jerrelind, J. Edrén, S. Li *et al.*, “Exploring active camber to enhance vehicle performance and safety,” in *23rd Int. Symp. Dynamics Vehicles Roads Tracks*, 2013.
- [82] P. Gáspár and B. Németh, “Integrated control design for driver assistance systems based on LPV methods,” *Int. J. Control.*, vol. 89, no. 12, pp. 2420–2433, Mar. 2016.
- [83] T. Yoshino and H. Nozaki, “Effect of direct yaw moment control based on steering angle velocity and camber angle control,” in *SAE Technical Paper Series*. SAE International, Sep. 2014.
- [84] S. Drakunov, B. Ashrafi, and A. Rosiglioni, “Yaw control algorithm via sliding mode control,” in *Proceedings of the 2000 American Control Conference*. IEEE, 2000.
- [85] K. Uematsu and J. C. Gerdes, “A comparison of several sliding surfaces for stability control,” in *Proc. AVEC*, 2002, pp. 601–608.
- [86] J. Wang and R. Longoria, “Coordinated and reconfigurable vehicle dynamics control,” *IEEE Trans. Control Syst. Technol.*, vol. 17, no. 3, pp. 723–732, May 2009.
- [87] M. Polesel, B. Shyrokau, M. Tanelli *et al.*, “Hierarchical control of overactuated vehicles via sliding mode techniques,” in *53rd IEEE Conf. Decision Control (CDC)*, Dec. 2014, pp. 4095–4100.
- [88] Z. Shuai, H. Zhang, J. Wang *et al.*, “Combined AFS and DYC control of four-wheel-independent-drive electric vehicles over CAN network with time-varying delays,” *IEEE Trans. Veh. Technol.*, vol. 63, no. 2, pp. 591–602, Feb. 2014.

- [89] L. Zhai, T. Sun, and J. Wang, "Electronic stability control based on motor driving and braking torque distribution for a four in-wheel motor drive electric vehicle," *IEEE Trans. Veh. Technol.*, vol. 65, no. 6, pp. 4726–4739, Jun. 2016.
- [90] Z. Shuai, H. Zhang, J. Wang *et al.*, "Lateral motion control for four-wheel-independent-drive electric vehicles using optimal torque allocation and dynamic message priority scheduling," *Control Eng. Pract.*, vol. 24, pp. 55–66, Mar. 2014.
- [91] B. Lenzo, G. D. Filippis, A. M. Dizqah *et al.*, "Torque distribution strategies for energy-efficient electric vehicles with multiple drivetrains," *Journal of Dynamic Systems, Measurement, and Control*, vol. 139, no. 12, p. 121004, Aug. 2017.
- [92] B. Zhao, N. Xu, H. Chen *et al.*, "Stability control of electric vehicles with in-wheel motors by considering tire slip energy," *Mechanical Systems and Signal Processing*, vol. 118, pp. 340–359, Mar. 2019.
- [93] D. Q. Mayne, J. B. Rawlings, C. V. Rao, and P. O. M. Scokaert, "Constrained model predictive control: Stability and optimality," *Automatica*, vol. 36, no. 6, pp. 789–814, Jun. 2000.
- [94] P. Falcone, H. E. Tseng, J. Asgari *et al.*, "Integrated braking and steering model predictive control approach in autonomous vehicles," *IFAC Proceedings Volumes*, vol. 40, no. 10, pp. 273–278, 2007.
- [95] P. Falcone, F. Borrelli, H. E. Tseng *et al.*, "Low complexity MPC schemes for integrated vehicle dynamics control problems," in *Proc. AVEC*, 2008, pp. 875–880.
- [96] J. Gallop, V. Govender, and S. Müller, "Model predictive lateral vehicle guidance using a position controlled EPS system," *IFAC-PapersOnLine*, vol. 50, no. 2, pp. 265–270, Dec. 2017.
- [97] ISO, *Passenger cars - Test track for a severe lane-change manoeuvre - Part 1: Double lane change*, ISO Std. 3888-1: 2018, IDT, 2018.
- [98] M. Diehl and S. Gros, *Numerical Optimal Control*, 2020, Unpublished.
- [99] G. A. Hicks and W. H. Ray, "Approximation methods for optimal control synthesis," *The Canadian Journal of Chemical Engineering*, vol. 49, no. 4, pp. 522–528, Aug. 1971.
- [100] H. G. Bock and K. J. Plitt, "A multiple shooting algorithm for direct solution of optimal control problems," in *Proc. 9th IFAC World Congr.*, vol. 17, no. 2, 1984, pp. 1603–1608, 9th IFAC World Congress: A Bridge Between Control Science and Technology, Budapest, Hungary, 2-6 July 1984.

- [101] T. H. Tsang, D. M. Himmelblau, and T. F. Edgar, “Optimal control via collocation and non-linear programming,” *International Journal of Control*, vol. 21, no. 5, pp. 763–768, May 1975.
- [102] A. Wächter and L. T. Biegler, “On the implementation of an interior-point filter line-search algorithm for large-scale nonlinear programming,” *Math. Program.*, vol. 106, no. 1, pp. 25–57, Apr. 2005.
- [103] M. J. Risbeck and J. B. Rawlings. (2015) MPCTools: Nonlinear model predictive control tools for CasADi (Python interface). [Online]. Available: <https://bitbucket.org/rawlings-group/mpc-tools-casadi>
- [104] J. Gillis. (2020) rockit. [Online]. Available: <https://gitlab.kuleuven.be/mec-o-software/rockit>
- [105] D. Systèmes. (2018) FMPy. [Online]. Available: <https://github.com/CATIA-Systems/FMPy>
- [106] C. R. Harris, K. J. Millman, S. J. van der Walt *et al.*, “Array programming with NumPy,” *Nature*, vol. 585, no. 7825, pp. 357–362, Sep. 2020.
- [107] P. Virtanen, R. Gommers, T. E. Oliphant *et al.*, “SciPy 1.0: Fundamental Algorithms for Scientific Computing in Python,” *Nature Methods*, vol. 17, pp. 261–272, 2020.
- [108] J. D. Hunter, “Matplotlib: A 2D graphics environment,” *Computing in Science & Engineering*, vol. 9, no. 3, pp. 90–95, 2007.
- [109] Python. (2020) Python. [Online]. Available: <https://www.python.org/>
- [110] Spyder. (2020) Spyder: The scientific python development environment. [Online]. Available: <https://www.spyder-ide.org/>
- [111] Git. (2020) Git. [Online]. Available: <https://git-scm.com/>
- [112] J. A. E. Andersson, J. Gillis, G. Horn *et al.*, “CasADi – A software framework for nonlinear optimization and optimal control,” *Mathematical Programming Computation*, vol. 11, no. 1, pp. 1–36, Jul. 2019.
- [113] HSL. (2014) A collection of Fortran codes for large scale scientific computation. [Online]. Available: <http://www.hsl.rl.ac.uk/>
- [114] R. Serban and A. C. Hindmarsh, “CVODES: The sensitivity-enabled ODE solver in SUNDIALS,” in *Volume 6: 5th Int. Conf. Multibody Systems, Nonlinear Dynamics, and Control, Parts A, B, and C*, 2005, pp. 257–269.
- [115] R. E. Bellman, *Dynamic Programming*, ser. Princeton Landmarks in Mathematics and Physics. NJ: Princeton University Press, Jul. 2010.

- [116] H. Ferreau, S. Almér, R. Verschueren *et al.*, “Embedded optimization methods for industrial automatic control,” *IFAC-PapersOnLine*, vol. 50, no. 1, pp. 13 194–13 209, Jul. 2017.

Appended papers

Paper A

“Advanced vehicle state monitoring: Evaluating moving horizon estimators and unscented Kalman filter”,

Wenliang Zhang, Zhenpo Wang, Changfu Zou, Lars Drugge and Mikael Nybacka,
IEEE Transactions on Vehicular Technology, vol. 68, no. 6, 2019.

Paper A

Advanced Vehicle State Monitoring: Evaluating Moving Horizon Estimators and Unscented Kalman Filter

Wenliang Zhang [✉], Zhenpo Wang, Changfu Zou [✉], Member, IEEE, Lars Drugge [✉], and Mikael Nybacka [✉]

Abstract—Active safety systems must be used to manipulate the dynamics of autonomous vehicles to ensure safety. To this end, accurate vehicle information, such as the longitudinal and lateral velocities, is crucial. Measuring these states, however, can be expensive, and the measurements can be polluted by noise. The available solutions often resort to Bayesian filters, such as the Kalman filter, but can be vulnerable and erroneous when the underlying assumptions do not hold. With its clear merits in handling nonlinearities and uncertainties, moving horizon estimation (MHE) can potentially solve the problem and is thus studied for vehicle state estimation. This paper designs an unscented Kalman filter, standard MHE, modified MHE, and recursive least squares MHE to estimate critical vehicle states, respectively. All the estimators are formulated based upon a highly nonlinear vehicle model that is shown to be locally observable. The convergence rate, accuracy, and robustness of the four estimation algorithms are comprehensively characterized and compared under three different driving maneuvers. For MHE-based algorithms, the effects of horizon length and optimization techniques on the computational efficiency and accuracy are also investigated.

Index Terms—Moving horizon estimation, vehicle state estimation, kalman filter, nonlinear observability.

I. INTRODUCTION

AUTONOMOUS vehicles (AVs) have been drawing the attention of both traditional car manufacturers, e.g., Volvo and Audi, and technology companies like Google and Baidu. With the advance of AV technology, active safety systems such as electronic stability control (ESC) and anti-lock braking system

Manuscript received October 18, 2018; revised February 6, 2019; accepted March 18, 2019. Date of publication April 9, 2019; date of current version June 18, 2019. This work was supported in part by the KTH-CSC (China Scholarship Council) Programme, in part by the National Key R&D Programme of China under Grant 2017YFB0103600, and in part by Modelon. The review of this paper was coordinated by Dr. M. S. Ahmed. (*Corresponding authors:* Zhenpo Wang and Changfu Zou.)

W. Zhang is with the National Engineering Laboratory for Electric Vehicles and the Collaborative Innovation Centre for Electric Vehicles in Beijing, Beijing Institute of Technology, Beijing 100081, China, and also with the Department of Aeronautical and Vehicle Engineering, KTH Royal Institute of Technology, SE-10044 Stockholm, Sweden (e-mail: wez@kth.se).

Z. Wang is with the National Engineering Laboratory for Electric Vehicles and the Collaborative Innovation Centre for Electric Vehicles in Beijing, Beijing Institute of Technology, Beijing 100081, China (e-mail: wangzhenpo@bit.edu.cn).

C. Zou is with the Department of Electrical Engineering, Chalmers University of Technology, SE-41296 Gothenburg, Sweden (e-mail: changfu.zou@chalmers.se).

L. Drugge and M. Nybacka are with the Department of Aeronautical and Vehicle Engineering, KTH Royal Institute of Technology, SE-10044 Stockholm, Sweden (e-mail: larss@kth.se; mnybacka@kth.se).

Digital Object Identifier 10.1109/TVT.2019.2909590

(ABS) are playing an increasingly important role, especially in safety-critical situations. For example, in 2015 ESC saved 1,949 lives in passenger vehicle crashes in the USA, while there were still 2,272 fatalities resulting from these accidents [1]. To ensure the best possible performance from such life-saving systems, an accurate knowledge of vehicle states is important. However, states like longitudinal and lateral velocities cannot be measured directly with cost-effective sensors, leading to a demand for reliable online estimation algorithms.

Kinematics-based techniques, typically utilising various sensor measurements and the transformation among sensor positions, have been widely used to estimate desired vehicle states [2]–[4]. To describe where the measuring devices are installed, four different frames or their combinations are often employed, including the earth frame for which the global positioning system (GPS) is employed, the vehicle body frame for inertial measurement unit (IMU) installation, the vehicle frame for describing the vehicle motion, and the wheel frame [5]. In this class of approaches, the vehicle sideslip angle is usually estimated by directly integrating noisy/biased IMU measurements, subtracting the heading angle from measured GPS course angle, or the combination of the two. Although being easy to implement, these schemes are vulnerable to sensor bias and faults, and potential GPS outages. Moreover, they are limited by low update frequencies or a high cost of GPS devices [6].

To compensate for the limitation of kinematics-based techniques, dynamics-based approaches have been proposed for state estimation, requiring vehicle and tyre models together with physical parameters. These approaches are often realised by fusing different vehicle/tyre models and real-time state estimation techniques. For instance, based on a bicycle model of the vehicle and a linear tyre model, Anderson and Bevly [7] adopted the Kalman filter (KF) to detect sideslip angle and yaw rate. By using the KF and recursive least squares embedded similar system models, Nam *et al.* [8] estimated the sideslip and roll angles of electric vehicles using lateral tire force sensors. These linear model-based algorithms are superior in computational efficiency but suffer from large model uncertainties because the small angle assumption underpinning the bicycle model cannot hold when the vehicle/tyre behaves in some highly nonlinear regions [9].

To maintain the estimation performance in all possible operating regions, complicated nonlinear vehicle models and tyre models, such as the Pacejka tyre model [10], have been pursued

in estimator design. Based upon these nonlinear models, extended Kalman filters (EKFs) [11], [12] and unscented Kalman filters (UKFs) [13]–[15] have been widely exploited to gauge different vehicle states. To some degree address the modelling error, Katriniok and Abel [16] introduced two additional adaptation states to scale longitudinal and lateral tire forces within the EKF framework. For the same purpose, Liu *et al.* [17] proposed the minimum model error criterion combined with the EKF. Techniques and applications of adaptive UKFs for state estimation have been well documented in [18], [19]. Although these KF-type estimators have shown promising results, relying on linearisation or unscented transformation to approximate the nonlinear system will potentially introduce additional modelling errors, thus lowering the estimator performance such as accuracy and convergence rate. Equipped with Monte Carlo algorithms, the Rao-Blackwellized particle filter (PF) have been applied to jointly estimate key variables in active safety systems, such as the longitudinal velocity, roll angle, and wheel slip for all four wheels [20]. In addition to the computational burden, this PF estimator turned to be not sufficiently robust in dealing with unknown persistent disturbances and noise.

As different to the above estimation methods that merely involve the current measurement, the moving horizon estimation (MHE) algorithm derives state estimates by solving an optimisation problem in terms of a window of the most recent measurements at each time step [21], [22]. By incorporating various sequential measurements for state estimation, MHE tends to be more adaptive and robust in response to uncertainties stemmed from modelling, parametrisation, and measurements. Moreover, nonlinear vehicle/tyre models can be formulated naturally into the MHE framework, thus maintaining a high model fidelity for state prediction. In light of these two aspects, the MHE has emerged in the field of vehicle state/parameter estimation, e.g., [23]–[25]. These salient upsides, however, are achieved at the cost of extensive computational resources that are required to solve the nonlinear optimisation problem in real-time, especially when multiple state variables exist and a large horizon is considered. Therefore, the implementation of MHE for advanced monitoring and management of vehicle dynamics is subject to competing objectives, such as system complexity and estimation accuracy, and well balancing different objectives is of great importance.

From the above discussions, it is clear that a comprehensively comparative study of different MHE and KF-type estimation algorithms is desired in the context of vehicle state estimation. This research problem is meticulously addressed in the present work for estimating vital vehicle states. Three contributions are made to distinguish this work from available vehicle estimation efforts. First, with a nonlinear system model synthesised from the double-track vehicle model and simplified Pacejka tyre model, an observability analysis is conducted and shows that the system model is locally observable. Then, the standard MHE, a modified MHE (mMHE) adopted from [26], the recursive least squares MHE (RLS-MHE), and the UKF are designed successively to monitor the longitudinal and lateral velocities, yaw rate, yaw angle, and position of the vehicle. Their convergence rates, accuracy and robustness are characterised and compared under three

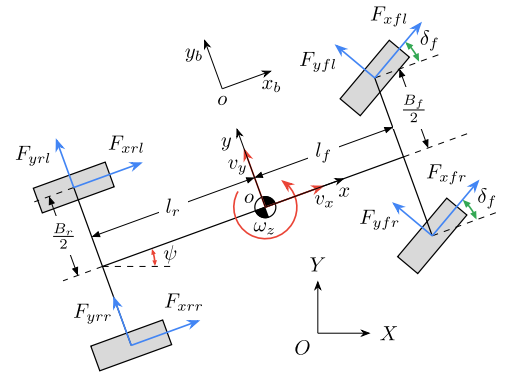


Fig. 1. Illustration of the planar vehicle model considering longitudinal, lateral, and yaw movements.

different driving manoeuvres. In addition, the effects of horizon length and optimisation techniques are evaluated in terms of the estimation performance and computational efficiency.

II. VEHICLE DYNAMICS MODELING

This section details the system model that governs vehicle motion, tyre forces, and vertical forces for estimation application. This is followed by introduction of a more accurate yet complex model that will be used to mimic the system plant and evaluate the estimation-oriented model in simulation studies. Both models are formulated in the frames in accordance with the ISO forward-leftward-upward (FLU) definition [5].

A. Model for Estimation

As illustrated in Fig. 1, the planar vehicle model synthesised from [17] and [27] is used to describe the system dynamics that consider longitudinal, lateral and yaw movements. Three frames, namely the earth frame XOY , the vehicle body frame xoy_b , and the vehicle frame xoy , are combined to define the state variables. By using the symbols defined in Table I, the planar vehicle model can be readily mathematically formulated with the governing equations as

$$\begin{aligned} mv_x &= (F_{xfl} + F_{xfrr}) \cos \delta_f - (F_{yfl} + F_{yfr}) \sin \delta_f \\ &\quad + F_{xrl} + F_{xrr} + mv_y \omega_z \end{aligned} \quad (1)$$

$$\begin{aligned} mv_y &= (F_{xfl} + F_{xfrr}) \sin \delta_f + (F_{yfl} + F_{yfr}) \cos \delta_f \\ &\quad + F_{yrl} + F_{yrr} - mv_x \omega_z \end{aligned} \quad (2)$$

$$\begin{aligned} I_z \dot{\omega}_z &= \frac{B_f}{2} ((F_{xfrr} - F_{xfl}) \cos \delta_f + (F_{yfl} - F_{yfr}) \sin \delta_f) \\ &\quad + \frac{B_r}{2} (F_{xrr} - F_{xrl}) + l_f ((F_{xfl} + F_{xfrr}) \sin \delta_f \\ &\quad + (F_{yfl} + F_{yfr}) \cos \delta_f) - l_r (F_{yrl} + F_{yrr}) \end{aligned} \quad (3)$$

$$\dot{\psi} = \omega_z \quad (4)$$

$$\dot{X} = v_x \cos \psi - v_y \sin \psi \quad (5)$$

$$\dot{Y} = v_x \sin \psi + v_y \cos \psi \quad (6)$$

TABLE I
GLOBAL NOMENCLATURE AND NOTATION

\mathcal{A}	A set in which the elements denote the front left, front right, rear left and rear right wheels, respectively, $= \{fl, fr, rl, rr\}$.
v_x	Longitudinal velocity at centre of gravity (CoG) (m/s).
v_y	Lateral velocity at CoG (m/s).
ω_z	Yaw rate around CoG (rad/s).
ψ	Yaw angle (rad).
X	Longitudinal position (m).
Y	Lateral position (m).
a_x	Longitudinal acceleration (m/s ²).
a_y	Lateral acceleration (m/s ²).
δ_f	Steering angle, mean of two front wheels (rad).
ω_i	Angular velocity of the wheel (rad/s) ($i \in \mathcal{A}$).
κ_i	Tyre slip ratio ($i \in \mathcal{A}$).
α_i	Tyre slip angle (rad) ($i \in \mathcal{A}$).
F_{zi}	Vertical tyre force (N) ($i \in \mathcal{A}$).
F_{xi}	Longitudinal tyre force (N) ($i \in \mathcal{A}$).
F_{yi}	Lateral tyre force (N) ($i \in \mathcal{A}$).
m	Vehicle mass (kg).
I_z	Vehicle yaw inertia (kg · m ²).
g	Gravitational acceleration (m/s ²).
B_f	Front track width (m).
B_r	Rear track width (m).
l_f	Distance from CoG to front axle (m).
l_r	Distance from CoG to rear axle (m).
h_g	Height of CoG (m).
r_e	Tyre radius (m).

where (1)–(3) convert the dynamics of the vehicle body frame to those of the vehicle frame, and (4)–(6) transform the motion in the vehicle frame into that in the earth frame.

To calculate the longitudinal and lateral tyre forces, F_{xi} and F_{yi} , required in (1)–(3), G_{xoi} and G_{yoi} represent the effect of the lateral/longitudinal slip on the longitudinal/lateral tyre forces; $B_{x\alpha i}$, $B_{y\kappa i}$, $C_{x\alpha i}$ and $C_{y\kappa i}$ are the corresponding coefficients determining that effect. These coefficients rely on the tyre parameters r_{bx1i} , r_{bx2i} , r_{cx1i} , r_{by1i} , r_{by2i} , r_{by3i} and r_{cy1i} . According to [28], the longitudinal and lateral tyre forces can be derived through a simplified Pacejka tyre model

$$F_{xi} = G_{x\alpha i} \cdot F_{x0i}, \quad F_{yi} = G_{y\kappa i} \cdot F_{y0i} \quad (7a)$$

$$G_{x\alpha i} = \cos(C_{x\alpha i} \arctan(B_{x\alpha i} \tan \alpha_i)) \quad (7b)$$

$$G_{y\kappa i} = \cos(C_{y\kappa i} \arctan(B_{y\kappa i} \kappa_i)) \quad (7c)$$

$$B_{x\alpha i} = r_{bx1i} \cos(\arctan(r_{bx2i} \kappa_i)) \quad (7d)$$

$$B_{y\kappa i} = r_{by1i} \cos(\arctan(r_{by2i} (\tan \alpha_i - r_{by3i}))) \quad (7e)$$

$$C_{x\alpha i} = r_{cx1i}, \quad C_{y\kappa i} = r_{cy1i} \quad (7f)$$

where F_{x0i} and F_{y0i} ($i \in \mathcal{A}$) denote the longitudinal and lateral tyre forces, respectively, under the pure slip condition. F_{x0i} and F_{y0i} can be calculated from the Pacejka tyre equations [10, eqs. (4.E9) and (4.E19)]. For simplicity in this calculation, the effect

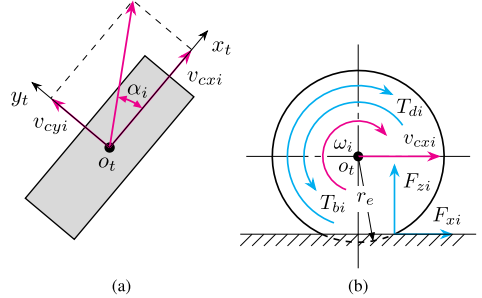


Fig. 2. Wheel frame and rotational motion. (a) and (b) show the top and side views, respectively.

of the camber angle and the pneumatic pressure is usually not considered, and the friction coefficient is not scaled. The two aspects are adopted in this work to develop a vehicle model for estimator design.

The expressions for the tyre slip ratio κ_i and slip angle α_i are given as [10]

$$\kappa_i = \frac{\omega_i r_e - v_{cxi}}{v_{cxi}}, \quad \alpha_i = \tan \frac{v_{cyi}}{v_{cxi}} \quad (8)$$

where v_{cxi} and v_{cyi} stand for the longitudinal and lateral velocities at the wheel centre, respectively, in the wheel frame $x_t o_t y_t$, as shown in Fig. 2(a). The velocities in this wheel frame are related to those in the vehicle frame by [17]

$$\begin{bmatrix} v_{xfl} \\ v_{xfr} \\ v_{xrl} \\ v_{xrr} \end{bmatrix} = \begin{bmatrix} v_x - B_f \omega_z / 2 \\ v_x + B_f \omega_z / 2 \\ v_x - B_r \omega_z / 2 \\ v_x + B_r \omega_z / 2 \end{bmatrix} \quad \begin{bmatrix} v_{yfl} \\ v_{yfr} \\ v_{yrl} \\ v_{yrr} \end{bmatrix} = \begin{bmatrix} v_y + l_f \omega_z \\ v_y + l_f \omega_z \\ v_y - l_r \omega_z \\ v_y - l_r \omega_z \end{bmatrix} \quad (9a)$$

$$\begin{bmatrix} v_{cxj} \\ v_{cyj} \end{bmatrix} = \begin{bmatrix} \cos \delta_f & \sin \delta_f \\ -\sin \delta_f & \cos \delta_f \end{bmatrix} \begin{bmatrix} v_{xj} \\ v_{yj} \end{bmatrix}, \quad j \in \{fl, fr\} \quad (9b)$$

$$\begin{bmatrix} v_{cxj} \\ v_{cyj} \end{bmatrix} = \begin{bmatrix} v_{xj} \\ v_{yj} \end{bmatrix}, \quad j \in \{rl, rr\} \quad (9c)$$

where v_{xi} and v_{yi} are the longitudinal and lateral velocities (at the wheel centre), respectively, in the vehicle frame xoy .

To determine the longitudinal and lateral tyre forces defined by (7), the vertical tyre forces are also required in addition to (8). Without considering the coupling effect between the pitch and roll dynamics, the steady-state vertical forces can be approximated by [11]

$$F_{zfl} = \frac{l_r mg}{2(l_f + l_r)} - \frac{h_g m a_x}{2(l_f + l_r)} - \frac{l_r h_g m a_y}{B_f(l_f + l_r)} \quad (10a)$$

$$F_{zfr} = \frac{l_r mg}{2(l_f + l_r)} - \frac{h_g m a_x}{2(l_f + l_r)} + \frac{l_r h_g m a_y}{B_f(l_f + l_r)} \quad (10b)$$

$$F_{zrl} = \frac{l_f mg}{2(l_f + l_r)} + \frac{h_g m a_x}{2(l_f + l_r)} - \frac{l_f h_g m a_y}{B_r(l_f + l_r)} \quad (10c)$$

$$F_{zrr} = \frac{l_f mg}{2(l_f + l_r)} + \frac{h_g m a_x}{2(l_f + l_r)} + \frac{l_f h_g m a_y}{B_r(l_f + l_r)}. \quad (10d)$$

The measurement equations that correspond to the longitudinal and lateral accelerations, a_x and a_y , are given as

$$\begin{aligned} a_x &= \frac{1}{m} ((F_{xfl} + F_{xfr}) \cos \delta_f - (F_{yfl} + F_{yfr}) \sin \delta_f \\ &\quad + F_{xrl} + F_{xrr}) \end{aligned} \quad (11)$$

$$\begin{aligned} a_y &= \frac{1}{m} ((F_{xfl} + F_{xfr}) \sin \delta_f + (F_{yfl} + F_{yfr}) \cos \delta_f \\ &\quad + F_{yrl} + F_{yrr}). \end{aligned} \quad (12)$$

By combining (1)–(12), a nonlinear model describing the vehicle dynamics has been derived. The measured longitudinal and lateral accelerations are denoted by a_x^m and a_y^m , respectively. For simplicity of presentation, the system state vector x , the input vector u and the output vector y are defined as

$$x = [v_x \ v_y \ \omega_z \ \psi \ X \ Y]^T \quad (13a)$$

$$u = [\delta_f \ \omega_{fl} \ \omega_{fr} \ \omega_{rl} \ \omega_{rr} \ a_x^m \ a_y^m]^T \quad (13b)$$

$$y = [a_x \ a_y \ \omega_z \ X \ Y]^T. \quad (13c)$$

As can be seen from (10), the vehicle acceleration is used to calculate the vertical tyre forces which are then used to determine the longitudinal and lateral tyre forces. Besides, the acceleration is also selected as the output variable, thus resulting in an implicit output function. This issue was tackled in [15] by calculating the vertical forces through vertical stiffness and suspension displacement and in [16] by introducing a correlated covariance term in the designed estimator. In this study, this problem is addressed outside the estimator framework by using the measurements a_x^m and a_y^m instead of unknown a_x and a_y to compute the vertical forces in (10).

With the definition in (13), the system model is represented in a compact state-space form

$$\dot{x}(t) = f_c(x(t), u(t)) \quad (14a)$$

$$y(t) = h_c(x(t), u(t)) \quad (14b)$$

where $f_c(\cdot)$ and $h_c(\cdot)$ are the continuous-time state and output functions, respectively, with the explicit form in (1)–(12).

For the sake of digital implementation, the above continuous-time system (14) is discretised using the forward Euler method with sampling time T_s . The obtained discrete-time system is given by

$$x_{k+1} = f(x_k, u_k) \quad (15a)$$

$$y_k = h(x_k, u_k) \quad (15b)$$

where $f(\cdot)$ and $h(\cdot)$ are the discrete-time state and output functions derived from $f_c(\cdot)$ and $h_c(\cdot)$, respectively.

B. Vehicle Plant

A model with seven degrees of freedom (DoF) is utilised to simulate the vehicle plant and to generate the measurement signals. Besides the longitudinal, lateral and yaw motions, the rotational motion of the four wheels is also taken into consideration, as shown in Fig. 2(b). The wheel dynamics are described by

$$I_{wi}\dot{\omega}_i = T_{di} - T_{bi} - r_e F_{xi} - C_{ri}r_e F_{zi} \quad (16)$$

where I_{wi} , T_{di} , T_{bi} and C_{ri} ($i \in \mathcal{A}$) are the rotational inertia, driving torque, braking torque and rolling resistance at the wheel, respectively.

In the seven-DoF vehicle plant model, the air drag force is included in the longitudinal dynamics, which results in an equation that is slightly different from (1). The new longitudinal dynamics are governed by

$$\begin{aligned} mv_x &= (F_{xfl} + F_{xfr}) \cos \delta_f - (F_{yfl} + F_{yfr}) \sin \delta_f \\ &\quad + F_{xrl} + F_{xrr} + mv_y \omega_z - C_d A_f \frac{D_a v_x^2}{2} \end{aligned} \quad (17)$$

where C_d , A_f and D_a are the drag coefficient, frontal area and air density, respectively.

An additional characteristic of the seven-DoF vehicle plant model is that the complete Pacejka tyre equations [10, eqs. (4.E1)–(4.E67)] are used to determine the longitudinal and lateral tyre forces in the combined slip condition. Similar to the case when calculating F_{x0i} and F_{y0i} , the camber, pneumatic pressure change and friction coefficient scaling are not taken into account here. The entire vehicle plant model is comprised of (2)–(6), (8)–(12), (16)–(17) and the Pacejka tyre model.

C. Model Evaluation

This section validates the simplified model in Section II-A against the plant model in Section II-B. This is performed under three manoeuvres, including a modified double lane change (DLC) [27], an ISO DLC [29] and a circular driving manoeuvre. In the modified DLC manoeuvre, the vehicle is controlled to track the reference path and to have a constant longitudinal velocity. In the ISO DLC manoeuvre, the vehicle first accelerates from a given initial velocity and then runs at an approximately constant speed; meanwhile, the vehicle is controlled to follow the predefined path. The circular manoeuvre represents a very harsh driving condition under which the vehicle accelerates and tries to maintain a reference yaw rate, $\omega_{zref} = v_x/R$, with R being the radius of the desired circular path. In these three driving scenarios, vehicle measurements are sampled at 0.01 s. The model parameters are taken from the software package CarSim [30]. Specifically, the tyre parameters follow the module CS_car225_60R18. The vehicle parameters are set up as: $I_z = 3234 \text{ kg} \cdot \text{m}^2$, $B_f = 1.6 \text{ m}$, $B_r = 1.6 \text{ m}$, $l_f = 1.4 \text{ m}$, $l_r = 1.65 \text{ m}$, $r_e = 0.3636 \text{ m}$, $C_d = 0.3$, $A_f = 2.8 \text{ m}^2$, $C_{ri} = 0.018$ ($i \in \mathcal{A}$), $m = 1759.14 \text{ kg}$, $h_g = 0.53 \text{ m}$, and $I_{wi} = 1.636 \text{ kg} \cdot \text{m}^2$ ($i \in \mathcal{A}$). The gravitational acceleration is $g = 9.81 \text{ m/s}^2$ and the air density is considered as $D_a = 1.206 \text{ kg/m}^2$.

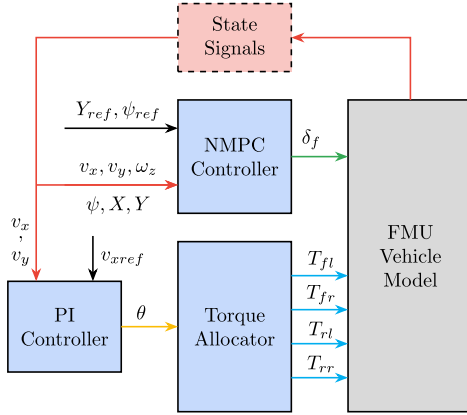


Fig. 3. Vehicle dynamics co-simulation using an FMU.

The vehicle plant model is first built in Dymola and then is exported into MATLAB/Simulink in the form of an FMU (a functional mock-up unit) for co-simulation. The block diagram for simulating vehicle dynamics is given in Fig. 3, where the vehicle control system mainly consists of a nonlinear model predictive controller (NMPC) and a proportional-integral (PI) controller. The NMPC utilises the vehicle signals v_x , v_y , ω_z , ψ , X and Y to determine the current state of the vehicle, and takes Y_{ref} and ψ_{ref} as references, as conducted in [27], [31]. By tracking these reference signals, the front steering angle δ_f is obtained. The PI controller is designed to track the reference longitudinal velocity v_{xref} , and a commanded pedal position signal θ is the output from this controller. The pedal position signal is utilised by the torque allocator to distribute the torque equally to the four individual wheels. The torque command together with the steering angle is employed for vehicle control. Note that the controllers are not tuned further since the control performance is not the focus of this study. Additionally, the variable-step ODE45 (Dormand-Prince) solver [32] is used within MATLAB/Simulink during the simulations.

The results from the model evaluation for the modified DLC manoeuvre are displayed in Fig. 4. As can be seen, the simplified model is able to well match the plant model. In particular, the root mean square (RMS) errors of v_x , v_y and ψ are 0.041 m/s, 0.050 m/s and 0.002 rad, respectively; the maximum errors are 0.104 m/s, 0.204 m/s and 0.004 rad, respectively. Similar results can be observed for the ISO DLC manoeuvre (figure not shown for brevity).

The model outputs for the circular driving manoeuvre are shown in Fig. 5. The system model cannot well capture the plant dynamics except those of v_x , and the modelling errors for v_y , ϕ and w_z in general are increasing with time, leading to not satisfactory model prediction results. The obvious modelling errors are mainly caused from the simplification of tyre model (7). Specifically, due to the neglect of some combined slip components, this simplified tyre model cannot well reproduce the true tyre behaviour during the circular manoeuvre where a heavy interaction between the lateral and longitudinal

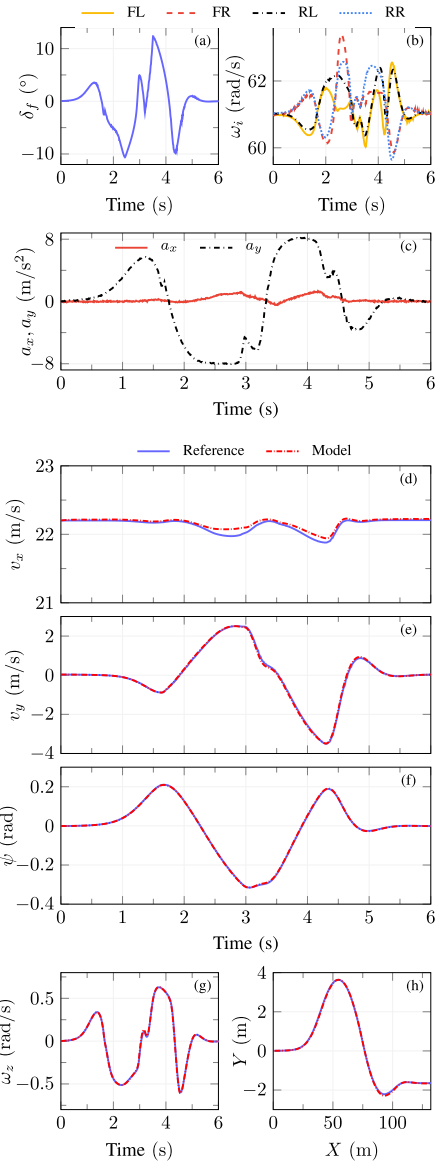


Fig. 4. Modified DLC manoeuvre input signals and model output. (a)–(c) show the input signals, where ‘FL’, ‘FR’, ‘RL’, and ‘RR’ denote the front left, front right, rear left, and rear right wheels, respectively. (d)–(h) present the model output, where ‘Reference’ and ‘Model’ denote the output from the model described in Section II-B and II-A, respectively.

slip exists. This circular driving manoeuvre is intentionally designed and will also be used in Section IV to test the capability of designed estimators in compensating for large model-plant mismatch.

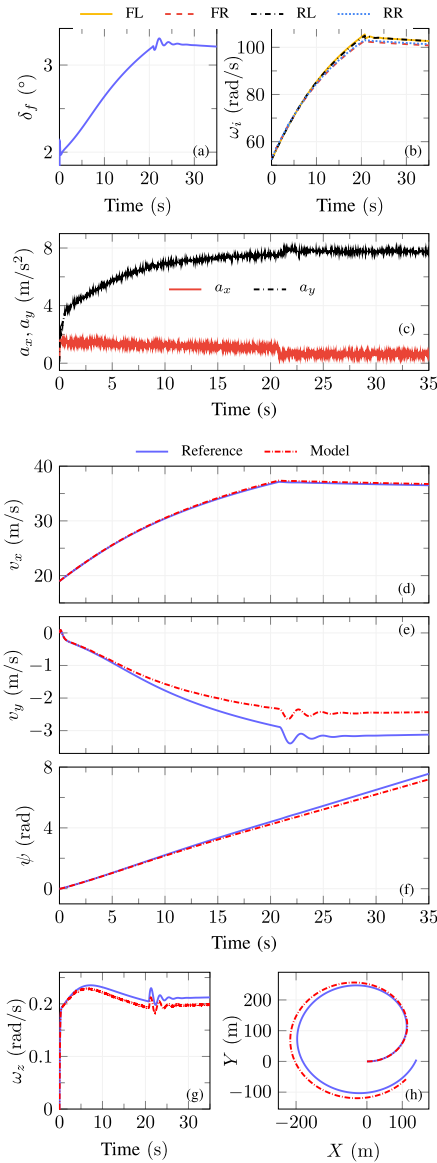


Fig. 5. Circular manoeuvre input signals and model output. (a)–(c) show the input signals. (d)–(h) present the model output.

III. ESTIMATOR DESIGN

In this section, the observability of the nonlinear system (14) described in Section II-A is analysed. This is followed by the design of three MHE-type estimators, including a standard one and two variants, as well as the UKF, based on the vehicle model (15).

A. Observability Analysis

The observability of a linear time-invariant system can be determined by examining the observability Gramian. For a nonlinear system, the observability, however, cannot be evaluated directly from the linearised system. The nonlinear system, (14), is said to be locally observable at the current operating point (x_0, u_0) if the following *observability matrix* \mathcal{O} has the same rank as the dimension of the state vector denoted n_x [33]:

$$\mathcal{O} = \begin{bmatrix} \frac{\partial L_f^0 h}{\partial x} & \frac{\partial L_f^1 h}{\partial x} & \cdots & \frac{\partial L_f^{n_x-1} h}{\partial x} \end{bmatrix}_{(x_0, u_0)}^T \\ := \begin{bmatrix} J_{L_f^0 h} & J_{L_f^1 h} & \cdots & J_{L_f^{n_x-1} h} \end{bmatrix}_{(x_0, u_0)}^T \quad (18)$$

where $L_f^i h$ is the i -th order Lie derivative, and $J_{L_f^i h}$ is the corresponding Jacobian matrix.

Combining (1)–(12), the first two components in \mathcal{O} are derived as

$$J_{L_f^0 h} = \begin{bmatrix} J_{0,11} & J_{0,12} & J_{0,13} & 0 & 0 & 0 \\ J_{0,21} & J_{0,22} & J_{0,23} & 0 & 0 & 0 \\ 0 & 0 & 1 & 0 & 0 & 0 \\ 0 & 0 & 0 & 0 & 1 & 0 \\ 0 & 0 & 0 & 0 & 0 & 1 \end{bmatrix} \quad (19a)$$

$$J_{L_f^1 h} = \begin{bmatrix} J_{1,11} & J_{1,12} & J_{1,13} & 0 & 0 & 0 \\ J_{1,21} & J_{1,22} & J_{1,23} & 0 & 0 & 0 \\ J_{1,31} & J_{1,32} & J_{1,33} & 0 & 0 & 0 \\ \cos \psi & -\sin \psi & 0 & J_{1,44} & 0 & 0 \\ \sin \psi & \cos \psi & 0 & J_{1,54} & 0 & 0 \end{bmatrix} \quad (19b)$$

where $J_{0,ij}$ and $J_{1,ij}$ are elements of the corresponding Jacobian matrices, and $J_{1,44} = -v_x \sin \psi - v_y \cos \psi$ and $J_{1,54} = v_x \cos \psi - v_y \sin \psi$.

As can be seen from (19a), the maximum possible rank of $J_{L_f^0 h}$ is 5. Since this maximum value is very close to the rank requirement of 6, it is possible to omit some orders of the Lie derivative in the observability matrix. From the equations of $J_{1,44}$ and $J_{1,54}$, it can be inferred that $J_{1,44}$ and $J_{1,54}$ will not be zero at the same time if v_x or v_y is nonzero. This is true when the vehicle is moving. Moreover, only the fourth column of $L_f^0 h$ is filled with constant zeros. Therefore, it is viable to use only the first two terms in \mathcal{O} to examine whether the system is locally observable or not. For this purpose, a new observability matrix, \mathcal{O}_2 , is used for observability evaluation

$$\mathcal{O}_2 = \begin{bmatrix} \frac{\partial L_f^0 h}{\partial x} \\ \frac{\partial L_f^1 h}{\partial x} \end{bmatrix}_{(x_0, u_0)} = \begin{bmatrix} J_{L_f^0 h} \\ J_{L_f^1 h} \end{bmatrix}_{(x_0, u_0)}. \quad (20)$$

By numerically calculating the rank of \mathcal{O}_2 at each time step, the system is validated to be locally observable since the rank plot is a horizontal line of rank 6.

B. Estimator Design

1) MHE: MHE can be formed in two frameworks: a deterministic one and a stochastic one [34]. For MHE in the first framework, the component corresponding to process noise should receive a small weighting (large covariance) if one has more faith in measurements, and a large weighting (small covariance) if one has less faith in measurements. In the stochastic framework, the covariances can be treated in the same way as in the EKF formulation. Given a time window of measurements, the MHE problem can be formulated as [35]

$$\begin{aligned} \min_{\mathbf{x}, \mathbf{w}, \mathbf{v}} & \|x_{k-N} - x_{k-N|k-N-1}\|_{P_{k-N|k-N-1}^{-1}}^2 \\ & + \sum_{i=k-N}^{k-1} \|w_i\|_{Q^{-1}}^2 + \sum_{i=k-N}^k \|v_i\|_{R^{-1}}^2 \end{aligned} \quad (21a)$$

$$\text{s.t. } x_{i+1} = f(x_i, u_i) + w_i \quad (21b)$$

$$y_i = h(x_i, u_i) + v_i \quad (21c)$$

where $\mathbf{x} = [x_{k-N}, \dots, x_k]$, $\mathbf{w} = [w_{k-N}, \dots, w_{k-1}]$ and $\mathbf{v} = [v_{k-N}, \dots, v_k]$ are the state variable, process noise and measurement noise sequences, respectively, and N is the length of the estimation window (horizon length). The process and measurement noise covariances are represented by Q and R , respectively. A state estimate with the subscript $i|k$ denotes the estimate at time step i with measurements until time step k . With this definition, $x_{k-N|k-N-1}$ and $P_{k-N|k-N-1}$ are called the *a priori* state estimate and the corresponding error covariance at time step $k-N$, respectively. Similarly, $x_{k-N|k-N}$ and $P_{k-N|k-N}$ are the *a posteriori* state estimate and error covariance at time step $k-N$, respectively. It is intuitive to see that a small weighting, i.e. Q^{-1} , should be given to the second component in (21a) if a large covariance Q is used, meaning that little trust is put on the model, and vice versa. This is also the reason for $P_{k-N|k-N-1}^{-1}$ and R^{-1} being used in the cost function.

Ideally, all the past measurements can be used to estimate the states at each time step, but this will cause overly demanding computational burden. By contrast, only $N+1$ measurements are considered in the MHE formulation in (21). To summarise the missing past information, an arrival cost term, the first term in (21), is required. The arrival cost can be updated by EKF and UKF-based approaches [36], [37], or filtering/smoothing update strategy [21].

When EKF is employed for updating the arrival cost, the EKF formulation needs to be modified to prevent the repeated usage of some measurements [36, eqs. (40)–(45)]. In the present study, for simpler implementation the standard EKF formulation has been utilised. The measurement correction step, (22a)–(22c), and prediction step, (22d)–(22e), are given as [38]

$$\begin{aligned} K_{k-N} &= P_{k-N|k-N-1} C_{k-N|k}^T R \\ &+ C_{k-N|k} P_{k-N|k-N-1} C_{k-N|k}^T)^{-1} \end{aligned} \quad (22a)$$

$$\begin{aligned} x_{k-N|k-N} &= x_{k-N|k-N-1} + K_{k-N}(y_{k-N} \\ &- h(x_{k-N|k}, u_{k-N})) \end{aligned} \quad (22b)$$

$$P_{k-N|k-N} = (I - K_{k-N} C_{k-N|k}) P_{k-N|k-N-1} \quad (22c)$$

$$x_{k-N+1|k-N} = f(x_{k-N|k}, u_{k-N}) \quad (22d)$$

$$P_{k-N+1|k-N} = A_{k-N|k} P_{k-N|k-N} A_{k-N|k}^T + Q \quad (22e)$$

where K_k is the Kalman gain. The Jacobian matrices $A_{k-N|k}$ and $C_{k-N|k}$, which are linearised around the smoothed estimate $x_{k-N|k}$, are defined as

$$A_{k-N|k} = \left. \frac{\partial f}{\partial x} \right|_{x_{k-N|k}} \quad C_{k-N|k} = \left. \frac{\partial h}{\partial x} \right|_{x_{k-N|k}}. \quad (23)$$

The above updating strategy for the arrival cost is developed for the case when $t > N$. On other occasions, MHE can be implemented either by forging faked measurements or by truncating the horizon [39]. In the present study, the latter procedure has been adopted, in which the MHE horizon length is initialised at zero. Then the horizon is increased gradually to N , after which the MHE estimator operates with a fixed horizon.

2) mMHE: The MHE (21)–(23) can be tailored to not estimate the process noise for reduced computational overhead. A possible way is to treat the process model as deterministic by following [26]. As a result, the process noise term w is removed from the model and objective function, leading to the mMHE estimator being formulated as

$$\begin{aligned} \min_{\mathbf{x}, \mathbf{v}} & \|x_{k-N} - x_{k-N|k-N-1}\|_{P_{k-N|k-N-1}^{-1}}^2 \\ & + \sum_{i=k-N}^k \|v_i\|_{R^{-1}}^2 \end{aligned} \quad (24a)$$

$$\text{s.t. } x_{i+1} = f(x_i, u_i) \quad (24b)$$

$$y_i = h(x_i, u_i) + v_i. \quad (24c)$$

Note that even though the uncertainty in the process is not directly included in (24), the effect of process noise is partly taken into account in the arrival cost term. In other words, by approximating the arrival cost with (22), the process noise is partly handled by the covariance Q in (22e).

3) RLS-MHE: The RLS-MHE estimator is a further simplified version of the MHE estimator. In addition to the process noise, the arrival cost term in the objective function is also discarded. The resulted estimator is given by

$$\min_{\mathbf{v}} \sum_{i=k-N}^k \|v_i\|_{R^{-1}}^2 \quad (25a)$$

$$\text{s.t. } x_{i+1} = f(x_i, u_i) \quad (25b)$$

$$y_i = h(x_i, u_i) + v_i. \quad (25c)$$

4) UKF: Similar to EKF, UKF also consists of a time update step and a measurement correction step. However, instead of approximating the nonlinear system with first-order transformation of mean and covariance like EKF, unscented transformation (UT) is used by UKF, which produces a third-order accuracy. By utilising UT a small number of sigma points that have the desired mean and covariance are selected. Each of the sigma points

is then propagated with the nonlinear function, yielding transformed sigma points. These transformed points are subsequently used to obtain an estimate of the mean and covariance resulting from the nonlinear transformation. In the present study, the UKF time and measurement update steps are derived by following [38, eqs. (14.56)–(14.67)], and their explicit formulation is ignored here for brevity.

IV. RESULTS AND DISCUSSION

The four estimation algorithms formulated in the previous section are now implemented and comprehensively compared. Trajectories of the system input u are generated from the manoeuvres mentioned earlier, i.e., the modified DLC, ISO DLC and circular manoeuvres. In each driving scenario, the vehicle plant model described in Section II-B is used to simulate the true vehicle and to generate measurement signals. To test the robustness of each estimator, the measurements are polluted by adding artificial noise of normal distribution with mean 0 and standard deviation 0.05 m/s^2 , 0.03 m/s^2 , 0.005 rad/s , 0.1 m , and 0.1 m for the longitudinal acceleration, lateral acceleration, yaw rate, longitudinal position, and lateral position, respectively.

The MHE and variants are all implemented in MPCTools [39], which is an interface to CasADi [40]. CasADi provides the first and second-order derivatives to the optimisation package IPOPT [41] and the solver MA27 [42]. Within IPOPT and MA27, the nonlinear optimisation problems are solved to full convergence with default solver settings, except for a time limit 20 s for the RLS-MHE. Furthermore, all simulations are performed in MATLAB R2016b running on a laptop computer configured with an Intel i7-6820HQ processor.

For a fair comparison, the tuning parameters of the four estimators are chosen to be the same. The prior guess covariance P_0 , the process and measurement noise covariances Q and R , and the horizon length N (for MHE-type estimators) are set as

$$P_0 = \text{diag}([0.005 \ 0.005 \ 0.01 \ 0.1 \ 0.1 \ 0.1])^2 \quad (26a)$$

$$Q = \text{diag}([0.02 \ 0.05 \ 0.01 \ 0.03 \ 0.1 \ 0.1])^2 \quad (26b)$$

$$R = \text{diag}([0.01 \ 0.03 \ 0.001 \ 0.01 \ 0.01])^2 \quad (26c)$$

$$N = 10. \quad (26d)$$

In addition, to test their robustness and convergence rate, the estimators are initialised with poor prior guesses. Specifically, a 15 % error for v_x and a fixed deviation for the other states are subtracted from the true initial state x_0 . The initial guess used in the modified DLC manoeuvre is $x_0 = [3.33 \ 1 \ 0.3 \ 0.5 \ 1 \ 1]^T$, while the initial guesses in both the ISO DLC and circular manoeuvres are $x_0 = [2.85 \ 1 \ 0.3 \ 0.5 \ 1 \ 1]^T$.

A. Convergence and Accuracy

Prior to presenting the results, the time to converge denoted t_{cvg} is used as an evaluation index. As unknown noise and disturbance exist persistently, the convergence of estimation errors to the origin may not be possible. To facilitate the comparison, all estimators are considered to have converged if at time step k

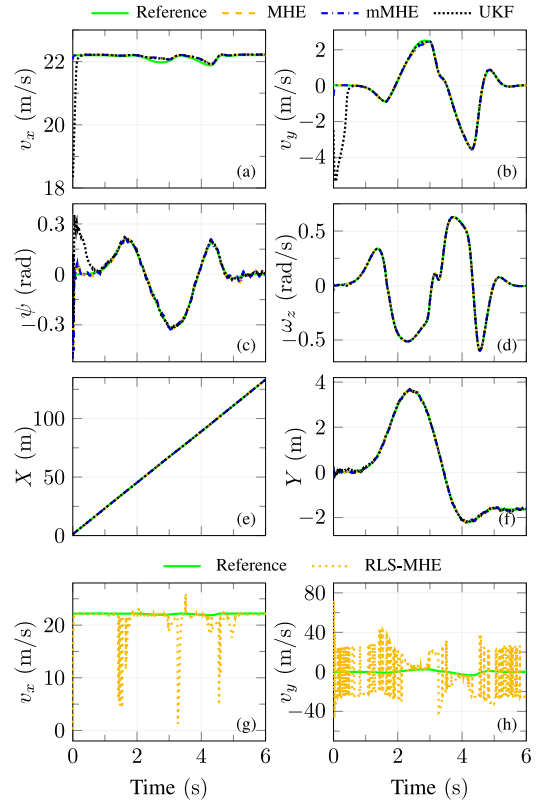


Fig. 6. Modified DLC manoeuvre estimation. (a)–(f) show a comparison without the RLS-MHE estimator. (g) and (h) present only the velocity estimates from the RLS-MHE estimator.

the true state x_k and the estimated state $x_{k|k}$ satisfy

$$|x_k - x_{k|k}| \leq [0.2 \ 0.2 \ 0.1 \ 0.04 \ 0.3 \ 0.3]^T. \quad (27)$$

The values selected on the right-hand side of (27) are reasonable for this study with specifications and parameters defined before, though they are not rigorous, nor sufficiently general for all vehicles under various driving situations.

The vehicle state estimates for the modified DLC and ISO DLC manoeuvres are revealed in Figs. 6–7 and Tables II–III. In the modified DLC manoeuvre (see Table II and Fig. 6), the MHE converges to the true values in only 0.21 seconds, which is more than two times faster than the corresponding convergence of the UKF. Besides, the v_y estimate from the MHE starts to converge once the estimator is initialised, while that from the UKF initially deviates abruptly from the poor prior guess (-1 m/s). This can be explained as follows. As mentioned earlier, the MHE is initialised with a truncated horizon. This means that the number of measurements included in the MHE formulation, (21)–(23), increases with an increasing horizon length when $t \leq N$. As a result, the arrival cost term, or poor prior guess, in (21) plays a

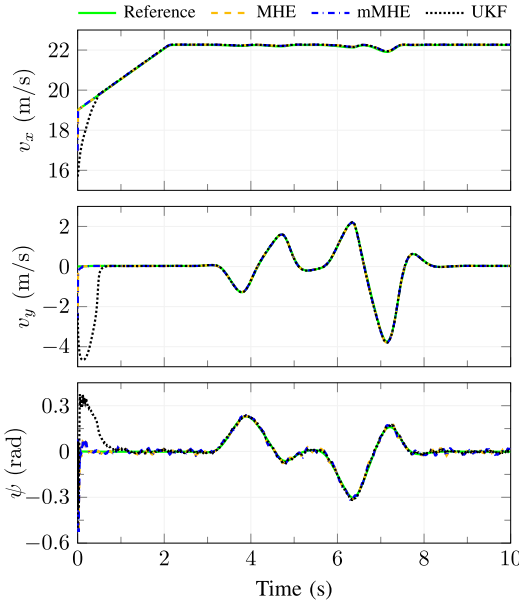


Fig. 7. ISO DLC manoeuvre estimation.

TABLE II
MODIFIED DLC MANOEUVRE ESTIMATION

Estimator	v_x (m/s)		v_y (m/s)		ψ (rad)		t_{cvg} (s)
	e_{max}	e_{rms}	e_{max}	e_{rms}	e_{max}	e_{rms}	
MHE	0.137	0.049	0.606	0.064	0.500	0.034	0.21
mMHE	0.137	0.049	0.606	0.063	0.500	0.034	0.21
RLS-MHE	22.00	2.994	72.66	22.30	55.60	7.813	> 6
UKF	3.864	0.345	5.368	1.033	0.500	0.067	0.58

a Concerning Table II and the following tables, t_{cvg} is calculated in such a way that all the estimated states converged to the true vehicle states.

b Some estimated states from the RLS-MHE estimator deviate too far from the ground truth, which makes the estimation meaningless, and therefore those values are represented by –.

TABLE III
ISO DLC MANOEUVRE ESTIMATION

Estimator	v_x (m/s)		v_y (m/s)		ψ (rad)		t_{cvg} (s)
	e_{max}	e_{rms}	e_{max}	e_{rms}	e_{max}	e_{rms}	
MHE	2.034	0.067	2.645	0.088	0.526	0.029	0.22
mMHE	2.034	0.068	2.645	0.088	0.526	0.029	0.22
RLS-MHE	–	–	–	–	98.99	17.70	> 10
UKF	3.319	0.318	4.683	0.848	0.500	0.065	0.68

less important role in the solution-finding process, and therefore the MHE is less affected by the inaccurate initialisation. The mMHE has similar performance to that of the MHE, because the model mismatch under such a manoeuvre is small so that the hypothesis of a deterministic model underlying (24) holds.

Quantitatively, the maximum and RMS errors of v_x , v_y and ψ estimates from the MHE are 0.137 m/s and 0.049 m/s, 0.606 m/s and 0.064 m/s, and 0.500 rad and 0.034 rad, respectively. These errors are similar to those from the mMHE but are at least 49 % smaller (except for the e_{max} of ψ) than those from the UKF. The RLS-MHE behaves much worse than the UKF. Specifically, it does not converge in the tested scenarios, as indicated in Fig. 6(g)–(h) and Table II. A similar behaviour was also reported in [26] for a chemical process monitoring and in [43] for battery state estimation, where large deviations and abrupt changes were observed from the RLS-MHE. The divergence of the RLS-MHE is mainly due to the missing the *a priori* estimate in its objective function, (25a), and the only tunable parameter is R . These factors combined could lead to the system uncertainty being addressed less effectively by the RLS-MHE than by the other estimators. Since the results from the RLS-MHE deviate considerably from the true values, they are only partly shown in Fig. 6(g)–(h) and in the tables following them. Moreover, the RLS-MHE estimator is not analysed further hereafter. For the ISO DLC manoeuvre (see Table III and Fig. 7), similar results to those presented above can be observed.

From Fig. 6, it is also observed that the yaw rate and vehicle position estimates from the MHE, mMHE and UKF estimators are barely affected by the poor prior guess. One possible explanation for this is that a higher trust is given to the measurements although these states exist both in the state vector, (13a), and the output vector, (13c). In fact, even the RLS-MHE estimator gives reliable estimates for these states. For this reason, these states are not shown in Table II or in the following tables and figures.

B. Robustness Test

To test the robustness of the designed estimators, three scenarios are considered, including increased initial deviation, modelling error and external disturbance.

1) *Large Initial Deviation*: A simple sensitivity analysis is conducted to test the robustness of the estimators in dealing with even larger initial errors. In the ISO DLC manoeuvre, even when the initial v_y or ψ deviation is increased to double its original value, the results from all the estimators do not change much with regard to the convergence time, but there are slightly larger maximum and RMS errors. However, if the v_x deviation is increased from 15 % to 25 %, it takes the UKF more than 7 seconds to converge, but this increase barely affects the convergence of the MHE and mMHE. As mentioned earlier, other states are measured directly and the measurements are given a high level of trust, so the initial deviation of those variables has little effect on the convergence. The above observations indicate that the estimators are more sensitive to v_x deviation, and the UKF estimator is more sensitive to larger initialisation errors than the MHE and mMHE estimators.

2) *Large Modeling Errors*: As observed earlier, the modelling errors increase dramatically with time in the circular manoeuvre. For example, the v_y error at 30 s becomes as large as –22.4 % of the true value. The modelling errors are to a high degree compensated for by the UKF estimator, as can be seen from Fig. 8 and Table IV. The errors are restrained further by the MHE

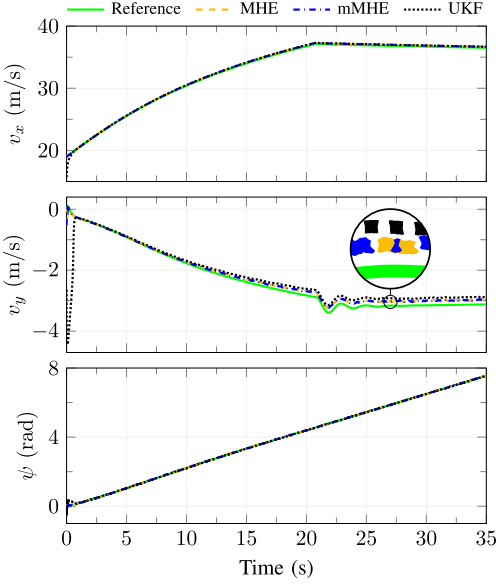


Fig. 8. Circular manoeuvre estimation.

TABLE IV
CIRCULAR MANOEUVRE ESTIMATION

Estimator	v_x (m/s)	v_y (m/s)	ψ (rad)	t_{cvg} (s)			
	e_{max}	e_{rms}	e_{max}				
MHE	0.191	0.134	0.523	0.110	0.526	0.017	0.22
mMHE	0.190	0.135	0.523	0.112	0.526	0.018	0.22
RLS-MHE	—	64.70	—	—	327.3	14.09	> 35
UKF	3.308	0.198	4.517	0.478	0.500	0.033	0.75

and mMHE estimators, as indicated in Fig. 8, especially when the errors become more obvious ($t > 20$ s). Specially, the v_y error from the MHE and mMHE at 30 s is -0.157 m/s, which is 37 % better than the results obtained with the UKF. The MHE and mMHE are also considerably better than the others when evaluating on the basis of the maximum and RMS errors.

3) *External Disturbance:* In this test the system is assumed to be perturbed by a measurement disturbance $y_{dstb} = [5 \ 5 \ 5 \ 0 \ 0]^T$ for one sample at the time instant $t = 4.5$ s. As can be seen from Fig. 9, in general the MHE has a markedly smaller estimation error than all the other estimators, especially for the v_y and ψ estimates. The mMHE, on the other hand, is even worse than the UKF. This can be explained from an optimisation point of view. As discussed previously, after eliminating the equality constraints, there are $(N + 1) \times n_x$ optimisation variables in the MHE, but only n_x such variables in the mMHE. Likewise, the EKF is similar to the MHE with a horizon length of 1 [21]. This means that the MHE has the largest number of optimisation variables, while the mMHE has much fewer such variables (undisturbed components), with the result that the mMHE is easily contaminated by disturbances. The behaviour of the

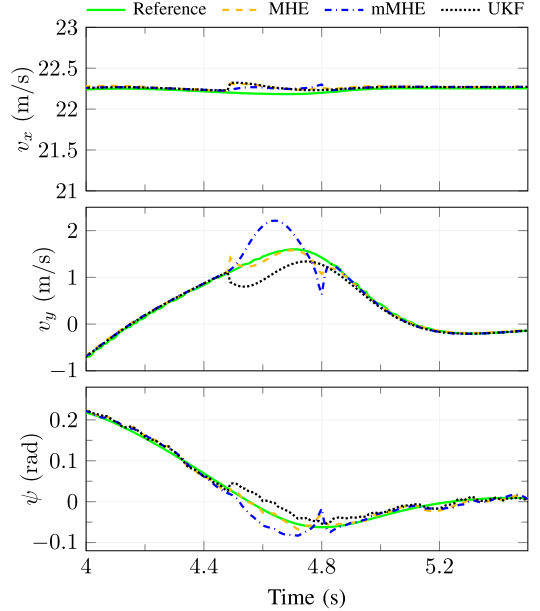


Fig. 9. ISO DLC manoeuvre estimation with measurement disturbance.

UKF, in this regard, can be explained analogously to that of the EKF. In this case study, the horizon length of the MHE and mMHE is increased to 30 to lower the negative effect of the perturbed measurements further. This measure is taken because, as stated in [21], using a short horizon may cause unexpected estimation errors if the system is contaminated by an unmodelled disturbance.

C. Effect of Horizon Length and Optimization Techniques

The effect of horizon length on the performance of the MHE and mMHE estimators in the circular manoeuvre is displayed in Fig. 10. As can be seen, the accuracy of the MHE does not apparently improve with the increasing horizon length. This is mainly because large modelling errors exist in the circular manoeuvre and compromise the optimisation process although more measurements are available. Still, the MHE in general yields considerably better results than the mMHE as the horizon length increases. Specifically, the RMS error of v_y resulting from the MHE is 37 % smaller than that from the mMHE, with the horizon length being 60. This is again due to the fact that the process model is assumed to be a perfect one in the mMHE without completely considering the modelling errors.

An additional consequence of having a large horizon length is the increased computational burden in the optimisation process. The change of computation time, which is evaluated using the solver output from the MPCTools, with the horizon length is illustrated in Fig. 10(d). In particular, it takes the MHE 6.47 ms and the mMHE 6.29 ms to solve the optimisation problem with a horizon length of 10. Moreover, their computation time grows

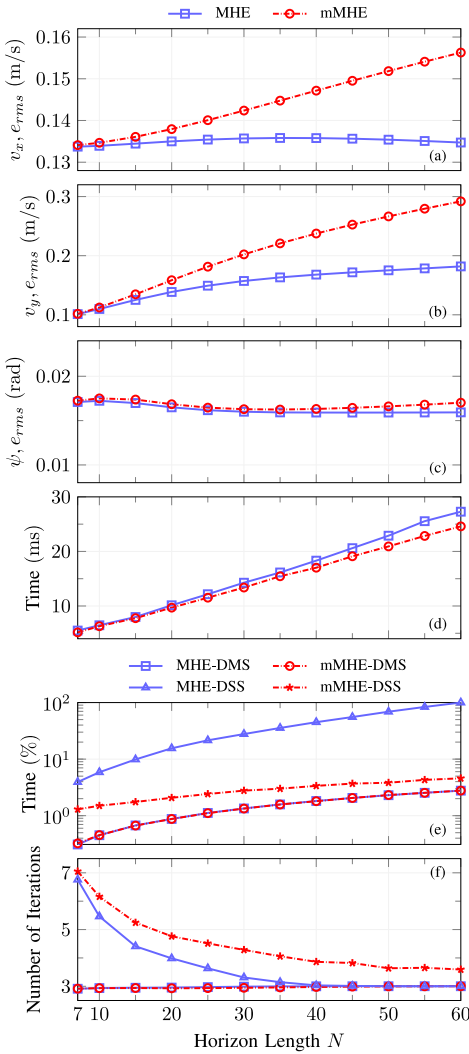


Fig. 10. Effect of horizon length and optimisation technique in the circular manoeuvre. (a)–(c) show the RMS errors with the direct multiple shooting. (d) shows the average computation time per optimisation step with the direct multiple shooting. (e) and (f) show the average computation time per optimisation step (the y tick value has been scaled with respect to the maximum value), and the average number of iterations per optimisation step, both with the CasADi Opti. “DMS” and “DSS” denote direct multiple shooting and direct single shooting, respectively.

dramatically with an increasing horizon length. However, the computation of the MHE does not vary much from that of the mMHE, which is contrary to the results obtained in [26] and [43]. This is because a different optimisation technique, direct multiple shooting [44], is used in the present study. With the direct multiple shooting method, the equality constraints (21b)–(21c) in the MHE and (24b)–(24c) in the mMHE are

handled as defect constraints to ensure continuity [45]. Furthermore, x , w and v are all treated as optimisation variables. As a result, there are $(N + 1) \times (n_x + n_y) + N \times n_x$ optimisation variables and $N \times n_x + (N + 1) \times n_y$ equality constraints in the MHE, where n_y is the number of output variables. Similarly, there are $(N + 1) \times (n_x + n_y)$ optimisation variables and $N \times n_x + (N + 1) \times n_y$ equality constraints in the mMHE.

In [26] and [43], however, the single shooting method was utilised to solve the optimisation problem, where the equality constraints were eliminated from the problem formulation. Consequently, there were $(N + 1) \times n_x$ and n_x optimisation variables in the MHE and the mMHE, respectively. Moreover, no equality constraints were considered there. It is apparent that the complexity of the optimisation problem does not differ between the MHE and mMHE estimators in the present study as much as it differs between them in [26] and [43], thus resulting in a similar computation time for the estimators in the present study.

To investigate further the effect of different optimisation techniques, a second study of the computational time is carried out where both estimators are implemented using the CasADi Opti functionality to be more comparable. Specifically, the MHE and mMHE are both solved by the direct multiple shooting and direct single shooting methods, respectively. As can be seen from Fig. 10(e), the choice of the shooting techniques significantly affects the computational efficiency of the two algorithms. Firstly, the computation time of the two estimators with the direct multiple shooting is substantially less than that with the direct single shooting, which is particularly obvious for the MHE. Secondly, with the direct multiple shooting the computation of the MHE again grows similarly to that of the mMHE as the horizon length increases, but the computational cost of the MHE increases incredibly faster than that of the mMHE when the direct single shooting is used.

The main advantages of the direct multiple shooting over the direct single shooting can be attributed to the simultaneous integration on each time segment, the initialisation for state trajectory, and the improved convergence especially for nonlinear and unstable systems [21]. It is worth pointing out that, as discussed earlier, more optimisation variables and equality constraints result from the direct multiple shooting than from the direct single shooting. In other words, a larger nonlinear programming (NLP) problem is produced from the direct multiple shooting. Fortunately, the resulting larger but sparser NLP can be exploited by tools like IPOPT [46], which still makes the direct multiple shooting considerably faster. It is also interesting to note that the number of iterations per optimisation step resulting from the direct multiple shooting is fewer than that resulting from the direct single shooting, as shown in Fig. 10(f). This may also contribute to the reduced computational cost in the direct multiple shooting. In summary, with a proper optimisation technique, especially for a complicated system like the present one, MHE is still a favourable choice at the cost of slightly increased computational time.

The effects of horizon length and optimisation techniques have been ascertained, but discussions on the real-time implementability of MHE-type approaches are far from complete. The main driving force to deploy them in autonomous vehicles is to

reduce the computational costs. Further investigation of algorithmic and technical simplification is of great importance, such as real-time iteration techniques, computation delay compensations, separation of preparation and feedback phases, and new code generation methods, as proposed in [21], [47], [48]. In addition, the computational burden of MHE-type approaches can also be considerably relieved or eliminated when there are richer computing resources within the considered vehicle or timely accesses to the cloud platform are available.

V. CONCLUSION

This paper has performed a comprehensive evaluation of MHE, mMHE, RLS-MHE and UKF for online estimating critical vehicle states in the presence of persistent noise, modelling error and external disturbance. This was based upon a highly nonlinear vehicle and tyre model that was justified to be locally observable. The accuracy, convergence, robustness and computational efficiency of these estimation algorithms were systematically compared under three driving manoeuvres and with different tuning parameters or optimisation techniques.

Illustrative results demonstrated that regarding the convergence rate and estimation accuracy, MHE had similar performance as mMHE but was clearly superior to UKF and RLS-MHE under all three manoeuvres. During robustness tests, mMHE could well mimic MHE in terms of compensating for deviated initialisation and modelling errors, but not in handling external disturbance. Meanwhile, MHE had better performance than UKF in all the three robustness tests. Under the circular manoeuvre where relatively large modelling uncertainties exist, mMHE suffered from increased estimation errors when considering longer horizons. When direct multiple shooting was employed, MHE was as computationally efficient as mMHE.

Future research will be concentrated on rigorous analysis of these estimation algorithms and exploring theoretical insights regarding the effects of different tuning parameters and operating conditions. Techniques to further improve the MHE computational efficiency will also be developed with experimental demonstration in autonomous vehicles.

ACKNOWLEDGMENT

The authors would like to gratefully acknowledge Dr. M. J. Risbeck from University of Wisconsin-Madison for his advice on implementing the MHE algorithms, and Senior Researcher M. Jonasson at Chalmers University of Technology for valuable discussions on tyre modeling.

REFERENCES

- [1] C. N. Webb, "Estimating lives saved by electronic stability control, 2011–2015," NHTSA, U.S. Dept. of Transportation, Washington, DC, Traffic Safety Facts Research Note DOT HS 812 391, Mar. 2017.
- [2] D. M. Bevly, J. C. Gerdes, and C. Wilson, "The use of GPS based velocity measurements for measurement of sideslip and wheel slip," *Veh. Syst. Dyn.*, vol. 38, no. 2, pp. 127–147, 2002.
- [3] D. M. Bevly, J. Ryu, and J. C. Gerdes, "Integrating INS sensors with GPS measurements for continuous estimation of vehicle sideslip, roll, and tire cornering stiffness," *IEEE Trans. Intell. Transp. Syst.*, vol. 7, no. 4, pp. 483–493, Dec. 2006.
- [4] D. Selmanaj, M. Corno, G. Panzani, and S. M. Savaresi, "Vehicle sideslip estimation: A kinematic based approach," *Control Eng. Pract.*, vol. 67, pp. 1–12, Oct. 2017.
- [5] *Road Vehicles – Vehicle Dynamics and Road-Holding Ability – Vocabulary*, ISO Standard 8855:2011.
- [6] K. T. Leung, J. F. Whidborne, D. Purdy, and A. Dunoyer, "A review of ground vehicle dynamic state estimations utilising GPS/INS," *Veh. Syst. Dyn.*, vol. 49, no. 1–2, pp. 29–58, 2011.
- [7] R. Anderson and D. M. Bevly, "Using GPS with a model-based estimator to estimate critical vehicle states," *Veh. Syst. Dyn.*, vol. 48, no. 12, pp. 1413–1438, 2010.
- [8] K. Nam, S. Oh, H. Fujimoto, and Y. Hori, "Estimation of sideslip and roll angles of electric vehicles using lateral tire force sensors through RLS and Kalman filter approaches," *IEEE Trans. Ind. Electron.*, vol. 60, no. 3, pp. 988–1000, Mar. 2013.
- [9] R. Rajamani, *Vehicle Dynamics and Control*, 2nd ed. New York, NY, USA: Springer, 2012.
- [10] H. Pacejka, *Tire and Vehicle Dynamics*, 3rd ed. Oxford, U.K.: Elsevier, 2012.
- [11] M. Doumiati, A. Charara, and A. Victorino, *Vehicle Dynamics Estimation Using Kalman Filtering: Experimental Validation*, 1st ed. London, U.K.: ISTE Ltd, 2012.
- [12] H. Guo, H. Chen, F. Xu, F. Wang, and G. Lu, "Implementation of EKF for vehicle velocities estimation on FPGA," *IEEE Trans. Ind. Electron.*, vol. 60, no. 9, pp. 3823–3835, Sep. 2013.
- [13] B. Gao, G. Hu, S. Gao, Y. Zhong, and C. Gu, "Multi-sensor optimal data fusion for INS/GNSS/CNS integration based on unscented Kalman filter," *Int. J. Control Autom. Syst.*, vol. 16, no. 1, pp. 129–140, 2018.
- [14] M. Doumiati, A. C. Victorino, A. Charara, and D. Lechner, "Onboard real-time estimation of vehicle lateral tire-road forces and sideslip angle," *IEEE/ASME Trans. Mechatronics*, vol. 16, no. 4, pp. 601–614, Aug. 2011.
- [15] S. Antonov, A. Fehn, and A. Kugi, "Unscented Kalman filter for vehicle state estimation," *Veh. Syst. Dyn.*, vol. 49, no. 9, pp. 1497–1520, Sep. 2011.
- [16] A. Katriniok and D. Abel, "Adaptive EKF-based vehicle state estimation with online assessment of local observability," *IEEE Trans. Control Syst. Technol.*, vol. 24, no. 4, pp. 1368–1381, Jul. 2016.
- [17] W. Liu, H. He, and F. Sun, "Vehicle state estimation based on minimum model error criterion combining with extended Kalman filter," *J. Franklin Inst.*, vol. 353, no. 4, pp. 834–856, Mar. 2016.
- [18] B. Gao, G. Hu, S. Gao, Y. Zhong, and C. Gu, "Multi-sensor optimal data fusion based on the adaptive fading unscented Kalman filter," *Sensors*, vol. 18, no. 2, p. 488, Feb. 2018.
- [19] B. Gao, S. Gao, Y. Zhong, G. Hu, and C. Gu, "Interacting multiple model estimation-based adaptive robust unscented Kalman filter," *Int. J. Contr. Autom. Syst.*, vol. 15, no. 5, pp. 2013–2025, 2017.
- [20] K. Berntorp, "Joint wheel-slip and vehicle-motion estimation based on inertial GPS, and wheel-speed sensors," *IEEE Trans. Control Syst. Technol.*, vol. 24, no. 3, pp. 1020–1027, May 2016.
- [21] J. B. Rawlings, D. Q. Mayne, and M. M. Diehl, *Model Predictive Control: Theory, Computation, and Design*, 2nd ed. Madison, WI, USA: Nob Hill Publishing, 2017.
- [22] B. Gao, S. Gao, G. Hu, Y. Zhong, and C. Gu, "Maximum likelihood principle and moving horizon estimation based adaptive unscented Kalman filter," *Aerospace Sci. Technol.*, vol. 73, pp. 184–196, Feb. 2018.
- [23] M. Canale, L. Fagiano, and C. Novara, "A direct moving horizon approach to vehicle side-slip angle estimation," in *Proc. 49th IEEE Conf. Decis. Control*, 2010, pp. 2898–2903.
- [24] M. Zanon, J. Frasch, and M. Diehl, "Nonlinear moving horizon estimation for combined state and friction coefficient estimation in autonomous driving," in *Proc. Eur. Control Conf.*, 2013, pp. 4130–4135.
- [25] J. Frasch, T. Kraus, W. Saeyns, and M. Diehl, "Moving horizon observation for autonomous operation of agricultural vehicles," in *Proc. Eur. Control Conf.*, 2013, pp. 4148–4153.
- [26] R. Xiong and M. A. Grover, "A modified moving horizon estimator for in situ sensing of a chemical vapor deposition process," *IEEE Trans. Control Syst. Technol.*, vol. 17, no. 5, pp. 1228–1235, Sep. 2009.
- [27] P. Falcone, F. Borrelli, J. Asgari, H. E. Tseng, and D. Hrovat, "Predictive active steering control for autonomous vehicle systems," *IEEE Trans. Control Syst. Technol.*, vol. 15, no. 3, pp. 566–580, May 2007.
- [28] J. Van Ginkel, "Estimating the tire-road friction coefficient based on tire force measurements," M.S. thesis, Dept. Biomechanical Eng., Delft University of Technology, Delft, The Netherlands, 2014.
- [29] *Passenger Cars – Test Track For a Severe Lane-Change Manoeuvre – Part 1: Double Lane-Change*, ISO Standard 3888-1:1999.

- [30] Mechanical Simulation Corporation. CarSim, (2016). [Online]. Available: <https://www.carsim.com/>
- [31] J. Gong, Y. Jiang, and W. Xu, *Model Predictive Control For Self-driving Vehicles*. Beijing, China: BIT Press (in Chinese), 2014.
- [32] L. F. Shampine and M. W. Reichelt, "The MATLAB ODE suite," *SIAM J. Scientific Comput.*, vol. 18, no. 1, pp. 1–22, Jan. 1997.
- [33] R. Hermann and A. Krener, "Nonlinear controllability and observability," *IEEE Trans. Autom. Control*, vol. 22, no. 5, pp. 728–740, Oct. 1977.
- [34] R. Suwantong, "Development of the moving horizon estimator with pre-estimation (MHE-PE). Application to space debris tracking during the re-entries," Ph.D. dissertation, Dept. Syst. Design Performance Evaluation, Supélec, Paris, France, 2014.
- [35] C. V. Rao and J. B. Rawlings, "Constrained process monitoring: Moving-horizon approach," *AIChE J.*, vol. 48, no. 1, pp. 97–109, Jan. 2002.
- [36] D. G. Robertson, J. H. Lee, and J. B. Rawlings, "A moving horizon-based approach for least-squares estimation," *AIChE J.*, vol. 42, no. 8, pp. 2209–2224, Aug. 1996.
- [37] C. C. Qu and J. Hahn, "Computation of arrival cost for moving horizon estimation via unscented Kalman filtering," *J. Process Control*, vol. 19, no. 2, pp. 358–363, Feb. 2009.
- [38] D. Simon, *Optimal State Estimation: Kalman, H_{infinity}, and Nonlinear Approaches*. New York, NY, USA: Wiley, 2006.
- [39] M. Risbeck and J. Rawlings, MPCTools: Nonlinear model predictive control tools for CasADi (Octave interface). (2016). [Online]. Available: <https://bitbucket.org/rawlings-group/octave-mptools>
- [40] J. A. E. Andersson, J. Gillis, G. Horn, J. B. Rawlings, and M. Diehl, "CasADi – A software framework for nonlinear optimization and optimal control," *Math. Program. Comput.*, vol. 11, pp. 1–36, 2018.
- [41] A. Wächter and L. T. Biegler, "On the implementation of an interior-point filter line-search algorithm for large-scale nonlinear programming," *Math. Program.*, vol. 106, no. 1, pp. 25–57, Apr. 2005.
- [42] HSL, A collection of Fortran codes for large scale scientific computation. (2014). [Online]. Available: <http://www.hsl.rl.ac.uk/>
- [43] X. Hu, D. Cao, and B. Egardt, "Condition monitoring in advanced battery management systems: Moving horizon estimation using a reduced electrochemical model," *IEEE/ASME Trans. Mechatronics*, vol. 23, no. 1, pp. 167–178, Feb. 2018.
- [44] H. G. Bock and K. J. Plitt, "A multiple shooting algorithm for direct solution of optimal control problems," in *Proc. 9th IFAC World Congr.*, 1984, pp. 1603–1608.
- [45] J. T. Betts, *Practical Methods For Optimal Control and Estimation Using Nonlinear Programming*, 2nd ed. Philadelphia, PA, USA: SIAM, 2010.
- [46] L. T. Biegler, *Nonlinear Programming: Concepts, Algorithms, and Applications to Chemical Processes*. Philadelphia, PA, USA: SIAM, 2010.
- [47] M. Diehl, H. J. Ferreau, and N. Haverbeke, "Efficient numerical methods for nonlinear MPC and moving horizon estimation," in *Nonlinear Model Predictive Control*. Berlin, Heidelberg, Germany: Springer, 2009, pp. 391–417.
- [48] H. Ferreau *et al.*, "Embedded optimization methods for industrial automatic control," *IFAC-PapersOnLine*, vol. 50, no. 1, pp. 13 194–13 209, Jul. 2017.



Wenliang Zhang is a Ph.D. student at the School of Mechanical Engineering, Beijing Institute of Technology, Beijing, China, and at the Department of Aeronautical and Vehicle Engineering, KTH Royal Institute of Technology, Stockholm, Sweden.

His research interests include vehicle state estimation and vehicle dynamics control.



Zhenpo Wang received the Ph.D. degree in automotive engineering from the Beijing Institute of Technology, Beijing, China, in 2005. He is currently a Professor with the Beijing Institute of Technology, and the Deputy Director with the National Engineering Laboratory for Electric Vehicles and the Collaborative Innovation Center for Electric Vehicles in Beijing, China.

He has authored four monographs and translated books as well as more than 60 technical papers. He also holds more than 20 patents. His current research interests include pure electric vehicle integration, packaging and energy management of battery system, and analytics of EV big data.

Dr. Wang was the recipient of numerous awards, including the second National Prize for Progress in Science and Technology and the first Prize for Progress in Science and Technology from the Ministry of Education.



Changfu Zou (M'16) received the B.E. degree in automotive engineering from the Beijing Institute of Technology, Beijing, China, and the Ph.D. degree in automation and control engineering from The University of Melbourne, Parkville, VIC, Australia, in 2011 and 2017, respectively.

He was a Visiting Student Researcher with the Energy, Controls & Applications Lab, University of California, Berkeley, CA, USA, from 2015 to 2016. In 2017–2018, he was a Postdoctoral Researcher with the Department of Electrical Engineering, Chalmers University of Technology, Gothenburg, Sweden, where he is currently an Assistant Professor. His research interests include modeling and control of energy storage, electrified vehicles, and transport systems.



Lars Drugge received the M.Sc. degree in mechanical engineering in 1994 and the Ph.D. degree in computer aided design in 2000 from the Luleå University of Technology, Luleå, Sweden.

He is an Associate Professor in Vehicle Dynamics with the Department of Aeronautical and Vehicle Engineering, School of Engineering Sciences, Kungliga Tekniska högskolan (KTH) Royal Institute of Technology, Stockholm, Sweden. He is currently the Head of the Vehicle Dynamics, Rail Vehicles, Aerodynamics and Conceptual Vehicle Design group at KTH. He has coauthored more than 60 scientific publications in international journals and conference proceedings. His current research interests include vehicle dynamics of over-actuated vehicles, fault-tolerant control, driver vehicle interaction, and driving simulators.



Mikael Nybacka received the Mechanical Engineering degree in 2005 from the Luleå University of Technology, Luleå, Sweden, where he also received the Ph.D. degree in 2009. He currently works with KTH Royal Institute of Technology, Stockholm, Sweden, as an Associate Professor in Vehicle Dynamics engaged in research, leadership of centre, and education in vehicle dynamics and applied vehicle dynamics control.

He has authored ten journal papers, 17 conference proceedings, and three technical reports. His current research interests include vehicle validation and driver vehicle interaction, urban vehicle concepts, autonomous vehicles, fault-tolerant control, and over-actuated vehicles.

Paper B

“Active camber for enhancing path following and yaw stability of over-actuated autonomous electric vehicles”,

Wenliang Zhang, Lars Drugge, Mikael Nybacka and Zhenpo Wang,
Vehicle System Dynamics, vol. 59, no. 5, 2020.

Paper B



Active camber for enhancing path following and yaw stability of over-actuated autonomous electric vehicles

Wenliang Zhang ^{a,b}, Lars Drugge  ^a, Mikael Nybacka  ^a and Zhenpo Wang  ^b

^aDepartment of Engineering Mechanics, KTH Royal Institute of Technology, Stockholm, Sweden; ^bSchool of Mechanical Engineering, Beijing Institute of Technology, Beijing, People's Republic of China

ABSTRACT

Active safety systems contribute significantly to the safe driving of autonomous vehicles in hazardous circumstances. However, conventional active safety systems that mainly depend on braking intervention may not yield the desired vehicle behaviour in critical situations where the tyre forces tend to saturate. Over-actuation through individually cambering the wheels provides a possibility of overcoming this difficulty, as extra lateral tyre forces can potentially be produced. This paper presents active camber for improving the path following and yaw stability performance of over-actuated autonomous electric vehicles (AEVs). With a modified Dugoff tyre model, the camber effect on the lateral tyre force is modelled as an effective linear component. The modified tyre model, together with a double-track vehicle model, is utilised for active camber of the AEVs. The camber controller is developed in the framework of model predictive control (MPC), including both actuator- and safety-related constraints. The camber controller is investigated at different camber rates and road friction levels, in terms of path following, yaw stability and vehicle velocity gain.

ARTICLE HISTORY

Received 12 September 2019

Revised 2 January 2020

Accepted 22 January 2020

KEYWORDS

Active camber; model predictive control; path following; yaw stability; over-actuation; autonomous vehicle; camber rate; electric vehicle

1. Introduction

Active safety systems are playing an important role in ensuring a secure driving environment in the transport sector, especially with the development of autonomous vehicle (AV) technology. For instance, in 2015 electronic stability control (ESC) system was estimated to have saved 1949 lives in 2272 fatal accidents resulting from passenger vehicle crashes in the USA [1]. For the safe operation of an AV in critical driving conditions, the planned path needs to be followed and, at the same time, the yaw stability must be guaranteed. Systems based on active steering and/or braking control are approaches commonly adopted to accomplish these two objectives for vehicles with a single drive unit, e.g. vehicles with a single internal combustion engine or electric motor [2–4]. However, active safety systems depending mainly on braking intervention may not produce the desired performance in cases where the tyre forces tend to saturate, and such safety systems can deteriorate the ride comfort.

CONTACT Zhenpo Wang  wangzhenpo@bit.edu.cn

© 2020 Informa UK Limited, trading as Taylor & Francis Group

By exploiting over-actuation, the degrees of controllability can be increased, which is enabled by the current trend of increasing number of accessible vehicle actuators (e.g. actuators for steering, traction, braking and cambering), and thus the vehicle performance can be improved. For instance, the use of hub/in-wheel motors contributes to a fast and accurate torque generation and easy torque measurement, in addition to an improved vehicle configuration [5]. Taking advantage of this, an enhanced active safety can be achieved. Specifically, the utilisation of torque vectoring through individually controlling the hub/in-wheel motors to enhance the yaw stability has been exploited in several studies [6–9]. These studies mainly examined how to stabilise the vehicle by generating a supplementary yaw moment via regulation of the amount of torque output from the hub/in-wheel motors, without degenerating the ride comfort. This regulation was achieved with approaches like the linear quadratic regulator, the sliding mode control and the fuzzy proportional–integral–derivative, and the results of these studies are promising.

Besides torque vectoring through controlling the in-wheel motors, the camber control of over-actuated electric vehicles (EVs) has also been studied for various purposes. The wheel camber angle is the angle between the wheel plane and the plane perpendicular to the road [10], and it is an important factor determining the magnitude of the tyre forces. Camber control was applied to improve the steering feel in Roethof et al. [11], and it was found that the studied vehicle was easier to control when active camber was implemented than when it was deactivated, and that in the latter state the vehicle tended to run on the limit. Moreover, it was reported by Braghin et al. [12] that the maximum lateral acceleration increased in a ramp steer manoeuvre when camber control was activated. Furthermore, camber control was shown by Sun et al. [13] to improve the energy efficiency during a steady-state cornering manoeuvre.

Studies on camber control have also been extended to cover the fulfilment of active safety-related objectives, due to the potentiality of camber control for extracting additional lateral tyre forces through cambering the wheel. Mercedes-Benz developed the F400 Carving Concept with the active tyre tilt control, and it was shown that, by combining camber control and special tyre material, the lateral tyre force was increased by 30% to 50% [14]. Detailed components of this active camber system can be found in [15]. Jerrelind et al. [16] revealed that active camber was able to improve the vehicle safety during an evasive manoeuvre. Gáspár and Németh [17] utilised camber control to enhance the trajectory tracking performance. Yoshino and Nozaki [18] applied camber control to increase the vehicle cornering margins. However, in previous studies, researchers have either modelled the camber effect with simple rule-based strategies, e.g. by relating the camber angle linearly to a certain vehicle state, or utilised camber control for simple tasks. When studying the literature in this field, the present authors found no studies where the camber effect on the tyre force had been modelled effectively for vehicle control applications, and where active camber had been explored for the purpose of enhancing the path following and yaw stability of over-actuated autonomous electric vehicles (AEVs).

The aim of the present study is to develop a camber controller for enhancing the path following and yaw stability of over-actuated AEVs in the framework of model predictive control (MPC). Three main contributions are made by this study to this field of research. Firstly, a control-oriented tyre model with camber contribution is developed,

where the camber effect on the lateral tyre force is modelled with a simple yet effective linear component. The tyre model incorporated with the camber component, together with a double-track vehicle model, is integrated to achieve active camber for over-actuated AEVs. Secondly, the problem of the path following and yaw stability of the AEVs is examined by coordinating active camber with active front steering, and is formulated as a constrained MPC problem where both actuator- and safety-related constraints are included. The MPC problem is discretised with the efficient direct collocation method. Finally, the benefits of active camber and the effects of the camber rate and road friction are extensively investigated, in terms of the vehicle velocity gain and the path following and yaw stability performance. The remainder of this paper is arranged as follows. The vehicle and tyre modelling is presented in Section 2, after which the development of the camber controller is described in Section 3. The results of an evaluation of the camber controller are presented and discussed in Section 4, after which the final conclusions drawn from the research results are provided in Section 5.

2. Modelling

This section presents the modelling of the vehicle movement, the tyre dynamics with a camber influence, and the vertical tyre forces.

2.1. Vehicle model

A planar model is utilised to describe the dynamics and motion of the considered vehicle, as illustrated by Figure 1. The model includes the vehicle dynamics in the longitudinal,

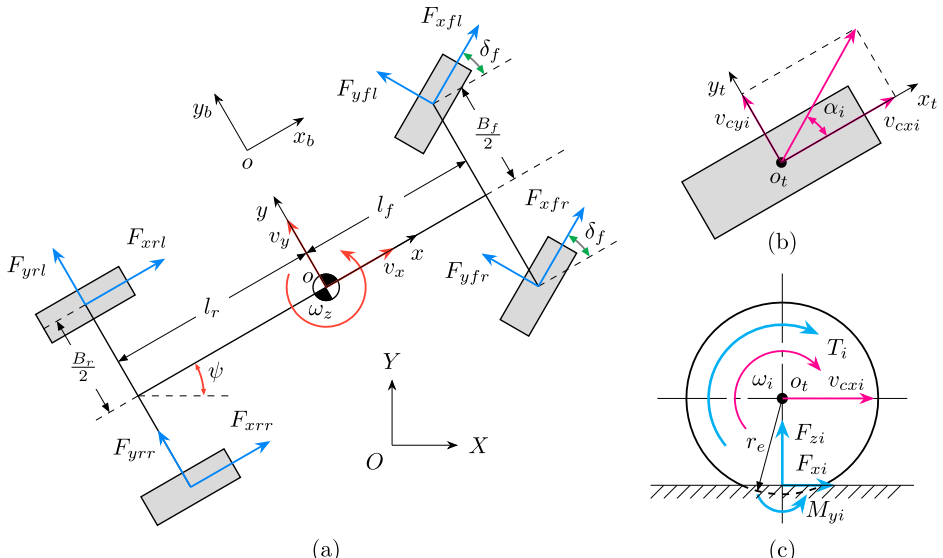


Figure 1. Vehicle model and wheel motion. (a) shows the vehicle model, and (b) and (c) show the top and side views of the wheel motion, respectively.

lateral and yaw directions, and the wheel movement in the rotational direction. Combining equations from [2,19], this vehicle model is given by

$$m\dot{v}_x = mv_y\omega_z - (F_{yfl} + F_{yfr}) \sin \delta_f + (F_{xfl} + F_{xfr}) \cos \delta_f + F_{xrl} + F_{xrr} \quad (1)$$

$$m\dot{v}_y = -mv_x\omega_z + (F_{yfl} + F_{yfr}) \cos \delta_f + F_{yrl} + F_{yrr} + (F_{xfl} + F_{xfr}) \sin \delta_f \quad (2)$$

$$\begin{aligned} I_z\dot{\omega}_z &= l_f(F_{yfl} + F_{yfr}) \cos \delta_f - l_r(F_{yrl} + F_{yrr}) + \frac{B_f}{2}(F_{xfr} - F_{xfl}) \cos \delta_f \\ &\quad + \frac{B_r}{2}(F_{xrr} - F_{xrl}) \end{aligned} \quad (3)$$

$$\dot{X} = v_x \cos \psi - v_y \sin \psi \quad (4)$$

$$\dot{Y} = v_x \sin \psi + v_y \cos \psi \quad (5)$$

$$\dot{\psi} = \omega_z \quad (6)$$

$$I_{wi}\dot{\omega}_i = T_i - r_e F_{xi} \quad (i \in \mathcal{A}). \quad (7)$$

Of these equations, (1)–(6) express the movement of the vehicle body as a result of the longitudinal and lateral tyre forces, F_{xi} and F_{yi} , and (7) relates the motion of the individual wheels to the tyre forces and the drive/braking torques.

2.2. Tyre model

The tyre forces exert an extremely important influence on the vehicle behaviour, as detailed by (1)–(7). Further, the tyre force exhibits highly nonlinear characteristics, due to the interaction between the longitudinal and lateral operation of the vehicle and thus the tyres. Therefore, it is essential that a nonlinear yet simple tyre model be employed for the sake of effectiveness and computational simplicity. In this study, a modified version of the Dugoff tyre model [20] is used:

$$F_{xi} = C_{\kappa i} \frac{\kappa_i}{1 + \kappa_i} f(\lambda_i) \quad (8a)$$

$$F_{yi} = C_{\alpha i} \frac{\tan \alpha_i}{1 + \kappa_i} f(\lambda_i) + C_{\gamma i} \gamma_i \quad (8b)$$

$$\lambda_i = \frac{\mu F_{zi}(1 + \kappa_i)}{2((C_{\kappa i}\kappa_i)^2 + (C_{\alpha i} \tan \alpha_i)^2)^{1/2}} \quad (8c)$$

$$f(\lambda_i) = \begin{cases} (2 - \lambda_i)\lambda_i, & \text{if } \lambda_i < 1 \\ 1, & \text{if } \lambda_i \geq 1 \end{cases} \quad (8d)$$

Note that the camber angle γ is defined here as positive if it contributes to a negative lateral tyre force, for consistency with the sign definition of the lateral tyre slip, α . Moreover, for simplicity, the delay of tyre force build-up is neglected in (8).

As can be seen in (8b), a linear component which is used to capture the camber effect on the lateral tyre force F_{yi} is added to the original Dugoff tyre equation. Moreover, it can be observed in Figure 2(c) that the magnitude of the camber stiffness around the origin is deeply affected by the lateral tyre slip (this point will be further discussed in Section 2.3). Consequently, with $C_{\gamma 0i}$ and $C_{\gamma \alpha i}$ denoting the camber stiffness with zero lateral tyre slip

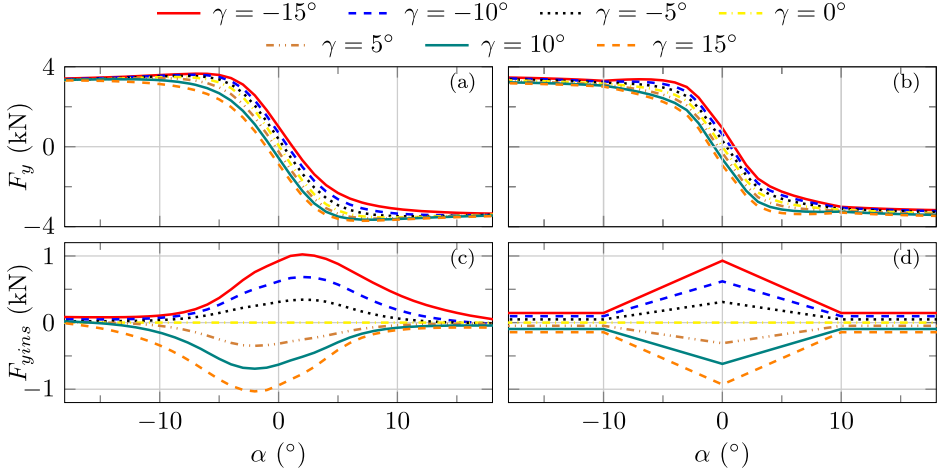


Figure 2. Validation of the tyre model with a camber effect on a high-friction road ($\mu = 1$). (a) and (c) show the lateral tyre force F_y and the gain due to camber F_{yins} , respectively, from the original Pacejka tyre equations [10, Equations (4.E1)–(4.E78)], and (b) and (d) show F_y and F_{yins} , respectively, from the adapted Dugoff tyre model in (8).

and the change in the camber stiffness with respect to the lateral tyre slip, respectively, the camber stiffness $C_{\gamma i}$ is calculated by

$$C_{\gamma i} = \begin{cases} C_{\gamma 0i} + C_{\gamma \alpha i} |\alpha_i|, & \text{if } |\alpha_i| < \alpha_{\lim} \\ C_{\gamma 0i}, & \text{if } |\alpha_i| \geq \alpha_{\lim} \end{cases}. \quad (9)$$

In this study, α_{\lim} , a limiting value depending on the tyre property, is set to 10° when $\mu = 1$ and 0.6 , and 2° when $\mu = 0.3$.

As required by the tyre forces calculation in (8) and (9), the tyre slip ratio κ_i and slip angle α_i are expressed as

$$\kappa_i = \frac{\omega_i r_e - v_{cxi}}{v_{cxi}} \quad \alpha_i = \arctan \frac{v_{cyi}}{v_{cxi}} \quad (10)$$

where v_{cxi} and v_{cyi} are calculated as follows:

$$\begin{bmatrix} v_{xfl} \\ v_{xfr} \\ v_{xrl} \\ v_{xrr} \end{bmatrix} = \begin{bmatrix} v_x - B_f \omega_z / 2 \\ v_x + B_f \omega_z / 2 \\ v_x - B_r \omega_z / 2 \\ v_x + B_r \omega_z / 2 \end{bmatrix} \quad \begin{bmatrix} v_{yfl} \\ v_{yfr} \\ v_{yrl} \\ v_{yrr} \end{bmatrix} = \begin{bmatrix} v_y + l_f \omega_z \\ v_y + l_f \omega_z \\ v_y - l_r \omega_z \\ v_y - l_r \omega_z \end{bmatrix} \quad (11a)$$

$$\begin{bmatrix} v_{cxj} \\ v_{cyj} \end{bmatrix} = \begin{bmatrix} \cos \delta_f & \sin \delta_f \\ -\sin \delta_f & \cos \delta_f \end{bmatrix} \begin{bmatrix} v_{xj} \\ v_{yj} \end{bmatrix}, \quad j \in \{fl, fr\} \quad (11b)$$

$$\begin{bmatrix} v_{cxm} \\ v_{cym} \end{bmatrix} = \begin{bmatrix} v_{xm} \\ v_{ym} \end{bmatrix}, \quad m \in \{rl, rr\}. \quad (11c)$$

It should be noted that, strictly speaking, the slip radius, instead of the effective rolling radius r_e , should be used in (10) to define the tyre slip ratio κ_i . However, for reasons of

brevity, the effective rolling radius r_e is adopted as a reasonable alternative when defining the tyre slip ratio in the present study. Detailed discussions on this can be found in [10].

To determine the vertical tyre force F_{zi} , which is required in (8) to obtain the longitudinal and lateral tyre forces F_{xi} and F_{yi} , the vertical load transfer in the longitudinal and lateral directions can be taken into account, which usually requires knowledge of the longitudinal and lateral accelerations a_x and a_y . On the other hand, a_x and a_y need to be calculated by utilising the last four terms of the right-hand side of (1) and (2), respectively, where F_{xi} and F_{yi} are needed. With the use of the nonlinear tyre model (8) that considers the combined-slip situation, this results in an algebraic loop which increases the computational complexity if explicit expressions for a_x and a_y are to be solved. To alleviate this difficulty, the vertical tyre forces are calculated by neglecting the load transfer:

$$F_{zfl,fr} = \frac{l_r mg}{2(l_f + l_r)} \quad F_{zrl,rr} = \frac{l_f mg}{2(l_f + l_r)}. \quad (12)$$

2.3. Tyre model evaluation

Figure 2 illustrates the similarity and difference between the original Pacejka tyre model from [10] and the modified Dugoff tyre model given by (8). In Figure 2(c,d), it can be seen that the adapted tyre model reproduces satisfactorily the camber property of the original model; i.e. the camber stiffness decreases as the absolute value of the tyre slip angle, $|\alpha_i|$, increases. Moreover, the lateral force gain from the wheel camber becomes quite small as α_i moves outside a certain range ($\pm 10^\circ$ in this case). One fact worth noting is that with the simplified tyre model, the camber gain around $|\alpha_i| = 0^\circ$ is underestimated. This point is ignored when modelling the camber influence for the purpose of brevity. It is also shown in Figure 2(a,b) that the behaviour of the adapted model is consistent with that of the original model.

2.4. Model summary

Given the following definitions of the input, state and output vectors of the system, u , x and y , respectively,

$$u = [\delta_f \quad T_{fl} \quad T_{fr} \quad T_{rl} \quad T_{rr} \quad \gamma_f \quad \gamma_r]^T \quad (13a)$$

$$x = [v_x \quad v_y \quad \omega_z \quad \psi \quad X \quad Y \quad \omega_{fl} \quad \omega_{fr} \quad \omega_{rl} \quad \omega_{rr}]^T \quad (13b)$$

$$y = [v_x \quad \psi \quad Y \quad \omega_z \quad \beta]^T \quad (13c)$$

where $\beta = \arctan v_y/v_x \approx v_y/v_x$ (for a small sideslip angle), the system determined by (1)–(13) can be expressed in continuous-time form as

$$\dot{x} = f_c(x, u) \quad y = h_c(x). \quad (14)$$

The corresponding discrete-time form can be derived as

$$x_{k+1} = f(x_k, u_k) \quad y_k = h(x_k). \quad (15)$$

Note that methods for obtaining this discretised form will be discussed in Section 3.4.

3. Controller design

This section describes the camber controller design, which is based on the system model described in Section 2. The camber controller is designed for two main purposes, namely to enable the vehicle to follow a pre-defined path and to ensure yaw stability, through actively regulating the individual camber of the wheels. For the purpose of path following, MPC [21] is a scheme commonly adopted, due to its capability of handling future trajectories and constraints. Moreover, yaw stability can be achieved within the MPC framework by controlling and limiting the yaw rate and sideslip angle.

3.1. Objective function

To achieve path following and yaw stability, the actual vehicle output, y , as defined by (13c), is pushed towards its reference, $y_{k+p|k}^{ref} = [v_{xref} \ \psi_{ref} \ Y_{ref} \ \omega_{zref} \ \beta_{ref}]$. For notational convenience, this objective is expressed in the discrete-time form as follows:

$$\begin{aligned}
J(\mathbf{x}, \mathbf{u}, \Delta\mathbf{u}, \mathbf{s}) = & \underbrace{\sum_{p=0}^{N-1} \|y_{k+p|k} - y_{k+p|k}^{ref}\|_{Q_y}^2}_{\text{tracking error}} + \underbrace{\sum_{p=0}^{N-1} \|s_{k+p|k}\|_{Q_s}^2}_{\text{slack term}} \\
& + \underbrace{\sum_{p=0}^{N-1} \|u_{k+p|k}\|_{R_u}^2}_{\text{control action}} + \underbrace{\sum_{p=0}^{N-1} \|\Delta u_{k+p|k}\|_{R_{du}}^2}_{\text{change of control action}} \\
& + \underbrace{\|y_{k+N|k} - y_{k+N|k}\|_{Q_{yf}}^2}_{\text{terminal cost of tracking error}} + \underbrace{\|s_{k+N|k}\|_{Q_{sf}}^2}_{\text{terminal cost of slack variable}}
\end{aligned} \tag{16}$$

where the sequence of state vectors over the prediction horizon is expressed as $\mathbf{x} = [x_{k+1|k}, \dots, x_{k+N|k}]$. Similarly, the sequences of control actions, changes of control actions and slack vectors are given as $\mathbf{u} = [u_{k|k}, \dots, u_{k+N-1|k}]$, $\Delta\mathbf{u} = [\Delta u_{k|k}, \dots, \Delta u_{k+N-1|k}]$ and $\mathbf{s} = [s_{k|k}, \dots, s_{k+N|k}]$, respectively. Positive slack, $s_{k+p|k}$, is imposed to avoid possible infeasibility of the optimisation problem, as given by (24) below, and to penalise possible violations of the corresponding constraints. Besides, as detailed in the second row of (16), the control action and its change are penalised to limit the cost and chattering of actuators. Moreover, the third row of (16) penalises the terminal cost. All the above penalties are weighted with the corresponding tunable matrices Q_y , Q_s , R_u , R_{du} , Q_{yf} and Q_{sf} , respectively. Note that the initial state $x_{k|k}$, which is used as a starting point for determining the future state trajectory over the prediction horizon, is excluded from the state sequence \mathbf{x} because it is available from vehicle measurements and state estimators.

3.2. References

The way of generating the reference vector $y_{k+p|k}^{ref}$ as required in (16), is described as follows. Firstly, the reference longitudinal velocity, v_{xref} , is kept constant during the test

scenarios, although the controller is capable of tracking a varying longitudinal velocity. Secondly, the desired lateral position and yaw angle, Y_{ref} and ψ_{ref} , are given by some path planner, which is not the focus of the present study and is thus not discussed further. Thirdly, the reference yaw rate, ω_{zref} , along the prediction horizon of the MPC controller is calculated as the time derivative of the corresponding reference yaw angle, given knowledge of the desired longitudinal velocity and the sampling interval of the MPC controller. Moreover, it is expected that the path planner guarantees that the desired yaw rate does not violate the handling limit of the vehicle, which will be derived in the next paragraph. The main reason that the reference yaw rate is not determined from some approaches commonly adopted, e.g. from a steady-state bicycle model, is that there may be some conflict of needs between the desired yaw rate and the desired yaw angle if the former is not determined directly from the latter. Finally, the desired sideslip angle, β_{ref} , is set as zero in the present study for simplicity.

Considering the handling limit of the vehicle, a constraint commonly adopted on the reference yaw rate was derived in [19] and it has the following form:

$$\omega_{zupper} = \frac{\mu g}{v_x}. \quad (17)$$

It should be noted that, as stated in [19], when deriving (17), two terms concerning the transient behaviour of the vehicle were not considered. Specifically, the last two terms of the right-hand side of the following equation were neglected:

$$\omega_{zupper} = \frac{\mu g}{v_x} - \tan(\beta) \frac{\dot{v}_x}{v_x} - \frac{\dot{\beta}}{\sqrt{1 + \tan^2 \beta}}. \quad (18)$$

Since in the present study it is desired to achieve a small sideslip angle, it can be reasonable to treat $\tan^2 \beta$ and also the second term of the right-hand side of (18) as zero. Considering this fact, (18) reduces to

$$\omega_{zupper} = \frac{\mu g}{v_x} - \dot{\beta}. \quad (19)$$

However, the third term of the right-hand side of (18), i.e. the second term of the right-hand side of (19), cannot be ignored when the vehicle runs in critical situations. For instance, when the vehicle operates in the double lane change (DLC) manoeuvre [22] with a high velocity or on a low-friction road, $\dot{\beta}$ can be relatively large (both positive and negative values are possible). This means that the upper limit on the reference yaw rate determined with (17), compared with that determined with (19), can be too conservative when $\dot{\beta}$ is negative. Therefore, the upper limit on the reference yaw rate considered in the present study is determined with (19). For the lower limit, a similar analysis and equation can be readily applied.

To validate if the actual yaw rate complies with the handling limit, a test is implemented in the low-friction condition ($\mu = 0.3$) with $v_{xref} = 54$ km/h, as the handling constraint in this condition can be stricter (indicated by the smaller value of μ/v_x) than that in the high- and middle-friction conditions. The results of this validation is given in Figure 3. As can be seen, the handling limit on the yaw rate determined with (19) is complied during the entire DLC manoeuvre, although the limit determined with (17) is occasionally violated.

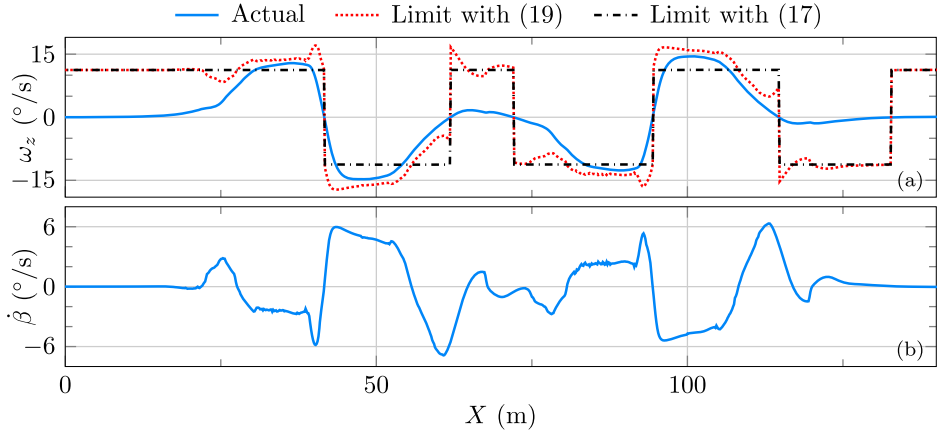


Figure 3. Yaw rate and handling limits in the low-friction condition ($\mu = 0.3$) with $v_{xref} = 54 \text{ km/h}$. (a) shows the actual yaw rate and the handling limits determined with (17) and (19), and (b) shows the time derivative of the sideslip angle.

3.3. Constraints

To obtain $J(\cdot)$ in (16), the system dynamics need to evolve over the prediction horizon. Thus, the following constraints need to be satisfied for $p \in \{0, 1, \dots, N\}$:

$$x_{k+p+1|k} = f(x_{k+p|k}, u_{k+p|k}) \quad y_{k+p|k} = h(x_{k+p|k}). \quad (20)$$

Additionally, the variation in control variables has to satisfy

$$\Delta u_{k+p|k} = \begin{cases} u_{k+p|k} - u_{k+p-1|k}, & \text{if } p \geq 1 \\ u_{k|k} - u_{k-1|k-1}, & \text{if } p = 0 \end{cases}. \quad (21)$$

Due to the physical limits of vehicle actuators, the drive/braking, camber and steering inputs are constrained by

$$T_{\min} \leq u(2, 3, 4, 5)_{k+p|k} \leq T_{\max} \quad \Delta T_{\min} \leq \Delta u(2, 3, 4, 5)_{k+p|k} \leq \Delta T_{\max} \quad (22a)$$

$$\gamma_{\min} \leq u(6, 7)_{k+p|k} \leq \gamma_{\max} \quad \Delta \gamma_{\min} \leq \Delta u(6, 7)_{k+p|k} \leq \Delta \gamma_{\max} \quad (22b)$$

$$\delta_f \min \leq u(1)_{k+p|k} \leq \delta_f \max \quad \Delta \delta_f \min \leq \Delta u(1)_{k+p|k} \leq \Delta \delta_f \max. \quad (22c)$$

Note that the torque output from the four drive/braking actuators is, in addition, set as equal to restrain torque vectoring, since the aim of this study is to focus on the performance of active camber:

$$u(2)_{k+p|k} = u(3)_{k+p|k} = u(4)_{k+p|k} = u(5)_{k+p|k}. \quad (23)$$

To accomplish yaw stability during critical situations, the vehicle yaw rate and sideslip angle have to be kept within the following safety margins by utilising the slack variable s , which is explained earlier:

$$\omega_{z\min} - s(1)_{k+p|k} \leq \omega_{z,k+1|k} \leq \omega_{z\max} + s(1)_{k+p|k} \quad (24a)$$

$$\beta_{\min} - s(2)_{k+p|k} \leq \beta_{k+1|k} \leq \beta_{\max} + s(2)_{k+p|k}. \quad (24b)$$

For ease of implementation, the equality and inequality constraints, (23) and (24), can be transformed into the following compact matrix form:

$$\mathcal{H}(x_{k+p|k}, u_{k+p|k}, s_{k+p|k}) = \begin{bmatrix} \omega_{z\min} - \omega_{z,k+1|k} - s(1)_{k+p|k} \\ \beta_{\min} - \beta_{k+1|k} - s(2)_{k+p|k} \\ \omega_{z,k+1|k} - \omega_{z\max} - s(1)_{k+p|k} \\ \beta_{k+1|k} - \beta_{\max} - s(2)_{k+p|k} \\ u(2)_{k+p|k} - u(3)_{k+p|k} \\ u(3)_{k+p|k} - u(4)_{k+p|k} \\ u(4)_{k+p|k} - u(5)_{k+p|k} \\ u(3)_{k+p|k} - u(2)_{k+p|k} \\ u(4)_{k+p|k} - u(3)_{k+p|k} \\ u(5)_{k+p|k} - u(4)_{k+p|k} \end{bmatrix} \leq 0. \quad (25)$$

3.4. MPC discretisation

As stated earlier, combining (1)–(13) results in a continuous-time system dynamics which would produce a continuous-time MPC problem with an infinite number of optimisation variables and constraints. Fortunately, with direct optimal control the infinite-dimensional optimisation problem can be converted into a finite one, and thus the size of the optimisation problem can be reduced.

The prevailing direct optimal control techniques include direct single shooting (DSS), direct multiple shooting (DMS) [23] and direct collocation (DC) [24]. With DMS, both the state and the control variables are treated as optimisation variables. This yields the objective function, (16), and the equality constraints, (20) and (21). If the sequences of the state vector, \mathbf{x} , and the change of control, $\Delta\mathbf{u}$, are eliminated from (16) by directly inserting (20) and (21) into (16) (instead of treating them separately as equality constraints), a DSS optimal control problem (OCP) is obtained. It is obvious that the DMS formulation produces more optimisation variables and equality constraints than the DSS formulation does. However, DMS yields a larger but sparser OCP than DSS. OCPs with this type of structure can be exploited by optimisation tools like IPOPT [25], which can contribute to a faster convergence for the DMS formulation than for the DSS formulation. In fact, this point was discussed by Zhang et al. [26], who performed a computational comparison for a moving horizon estimation problem which was similar to the corresponding MPC formulation.

The DC method takes a step further than the DMS approach. Besides the N intervals over the prediction horizon, the DC method divides each time interval $[t_k \ t_{k+1}]$ further into $N_c + 1$ sub-intervals, with each of such point corresponding to a collocation state $x_{c,k,q}$ ($q \in 1, 2, \dots, N_c$). The collocation states in the time interval $[t_k \ t_{k+1}]$ can be bonded together by a polynomial $\Pi(x_k, \mathbf{x}_c, \mathbf{u}, \Delta\mathbf{u}, \mathbf{s})$, where $\mathbf{x}_{c,k} = [x_{c,k,1}, x_{c,k,2}, \dots, x_{c,k,N_c}]$ is a sequence of collocation states in the corresponding time interval.

The DC method is adopted in the present study for MPC discretisation. Consequently, according to the above discussion and the problem formulation given in [27], the left-hand side of (16) needs to be updated as $J(\mathbf{x}, \mathbf{x}_c, \mathbf{u}, \Delta\mathbf{u}, \mathbf{s})$, while the right-hand side remains the same. Here, $\mathbf{x}_c = [x_{c,k}|_{k,1}, x_{c,k}|_{k,2}, \dots, x_{c,k}|_{k,N_c}, \dots, x_{c,k+N-1}|_{k,N_c}]$ is a sequence of

$N \times N_c$ collocation states over the entire prediction horizon. In addition to a refreshing of the objective function, the following collocation constraint needs to be satisfied for $p \in \{0, 1, \dots, N - 1\}$ and $q \in \{0, 1, \dots, N_c\}$:

$$\dot{\Pi}(x_k, \mathbf{x}_{c,k}, x_{c,k+p|k}, u_{k+p|k}) = f_c(x_{c,k+p|k}, q, u_{k+p|k}). \quad (26)$$

It can be seen that the DC method produces even more optimisation variables and equality constraints than the DMS method. Specifically, the $N \times N_c$ additional collocation states result in $N \times N_x \times N_c$ more optimisation variables. Moreover, the collocation constraint, (26), leads to $N \times N_x \times N_c$ more equality constraints. Nevertheless, the optimisation problem resulting from the DC method is larger but sparser than that resulting from the DMS formulation. This feature can again be exploited by programmes like IPOPT, which can make the DC method exceedingly effective.

3.5. Controller summary

For notational simplicity, the physical limits of the vehicle actuators, as given in (22), are summarised as u_{\min} , u_{\max} , Δu_{\min} and Δu_{\max} . Summing up the discussions presented in Sections 3.1–3.4, the overall camber controller formulation for the path following and yaw stability of over-actuated AEVs, which is discretised with the direct collocation method, then reads as follows:

$$\begin{aligned} \min_{\mathbf{x}_c, \mathbf{u}, \Delta \mathbf{u}, s} \quad & \sum_{p=0}^{N-1} \|y_{k+p|k} - y_{k+p|k}^{\text{ref}}\|_{Q_y}^2 + \sum_{p=0}^{N-1} \|s_{k+p|k}\|_{Q_s}^2 + \sum_{p=0}^{N-1} \|u_{k+p|k}\|_{R_u}^2 \\ & + \sum_{p=0}^{N-1} \|\Delta u_{k+p|k}\|_{R_{du}}^2 + \|y_{k+N|k} - y_{k+N|k}\|_{Q_{yf}}^2 + \|s_{k+N|k}\|_{Q_{sf}}^2 \end{aligned} \quad (27a)$$

$$\text{s.t.} \quad x_{k+p+1|k} = f(x_{k+p|k}, u_{k+p|k}) \quad y_{k+p|k} = h(x_{k+p|k}) \quad (27b)$$

$$\dot{\Pi}(x_k, \mathbf{x}_{c,k}, x_{c,k+p|k}, u_{k+p|k}) = f_c(x_{c,k+p|k}, q, u_{k+p|k}) \quad q \in \{0, 1, \dots, N_c\} \quad (27c)$$

$$\Delta u_{k+p|k} = \begin{cases} u_{k+p|k} - u_{k+p-1|k}, & \text{if } p \geq 1 \\ u_{k|k} - u_{k-1|k-1}, & \text{if } p = 0 \end{cases} \quad (27d)$$

$$\mathcal{H}(x_{k+p|k}, u_{k+p|k}, s_{k+p|k}) \leq 0 \quad (27e)$$

$$\Delta u_{\min} \leq \Delta u_{k+p|k} \leq \Delta u_{\max} \quad (27f)$$

$$u_{\min} \leq u_{k+p|k} \leq u_{\max} \quad (27g)$$

$$s_{k+p|k} \geq 0. \quad (27h)$$

The general co-simulation scheme for the camber controller and the vehicle plant is illustrated by Figure 4. As can be seen, at time step k the vehicle signals provided by measurement devices and state estimators are transmitted to the MPC (camber) controller. These signals are utilised as the initial state, $x_{k|k}$, in the OCP defined by (27). Solving (27) yields the solution sequence, $\mathbf{u}^* = [u_{k|k}^*, \dots, u_{k+N-1|k}^*]$. Subsequently, the first component, $u_{k|k}^*$, is extracted from the solution sequence and is applied to the steering, drive/braking and camber actuators of the vehicle, resulting in a new vehicle state,

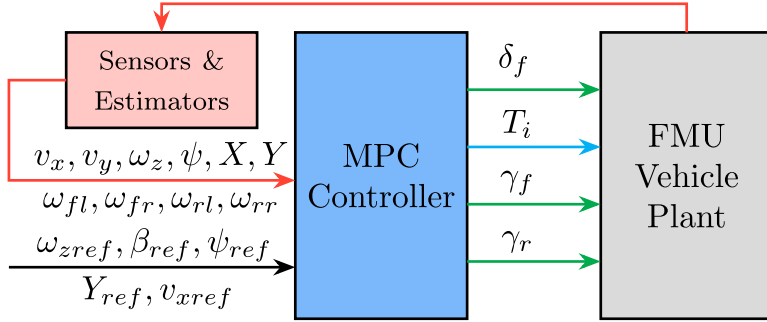


Figure 4. The co-simulation framework. FMU denotes the functional mock-up unit.

$x_{k+1|k+1}$. At the time instant $k + 1$, this solution-finding and control process is repeated, forming a closed-loop feedback control system.

4. Results and discussion

This section presents an evaluation of the camber controller described in Section 3, with different constraints on the camber rate. Specifically, four such rate-of-change constraints are selected, as given in (31). For the purpose of comparison, the results from a controller without active camber are also given in this section. This second controller is formulated in the same manner as the proposed one, with the only exception being that camber actuators are not utilised. Therefore, all the variables and parameters related to camber are removed from the problem formulation. The MPC problems of both controllers are implemented by utilising MPCTools [28], which is an interface to CasADi [29]. The resulting optimisation problem from the MPC is solved with the optimisation package IPOPT [25] and the solver MA27 [30].

During the evaluation, the vehicle plant model that is controlled features the KTH research concept vehicle (RCV) [31]. Specifically, this plant model has functionalities such as drive-by-wire, steer-by-wire and individual camber control. The plant model is developed with Dymola and is exported as an FMU for co-simulation with the controllers. This co-simulation framework is displayed in Figure 4. The aim of the controllers is to ensure that the vehicle tracks the pre-defined path and maintains yaw stability without hitting any cone of the DLC track. If the vehicle does hit any cone during the DLC manoeuvre, the controller is considered to have failed.

As explained in Section 3.1, the weightings in (16) are tunable parameters. In the present study, they are selected as follows:

$$\begin{aligned} Q_y &= \text{diag}([10 \quad 30 \quad 120 \quad 100 \quad 30]) & Q_s &= \text{diag}([10^6 \quad 10^6]) \\ R_u &= R_{du} = \text{diag}([10 \quad 10^{-5} \quad 10^{-5} \quad 10^{-5} \quad 10^{-5} \quad 10 \quad 10]) \\ Q_{yf} &= Q_y \quad Q_{sf} = Q_s \quad N = 20. \end{aligned} \quad (28)$$

Note that the sampling interval within the prediction horizon is selected as 0.05 s. This means that the controller is able to predict the path 1 s in advance, as the horizon length is chosen to be $N = 20$. For a fair comparison, both the controllers utilise the same tuning

parameters, except that, for the controller without camber, components associated with camber are eliminated for self-evident reasons.

From a yaw-stability point of view, the vehicle sideslip angle should be limited to a certain range. Specifically, the sideslip angle is constrained with equation from [19] by

$$\beta_{\max}, \beta_{\min} = \pm \arctan(0.02 \mu g) \text{ rad.} \quad (29)$$

On other hand, the yaw rate is limited by

$$\omega_{z\max}, \omega_{z\min} = \pm \max(\omega_{zref}) \text{ rad/s} \quad (30)$$

where $\omega_{zref} = [\omega_{zref,1} \dots \omega_{zref,k} \dots]$ is the reference yaw rate sequence. The main purpose of applying this constraint is to prevent the possible overshoot of yaw rate tracking. As explained in Section 3.1, the yaw rate is also constrained by considering the handling limit of the vehicle, which will be investigated in Section 4.3.

Due to physical limits, the vehicle actuators are selected to operate in the following range:

$$\begin{aligned} \gamma_{f,r\max}, \gamma_{f,r\min} &= \pm 15^\circ \quad \Delta\gamma_{f,r\max}, \Delta\gamma_{f,r\min} = \pm 15, 30, 45, 60^\circ/\text{s} \\ T_{\max}, T_{\min} &= \pm 400 \text{ N} \cdot \text{m} \quad \Delta T_{\max}, \Delta T_{\min} = \pm 20,000 \text{ N} \cdot \text{m/s} \\ \delta_f \max, \delta_f \min &= \pm 25^\circ \quad \Delta\delta_f \min = \pm 37^\circ/\text{s}. \end{aligned} \quad (31)$$

The main purpose of the inclusion of several camber rate constraints is to study how different camber velocities would influence the control performance.

As a performance metric, the tyre utilisation, t_u , is determined as follows:

- (i) The tyre utilisation of each wheel, t_{ui} , is calculated during the DLC manoeuvre with

$$\begin{aligned} t_{ui} &= \frac{\sqrt{F_{xi}^2 + F_{yi}^2}}{\mu \lambda_{yi} F_{zi}} \quad df_{zi} = \frac{F_{zi} - F_{z0i}}{F_{z0i}} \\ \lambda_{yi} &= (p_{Dy1i} + p_{Dy2i} df_{zi}) \end{aligned} \quad (32)$$

where $p_{Dy1i} = 0.8785$ and $p_{Dy2i} = -0.06451$, and λ_{yi} denotes the lateral peak friction coefficient as defined in [10, Equation (4.E23)].

- (ii) The root-mean-square (RMS) and maximum errors of t_{ui} , respectively, are calculated with respect to 0.
- (iii) The RMS and maximum t_{ui} , respectively, are averaged over the four wheels.

4.1. Benefits of active camber

The results for the controllers with and without active camber are shown in Table 1. As can be seen, on a high-friction road, with active camber ($\Delta\gamma_{f,r\min} = \pm 15^\circ/\text{s}$) the vehicle is able to complete the DLC manoeuvre successfully at 91 km/h, a velocity which is 8.3% higher than that in the no-camber-control case (84 km/h). Further, the velocity gain increases to 17.9% with $\Delta\gamma_{f,r\min} = \pm 30^\circ/\text{s}$. On a low-friction road, there is also an improvement of the passing velocity (by 9.6% with $\Delta\gamma_{f,r\min} = \pm 30^\circ/\text{s}$), compared with the corresponding velocity in the no-camber-control case, which will be discussed in greater detail in

Table 1. Results obtained with camber control ($\Delta\gamma = 15\text{--}60^\circ/\text{s}$) and without camber control (—) in high-friction ($\mu = 1$) and low-friction ($\mu = 0.3$) conditions.

Road Friction	v_{xref} (km/h)	$\Delta\gamma$ ($^\circ/\text{s}$)	ω_z ($^\circ/\text{s}$)		β ($^\circ$)		ψ ($^\circ$)		Y (m)		t_u	
			e_{rms}	e_{max}	e_{rms}	e_{max}	e_{rms}	e_{max}	e_{rms}	e_{max}	rms	max
1	84	—	3.64	7.28	1.67	3.52	1.16	2.30	0.09	0.17	0.53	0.95
		15	3.47	7.13	1.65	3.62	1.11	2.11	0.11	0.21	0.58	0.96
		30	3.68	10.20	1.58	3.44	1.09	1.78	0.13	0.27	0.62	1.07
		45	3.03	9.64	1.25	2.51	0.88	1.52	0.12	0.27	0.60	1.04
	60	2.95	9.35	1.17	2.36	0.83	1.33	0.12	0.27	0.60	1.01	
0.3	52	—	2.87	6.10	0.43	0.94	0.75	1.45	0.08	0.16	0.68	1.01
		15	1.85	4.13	0.94	2.45	0.60	1.56	0.07	0.14	0.71	1.14
		30	1.62	3.76	1.04	2.40	0.62	1.48	0.06	0.13	0.72	1.29
	57	30	1.98	4.23	1.50	3.23	0.89	2.13	0.09	0.19	0.75	1.35

^aThe RMS and maximum errors are calculated during the period when the vehicle runs on the DLC track (which is 125 m long in this study).

^bAlthough the controllers are tested both with different camber rates and without camber control, only the results corresponding to the highest passing velocity of each scenario are shown, for the purpose of brevity.

Section 4.3. Moreover, it can be seen that with camber control, the tyre is utilised more than in the case without active camber, as indicated by the higher t_u values. This means that active camber results in a higher tyre usage, which then contributes to a performance improvement.

Besides the higher passing velocity, on the high-friction road, camber control in general yields smaller reference-tracking errors for path following (ψ and Y) and yaw stability (ω_z and β), even when comparing the results for active camber with $v_{xref} = 91$ km/h to those for no camber control with $v_{xref} = 84$ km/h, as shown in Table 1. In the medium-friction ($\mu = 0.6$) condition, similar benefits with active camber can be observed, as detailed in Table 2. The improved path following and yaw stability are mainly achieved as a result of increased lateral tyre forces and an additional yaw moment provided through camber control, which is explained in greater detail in the following sections. As the actual longitudinal

Table 2. Comparison of the effects of different camber rates at different reference velocities on the medium-friction road ($\mu = 0.6$).

v_{xref} (km/h)	$\Delta\gamma$ ($^\circ/\text{s}$)	ω_z ($^\circ/\text{s}$)		β ($^\circ$)		ψ ($^\circ$)		Y (m)		Reduc. (%)		t_u	
		e_{rms}	e_{max}	e_{rms}	e_{max}	e_{rms}	e_{max}	e_{rms}	e_{max}	e_{rms}	e_{max}	rms	max
79	—	4.65	10.91	2.08	4.41	1.59	2.69	0.12	0.26	0	0	0.67	0.99
	15	3.15	8.00	1.50	3.25	1.03	1.73	0.10	0.22	-27	-26	0.68	1.10
	30	2.21	5.40	1.19	2.53	0.74	1.28	0.09	0.21	-43	-41	0.69	1.18
	45	1.95	5.40	1.04	2.30	0.63	1.21	0.09	0.20	-49	-44	0.69	1.18
	60	1.85	5.03	1.04	2.32	0.61	1.19	0.09	0.20	-50	-45	0.69	1.19
81	15	3.46	7.89	1.76	3.79	1.21	2.09	0.12	0.24	0	0	0.70	1.12
	30	2.51	5.92	1.39	2.97	0.88	1.54	0.10	0.23	-22	-20	0.71	1.18
	45	2.09	5.46	1.15	2.57	0.69	1.30	0.10	0.22	-34	-28	0.70	1.20
	60	2.04	5.64	1.12	2.45	0.67	1.28	0.10	0.21	-35	-29	0.70	1.20
83	30	2.83	6.53	1.59	3.33	1.04	1.87	0.12	0.24	0	0	0.73	1.18
	45	2.28	5.67	1.32	2.80	0.81	1.41	0.11	0.23	-17	-15	0.72	1.23
	60	2.23	6.01	1.21	2.61	0.73	1.36	0.10	0.23	-21	-16	0.72	1.24
86	45	2.73	6.62	1.55	3.10	1.00	1.74	0.12	0.26	0	0	0.75	1.25
	60	2.45	6.36	1.33	2.85	0.80	1.49	0.12	0.25	-12	-7	0.74	1.26
88	60	2.78	6.68	1.53	3.00	1.00	1.75	0.13	0.27	0	0	0.77	1.26

^a'Reduc.' denotes the average error reduction of ω_z , β , ψ and Y compared to the base. In this table the base corresponds to the cases where there is zero reduction.

velocity v_x is quite similar to its reference during the DLC manoeuvre and the errors for the two controllers are rather close, the results for v_x are not given in Table 1 or the following tables.

One matter worth discussing is the energy consumed and the power required by the camber actuators during the entire DLC manoeuvre. Take as an example the extreme case on the high-friction road ($v_{xref} = 99 \text{ km/h}$ and $\Delta\gamma = 60^\circ/\text{s}$), the peak power of the four camber actuators during the DLC manoeuvre is 0.97 kW, which is considerably lower than that of the drive motors (5.66 kW). Moreover, to complete the DLC manoeuvre the camber actuators consume 0.75 kJ of energy, which is merely 1.05% of that consumed by the drive motors (71.55 kJ). Note that the amount of camber power is determined by multiplying the wheel over-turning moment by the wheel camber velocity, and the system efficiency and additional weight of the active camber system are not considered in the discussion above. With this method of power calculation, one sometimes obtains a negative camber power. For instance, when the vehicle turns left with a decreasing steering angle, the camber power of the rear right wheel is negative, as a result of the wheel's over-turning behaviour. Therefore, to achieve greater realism, the negative part of the camber power is removed from the above camber energy calculation. Nevertheless, the 'negative energy consumption' is calculated separately to be -0.64 kJ , which is of the same magnitude as the camber energy cost obtained earlier. This 'free energy' can be of interest when designing the active suspension with the functionality of energy recuperation.

4.2. Effect of camber rate

The results for the control performance and the tyre forces with different camber rates are shown in Table 2 and Figures 5–6. As can be seen in this table and these figures, on the medium-friction road, a larger camber rate constraint again contributes to a higher passing velocity. Specifically, compared to the case of no camber control, with $\Delta\gamma_{f,r\min} = \pm 30^\circ/\text{s}$ the passing velocity increases by 5.1%. Further, the velocity gain rises to 11.4% with $\Delta\gamma_{f,r\min} = \pm 60^\circ/\text{s}$.

Another consequence of having a larger camber rate constraint is an enhanced path following and yaw stability. On the medium-friction road with $v_{xref} = 79 \text{ km/h}$, compared with the case of no camber control, when $\Delta\gamma = 15^\circ/\text{s}$, the percentage improvements of the reference-tracking accuracy for ω_z (yaw stability), β (yaw stability) and ψ (path following) range from 26.4% to 35.7%. When $\Delta\gamma = 30^\circ/\text{s}$, the corresponding percentage improvements range from 42.5% to 53.4%; when $\Delta\gamma = 45^\circ/\text{s}$, the corresponding percentage improvements range from 47.8% to 60.6%; and when $\Delta\gamma = 60^\circ/\text{s}$, the corresponding percentage improvements range from 47.4% to 61.7%. One fact worth noting is that even when the longitudinal velocity increases to 88 km/h, on the medium-friction road the tracking errors for ω_z , β and ψ when $\Delta\gamma = 60^\circ/\text{s}$ are still at least 26.3% smaller than the corresponding errors in the case without camber control when $v_{xref} = 79 \text{ km/h}$.

The gains from active camber can mainly be attributed to two factors. Firstly, with camber control the lateral tyre forces can be increased considerably, which is an important factor for keeping a vehicle stable. In fact, this also explains why, with active camber, the tyre utilisation is larger than 1, while, without camber, the tyre usage is smaller, as can be seen from the values of t_u in Tables 1–2. Secondly, the fact that a different amount

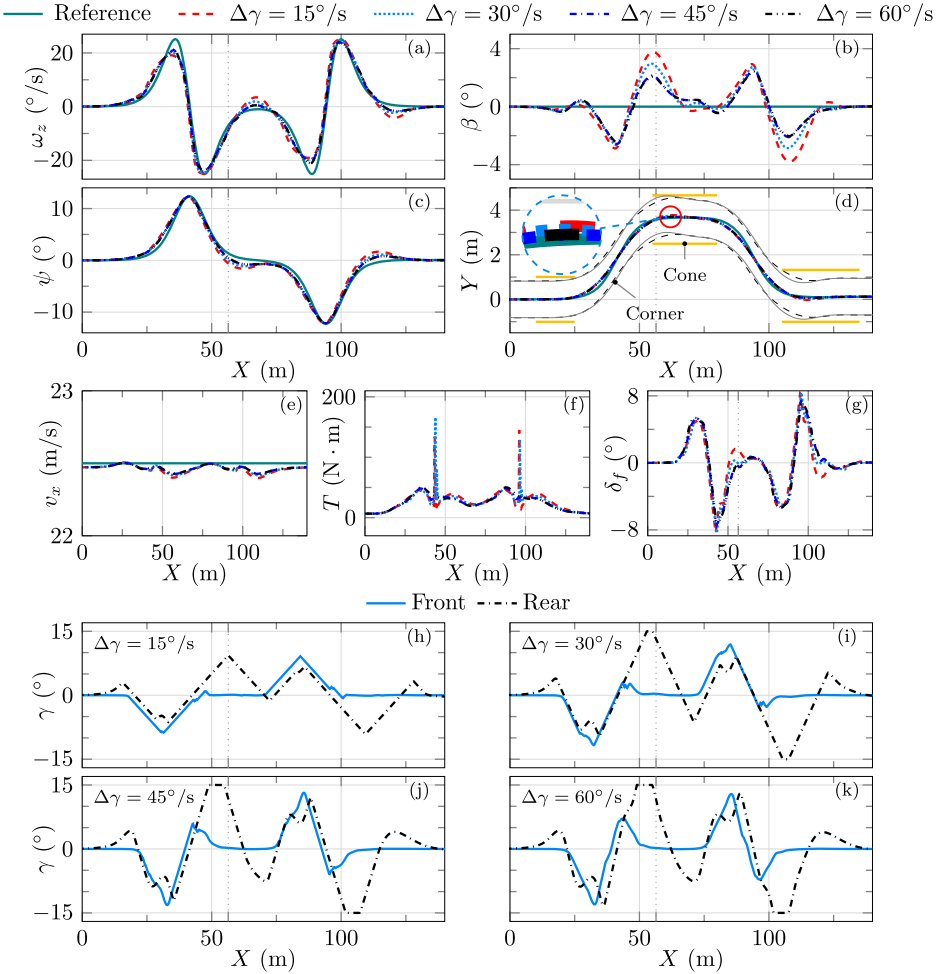


Figure 5. Tracking performance and control action from the camber controller with road friction $\mu = 0.6$. (a)–(e) show the yaw rate, sideslip angle, yaw angle, position and longitudinal velocity, respectively; (f) and (g) present the commanded torque and steering, respectively; and (h)–(k) denote the commanded camber. In (d), ‘Cone’ shows the position of the cones defining the boundary of the DLC track, and ‘Corner’ indicates the trajectory of the vehicle corners for $\Delta\gamma = 15^\circ/\text{s}$. ‘Front’ and ‘Rear’ denote the camber of the two front and the two rear wheels, respectively.

of camber is applied to the front and rear wheels ensures that the desired yaw moment can be partly achieved by controlling the wheel camber. Specifically, at the position of $X = 56.41 \text{ m}$, a positive yaw moment is generated through cambering the wheels given the fact that $\gamma_f = 0.11^\circ$ and $\gamma_r = 9.36^\circ$, as indicated in Figure 5(h), and a positive camber produces a negative lateral tyre force. At this location it can also be seen that the tyre usage of the rear left wheel is higher than 1, as indicated in Figure 6(a).

The necessity of having a fast enough camber response is mainly due to the fact that the desired wheel camber sometimes cannot be reached in a limited period if a slow camber actuator is used. For instance, at the position of $X = 56.41 \text{ m}$, the camber angle remains

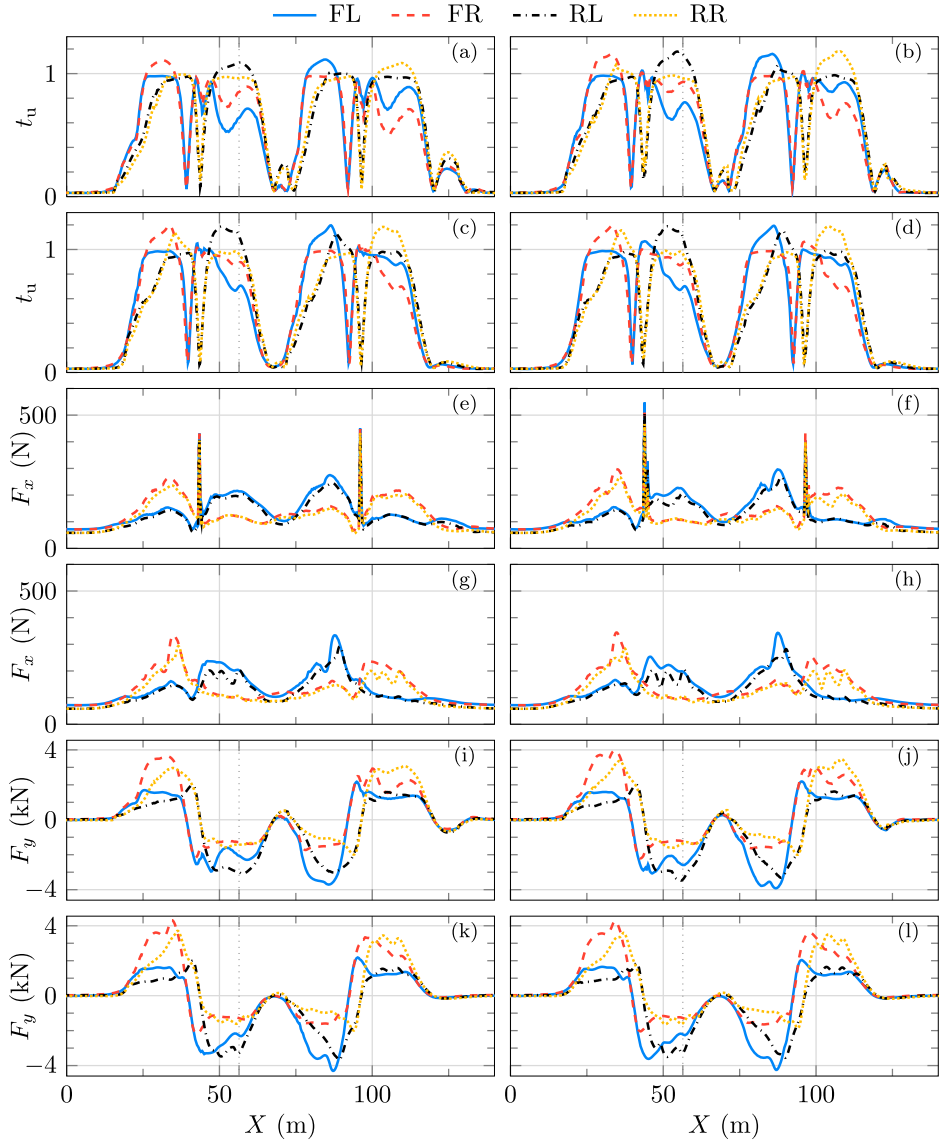


Figure 6. Tyre utilisation and forces from the camber controller with the road friction $\mu = 0.6$. [(a), (e), (i)], [(b), (f), (j)], [(c), (g), (k)] and [(d), (h), (l)] show the results obtained with $\Delta\gamma = 15, 30, 45$ and $60^\circ/\text{s}$, respectively.

below 10° when the camber rate constraint is set to $\pm 15^\circ/\text{s}$, although the constraint on the camber angle is selected as $\pm 15^\circ$. When $\Delta\gamma = 30, 45$ and $60^\circ/\text{s}$, however, the wheel camber at this position reaches a higher value than 10° , as illustrated in Figure 5(i-k). Correspondingly, the lateral tyre forces and thus the tyre utilisation at this position with larger camber rate constraints are higher than those with $\Delta\gamma = 15^\circ/\text{s}$, as shown in Figure 6(i-l) and (a-d).

On the other hand, it is less beneficial to use a faster camber actuator when the camber rate reaches a certain threshold. Specifically, on the medium-friction road, the average error reduction (e_{\max} of ‘Reduc’ in Table 2) decreases merely by 1% with $v_{xref} = 79, 81$ and 83 km/h, when the camber rate constraint increases from 45 to $60^\circ/\text{s}$. A similar phenomenon can be seen in the high-friction case, where with the same camber rate increment, there is a small accuracy improvement with $v_{xref} = 99$ km/h. This can be attributed to the fact that it is less efficient to generate the required tyre forces and yaw moment by only enlarging the camber rate, as is evident from the barely changed t_u values in the above cases.

4.3. Effect of road friction

As discussed earlier, on the low-friction road, a relatively high velocity gain is obtained by utilising active camber, as shown in Table 1. On the other hand, the path following and yaw stability performance in the low-friction case does not improve with an increase in

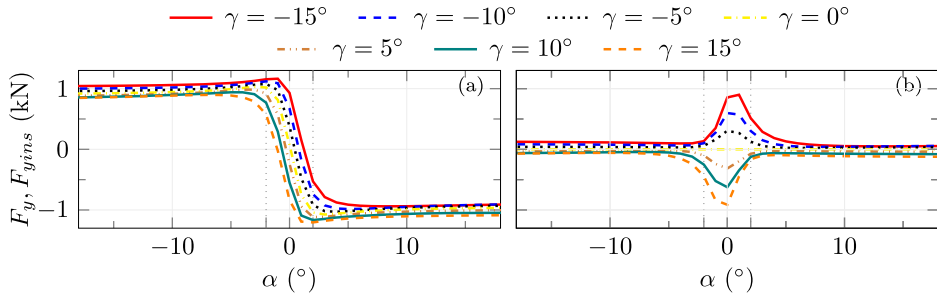


Figure 7. Original Pacejka tyre model with a camber effect on a low-friction road ($\mu = 0.3$). (a) and (b) show the lateral tyre force F_y and the gain due to camber F_{yins} , respectively.

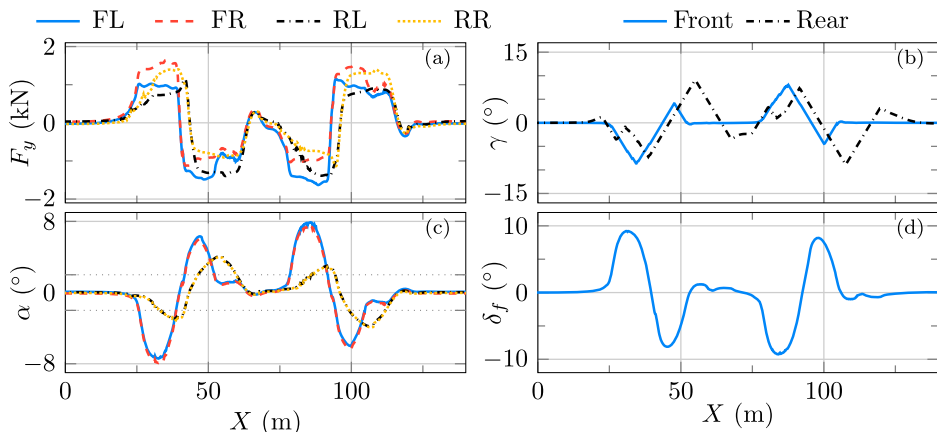


Figure 8. Lateral tyre force and control input on a low-friction road ($\mu = 0.3$) with $v_{xref} = 54$ km/h and $\Delta\gamma = 15^\circ/\text{s}$. (a) and (c) show the lateral tyre forces and tyre slip angles, respectively, and (b) and (d) show the commanded camber and steering, respectively.

the camber rate as obviously as it does in the high- and medium-friction cases. This is mainly because the rate of variation of the camber stiffness with respect to the tyre slip angle increases considerably as the road friction decreases, although the camber stiffness at a zero-slip angle only decreases slightly. In other words, it is less effective to produce additional lateral tyre forces through cambering the wheels in the case where the road friction is low and the tyre slip angle is relatively large.

Specifically, on the low-friction road, it is inefficient to exploit active camber when the tyre slip angle is outside the range of $\pm 2^\circ$, as can be seen when comparing Figures 7 and 2. However, in this road condition ($\mu = 0.3$) the tyre slip angles are outside the range of $\pm 2^\circ$ for more than 34% of the time when the vehicle is running on the DLC track, as shown in Figure 8(c). In fact, it is in this critical period, which lasts for more than 34% of the time on the DLC track, that camber control, i.e. a large lateral tyre force, is desired to achieve better path tracking and yaw stability. This conflict of needs makes it less beneficial to utilise active camber (and thus a high camber rate) for path following and yaw stability improvement on the low-friction road.

5. Conclusion

In this paper, a camber controller has been presented for enhancing the path following and yaw stability of over-actuated autonomous electric vehicles. The camber controller was formulated in the MPC framework based on a nonlinear two-track vehicle model and a modified Dugoff tyre model, with both actuator and safety constraints considered. With the modified tyre model, the camber effect on the lateral tyre force was represented by a simple but effective linear component. Tests on the camber controller were carried out at various camber rates in various road conditions, with regard to path following and yaw stability improvement and velocity gain.

The main findings concerning active camber in the DLC manoeuvre can be summarised as follows. Firstly, active camber was able to facilitate a higher passing velocity and improved path following and yaw stability in all three road conditions. Secondly, in the high- and medium-friction conditions, $\Delta\gamma = 45^\circ/\text{s}$ was the preferred camber rate for the achievement of a relatively high velocity and, at the same time, a better path following and yaw stability performance. In the low-friction condition, there was a relatively high vehicle velocity gain with $\Delta\gamma = 30^\circ/\text{s}$, but the path following and yaw stability enhancement was not as effective as it was in the high- and medium-friction conditions with either $\Delta\gamma = 30^\circ/\text{s}$ or a higher camber rate, due to the narrow effective camber region in the tyre characteristics. In addition, the energy required to camber the wheels was negligible compared with that required to actuate the drive motors. Future research will be carried out to validate the proposed active camber strategy through studies to be performed on an experimental vehicle.

Nomenclature and notation

General symbols

- | | |
|---------------|---|
| \mathcal{A} | A set in which the elements denote the front left, front right, rear left and rear right wheels, respectively, $= \{fl, fr, rl, rr\}$. |
|---------------|---|

XOY	Earth frame; for global positioning system.
$x_b oy_b$	Vehicle body frame; for inertial measurement unit.
xoy	Vehicle frame; for describing vehicle motion.
$x_t oy_t$	Wheel frame; for describing wheel motion.
$f_c(\cdot), h_c(\cdot)$	Continuous-time state, output equation.
$f(\cdot), h(\cdot)$	Discrete-time state, output equation.
$J(\cdot)$	Objective function.
$\mathcal{H}(\cdot)$	Constraint matrix.
$\Pi(\cdot)$	Collocation polynomial.

Model variables

x, u, y	State, input, output vector.
v_x, v_y	Longitudinal, lateral velocity at centre of gravity (CoG) in frame xoy (m/s).
ω_z	Yaw rate around CoG in frame xoy (rad/s).
ψ	Yaw angle in frame XOY (rad).
X, Y	Longitudinal, lateral position in frame XOY (m).
ω_i	Angular velocity of the wheel in frame $x_t oy_t$ (rad/s) ($i \in \mathcal{A}$).
β	Sideslip angle (rad).
a_x, a_y	Longitudinal, lateral acceleration in frame $x_b oy_b$ (m/s ²).
v_{xi}, v_{yi}	Longitudinal, lateral velocity at the wheel centre in frame xoy (m/s) ($i \in \mathcal{A}$).
v_{cxi}, v_{cyi}	Longitudinal, lateral velocity at the wheel centre in frame $x_t oy_t$ (m/s) ($i \in \mathcal{A}$).
α_i	Tyre slip angle in frame $x_t oy_t$ (rad) ($i \in \mathcal{A}$).
κ_i	Tyre slip ratio in frame $x_t oy_t$ ($i \in \mathcal{A}$).
δ_f	Steering angle, mean of two front wheels in frame xoy (rad).
γ_f, γ_r	Front, rear camber angle in frame xoy (rad).
T_i	Drive/braking torque on the wheel in frame $x_t oy_t$ (N · m) ($i \in \mathcal{A}$).
F_{xi}, F_{yi}	Longitudinal, lateral tyre force in frame $x_t oy_t$ (N) ($i \in \mathcal{A}$).
F_{zi}	Vertical tyre force in frame $x_t oy_t$ (N) ($i \in \mathcal{A}$).
M_{yi}	Rolling resistance moment in frame $x_t oy_t$ (N · m) ($i \in \mathcal{A}$).
t_u	Tyre utilisation.

Model parameters

$C_{\gamma i}$	Tyre camber stiffness (N/rad) ($i \in \mathcal{A}$).
$C_{\alpha i}$	Tyre cornering stiffness (N/rad) ($i \in \mathcal{A}$).
$C_{\kappa i}$	Tyre longitudinal stiffness (N) ($i \in \mathcal{A}$).
F_{z0i}	Nominal wheel load (N) ($i \in \mathcal{A}$).
I_{wi}	Tyre rotational inertia (kg · m ²) ($i \in \mathcal{A}$).
r_e	Tyre effective rolling radius (m).
p_{Dy1i}	Tyre lateral friction ($i \in \mathcal{A}$).
p_{Dy12}	Variation of tyre lateral friction with load ($i \in \mathcal{A}$).
m	Vehicle mass (kg).
I_z	Vehicle yaw inertia (kg · m ²).
B_f, B_r	Front, rear track width (m).
l_f, l_r	Distance from CoG to front, rear axle (m).

h_g	Height of CoG (m).
μ	Road friction coefficient.
g	Gravitational acceleration (m/s^2).

Controller variables

x, x_c	Sequence of states, collocation states.
$u, \Delta u, s$	Sequence of control actions, change of control actions, slack variables.

Controller variables

N	Prediction horizon.
N_c	Number of interior collocation points.
N_x	Length of state vector.
Q_y, Q_{yf}	Weight matrix for penalising stage, terminal output tracking.
R_u, R_{du}	Weight matrix for penalising control and change of control.
Q_s, Q_{sf}	Weight matrix for penalising stage, terminal slack.

Disclosure statement

No potential conflict of interest was reported by the author(s).

Funding

This work was supported by the Swedish Electromobility Centre , the National Key R&D Programme of China under Grant 2017YFB0103600, and TRENoP (Transport Research Environment with Novel Perspectives) at KTH Royal Institute of Technology.

ORCID

Wenliang Zhang  <http://orcid.org/0000-0002-4504-6059>

Lars Drugge  <http://orcid.org/0000-0001-8928-0368>

Mikael Nybacka  <http://orcid.org/0000-0002-2265-9004>

References

- [1] Webb CN. Estimating lives saved by electronic stability control, 2011–2015. Washington (DC): NHTSA, U.S. Dept. of Transportation; 2017. Traffic Safety Facts Research Note DOT HS 812 391.
- [2] Falcone P, Borrelli F, Asgari J, et al. Predictive active steering control for autonomous vehicle systems. IEEE Trans Control Syst Technol. 2007 May;15(3):566–580.
- [3] Falcone P, Tseng HE, Asgari J, et al. Integrated braking and steering model predictive control approach in autonomous vehicles. IFAC Proc Vol. 2007;40(10):273–278.
- [4] Liebemann EK, Meder K, Schuh J, et al. Safety and performance enhancement: the Bosch electronic stability control (ESP). Proceedings of SAE Convergence; 2004. p. 421–428.
- [5] Hori Y. Future vehicle driven by electricity and control-research on four-wheel-motored “UOT electric march II”. IEEE Trans Ind Electron. 2004 Oct;51(5):954–962.
- [6] Nam K, Fujimoto H, Hori Y. Lateral stability control of in-wheel-motor-driven electric vehicles based on sideslip angle estimation using lateral tire force sensors. IEEE Trans Veh Technol. 2012 Jun;61(5):1972–1985.

- [7] Shuai Z, Zhang H, Wang J, et al. Combined AFS and DYC control of four-wheel-independent-drive electric vehicles over CAN network with time-varying delays. *IEEE Trans Veh Technol*. 2014 Feb;63(2):591–602.
- [8] Alipour H, Sabahi M, Sharifian MBB. Lateral stabilization of a four wheel independent drive electric vehicle on slippery roads. *Mechatronics*. 2015 Sep;30:275–285.
- [9] Zhai L, Sun T, Wang J. Electronic stability control based on motor driving and braking torque distribution for a four in-wheel motor drive electric vehicle. *IEEE Trans Veh Technol*. 2016 Jun;65(6):4726–4739.
- [10] Pacejka H. Tire and vehicle dynamics. 3rd ed. Oxford: Elsevier; 2012.
- [11] Roethof D, Sezer T, Arat MA, et al. Influence of active camber control on steering feel. *SAE Int J Passeng Cars – Mech Syst*. 2016 Apr;9(1):124–134.
- [12] Braghin F, Prada A, Sabbioni E. Potentialities of active suspensions for the improvement of handling performances. 10th Biennial Conference on Engineering Systems Design and Analysis; 2010. p. 235–242.
- [13] Sun P, Trigell AS, Drugge L, et al. Exploring the potential of camber control to improve vehicles' energy efficiency during cornering. *Energies*. 2018 Mar;11(4):724.
- [14] Ammon D. Vehicle dynamics analysis tasks and related tyre simulation challenges. *Vehicle Syst Dyn*. 2005 Jan;43(Suppl.):30–47.
- [15] Schiehlen W, Schirle T. Modeling and simulation of hydraulic components for passenger cars. *Vehicle Syst Dyn*. 2006 Jan;44(Suppl.):581–589.
- [16] Jerrelind J, Edrén J, Li S, et al. Exploring active camber to enhance vehicle performance and safety. 23rd international symposium on Dynamics of Vehicles on Roads and Tracks; Aug 19–23; Qingdao, China; 2013.
- [17] Gáspár P, Németh B. Integrated control design for driver assistance systems based on LPV methods. *Int J Control*. 2016 Mar;89(12):2420–2433.
- [18] Yoshino T, Nozaki H. Effect of direct yaw moment control based on steering angle velocity and camber angle control. *SAE Technical Paper Series*; Sep. SAE International; 2014.
- [19] Rajamani R. Vehicle dynamics and control. 2nd ed. New York (NY): Springer; 2012.
- [20] Dugoff H, Fancher PS, Segel L. Tire performance characteristics affecting vehicle response to steering and braking control inputs. Washington (DC): U.S. National Bureau of Standards; 1969. Contract CST-460.
- [21] Rawlings JB, Mayne DQ, Diehl MM. Model predictive control: theory, computation, and design. 2nd ed. Madison (WI): Nob Hill Publishing; 2017.
- [22] Passenger cars – test track for a severe lane-change manoeuvre – part 1: double lane-change, ISO Standard 3888-1:1999; 1999.
- [23] Bock HG, Plitt KJ. A multiple shooting algorithm for direct solution of optimal control problems. *IFAC Proc*. 1984;17(2):1603–1608.
- [24] Tsang TH, Himmelblau DM, Edgar TF. Optimal control via collocation and non-linear programming. *Int J Control*. 1975 May;21(5):763–768.
- [25] Wächter A, Biegler LT. On the implementation of an interior-point filter line-search algorithm for large-scale nonlinear programming. *Math Program*. 2005 Apr;106(1):25–57.
- [26] Zhang W, Wang Z, Zou C, et al. Advanced vehicle state monitoring: evaluating moving horizon estimators and unscented Kalman filter. *IEEE Trans Veh Technol*. 2019 Jun;68(6):5430–5442.
- [27] Diehl M, Gros S. Numerical optimal control. Expected to have been published in 2018.
- [28] Risbeck MJ, Rawlings JB. MPCTools: nonlinear model predictive control tools for CasADi (Python interface); 2015. Available from: <https://bitbucket.org/rawlings-group/mpc-tools-casadi>
- [29] Andersson JAE, Gillis J, Horn G, et al. CasADi – a software framework for nonlinear optimization and optimal control. *Math Program Comput*. 2019 Jul;11(1):1–36.
- [30] HSL. A collection of Fortran codes for large scale scientific computation; 2014. Available from: <http://www.hsl.rl.ac.uk/>
- [31] Wallmark O, Nybacka M, Malmquist D, et al. Design and implementation of an experimental research and concept demonstration vehicle. 2014 IEEE Vehicle Power and Propulsion Conference (VPPC); Oct 27–30; Coimbra, Portugal. IEEE; 2014. p. 1–6.

Paper C

“Evaluating model predictive path following and yaw stability controllers for over-actuated autonomous electric vehicles”,

Wenliang Zhang, Zhepo Wang, Lars Drugge and Mikael Nybacka,
IEEE Transactions on Vehicular Technology, vol. 69, no. 11, 2020.

Paper C

Evaluating Model Predictive Path Following and Yaw Stability Controllers for Over-Actuated Autonomous Electric Vehicles

Wenliang Zhang[✉], Zhenpo Wang[✉], Member, IEEE, Lars Drugge[✉], and Mikael Nybacka[✉]

Abstract—Active safety systems are of significant importance for autonomous vehicles operating in safety-critical situations like an obstacle-avoidance manoeuvre with high vehicle speed or poor road condition. However, a conventional electronic stability control system, may not always yield desired path following and yaw stability performance in such circumstances merely through brake intervention. This paper pursues a detailed investigation on utilising model predictive control (MPC) and torque vectoring for path following and yaw stability control of over-actuated autonomous electric vehicles (AEVs) in dangerous double lane change manoeuvre. The control problem of the AEV is formulated based on MPC by utilising active front steering and torque vectoring, and constraints are imposed explicitly on yaw rate and sideslip angle to ensure yaw stability. Four MPC-based controllers are designed based on double-track vehicle models. Specifically, they include two one-level controllers, i.e. one with torque vectoring and one with equal torque allocation, and two two-level controllers, i.e. one with optimisation-based torque allocation and one with rule-based allocation. These controllers are assessed extensively, with respect to passing velocity, tracking accuracy, tyre utilisation and robustness. The effect of horizon length on the control performance and computational efficiency is also investigated.

Index Terms—Model predictive control, yaw stability, torque vectoring, over-actuation, autonomous driving, electric vehicles.

Manuscript received December 10, 2019; revised June 1, 2020 and August 11, 2020; accepted September 20, 2020. Date of publication October 13, 2020; date of current version November 12, 2020. This work was supported in part by the KTH-CSC (China Scholarship Council) Programme, in part by Modelon, in part by the National Key R&D Programme of China under Grant 2017YFB0103600, in part by the Swedish Electromobility Centre, and in part by TRENOpT (Transport Research Environment with Novel Perspectives) at KTH Royal Institute of Technology. The review of this article was coordinated by Dr. Ricardo Pinto de Castro. (*Corresponding author: Zhenpo Wang*)

Wenliang Zhang is with the National Engineering Laboratory for Electric Vehicles and the Collaborative Innovation Centre for Electric Vehicles in Beijing, Beijing Institute of Technology, Beijing 100081, China, and also with the Department of Engineering Mechanics, KTH Royal Institute of Technology, SE-10044 Stockholm, Sweden (e-mail: wez@kth.se@bit.edu.cn).

Zhenpo Wang is with the National Engineering Laboratory for Electric Vehicles and the Collaborative Innovation Centre for Electric Vehicles in Beijing, Beijing Institute of Technology, Beijing 100081, China (e-mail: wangzhenpo@bit.edu.cn).

Lars Drugge and Mikael Nybacka are with the Department of Engineering Mechanics, KTH Royal Institute of Technology, SE-10044 Stockholm, Sweden (e-mail: larsd@kth.se; mnybacka@kth.se).

Digital Object Identifier 10.1109/TVT.2020.3030863

GLOBAL NOMENCLATURE AND NOTATION

General Symbols

\mathcal{A}	A set in which the elements denote the front left, front right, rear left and rear right wheels, respectively, $= \{fl, fr, rl, rr\}$.
XOY	Earth frame; for global positioning system.
x_{b0yb}	Vehicle body frame; for inertial measurement unit.
xoy	Vehicle frame; for describing vehicle motion.
x_{t0yt}	Wheel frame; for describing wheel motion.
$f_c(\cdot), h_c(\cdot)$	Continuous-time state, output equation.
$f(\cdot), h(\cdot)$	Discrete-time state, output equation.
$\Pi(\cdot)$	Collocation polynomial.

Model Variables

x, u, y	State, input, output vector.
v_x, v_y	Longitudinal, lateral velocity at centre of gravity (CoG) in frame xoy (m/s).
ω_z	Yaw rate around CoG in frame xoy (rad/s).
ψ	Yaw angle in frame XOY (rad).
X, Y	Longitudinal, lateral position in frame XOY (m).
ω_i	Angular velocity of the wheel in frame x_{t0yt} (rad/s) ($i \in \mathcal{A}$).
β	Sideslip angle (rad).
a_x, a_y	Longitudinal, lateral acceleration in frame x_{b0yb} (m/s ²).
v_{xi}, v_{yi}	Longitudinal, lateral velocity at the wheel centre in frame xoy (m/s) ($i \in \mathcal{A}$).
v_{cxi}, v_{cyi}	Longitudinal, lateral velocity at the wheel centre in frame x_{t0yt} (m/s) ($i \in \mathcal{A}$).
α_i	Tyre slip angle in frame x_{t0yt} (rad) ($i \in \mathcal{A}$).
κ_i	Tyre slip ratio in frame x_{t0yt} ($i \in \mathcal{A}$).
δ_f	Steering angle, mean of two front wheels in frame xoy (rad).
T_i	Drive/braking torque on the wheel in frame x_{t0yt} (Nm) ($i \in \mathcal{A}$).
F_{xi}, F_{yi}	Longitudinal, lateral tyre force in frame x_{t0yt} (N) ($i \in \mathcal{A}$).
F_{zi}	Vertical tyre force in frame x_{t0yt} (N) ($i \in \mathcal{A}$).
t_u	Tyre utilisation.
F_{xd}	Component of total longitudinal tyre forces in the x direction of frame xoy (N).

F_{yd}	Component of total longitudinal tyre forces in the y direction of frame xoy (N).	$F_{xdmax,min}$	Constraints on F_{xd} (N).
M_{zd}	Yaw moment generated with longitudinal tyre forces in frame xoy (Nm).	$\Delta F_{xdmax,min}$	Constraints on variation of F_{xd} (N/s).
		$F_{ydmax,min}$	Constraints on F_{yd} (N).
		$\Delta F_{ydmax,min}$	Constraints on variation of F_{yd} (N/s).
		$M_{zdmax,min}$	Constraints on M_{zd} (Nm).
		$\Delta M_{zdmin,max}$	Constraints on variation of M_{zd} (Nm/s).
Model Parameters			
$C_{\alpha i}$	Tyre cornering stiffness (N/rad) ($i \in \mathcal{A}$).		
$C_{\kappa i}$	Tyre longitudinal stiffness (N) ($i \in \mathcal{A}$).		
F_{z0i}	Nominal wheel load (N) ($i \in \mathcal{A}$).		
I_{wi}	Tyre rotational inertia ($\text{kg} \cdot \text{m}^2$) ($i \in \mathcal{A}$).		
r_e	Tyre radius (m).		
λ_{yi}	Tyre lateral peak friction ($i \in \mathcal{A}$).		
$pDy1i$	Tyre lateral friction ($i \in \mathcal{A}$).		
$pDy12$	Variation of tyre lateral friction with load ($i \in \mathcal{A}$).		
m	Vehicle mass (kg).		
I_z	Vehicle yaw inertia ($\text{kg} \cdot \text{m}^2$).		
B_f, B_r	Front, rear track width (m).		
l_f, l_r	Distance from CoG to front, rear axle (m).		
h_g	Height of CoG (m).		
μ	Road friction coefficient.		
g	Gravitational acceleration (m/s^2).		
Controller Variables			
\mathbf{x}_c	Sequence of states, collocation states.		
$\mathbf{u}, \Delta \mathbf{u}, s$	Sequence of control actions, variation of control actions, slack variables.		
$u_u, u_l, \Delta u_l$	Control input of upper-level for two-level controller, control input and its variation of lower-level for two-level controller.		
u_{lo}	Control input for last sampling instant from two-level controller, $= [T_{flo} \ T_{fro} \ T_{rlo} \ T_{rro}]$.		
Controller Parameters			
N	Prediction horizon.		
Q_y, Q_{yf}	Weight matrix for penalising stage, terminal output tracking.		
R_u, R_{du}	Weight matrix for penalising control and variation of control.		
Q_s, Q_{sf}	Weight matrix for penalising stage, terminal slack.		
Q_{lu}	Weight matrix for penalising allocation error for lower-level controller.		
R_{lu}, R_{ldu}	Weight matrix for penalising control, variation of control for lower-level controller.		
$C_{R_{lu}}, C_{R_{ldu}}$	Tuning parameters of the lower-level for two-level controller.		
T_s	Sampling interval (s).		
n_x, n_c, n_u, n_s	Number of state, collocation, input, slack variables.		
$\omega_{zmax,min}$	Constraints on yaw rate (rad/s).		
$\beta_{zmax,min}$	Constraints on sideslip angle (rad).		
$\delta f_{max,min}$	Constraints on steering wheel angle (rad).		
$\Delta \delta f_{max,min}$	Constraints on variation of steering wheel angle (rad/s).		
$T_{max,min}$	Constraints on motor torque (Nm).		
$\Delta T_{max,min}$	Constraints on variation of motor torque (Nm/s).		
Planner Parameters			
$y_{(\cdot)}^{ref}$	Reference trajectory vector,	$=$	
	$[\omega_{zref} \ \beta_{ref} \ \psi_{ref} \ Y_{ref} \ v_{xref}]^T$.		
$\omega_{zref,lower}$	Lower limit for reference yaw rate (rad/s).		
$\omega_{zref,upper}$	Upper limit for reference yaw rate (rad/s).		
R_{ref}	Radius of reference path (m).		

I. INTRODUCTION

ELCTRIC vehicles (EVs), with the benefit of reducing emissions and energy consumption in the road transport sector, have been gaining growing popularity around the world, e.g. in China, the United States, Japan, and Norway [1]. The electrification of vehicles provides additional possibilities for improved vehicle configuration and, more importantly, enhanced path following and active safety by exploiting over-actuation. Specifically, autonomous vehicles (AVs) with path following and active safety systems that mainly utilise steering control and brake intervention may not achieve the desired performance in some extremely dangerous situations. For instance, when an AV undergoes an obstacle-avoidance manoeuvre at a high speed or on a low-friction road, it can be difficult for the AV to follow the planned path with high accuracy while maintaining stability due to the possibly saturated tyre forces. With an over-actuated autonomous electric vehicle (AEV), however, improved path following and yaw stability performance can be accomplished through active steering and individually controlling the in-wheel motors, thereby the torques on each wheel.

To achieve safe driving in dangerous situations, there are two significant objectives for the AV: path following and yaw stability. Path following is usually achieved by utilising model predictive control (MPC) due to its exclusive capability of handling future trajectories and system constraints [2]. Falcone *et al.* [3] proposed the nonlinear and linear-time-varying MPC (NMPC and LTV MPC) which control the front steering wheel angle for path following. The NMPC adopts the yaw angle and lateral position as the system output variables, and the LTV MPC includes an additional yaw rate in the output vector. The LTV MPC presented in [4], with a one-level structure, determines directly the front steering wheel angle and braking actions, and treats the yaw angle, yaw rate, lateral position and longitudinal velocity as the output variables. The controller designed in [5], with the same output vector as [4], has a two-level structure, where upper-level determines the steering wheel angle and intermediate control inputs and the lower-level allocates the intermediate control inputs as the braking actions to individual wheels. These studies mainly considers the vehicle stability through limiting the tyre slip angle either by using a nonlinear tyre model or by applying constraints to the tyre slip angle. However, the reference yaw rate and sideslip angle are not

tracked together with the reference path, and no explicit constraints are imposed to the vehicle sideslip angle and yaw rate to ensure yaw stability. Moreover, the involvement of braking system in path following can degrade ride comfort and vehicle velocity, although, compared with merely utilising active steering, it can contribute to a better path following.

Yaw stability can be achieved with the assistance of supplementary yaw moment generated from brake intervention [6] and active steering combined with brake control allocation [7]. Alternatively, aiming at enhanced yaw stability, studies have been extended to torque vectoring control on over-actuated EVs [8]–[11]. The stability controller of over-actuated EVs typically has a hierarchical structure, where the upper level determines the virtual forces/moment and the lower level allocates the torques to individual wheels. In particular, the upper-level controller, targeting tracking desired yaw rate (and sideslip angle), has been designed based on linear quadratic regulator (LQR) [12], sliding mode control (SMC) [13]–[15], and fuzzy proportional-integral-derivative (PID) [16]. To allocate the torques to individual wheels, rule-based methods have been employed in [9], [15]. Although this type of methods are simple to implement, they can be sub-optimal as factors like tyre forces and actuator constraints are generally not considered. To tackle this issue, optimisation-based torque allocation strategies with different purposes have been proposed. To better utilise tyre forces, Shuai *et al.* [17] allocated the torques to individual wheels by considering the allocation error, friction circle and torque constraints and tyre workload. Alternatively, the strategy proposed in [18] considered the allocation error, control efforts and tyre workload, and the weighting factors could be adjusted based on lateral acceleration. To improve energy efficiency, Lenzo *et al.* [19] minimised the overall power losses in their torque allocation strategy. To reduce tyre wear, Zhao and Xu [20] included tyre slip energy in their torque allocator.

Apart from the hierarchical structure, MPC controllers with a one-level structure have been adopted for achieving yaw stability for over-actuated EVs. Ren *et al.* [21] utilised the MPC controller to determine the steering angle and individual motor torques, where the output vector consists of the yaw rate and sideslip angle. The MPC controller proposed in [22] controls the motor torques of each wheel and tracks the reference yaw rate, lateral velocity and wheel angular speed. These studies mainly attempt to ensure vehicle stability by tracking the constrained reference yaw rate and sideslip angle and constraining the tyre slip ratio, while constraints are not imposed explicitly on the actual yaw rate and sideslip angle.

Although the aforementioned research has shown promising results of achieving path following and/or stability, vehicle sideslip angle and yaw rate are in general not directly controlled and constrained in the path following studies. Moreover, despite the fact that the previous yaw stability studies have considered the constraints on the reference yaw rate and/or sideslip angle, applying explicit constraints on the actual yaw rate and sideslip angle can be more effective to avoid possible tracking overshoot, especially in dangerous situations as shown in the present study. Furthermore, although both one-level and two-level controllers have been employed in the previous literature, there is a lack of comprehensive comparisons of applying these two types of

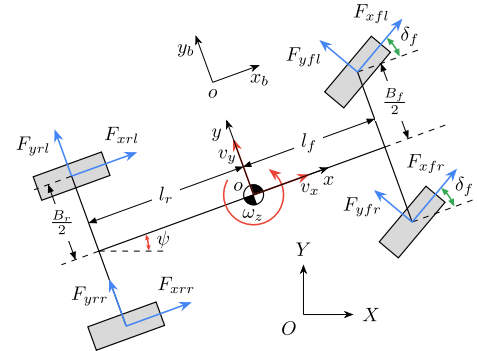


Fig. 1. Vehicle model.

controllers for path following and yaw stability. As the vehicles are becoming electrified, more redundant actuators can be available, e.g. drive, camber and steer actuators. Therefore, it is needed to investigate whether to control those actuators with a one-level or two-level structure for better control performance.

This paper presents an evaluation of applying MPC and torque vectoring to path following and yaw stability control of over-actuated AEVs during safety-critical driving scenarios. By the study presented in this work, three main contributions have been made. Firstly, an MPC scheme is proposed for concurrent path following and yaw stability control by utilising active front steering and torque vectoring, where constraints on sideslip angle and yaw rate are imposed explicitly to avoid tracking overshoot and ensure yaw stability. Secondly, four MPC-based controllers, including two one-level controllers, i.e. one with torque vectoring and one with equal torque allocation, and two two-level controllers, i.e. one with optimisation-based torque allocation and one with rule-based torque allocation, are designed, to evaluate the effect of controller structure and torque vectoring on the control performance. These controllers are comprehensively examined in terms of passing velocity, tracking accuracy, tyre utilisation and robustness. Thirdly, the effect of horizon length is evaluated with regard to the control performance and computational efficiency.

II. VEHICLE DYNAMICS MODELLING

A. Vehicle Model

A planar vehicle model is used to describe the vehicle dynamics, as shown in Fig. 1. This model, considering the longitudinal, lateral and yaw movement of the vehicle body, and the rotational motion of the four wheels, is given by combining the equations from [23] and [3]:

$$m\dot{v}_x = -(F_{yfl} + F_{yfr}) \sin \delta_f + mv_y \omega_z + F_{xd} \quad (1)$$

$$\begin{aligned} m\dot{v}_y = & (F_{yfl} + F_{yfr}) \cos \delta_f + F_{yrl} + F_{yrr} \\ & - mv_x \omega_z + F_{yd} \end{aligned} \quad (2)$$

$$\begin{aligned} I_z \dot{\omega}_z = & l_f(F_{yfl} + F_{yfr}) \cos \delta_f - l_r(F_{yrl} + F_{yrr}) \\ & + \frac{B_f}{2}(F_{yfl} - F_{yfr}) \sin \delta_f + M_{zd} \end{aligned} \quad (3)$$

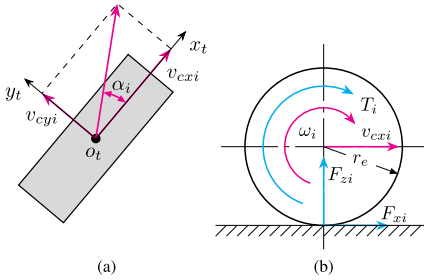


Fig. 2. Wheel motion. (a) and (b) show the top and side views, respectively.

$$\dot{\psi} = \omega_z$$

$$\dot{X} = v_x \cos \psi - v_y \sin \psi$$

$$\dot{Y} = v_x \sin \psi + v_y \cos \psi$$

$$I_{wi}\dot{\omega}_i = T_i - r_e F_{xi}$$

$$F_{xd} = (F_{xfl} + F_{xfr}) \cos \delta_f + F_{xrl} + F_{xrr}$$

$$F_{yd} = (F_{xfl} + F_{xfr}) \sin \delta_f$$

$$M_{zd} = \frac{B_f}{2}(F_{xfr} - F_{xfl}) \cos \delta_f + \frac{B_r}{2}(F_{xrr} - F_{xrl}) + l_f(F_{xfl} + F_{xfr}) \sin \delta_f. \quad (10)$$

B. Tyre Model

To determine the longitudinal and lateral tyre forces, F_{xi} and F_{yi} , as required in (1)–(10), the Dugoff tyre model from [24] is adopted:

$$F_{xi} = C_{\kappa i} \frac{\kappa_i}{1 + \kappa_i} f(\lambda_i) \quad F_{yi} = C_{\alpha i} \frac{\tan \alpha_i}{1 + \kappa_i} f(\lambda_i)$$

$$\lambda_i = \frac{\mu F_{zi}(1 + \kappa_i)}{2((C_{\kappa i}\kappa_i)^2 + (C_{\alpha i} \tan \alpha_i)^2)^{1/2}}$$

$$f(\lambda_i) = \begin{cases} (2 - \lambda_i)\lambda_i & \text{if } \lambda_i < 1 \\ 1 & \text{if } \lambda_i \geq 1. \end{cases} \quad (11)$$

Required by the tyre forces calculation, the tyre slip ratio and slip angle, κ_i and α_i , follow the definitions given in [25]:

$$\kappa_i = \frac{\omega_i r_e - v_{cxi}}{v_{cxi}} \quad \alpha_i = \arctan \frac{v_{cyi}}{v_{cxi}} \quad (12)$$

where in the wheel frame (x_t, y_t) the longitudinal and lateral velocities at the wheel centre, v_{cxi} and v_{cyi} , as shown in Fig. 2(a), are determined with equations from [26]:

$$\begin{bmatrix} v_{xfl} \\ v_{xfr} \\ v_{xrl} \\ v_{xrr} \end{bmatrix} = \begin{bmatrix} v_x - B_f \omega_z / 2 \\ v_x + B_f \omega_z / 2 \\ v_x - B_r \omega_z / 2 \\ v_x + B_r \omega_z / 2 \end{bmatrix} \begin{bmatrix} v_{yfl} \\ v_{yfr} \\ v_{yrl} \\ v_{yrr} \end{bmatrix} = \begin{bmatrix} v_y + l_f \omega_z \\ v_y + l_f \omega_z \\ v_y - l_r \omega_z \\ v_y - l_r \omega_z \end{bmatrix} \quad (13a)$$

$$\begin{bmatrix} v_{cxj} \\ v_{cyj} \end{bmatrix} = \begin{bmatrix} \cos \delta_f & \sin \delta_f \\ -\sin \delta_f & \cos \delta_f \end{bmatrix} \begin{bmatrix} v_{xj} \\ v_{yj} \end{bmatrix}, \quad j \in \{fl, fr\} \quad (13b)$$

$$\begin{bmatrix} v_{cxj} \\ v_{cyj} \end{bmatrix} = \begin{bmatrix} v_{xj} \\ v_{yj} \end{bmatrix}, \quad j \in \{rl, rr\}. \quad (13c)$$

C. Vertical Forces

In addition to the tyre slip ratio and slip angle, the longitudinal and lateral tyre forces are also dependent on the vertical tyre forces, which are calculated in the same manner as [27]:

$$F_{zfl} = \frac{l_r mg}{2(l_f + l_r)} - \frac{h_g m a_x}{2(l_f + l_r)} - \frac{l_r h_g m a_y}{B_f(l_f + l_r)} \quad (14a)$$

$$F_{zfr} = \frac{l_r mg}{2(l_f + l_r)} - \frac{h_g m a_x}{2(l_f + l_r)} + \frac{l_r h_g m a_y}{B_f(l_f + l_r)} \quad (14b)$$

$$F_{zrl} = \frac{l_f mg}{2(l_f + l_r)} + \frac{h_g m a_x}{2(l_f + l_r)} - \frac{l_f h_g m a_y}{B_r(l_f + l_r)} \quad (14c)$$

$$F_{zrr} = \frac{l_f mg}{2(l_f + l_r)} + \frac{h_g m a_x}{2(l_f + l_r)} + \frac{l_f h_g m a_y}{B_r(l_f + l_r)}. \quad (14d)$$

D. Model Summary

For the one-level controllers (see Section III-B), by combining (1)–(14), a nonlinear vehicle dynamics model is derived. For the One-Level Controller With Torque Vectoring (see Section III-B1), the system state, input and output vectors are, respectively, defined as

$$x = [v_x \ v_y \ \omega_z \ \psi \ X \ Y \ \omega_{fl} \ \omega_{fr} \ \omega_{rl} \ \omega_{rr}]^T \quad (15a)$$

$$u = [\delta_f \ T_{fl} \ T_{fr} \ T_{rl} \ T_{rr}]^T \quad (15b)$$

$$y = [\omega_z \ \beta \ \psi \ Y \ v_x]^T \quad (15c)$$

where $\beta = \arctan v_y/v_x \approx v_y/v_x$ (valid for a small sideslip angle). For the One-Level Controller With Equal Torque Allocation (see Section III-B2), the motor torques applied at individual wheels are the same, i.e. $T_{fl} = T_{fr} = T_{rl} = T_{rr}$. Therefore, the system vectors for this controller are given as

$$x = [v_x \ v_y \ \omega_z \ \psi \ X \ Y \ \omega_{fl} \ \omega_{fr} \ \omega_{rl} \ \omega_{rr}]^T \quad (16a)$$

$$u = [\delta_f \ T_{fl}]^T \quad (16b)$$

$$y = [\omega_z \ \beta \ \psi \ Y \ v_x]^T. \quad (16c)$$

For the two-level controllers (see Section III-C), by combining (1)–(6) and (11)–(14), a second nonlinear model is obtained. For the upper-level of these controllers, the system state, input and output vectors are expressed as

$$x = [v_x \ v_y \ \omega_z \ \psi \ X \ Y]^T \quad (17a)$$

$$u = [\delta_f \ F_{xd} \ F_{yd} \ M_{zd}]^T \quad (17b)$$

$$y = [\omega_z \ \beta \ \psi \ Y \ v_x]^T. \quad (17c)$$

The lower-level of these controllers is detailed in Section III-C.

With the above notation, the two controller models are represented in the following state-space form:

$$\dot{x} = f_c(x, u) \quad (18a)$$

$$y = h_c(x). \quad (18b)$$

Further, the continuous-time system, (18), can be discretised by using the collocation method [28] as follows:

$$x_{k+1} = f(x_k, u_k) \quad (19a)$$

$$y_k = h(x_k). \quad (19b)$$

Specifically, the direct collocation method with the number of interior collocation point $n_c = 1$ is used to obtain this discretised system. Note that more details on the use of the direct collocation method will be given in Section III-A1.

E. Vehicle Plant

The vehicle plant model that is used to test the performance of the controllers described in Section III features the KTH Research Concept Vehicle (RCV) [29] with functionalities of drive-by-wire, steer-by-wire and active camber, etc. The vehicle plant is developed in Dymola [30] by utilising the Modelica language and the Vehicle Dynamics Library. The main components of the Dymola plant include the front and rear suspensions of double wishbone type with spring, damper and stabiliser compliance applied, four wheels with Pacejka tyre model [25], drive, steering and camber actuators, and an aerodynamics package.

Specifically, for the Pacejka tyre model, equations [25, eqs. (4.E1)–(4.E67) and (4.E69)–(4.E78)] are utilised to determine the longitudinal and lateral tyre forces and aligning torque in the combined slip condition, the overturning couple, and the rolling resistance moment. In the present study, the pneumatic pressure change, road friction scaling, and transient response are neglected in the tyre modelling of the vehicle plant. Besides, the Pacejka tyre parameters are taken from the module CS_car225_60R18 in the simulation package CarSim [31]. Key model parameters are set as follows: $C_{\alpha i} = 55,000 \text{ N/rad}$ ($i \in \mathcal{A}$), $C_{\kappa i} = 95,000$ ($i \in \mathcal{A}$), $I_{wi} = 1.636 \text{ kg} \cdot \text{m}^2$ ($i \in \mathcal{A}$), $r_e = 0.3636 \text{ m}$, $m = 1759.14 \text{ kg}$, $I_z = 3234 \text{ kg} \cdot \text{m}^2$, $B_f = 1.6 \text{ m}$, $B_r = 1.6 \text{ m}$, $l_f = 1.4 \text{ m}$, $l_r = 1.65 \text{ m}$, $h_g = 0.53 \text{ m}$, and $g = 9.81 \text{ m/s}^2$.

The entire vehicle plant model built in Dymola is exported as an FMU for co-simulation with the controllers. The exported FMU model is a complicated system consisting of 44 continuous states and 57,330 variables. The relative complexity and completeness of the FMU vehicle model, compared with the model for controller design as given by (19), make it suitable for testing the robustness of the controllers to model mismatch.

III. CONTROLLER DESIGN

In this section, the formulation of the MPC problem is presented. Following that, the design of four controllers is described, including two one-level controllers and two two-level controllers.

A. MPC

1) Formulation: The control strategy presented in this work aims to ensure that (i) for path following and yaw stability the vehicle follows the reference trajectory as close as possible while operating within the safety margin, and (ii) for high passing velocity the vehicle completes the double lane change (DLC) manoeuvre [32] as fast as possible and without hitting any cones. To achieve these objectives, MPC is used for tracking the reference signals and limiting the yaw rate and sideslip angle. The MPC problem in the present study is defined as follows [33]:

$$\begin{aligned} & \min_{x, x_c, u, \Delta u, s} \sum_{i=0}^{N-1} \|y_{k+i|k} - y_{k+i|k}^{ref}\|_{Q_y}^2 + \|u_{k+i|k}\|_{R_u}^2 \\ & + \sum_{i=0}^{N-1} \|\Delta u_{k+i|k}\|_{R_{du}}^2 + \|s_{k+i|k}\|_{Q_s}^2 \\ & + \|y_{k+N|k} - y_{k+N|k}\|_{Q_{yf}}^2 + \|s_{k+N|k}\|_{Q_{sf}}^2 \end{aligned} \quad (20a)$$

$$\text{s. t. } x_{k+i+1|k} = f(x_{k+i|k}, u_{k+i|k}) \quad (20b)$$

$$y_{k+i|k} = h(x_{k+i|k}) \quad (20c)$$

$$\dot{\Pi}(x_k, x_c^k, x_{c,k+i|k,q}) = f_c(x_{c,k+i|k,q}, u_{k+i|k}), \quad q \in \{0, 1, \dots, n_c\} \quad (20d)$$

$$\Delta u_{k+i|k} = \begin{cases} u_{k+i|k} - u_{k+i-1|k} & \text{if } i \geq 1 \\ u_{k|k} - u_{k-1|k-1} & \text{if } i = 0 \end{cases} \quad (20e)$$

$$\begin{aligned} \omega_{zmin} - s(1)_{k+i|k} & \leq \omega_{z,k+i|k} \\ & \leq \omega_{zmax} + s(1)_{k+i|k} \end{aligned} \quad (20f)$$

$$\begin{aligned} \beta_{min} - s(2)_{k+i|k} & \leq \beta_{k+i|k} \\ & \leq \beta_{max} + s(2)_{k+i|k} \end{aligned} \quad (20g)$$

$$s_{k+i|k} \geq 0 \quad (20h)$$

where the sequences of states, control actions and variation of control actions over the prediction horizon are expressed as $x = [x_{k+1|k}, \dots, x_{k+N|k}]$, $u = [u_{k|k}, \dots, u_{k+N-1|k}]$ and $\Delta u = [\Delta u_{k|k}, \dots, \Delta u_{k+N-1|k}]$, respectively. The sequence of collocation states, which consists of $N \times n_c$ collocation variables, is given by $x_c = [x_{c,k|k,1}, x_{c,k|k,2}, \dots, x_{c,k|k,n_c}, \dots, x_{c,k+N-1|k,n_c}]$.

As can be seen from (20f) and (20g), explicit constraints are imposed on the yaw rate and sideslip angle, to avoid tracking overshoot and ensure yaw stability, where the slack vector sequence, denoted by $s = [s_{k|k}, \dots, s_{k+N-1|k}]$, is introduced to avoid possible infeasibility of the resulting optimisation problem and to penalise the violation of constraints on the yaw rate and sideslip angle. The reference trajectory vector, $y_{(\cdot)}^{ref}$, is detailed in Section III-A2.

The collocation constraint, (20d), is derived as follows. By using the direct collocation method, the time interval $[t_k \ t_{k+1}]$ is divided by the n_c interior collocation point(s) into $n_c + 1$ sub-intervals, where each of the collocation point corresponds to a collocation state $x_{c,k,q}$ ($q \in 1, 2, \dots, n_c$). The collocation

state(s) within the time interval $[t_k \ t_{k+1}]$ can be associated with each other with a polynomial $\Pi(x_c, x_c^k)$, where $x_c^k = [x_{c,k,1}, x_{c,k,2}, \dots, x_{c,k,n_c}]$ is a sequence of collocation state(s) within the corresponding time interval. To better approximate the original continuous-time system, (18a), each collocation state within the time interval $[t_k \ t_{k+1}]$ needs to satisfy the collocation constraint, (20d).

As can be seen, the MPC cost function, (20a), consists of six terms. The first four terms account for the penalties on tracking errors, control input, variation of control input, and violation of soft constraints, respectively. The corresponding weightings of diagonal structure are denoted by Q_y , R_u , R_{du} , and Q_s , respectively. The last two terms penalise the terminal costs with the corresponding weightings Q_{yf} and Q_{sf} .

2) References: The reference trajectory vector $y_{(\cdot)}^{ref}$, which corresponds to the output vectors (15c), (16c) and (17c), consists of the desired yaw rate, sideslip angle, yaw angle, lateral position and longitudinal velocity. For the purpose of path following, it is assumed that the reference yaw angle and lateral position, ψ_{ref} and Y_{ref} , are determined by a path planner, a key component of AVs. The reference longitudinal velocity, v_{xref} , is set as constant during the DLC manoeuvre.

To achieve yaw stability, the reference sideslip angle, β_{ref} , is determined by considering the reference lateral position, reference longitudinal velocity, and the steady-state sideslip angle as derived in [23]. Specifically, the radius of the reference path, R_{ref} , is first calculated from the reference lateral position with

$$\frac{1}{R_{ref}} = \frac{\frac{d^2 Y_{ref}(X)}{dX^2}}{\left(1 + \left(\frac{dY_{ref}(X)}{dX}\right)^2\right)^{\frac{3}{2}}}. \quad (21)$$

Subsequently, the reference sideslip angle is determined as follows:

$$\beta_{ref} = \frac{1}{R_{ref}} \left(l_r - \frac{l_f}{(C_{arl} + C_{arr})(l_f + l_r)} mv_{xref}^2 \right). \quad (22)$$

Moreover, the reference sideslip angle is bounded within $\pm \arctan(0.02\mu g)$ rad, as suggested in [23].

On the other hand, the reference yaw rate, ω_{zref} , is obtained with the method described in [3]. Specifically, it is derived as the time derivative of the reference yaw angle, i.e. the reference yaw angle difference between two consecutive sampling instants divided by the sampling interval, T_s . It should be noted that, as described in [3], this method can be relatively accurate in the case that the vehicle travels at a roughly constant speed within the prediction horizon, which is the case of the present study. Other methods can be used to generate more accurate reference yaw rate when the vehicle spins or side skids, which is not the focus of the present study.

Moreover, it is assumed that the constraints on the reference yaw rate are considered in the path planner by taking the vehicle handling limit into account. In the literature, an equation that is often used to calculate the upper limit on the reference yaw rate, $\omega_{zref,upper}$, is as follows [23]:

$$\omega_{zref,upper} = \frac{\mu g}{v_x}. \quad (23)$$

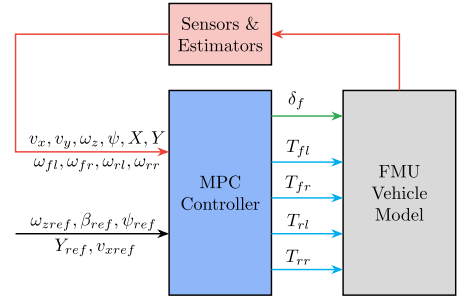


Fig. 3. One-level controller.

As stated in [23], (23) was derived without considering the transient behaviour of the vehicle, i.e. the two terms containing \dot{v}_x and $\dot{\beta}$ were discarded. In the present study, the term with \dot{v}_x can be discarded, as the reference longitudinal velocity is set to be constant. However, the effect of $\dot{\beta}$ on the value of $\omega_{zref,upper}$ may not be neglected, especially considering the fact that $\dot{\beta}$ can both be positive and negative. Therefore, in the present study the upper limit on the reference yaw rate is considered to be handled by the path planner as follows:

$$\omega_{zref,upper} = \frac{\mu g}{v_x} - \dot{\beta}. \quad (24)$$

Similarly, in the present study the lower limit on the reference yaw rate is derived as

$$\omega_{zref,lower} = -\frac{\mu g}{v_x} - \dot{\beta}. \quad (25)$$

In short, the reference yaw rate is determined by using the reference yaw angle from the path planner, and the handling limits (24) and (25) are assumed to be considered by the path planner. In fact, the main reason that the reference yaw rate is not determined with the approach commonly adopted, i.e. with a bicycle model, is that the demand of yaw rate tracking may conflict with the demand of yaw angle tracking if the reference yaw rate is not derived directly from the reference yaw angle.

B. One-Level Controller

The one-level controller, which consists of merely an MPC controller, determines directly the control efforts applied to the vehicle actuators, i.e. the front steering angle, δ_f , and the drive/braking torque, T_i ($i \in \mathcal{A}$), as illustrated by Fig. 3. The vehicle actuators are subject to the following constraints:

$$\delta_{fmin} \leq u(1)_{k+i|k} \leq \delta_{fmax} \quad (26a)$$

$$\Delta\delta_{fmin} \leq \Delta u(1)_{k+i|k} \leq \Delta\delta_{fmax} \quad (26b)$$

$$T_{min} \leq u(2, 3, 4, 5)_{k+i|k} \leq T_{max} \quad (26c)$$

$$\Delta T_{min} \leq \Delta u(2, 3, 4, 5)_{k+i|k} \leq \Delta T_{max}. \quad (26d)$$

1) One-Level Controller With Torque Vectoring (Controller OLT): At each time step, Controller OLT solves the optimal control problem (OCP) defined by (15), (19), (20) and (26), thus yielding an optimal control sequence $\mathbf{u}^* = [u_{k|k}^*, \dots, u_{k+N-1|k}^*]$.

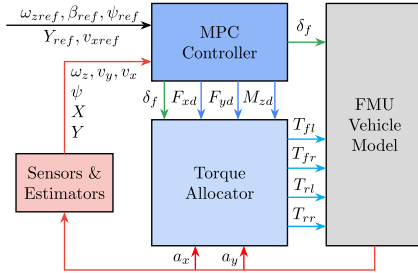


Fig. 4. Two-level controller.

Subsequently, the first component $u_{k|k}^*$ is applied to control the vehicle.

2) One-Level Controller With Equal Torque Allocation (Controller OLEA): Unlike Controller OLTV where torque vectoring is exploited, Controller OLEA allocates the drive/braking torques equally among individual wheels. From the formulation point of view, the only difference between Controller OLEA and Controller OLTV is that (16) is utilised in the former one while (15) is used in the latter one.

At each sampling instant, Controller OLEA solves the OCP determined by (16), (19), (20) and (26), and applies the first component of the optimal control sequence to the vehicle.

C. Two-Level Controller

By neglecting the wheel dynamics, (7), which are used in the one-level controller, the two-level controller is divided into an upper-level MPC controller and a lower-level torque allocator for reduced complexity of the optimisation problem, and thus decreased computational cost. As shown in Fig. 4, the MPC controller determines the front steering angle δ_f and the virtual forces/moment F_{xd} , F_{yd} and M_{zd} , which are subsequently distributed to the individual wheels by the torque allocator. The steering actuator and virtual forces/moment are constrained as follows:

$$\delta_{fmin} \leq u(1)_{k+i|k} \leq \delta_{fmax} \quad (27a)$$

$$\Delta\delta_{fmin} \leq \Delta u(1)_{k+i|k} \leq \Delta\delta_{fmax} \quad (27b)$$

$$F_{xemin} \leq u(2)_{k+i|k} \leq F_{xdmax} \quad (27c)$$

$$\Delta F_{xemin} \leq \Delta u(2)_{k+i|k} \leq \Delta F_{xdmax} \quad (27d)$$

$$F_{ydmmin} \leq u(3)_{k+i|k} \leq F_{ydmmax} \quad (27e)$$

$$\Delta F_{ydmmin} \leq \Delta u(3)_{k+i|k} \leq \Delta F_{ydmmax} \quad (27f)$$

$$M_{zdmmin} \leq u(4)_{k+i|k} \leq M_{zdmax} \quad (27g)$$

$$\Delta M_{zdmmin} \leq \Delta u(4)_{k+i|k} \leq \Delta M_{zdmax}. \quad (27h)$$

It should be noted that, since the wheel dynamics, (7), are not included in the upper-level of the two-level controllers, the angular velocity of each wheel, ω_i , at the first time instant of the prediction horizon is kept as constant within the prediction horizon, in order to obtain the longitudinal and lateral tyre forces with the combined-slip tyre model, (11).

At each sampling step, the OCP defined by (17), (19), (20) and (27) is solved, and the first component of the optimal control sequence is extracted and serves as the virtual forces/moment. Depending on the strategies for allocating the virtual forces/moment to the individual wheels, two two-level controllers are introduced as follows.

1) Two-Level Controller With Optimal Torque Allocation (Controller TLOA): Besides the upper-level controller defined by (17), (19), (20) and (27), Controller TLOA comprises an optimisation-based torque allocation algorithm, which is adapted from the one given in [16]. Specifically, an additional term containing Δu_l is added in (28f) to penalise possible chattering in the torque actuators. The modified optimal torque allocator determines the individual wheel torques according to

$$u_u = \begin{bmatrix} F_{xd} & F_{yd} & M_{zd} \end{bmatrix}^T \quad (28a)$$

$$u_l = \begin{bmatrix} T_{fl} & T_{fr} & T_{rl} & T_{rr} \end{bmatrix}^T \quad (28b)$$

$$M = \frac{1}{r_e} \begin{bmatrix} \cos \delta_f & \cos \delta_f & 1 & 1 \\ \sin \delta_f & \sin \delta_f & 0 & 0 \\ l_f \sin \delta_f & l_f \sin \delta_f & -\frac{B_r}{2} & \frac{B_r}{2} \\ -\frac{B_f}{2} \cos \delta_f & +\frac{B_f}{2} \cos \delta_f & \frac{B_r}{2} & \frac{B_r}{2} \end{bmatrix} \quad (28c)$$

$$R_{l_{tu}} = \frac{C_{R_{l_{tu}}}}{\mu r_e} \text{diag} \left(\left[\frac{1}{F_{zfl}} \quad \frac{1}{F_{zfr}} \quad \frac{1}{F_{zrl}} \quad \frac{1}{F_{zrr}} \right]^T \right) \quad (28d)$$

$$R_{l_{ldu}} = \frac{C_{R_{l_{ldu}}}}{\mu r_e} \text{diag} \left(\left[\frac{1}{F_{zfl}} \quad \frac{1}{F_{zfr}} \quad \frac{1}{F_{zrl}} \quad \frac{1}{F_{zrr}} \right]^T \right) \quad (28e)$$

$$\min_{u_l, \Delta u_l} \|Mu_l - u_u\|_{Q_{l_{tu}}}^2 + \|u_l\|_{R_{l_{tu}}}^2 + \|\Delta u_l\|_{R_{l_{ldu}}}^2 \quad (28f)$$

$$\text{s.t. } T_{min} \leq u_l(1, 2, 3, 4) \leq T_{max} \quad (28g)$$

$$\Delta T_{min} \leq \Delta u_l(1, 2, 3, 4) \leq \Delta T_{max} \quad (28h)$$

$$\Delta u_l = u_l - u_{lo}. \quad (28i)$$

2) Two-Level Controller With Rule-Based Torque Allocation (Controller TLRA): Similar to Controller TLOA, Controller TLRA also includes the upper-level controller defined by (17), (19), (20) and (27). Moreover, the global forces/torque are divided among each wheel with a rule-based torque allocator. As an addition to the strategy used in [16], (29b)–(29d) are employed to handle the physical limit on the torque actuator and its variation. The adapted rule-based torque allocation strategy is given as

$$\begin{bmatrix} T_{fl} \\ T_{fr} \\ T_{rl} \\ T_{rr} \end{bmatrix} = \frac{1}{4} \begin{bmatrix} r_e F_{xd} - \frac{r_e}{B_f/2} M_{zd} \\ r_e F_{xd} + \frac{r_e}{B_f/2} M_{zd} \\ r_e F_{xd} - \frac{r_e}{B_r/2} M_{zd} \\ r_e F_{xd} + \frac{r_e}{B_r/2} M_{zd} \end{bmatrix} \quad (29a)$$

$$T_{imin} = \max(T_{lo} + \Delta T_{min}, T_{min}) \quad (29b)$$

$$T_{imax} = \min(T_{lo} + \Delta T_{max}, T_{max}) \quad (29c)$$

$$T_i = \max(\min(T_i, T_{imax}), T_{imin}). \quad (29d)$$

D. Implementation

The MPC controllers are implemented, including the discretisation with the direct collocation method, by using MPCTools [34], which is an MPC interface to CasADI [35]. The resulting nonlinear programming (NLP) problems from the controllers are solved with the optimisation package IPOPT [36] and the solver MA27 [37], where the first and second order derivatives are provided by CasADI. Moreover, the MPC problems are solved with default solver settings, except that the option maximum number of iterations is set as 1000. Furthermore, the communication between the controllers and the FMU vehicle model is handled by employing the Python package FMPy [38], and the default CVODE [39] settings are used in the FMU model.

One fact worth noting is that different sampling intervals are used between the FMU vehicle plant and the four controllers. To mimic the sampling frequency of vehicle sensors, the vehicle plant is sampled at 10 ms. On the other hand, a sampling time of 50 ms is used for the controllers. This means that the control signals applied to the vehicle actuators are updated by the controllers every 50 ms, and in other periods the control actions in the current time step are kept the same as that in the last time instant. The main reasons for adopting this sampling strategy in the controllers are that, firstly, the computational efficiency can be improved and, secondly, in the present study, with a smooth path, the vehicle response may not change significantly during such a short period.

IV. RESULTS AND DISCUSSION

In this section, a comprehensive evaluation and comparison are presented of the two one-level controllers, Controllers OLTВ and OLEA, and the two two-level controllers, Controllers TLOA and TLRA. The evaluation and comparison are carried out in the DLC manoeuvre, where the vehicle plant model described in Section II-E is used to simulate the vehicle behaviour. To focus more on the controllers, it is assumed that the road friction information and all desired vehicle states are available from estimators/measurement devices. Moreover, all simulations are performed in Python on a laptop computer with an Intel i7-6820HQ processor.

To avoid tracking overshoot and ensure yaw stability, the actual vehicle sideslip angle and yaw rate are constrained by

$$\beta_{min} = -\arctan(0.02\mu g) \text{ rad} \quad (30a)$$

$$\beta_{max} = \arctan(0.02\mu g) \text{ rad}. \quad (30b)$$

$$\omega_{zmin} = \min(\omega_{zref}) \quad (30c)$$

$$\omega_{zmax} = \max(\omega_{zref}) \quad (30d)$$

where $\omega_{zref} = [\omega_{zref,1} \dots \omega_{zref,k} \dots]$ is the reference yaw rate sequence. Note that ω_{zmin} and ω_{zmax} can be determined as the reference yaw rate is available to the controllers. Considering the capability of the vehicle actuators, they are constrained by

$$\delta_{fmax,min} = \pm 25^\circ \quad \Delta\delta_{fmax,min} = \pm 1.85^\circ \quad (31a)$$

$$T_{max,min} = \pm 400 \text{ Nm} \quad \Delta T_{max,min} = \pm 800 \text{ Nm} \quad (31b)$$

$$F_{xdmax,min} = \pm 5000 \text{ N} \quad \Delta F_{xdmax,min} = \pm 10000 \text{ N} \quad (31c)$$

$$F_{ydmax,min} = \pm 1500 \text{ N} \quad \Delta F_{ydmax,min} = \pm 3000 \text{ N} \quad (31d)$$

$$M_{zdmax,min} = \pm 3500 \text{ Nm} \quad \Delta M_{zdmax,min} = \pm 7000 \text{ Nm}. \quad (31e)$$

It should be noted that the variation constraints on the vehicle actuators, i.e., $\Delta\delta_{fmax,min}$, $\Delta T_{max,min}$, $\Delta F_{xdmax,min}$, $\Delta F_{ydmax,min}$ and $\Delta M_{zdmax,min}$, are set as twice the value of the corresponding constraints on the actuators, meaning that the controllers are allowed to switch between the maximum and minimum torque/force requests within two consecutive sampling instants. This is to denote the capability of fast torque/force change by utilising electric actuators. Moreover, for a fair comparison between the one-level and two-level controllers, the constraints on the virtual forces/moment of the two-level controllers, i.e., $F_{xdmax,min}$, $F_{ydmax,min}$ and $M_{zdmax,min}$, are related to the one-level controllers as follows. Firstly, the one-level controllers are tested in all scenarios, as discussed in the following sections, and the resulted F_{xd} , F_{yd} and M_{zd} from the one-level controllers in these scenarios are calculated by using (8)–(10) and the measured tyre forces. Secondly, the limiting values of F_{xd} , F_{yd} and M_{zd} from the one-level controllers can be determined. Accordingly, F_{xd} , F_{yd} and M_{zd} of the two-level controllers are constrained as (31c)–(31e).

The weight matrices and horizon length of Controller OLTВ are set as follows:

$$R_u = \text{diag} \left(\begin{bmatrix} 10 & 5 \cdot 10^{-6} & 5 \cdot 10^{-6} & 5 \cdot 10^{-6} & 5 \cdot 10^{-6} \end{bmatrix} \right) \quad (32a)$$

$$R_{du} = \text{diag} \left(\begin{bmatrix} 10 & 5 \cdot 10^{-6} & 5 \cdot 10^{-6} & 5 \cdot 10^{-6} & 5 \cdot 10^{-6} \end{bmatrix} \right) \quad (32b)$$

$$Q_y = \text{diag} \left(\begin{bmatrix} 120 & 30 & 30 & 100 & 10 \end{bmatrix} \right) \quad (32c)$$

$$Q_s = \text{diag} \left(\begin{bmatrix} 10^6 & 10^6 \end{bmatrix} \right) \quad (32d)$$

$$Q_{yf} = Q_y \quad Q_{sf} = Q_s \quad (32e)$$

$$N = 20. \quad (32f)$$

Controller OLEA is set with the same tuning parameters as OLTВ, as given in (32), except for (32a) and (32b), because Controller OLEA has fewer input variables than OLTВ, as can be seen from (15b) and (16b). In addition, to make the control actions of Controller OLEA have the similar weight in the cost function (20a) as that of Controller OLTВ, (32a) and (32b) are updated for Controller OLEA as follows:

$$R_u = \text{diag} \left(\begin{bmatrix} 10 & 20 \cdot 10^{-6} \end{bmatrix} \right) \quad (33a)$$

$$R_{du} = \text{diag} \left(\begin{bmatrix} 10 & 20 \cdot 10^{-6} \end{bmatrix} \right). \quad (33b)$$

The above weight matrices are selected in the high-friction condition ($\mu = 1$) and in such a way that the terms of the cost function (20a) have a similar weight if the corresponding

components in the reference trajectory vector y^{ref} are desired to be tracked with the similar accuracy. Specifically, for Controller OLTV in the high-friction condition ($\mu = 1$) at the velocity $v_{xref} = 85 \text{ km/h}$, the mean-square tracking errors multiplied by the corresponding weighting matrices as given above are calculated for the key components as defined in (20a). The values that correspond to the yaw rate, sideslip angle, yaw angle, lateral position, steering angle and motor torque (rear left wheel) are in the magnitude of 0.1, 0.1, 0.01, 0.01, 0.01 and 0.01, respectively. From these values, it can be seen that accurately tracking the reference yaw rate and sideslip angle is valued more than tracking or limiting other components, to ensure yaw stability.

For a fair comparison with the one-level controllers, the tuning parameters for the two-level controllers are selected as

$$R_u = \text{diag} \left(\begin{bmatrix} 10 & 2.3 \cdot 10^{-7} & 0 & 4.7 \cdot 10^{-7} \end{bmatrix} \right) \quad (34a)$$

$$R_{du} = \text{diag} \left(\begin{bmatrix} 10 & 2.3 \cdot 10^{-7} & 0 & 4.7 \cdot 10^{-7} \end{bmatrix} \right) \quad (34b)$$

$$Q_y = \text{diag} \left(\begin{bmatrix} 120 & 30 & 30 & 100 & 10 \end{bmatrix} \right) \quad (34c)$$

$$Q_{lu} = \text{diag} \left(\begin{bmatrix} 100 & 0 & 100 \end{bmatrix} \right) \quad (34d)$$

$$Q_s = \text{diag} \left(\begin{bmatrix} 10^6 & 10^6 \end{bmatrix} \right) \quad (34e)$$

$$Q_{yf} = Q_y \quad Q_{sf} = Q_s \quad (34f)$$

$$C_{R_{lu}} = 0 \quad C_{R_{du}} = 0 \quad (34g)$$

$$N = 20 \quad (34h)$$

Note that R_u and R_{du} in (34) are tuned such that, in the high-friction condition ($\mu = 1$) at the velocity $v_{xref} = 85 \text{ km/h}$, Controller TLOA yields similar maximum F_{xd} and M_{zd} as that of Controller OLTV. Moreover, the component in (34d) that corresponds to F_{yd} is set as zero to avoid possibly over-constraining the optimisation problem. This is because, as can be seen from (9) and the last term of the right-hand-side of (10), M_{zd} is dependent on F_{yd} . Accordingly, the corresponding components in (34a) and (34b) are also set as zero.

Since the controllers are sensitive to vehicle velocity, they are evaluated at various target velocities (v_{xref}). Firstly, a maximum possible v_{xref} that ensures that, for all the controllers, the vehicle is able to successfully pass the DLC track (125 m) without hitting any cone is determined, and all the controllers are tested at this velocity. Subsequently, the reference velocity is increased at an interval of 1 km/h until one, two, three and, finally, all the controllers fail. This procedure is repeated on the high-, medium- and low-friction roads, respectively.

Prior to presenting the results, three performance indices are introduced as follows:

- The passing velocity for a successful completion of the DLC manoeuvre without hitting any cone, v_{xref} .
- The tracking errors of the yaw rate, ω_z , sideslip angle, β , yaw angle, ψ , and lateral position, Y . Specifically, their root-mean-square (RMS) and maximum errors of ω_z , β , ψ and Y are calculated between their respective actual and reference values during the DLC manoeuvre.

• The tyre utilisation, t_u , which measures the degree of tyre saturation. In particular, the closer t_u is to 1, the more saturated the tyre is. The tyre utilisation is determined with three steps:

- 1) The tyre utilisation of each wheel, t_{ui} , during the DLC manoeuvre is determined as follows:

$$\begin{aligned} t_{ui} &= \frac{\sqrt{F_{xi}^2 + F_{yi}^2}}{\mu \lambda_{yi} F_{zi}} \quad df_{zi} = \frac{F_{zi} - F_{z0i}}{F_{z0i}} \\ \lambda_{yi} &= (p_{Dy1i} + p_{Dy2i} df_{zi}) \end{aligned} \quad (35)$$

where λ_{yi} , a simplified version of the lateral peak friction coefficient defined in [25, eq. (4.E23)], is used to better reveal the tyre usage, as the lateral component F_{yi} dominates the tyre forces in the DLC manoeuvre.

- 2) The RMS and maximum errors of t_{ui} (compared with 0) are calculated for each wheel.
- 3) The RMS and maximum tyre utilisation of each wheel, t_{ui} , are, respectively, averaged over the four wheels, to obtain the RMS and maximum t_u .

To examine the necessity for yaw stability control, the vehicle is tested with merely the objective of path following without any yaw stability control. In this scenario, the vehicle is controlled to track ψ_{ref} , Y_{ref} and v_{xref} by using a modified version of Controller OLEA, i.e. the one-level controller with equal torque allocation. Specifically, the following changes are made to Controller OLEA:

- The output vector defined by (16c) is adjusted to $y = [\psi \quad Y \quad v_x]^T$.
- The terms penalising the slack variables in the cost function, (20a), i.e., the fourth and sixth terms, are removed.
- The constraints that correspond to the yaw rate and sideslip angle, i.e., (20f)–(20h), are discarded.
- The weighting matrix $Q_y = \text{diag}([120 \quad 100 \quad 10])$ is used.

Note that the relatively large component in Q_y , 120 (corresponding to the yaw angle), compared with the component 10 (corresponding to the longitudinal velocity), is used to improve the performance in the yaw direction, as the yaw rate and sideslip angle are not regulated in this scenario.

It is obvious from Fig. 5 that, without yaw stability control, the vehicle fails to pass the DLC track safely. Specifically, the vehicle collides with the cones in the middle and end parts of the track, with large steering effort. Moreover, at the position around $X = 44 \text{ m}$, the yaw rate exceeds the limit value. Subsequently, the sideslip angle goes beyond the safety margin. This test indicates the importance of considering yaw stability when implementing path following in the extreme DLC manoeuvre.

A. Effect of Controller Structure and Torque Vectoring

The results for the four path following and yaw stability controllers at various reference velocities in different road conditions are shown in Tables I–II and Fig. 6. In contrast to the results presented in Fig. 5, Table III shows that, by considering yaw stability in the problem formulation, Controller OLEA successfully controls the vehicle to pass the DLC track with considerably higher tracking accuracy in the medium-friction condition at the reference velocity 76 km/h. Also, with

TABLE I
COMPARISON OF THE FOUR CONTROLLERS AT VARIOUS REFERENCE VELOCITIES ON HIGH-FRICTION ROAD ($\mu = 1$)

v_{xref} (km/h)	Controller	ω_z (°/s)		β (°)		ψ (°)		Y (m)		t_u	
		e_{rms}	e_{max}	e_{rms}	e_{max}	e_{rms}	e_{max}	e_{rms}	e_{max}	rms	max
85	OLTV	4.1	8.4	1.3	3.1	1.2	2.4	0.08	0.18	0.56	0.98
	OLEA	4.6	9.5	1.5	3.3	1.4	2.9	0.10	0.18	0.54	0.96
	TLOA	4.4	9.7	1.4	3.3	1.3	3.0	0.10	0.17	0.58	1.03
	TLRA	4.6	10.0	1.5	3.3	1.4	3.1	0.10	0.17	0.58	1.03
86	OLTV	4.3	8.2	1.3	3.2	1.3	2.6	0.08	0.18	0.57	0.98
	OLEA	4.8	10.4	1.6	3.6	1.5	3.1	0.10	0.19	0.55	0.96
91	OLTV	5.2	9.0	1.6	3.7	1.6	3.2	0.11	0.22	0.61	0.99

^aConcerning Table I and the following tables, the maximum t_u being larger than 1 is mainly due to the fact that a smaller than 1 coefficient λ_{yi} is used to determine t_{ui} in (35).

^bConcerning Table I and the following tables, the values that are marked as blue correspond to the minimum values among all the controllers evaluated at the same velocity.

TABLE II
COMPARISON OF THE FOUR CONTROLLERS AT VARIOUS REFERENCE VELOCITIES ON LOW-FRICTION ROAD ($\mu = 0.3$)

v_{xref} (km/h)	Controller	ω_z (°/s)		β (°)		ψ (°)		Y (m)		t_u	
		e_{rms}	e_{max}	e_{rms}	e_{max}	e_{rms}	e_{max}	e_{rms}	e_{max}	rms	max
50	OLEA	2.8	6.7	0.4	0.8	0.8	1.6	0.08	0.20	0.67	0.99
52	TLOA	1.7	6.3	0.8	1.7	0.5	0.9	0.09	0.21	0.70	1.07
	TLRA	1.7	6.3	0.8	1.8	0.5	0.9	0.09	0.20	0.70	1.06
53	OLTV	1.8	4.6	0.9	2.0	0.6	1.5	0.09	0.20	0.72	1.13

^aFor simplicity, only the results corresponding to the highest passing velocity of each controller are shown, although the controllers are tested at various velocities.

TABLE III
COMPARISON OF THE FOUR CONTROLLERS AT VARIOUS REFERENCE VELOCITIES ON MEDIUM-FRICTION ROAD ($\mu = 0.6$)

v_{xref} (km/h)	Controller	ω_z (°/s)		β (°)		ψ (°)		Y (m)		t_u	
		e_{rms}	e_{max}	e_{rms}	e_{max}	e_{rms}	e_{max}	e_{rms}	e_{max}	rms	max
76	OLTV	3.6	9.1	1.1	2.8	1.1	2.2	0.09	0.22	0.67	1.04
	OLEA	4.3	10.9	1.5	3.5	1.4	2.5	0.10	0.23	0.66	0.99
	TLOA	3.2	5.9	1.3	3.1	1.1	2.3	0.10	0.18	0.70	1.06
	TLRA	3.2	5.9	1.4	3.2	1.1	2.3	0.10	0.18	0.70	1.06
78	OLTV	3.6	8.5	1.2	3.0	1.1	2.4	0.11	0.24	0.70	1.05
	OLEA	4.8	11.1	1.7	4.1	1.6	2.9	0.11	0.25	0.67	0.99

Controller OLEA, the vehicle is able to complete the test with a velocity 2 km/h higher, compared to the case without yaw stability control. Moreover, by imposing explicit constraints, the yaw rate and sideslip angle are all controlled within the limits, as shown in Fig. 6(a)–(b). Specifically, at the position around $X = 47$ and 100 m the constraints on the yaw rate are activated for all controllers, as indicated in Fig. 6(a). This is also true in the tests at even higher velocities.

Table I shows that, in the high-friction case, Controller OLTV outperforms the others in terms of passing velocity and tracking accuracy. Specifically, Controller OLTV has a passing velocity 5 km/h higher than Controller OLEA and 6 km/h higher than

Controllers TLOA and TLRA. Moreover, at the same velocity, Controller OLTV, in general, yields the highest tracking accuracy for path following (ψ and Y) and yaw stability (ω_z and β). In the low-friction case, similar benefits of Controller OLTV can be observed, as displayed in Table II. The benefits of Controller OLTV over other controllers are mainly attributed to the fact that it adopts the one-level structure and determines the steering angle and individual wheel torques optimally by directly solving the MPC problem. To clarify, it can be seen by comparing the structure of Controllers OLTV and TLOA that, if the wheel inertia, I_{wi} , in (7) is set as zero, then the main difference between OLTV and TLOA is that the former allocates

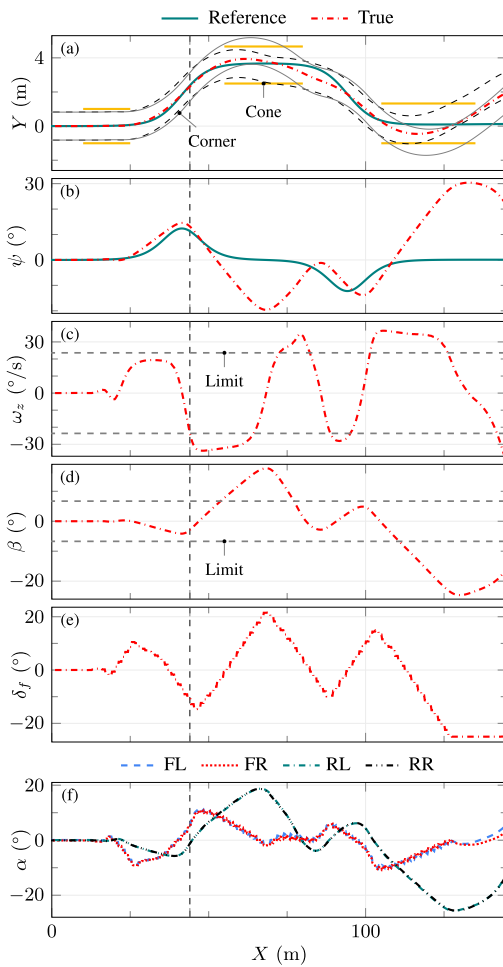


Fig. 5. Tracking performance and tyre behaviour without yaw stability control on medium-friction road ($\mu = 0.6$) with reference velocity 76 km/h. (a), (b), (c) and (d) show the lateral position, yaw angle, yaw rate and sideslip angle, respectively, and (e) and (f) present the front steering angle and tyre slip angle, respectively. In (a), “Cone” shows the position of the cones defining the boundary of the DLC track, and “Corner” indicates the trajectory of vehicle corners. Specifically, the black dashed lines show the trajectory of the two front corners, and the grey solid lines show the trajectory of the two rear corners. The “Limit” in (c) and (d) denotes the constraints given by (30c)–(30d) and (30a)–(30b), respectively.

the wheel torques within the entire prediction horizon while the latter only considers the first instant of the horizon. To validate this point, further tests are implemented with the wheel inertia whose value is considerably decreased. Specifically, the value of 0.01 is used in such tests, compared with the original value of 1.636. The results (not presented for brevity) show that with the decreased wheel inertia value, the performance of Controller OLTВ barely changes.

At the same velocity, Controller OLEA almost has the smallest tyre utilisation among the four controllers in all cases, as indicated by the t_u values in Tables I–II. With the same velocity and road condition, the longitudinal tyre forces of the four wheels would tend to deviate more from each other in the case torque vectoring is exploited than in the case torque vectoring is deactivated. As described in Section III, Controller OLEA applies the same torque to all four wheels. Therefore, it can be inferred from the definition of the tyre utilisation that it is due to the fact that torque vectoring and thus tyre forces are not reasonably utilised by Controller OLEA that makes it yields the larger tracking errors and lower passing velocity than OLTВ. This can also be observed from Fig. 6(h), where Controller OLEA results in much smaller yaw moment than other controllers. In other words, by better exploiting torque vectoring and thus the tyre utilisation than Controller OLEA, Controller OLTВ has an improved performance. For this reason, Controller OLEA will not be analysed in the following sections.

In general, Controller TLOA performs slightly better than TLRA, in terms of tracking accuracy and tyre utilisation, but the performance difference is not very obvious. This is mainly due to the fact that the induced F_{xd} and M_{zd} (calculated from the measured tyre forces) of the two controllers are rather similar, as can be seen in Fig. 7, although different torque allocation strategies are used. Nevertheless, it should be noted that there are more degrees of freedom in the design of the TLOA torque allocator. Specifically, the terms of the cost function can be adjusted and the weighting matrices can be further tuned. For these reasons and the fact that Controller TLOA merely requires a slightly higher computational time, which will be detailed in the next paragraph, Controller TLRA will not be discussed further in the subsequent sections.

In terms of computational efficiency, the average computation time per sampling step for Controllers OLTВ, OLEA, TLOA and TLRA are 47.2 ms, 44.2 ms, 35.5 ms and 33.0 ms, respectively, which are all smaller than the sampling interval of the controllers, 50 ms. This means that all the controllers are real-time implementable in the present study. Moreover, Controller OLTВ costs merely 6.8% more time per step than OLEA. Considering the benefits of applying torque vectoring, this time increase is trivial. Similarly, the time cost of Controller TLOA is 7.6% more than that of TLRA. Specifically, this computation time difference between TLOA and TLRA is caused by the fact that TLOA uses the optimal torque allocator in the lower-level controller while TLRA uses the rule-based torque allocator. It should be noted that the computation time of Controller TLOA given here considers both the upper-level MPC and the lower-level optimal torque allocator.

B. Robustness Test

As discussed earlier, Controller OLTВ has a better performance in the high- and low-friction conditions. To further examine the robustness of the controllers, tests are implemented in the medium-friction case. As can be seen from Table III, in this test scenario Controller OLTВ still has a higher passing velocity than TLOA. However, the yaw rate tracking errors of

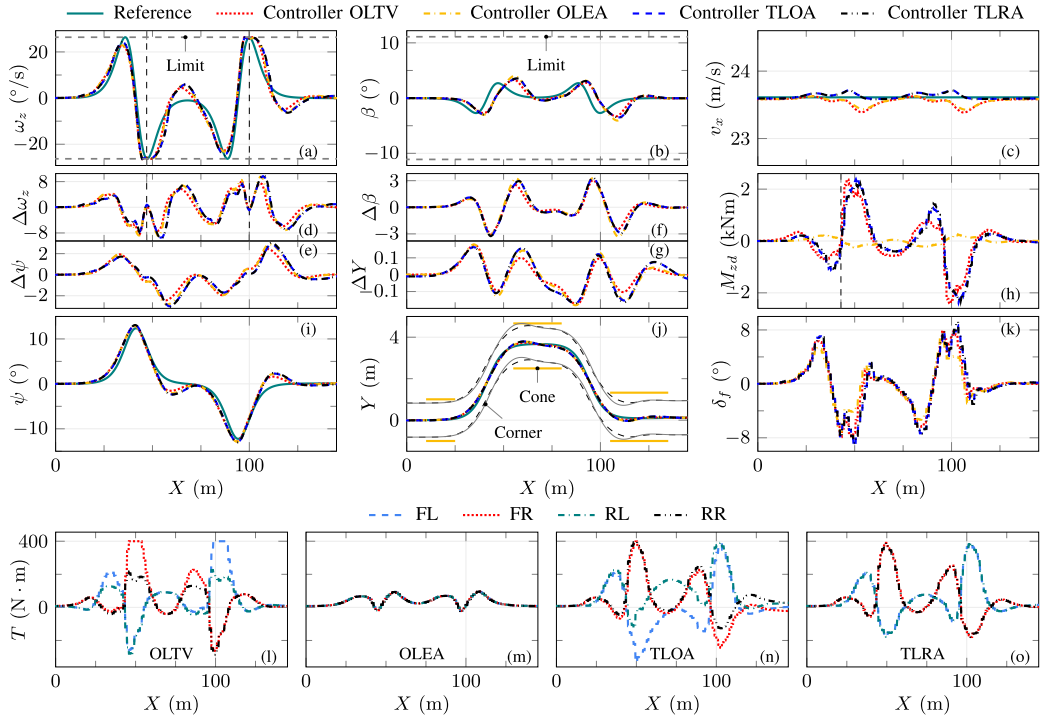


Fig. 6. Tracking performance and control actions of Controllers OLT, OLEA, TLOA and TLRA on high-friction road ($\mu = 1$) with reference velocity 85 km/h. (a)–(c) and (i)–(j) show the yaw rate, sideslip angle, longitudinal velocity, yaw angle and position, respectively. (d)–(g) display the tracking errors, (k) presents the commanded front steering, and (l)–(o) display the commanded drive/braking torques of Controllers OLT, OLEA, TLOA and TLRA, respectively. The “Limit” in (a) and (b) denotes the constraints given by (30c)–(30d) and (30a)–(30b), respectively. In (h), M_{zd} is calculated from the measured tyre forces by using (10). In (j), “Corner” indicates the trajectory of vehicle corners.

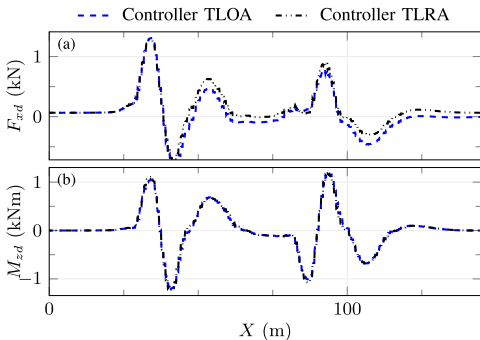


Fig. 7. Total longitudinal tyre force decomposed in the x direction and yaw moment induced with longitudinal tyre forces on low-friction road ($\mu = 0.3$) with reference velocity 52 km/h. In (a) and (b), F_{xrd} and M_{zrd} are calculated from the measured tyre forces by using (8) and (10), respectively.

OLT becomes larger than those of TLOA. Specifically, the maximum yaw rate tracking error, 9.1° , from OLT occur at the position $X = 42.9$ m. At around the same position, the yaw rate

tracking error from TLOA is 3.1° , which is much smaller than that from OLT. As shown in Fig. 8(a), at this position OLT induced a positive yaw moment (M_{zd} , 543 Nm), while TLOA a negative one (-698 Nm). With this difference in yaw moment excitation, the resulted system-required yaw moment difference ($I_z \dot{\omega}_z$) between the two controllers is as large as (-3155 Nm), which is 30% of the system-required yaw moment from TLOA.

When examining these values in the high-friction condition ($v_{xref} = 85$ km/h) at around the same position, it is found that the induced $I_z \dot{\omega}_z$ difference between the two controllers is only 4%, and the M_{zd} from the two controllers are much more similar, as can be seen in Fig. 6(h). Considering the fact that OLT results in smaller tracking errors than TLOA in the high-friction case, it can be inferred that it is the inaccurately generated yaw moment that makes OLT yields larger yaw rate tracking errors than TLOA. As discussed earlier, the main difference between OLT and TLOA is that, when allocating the wheel torques, the former considers the entire prediction horizon while the latter only takes into account the first instant of the horizon. This makes OLT a much more complicated optimisation problem than TLOA (see Section IV-C), meaning that the former can be more sensitive to parameter change (e.g. road friction) than

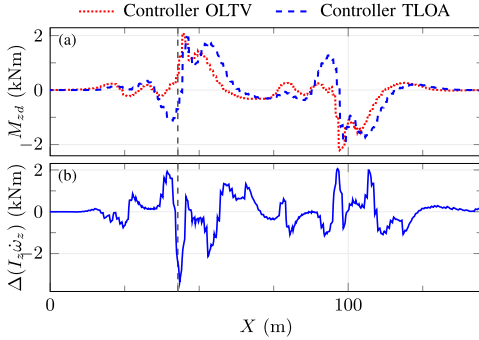


Fig. 8. Yaw moment induced with longitudinal tyre forces and system-required yaw moment difference on medium-friction road ($\mu = 0.6$) with reference velocity 76 km/h. In (a), M_{zd} is calculated from the measured tyre forces by using (10). In (b), $\Delta(I_z \dot{\omega}_z)$ is the system-required yaw moment [$I_z \dot{\omega}_z$, see (3)] difference between Controllers OLTB and TLOA; and $I_z \dot{\omega}_z$ is calculated from the measured yaw rate change.

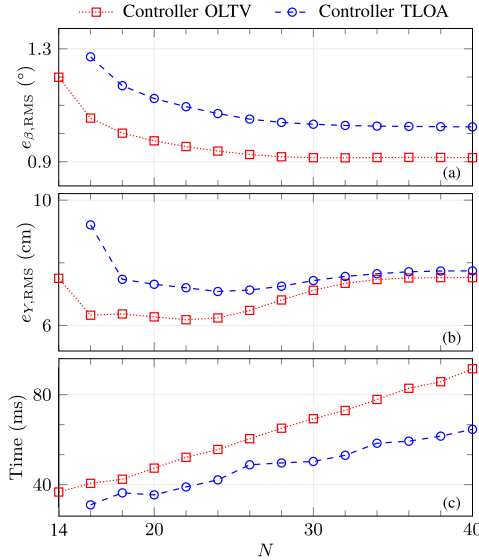


Fig. 9. Effect of horizon length on tracking accuracy and computation time of Controllers OLTB and TLOA on high-friction road ($\mu = 1$) with reference velocity 80 km/h. In (c), the computation time of Controller TLOA considers both the upper-level MPC and the lower-level optimal torque allocator.

the latter. It is especially important to consider whether to use a one- or two-level controller for better robustness when there are even more controllable vehicle actuators available, e.g. in-wheel motors, and wheel cambering and steering actuators.

C. Effect of Horizon Length

Fig. 9 presents the effect of horizon length on the tracking accuracy and computation time of Controllers OLTB and TLOA. In this test scenario, the horizon length is increased from 10 to 40 with an interval of 2, and only tests that successfully pass the

DLC track are shown. As can be seen, Controller OLTB is able to complete the DLC manoeuvre with a minimum horizon length of 14, while TLOA requires the horizon size of 16 to complete the test. Moreover, when the horizon length increases from 14 to 20, the RMS tracking errors of sideslip angle and lateral position from Controller TLOA decreases by 12% and 21%, respectively. In contrast, the tracking errors of Controller OLTB decrease less significantly as the horizon length further increases. In fact, the tracking error of lateral position from TLOA starts to increase when the horizon length becomes larger than 24. Similarly, the tracking errors from Controller OLTB decrease more obviously when the horizon length increases from 14 to 20 than they do when the horizon length further increases from 20.

The computation time per optimisation step of Controllers OLTB and TLOA increases almost linearly with respect to the horizon length, as shown in Fig. 9(c). Moreover, the computation time of Controller OLTB increases faster with the horizon length than TLOA does. Specifically, between Controllers OLTB and TLOA, the ratio of the increasing speed of computation time with respect to the horizon length is approximately 1.6. Given these facts, using the horizon length of 20 in previous discussions is a reasonable choice.

Given the MPC formulation defined by (20) and the way of implementing MPC problems within MPCTools, it can be derived that, for Controller OLTB and the upper-level of Controller TLOA, there are $N \times ((1 + n_c) \times n_x + 2 \times n_u) + (N + 1) \times n_s$ optimisation variables, $N \times ((1 + n_c) \times n_x + n_u)$ equality constraints and $2 \times N \times n_s$ inequality constraints. Considering (15), (17) and (20), the values of n_x , n_u and n_s are 10, 5 and 2, respectively, for Controller OLTB and 6, 4 and 2, respectively, for the upper-level of Controller TLOA.

As the horizon length increases, between Controller OLTB and the upper-level of Controller TLOA, the ratios of the number of optimisation variables, equality constraints and inequality constraints can be approximated as being linear with specific values of 1.5, 1.6 and 1, respectively. Moreover, as mentioned earlier, the direct collocation method is used for obtaining the discretised system, (19). Furthermore, the optimisation package IPOPT has the capability of exploiting the sparsity of the resulting optimisation problems. These facts can lead to the approximately linear increase of computation time of Controller OLTB and the upper-level of Controller TLOA with the horizon length, and also the faster increase of computation time of the former. Note that, for the computational analysis described here and in the last paragraph, the lower-level torque allocator of Controller TLOA is not included for two reasons. Firstly, as discussed in Section IV-A, the time cost of the TLOA torque allocator is merely 7.6% of that of the upper-level TLOA ($N = 20$). Secondly, it is not difficult to see after comparing (28) and (20) that the TLOA torque allocator is a considerably simpler optimisation problem and is independent of the horizon length.

V. CONCLUSION

In this paper, a comprehensive assessment has been presented of applying two one-level controllers, i.e. Controllers OLTB and OLEA, and two two-level controllers, i.e. Controllers TLOA and TLRA, to path following and yaw stability control of

over-actuated autonomous electric vehicles. Explicit constraints on yaw rate and sideslip angle were included within these controllers, and these constraints were validated to have prevented tracking overshoot and ensured yaw stability. The passing velocity, tracking accuracy, tyre utilisation and robustness of these controllers were compared, and the effect of horizon length on the tracking accuracy and computational efficiency was discussed. The main findings are summarised as follows:

- With the one-level structure, torque vectoring improved the tracking accuracy, and increased the passing velocity by up to 5 km/h.
- Controller OLTV produced the highest passing velocity in all road conditions, but its tracking accuracy, especially the yaw rate, degraded when the road friction varied. In contrast, Controllers TLOA and TLRA performed more consistently when the road condition changed.
- Compared with Controller TLOA, Controller TLRA was simple to implement and had the same passing velocity and similar tracking accuracy. On the other hand, Controller TLOA had more degrees of freedom in designing the cost function and tuning the weighting matrices.
- Controllers OLTV and TLOA had a significantly improved tracking accuracy as the horizon length increased, but their performance degraded with even larger horizon size.

The future plan of the present study is to validate these controllers with an experimental vehicle.

ACKNOWLEDGMENT

The authors would like to thank M. Jonasson for his advice on autonomous driving, as well as M. J. Risbeck for his suggestion in implementing the MPC algorithms.

REFERENCES

- [1] International Energy Agency, "Global EV outlook 2017: Two million and counting," OECD, 2017. [Online]. Available: https://www.oecd-ilibrary.org/energy/global-ev-outlook-2017_9789264278882-en
- [2] D. Q. Mayne, J. B. Rawlings, C. V. Rao, and P. O. M. Scokaert, "Constrained model predictive control: Stability and optimality," *Automatica*, vol. 36, no. 6, pp. 789–814, Jun. 2000.
- [3] P. Falcone, F. Borrelli, J. Asgari, H. E. Tseng, and D. Hrovat, "Predictive active steering control for autonomous vehicle systems," *IEEE Trans. Control Syst. Technol.*, vol. 15, no. 3, pp. 566–580, May 2007.
- [4] P. Falcone, H. E. Tseng, J. Asgari, F. Borrelli, and D. Hrovat, "Integrated braking and steering model predictive control approach in autonomous vehicles," *IFAC Proc. Volumes*, vol. 40, no. 10, pp. 273–278, 2007.
- [5] P. Falcone, F. Borrelli, H. E. Tseng, J. Asgari, and D. Hrovat, "Low complexity MPC schemes for integrated vehicle dynamics control problems," in *Proc. 9th Int. Symp. Adv. Vehicle Control*, 2008, pp. 875–880.
- [6] E. K. Liebemann, K. Meder, J. Schuh, and G. Nenninger, "Safety and performance enhancement: The Bosch electronic stability control (ESP)," in *Proc. SAE Convergence*, 2004, pp. 421–428.
- [7] J. Tjonnas and T. A. Johansen, "Stabilization of automotive vehicles using active steering and adaptive brake control allocation," *IEEE Trans. Control Syst. Technol.*, vol. 18, no. 3, pp. 545–558, May 2010.
- [8] M. Jonasson, J. Andreasson, S. Solyom, B. Jacobson, and A. S. Trigell, "Utilization of actuators to improve vehicle stability at the limit: From hydraulic brakes toward electric propulsion," *J. Dyn. Syst. Meas. Control*, vol. 133, no. 5, 2011, Art. no. 051003.
- [9] K. Nam, H. Fujimoto, and Y. Hori, "Lateral stability control of in-wheel-motor-driven electric vehicles based on sideslip angle estimation using lateral tire force sensors," *IEEE Trans. Veh. Technol.*, vol. 61, no. 5, pp. 1972–1985, Jun. 2012.
- [10] L. D. Novellis *et al.*, "Direct yaw moment control actuated through electric drivetrains and friction brakes: Theoretical design and experimental assessment," *Mechatronics*, vol. 26, pp. 1–15, Mar. 2015.
- [11] Z. Wang, Y. Wang, L. Zhang, and M. Liu, "Vehicle stability enhancement through hierarchical control for a four-wheel-independently-actuated electric vehicle," *Energies*, vol. 10, no. 7, pp. 947–964, Jul. 2017, doi: 10.3390/en10070947.
- [12] Z. Shuai, H. Zhang, J. Wang, J. Li, and M. Ouyang, "Combined AFS and DYC control of four-wheel-independent-drive electric vehicles over CAN network with time-varying delays," *IEEE Trans. Veh. Technol.*, vol. 63, no. 2, pp. 591–602, Feb. 2014.
- [13] J. Wang and R. Longoria, "Coordinated and reconfigurable vehicle dynamics control," *IEEE Trans. Control Syst. Technol.*, vol. 17, no. 3, pp. 723–732, May 2009.
- [14] M. Polesel, B. Shyrokau, M. Tanelli, D. Savitski, V. Ivanov, and A. Ferrara, "Hierarchical control of overactuated vehicles via sliding mode techniques," in *Proc. 53rd IEEE Conf. Decis. Control*, Dec. 2014, pp. 4095–4100.
- [15] H. Alipour, M. Sabahi, and M. B. B. Sharifian, "Lateral stabilization of a four wheel independent drive electric vehicle on slippery roads," *Mechatronics*, vol. 30, pp. 275–285, Sep. 2015.
- [16] L. Zhai, T. Sun, and J. Wang, "Electronic stability control based on motor driving and braking torque distribution for a four in-wheel motor drive electric vehicle," *IEEE Trans. Veh. Technol.*, vol. 65, no. 6, pp. 4726–4739, Jun. 2016.
- [17] Z. Shuai, H. Zhang, J. Wang, J. Li, and M. Ouyang, "Lateral motion control for four-wheel-independent-drive electric vehicles using optimal torque allocation and dynamic message priority scheduling," *Control Eng. Pract.*, vol. 24, pp. 55–66, Mar. 2014.
- [18] B. Li, A. Goodarzi, A. Khajepour, S. K. Chen, and B. Litkouhi, "An optimal torque distribution control strategy for four-independent wheel drive electric vehicles," *Veh. Syst. Dyn.*, vol. 53, no. 8, pp. 1172–1189, Apr. 2015.
- [19] B. Lenzo *et al.*, "Torque distribution strategies for energy-efficient electric vehicles with multiple drivetrains," *J. Dyn. Syst., Meas. Control*, vol. 139, no. 12, Aug. 2017, Art. no. 121004.
- [20] B. Zhao, N. Xu, H. Chen, K. Guo, and Y. Huang, "Stability control of electric vehicles with in-wheel motors by considering tire slip energy," *Mech. Syst. Signal Process.*, vol. 118, pp. 340–359, Mar. 2019.
- [21] B. Ren, H. Chen, H. Zhao, and L. Yuan, "MPC-based yaw stability control in in-wheel-motored EV via active front steering and motor torque distribution," *Mechatronics*, vol. 38, pp. 103–114, Sep. 2016.
- [22] M. Jalali, A. Khajepour, S. Ken Chen, and B. Litkouhi, "Integrated stability and traction control for electric vehicles using model predictive control," *Control Eng. Pract.*, vol. 54, pp. 256–266, Sep. 2016.
- [23] R. Rajamani, *Vehicle Dynamics and Control*, 2nd ed. New York, NY, USA: Springer, 2012.
- [24] H. Dugoff, P. S. Fancher, and L. Segel, "Tire performance characteristics affecting vehicle response to steering and braking control inputs," Office of Vehicle Systems Research, U.S. National Bureau of Standards, Washington, DC, USA, Tech. Rep. Contract CST-460, Aug. 1969.
- [25] H. Pacejka, *Tire and Vehicle Dynamics*, 3rd ed. Amsterdam, The Netherlands: Elsevier, 2012.
- [26] W. Liu, H. He, and F. Sun, "Vehicle state estimation based on minimum model error criterion combining with extended Kalman filter," *J. Franklin Inst.*, vol. 353, no. 4, pp. 834–856, Mar. 2016.
- [27] M. Doumiati, A. Charara, and A. Victorino, *Vehicle Dynamics Estimation Using Kalman Filtering: Experimental Validation*, 1st ed. London, U.K.: ISTE Ltd., 2012.
- [28] T. H. Tsang, D. M. Himmelblau, and T. F. Edgar, "Optimal control via collocation and non-linear programming," *Int. J. Control.*, vol. 21, no. 5, pp. 763–768, May 1975.
- [29] O. Wallmark, M. Nybacka, D. Malmquist, M. Burman, P. Wennhage, and P. Georen, "Design and implementation of an experimental research and concept demonstration vehicle," in *Proc. IEEE Veh. Power Propulsion Conf.*, 2014, pp. 1–6.
- [30] D. Systèmes, "Dymola 2017," 2016. [Online]. Available: <https://www.3ds.com/products-services/catia/products/dymola>
- [31] M. Simulation, "CarSim," 2016. [Online]. Available: <https://www.carsim.com/>
- [32] *Passenger Cars – Test Track for a Severe Lane-Change Manoeuvre – Part 1: Double Lane-Change*, ISO Std. 3888-1:1999.
- [33] J. B. Rawlings, D. Q. Mayne, and M. M. Diehl, *Model Predictive Control: Theory, Computation, and Design*, 2nd ed. Madison, WI, USA: Nob Hill Publishing, 2017.

- [34] M. J. Risbeck and J. B. Rawlings, "MPCTools: Nonlinear model predictive control tools for CasADI (Python interface)," 2015. [Online]. Available: <https://bitbucket.org/rawlings-group/mpc-tools-casadi>
- [35] J. A. E. Andersson, J. Gillis, G. Horn, J. B. Rawlings, and M. Diehl, "CasADI – A software framework for nonlinear optimization and optimal control," *Math. Program. Comput.*, vol. 11, no. 1, pp. 1–36, Jul. 2019.
- [36] A. Wächter and L. T. Biegler, "On the implementation of an interior-point filter line-search algorithm for large-scale nonlinear programming," *Math. Program.*, vol. 106, no. 1, pp. 25–57, Apr. 2005.
- [37] HSL. "A collection of Fortran codes for large scale scientific computation," 2014. [Online]. Available: <http://www.hsl.rl.ac.uk/>
- [38] D. Systèmes, "FMPy," 2018. [Online]. Available: <https://github.com/CATIA-Systems/FMPy>
- [39] R. Serban and A. C. Hindmarsh, "CVODES: The sensitivity-enabled ODE solver in SUNDIALS," in *Proc. 5th Int. Conf. Multibody Syst., Nonlinear Dyn. Control, Parts A, B, C*, 2005, pp. 257–269.



Lars Drugge received the M.Sc. degree in mechanical engineering and the Ph.D. degree in computer aided design from the Luleå University of Technology, Luleå, Sweden, in 1994 and 2000, respectively. He is currently an Associate Professor of vehicle dynamics with the Department of Engineering Mechanics, School of Engineering Sciences, KTH Royal Institute of Technology, Stockholm, Sweden. He is currently the Head of the Vehicle Dynamics, Rail Vehicles, Aerodynamics and Conceptual Vehicle Design group with KTH and is the coauthor of more than 70 scientific publications in international journals and conference proceedings. His current areas of research include vehicle dynamics of over-actuated vehicles, fault-tolerant control, driver vehicle interaction and driving simulators.

scientific publications in international journals and conference proceedings. His current areas of research include vehicle dynamics of over-actuated vehicles, fault-tolerant control, driver vehicle interaction and driving simulators.



Wenliang Zhang is currently working toward the Ph.D. degrees with the Department of Engineering Mechanics, KTH Royal Institute of Technology, Stockholm, Sweden and also with the School of Mechanical Engineering, Beijing Institute of Technology, Beijing, China. His research interests include state estimation and dynamics control of electric vehicles.



Mikael Nybacka received the Mechanical Engineering and Ph.D. degrees from Luleå University of Technology, Luleå, Sweden, in 2005 and 2009, respectively. He currently works with KTH Royal Institute of Technology as an Associate Professor of vehicle dynamics engaged in research and education in vehicle dynamics and applied vehicle dynamics control. He is also responsible for the Research Concept Vehicles with Integrated Transport Research Lab, KTH. His research interests focus are vehicle validation and driver vehicle interaction but also urban vehicle concepts, autonomous vehicles, fault-tolerant control and over-actuated vehicles. He has authored or coauthored 31 scientific publications.



Zhenpo Wang (Member, IEEE) received the Ph.D. degree in automotive engineering from the Beijing Institute of Technology, Beijing, China, in 2005.

He is currently a Professor with the Beijing Institute of Technology, and the Director of the National Engineering Laboratory for Electric Vehicles. His current research interests include pure electric vehicle integration, packaging and energy management of battery system, and analytics of EV big data.

He has been the recipient of numerous awards, including the second National Prize for Progress in Science and Technology, the first Prize for Progress in Science and Technology from the Ministry of Education and the second Prize for Progress in Science and Technology from Beijing Municipal, China. He has published four monographs and translated books as well as more than 80 technical papers. He also holds more than 60 patents.

Paper D

“Exploring model complexity for trajectory planning of autonomous vehicles in critical driving scenarios”,

Wenliang Zhang, Lars Drugge, Mikael Nybacka, Jenny Jerrelind, Zhenpo Wang and Junjun Zhu,

Advances in Dynamics of Vehicles on Roads and Tracks (IAVSD 2021), 2021.

Paper D

Exploring model complexity for trajectory planning of autonomous vehicles in critical driving scenarios

Wenliang Zhang^{1,2}, Lars Drugge¹, Mikael Nybacka¹, Jenny Jerrelind¹, Zhenpo Wang², and Junjun Zhu³

¹ Department of Engineering Mechanics, School of Engineering Sciences, KTH Royal Institute of Technology, SE-100 44 Stockholm, Sweden,
wez@kth.se

² School of Mechanical Engineering, Beijing Institute of Technology, Beijing 100081, China

³ State Key Laboratory of Automotive Safety and Energy, Tsinghua University,
Beijing 100084, China

Abstract. Trajectory planning is a crucial component of autonomous driving systems. However, using simple vehicle models for trajectory planning may result in unrealistic reference trajectories, especially in critical driving conditions, endangering the safe driving of autonomous vehicles. This study explores the effect of model complexity on the trajectory planning performance of autonomous vehicles in critical driving scenarios. Five trajectory planners of various levels of model complexity, including Planner STK (single-track kinematic model), Planner STDL (single-track dynamic vehicle model with a linear tyre model), Planner STD (single-track dynamic vehicle model with a simplified Pacejka tyre model), Planner DTB (double-track vehicle model with the brush tyre model), and Planner DTMlt (double-track vehicle model with load transfer consideration and the Pacejka tyre model), are designed. The trajectory planners are formulated as optimal control problems, where constraints for obstacle avoidance, yaw stability and the physical limits on vehicle actuators are explicitly considered. These planners are assessed in two severe driving manoeuvres, i.e. the double-lane change and single-lane change manoeuvres. Results indicate that Planner DTMlt outperforms DTB with higher passing velocity as well as smaller peak yaw rate and sideslip angle, and that Planners STD, STDL and STK are not suitable for use in these critical driving scenarios.

Keywords: model complexity, trajectory planning, autonomous vehicle, critical driving

1 Introduction

Autonomous driving has been gaining increasing attention in recent years, due to its potential in improving mobility and safety in the transport sector. With the operation of autonomous vehicles (AVs) and the development of vehicle components and control systems, the driving environment is becoming increasingly complicated and the possibility of vehicle component/sub-system failure is growing. This makes it especially significant to generate safe reference trajectories for the AVs operating in critical conditions, e.g. in an obstacle-avoidance or safe-stop manoeuvre.

Previous motion planning studies are mostly based on simple vehicle models. For example, the motion planning approach presented in [1] adopted a point-mass model. With more modelling details included, Lima [2] used a kinematic vehicle model in his motion planning algorithm. By incorporating linear lateral tyre forces into the problem formulation, dynamic

single-track vehicle models have been used for the motion planning studies presented in [3] and [4]. Although preceding motion planning studies have shown promising results in the studied cases by utilising the above-mentioned vehicle models, the planners' performance tends to degrade in highly dynamic conditions, due to the inadequate vehicle dynamics consideration.

When an AV drives in safety-critical driving scenarios, e.g. in an obstacle-avoidance manoeuvre at high speed or in low-friction condition, the longitudinal and lateral tyre forces are usually coupled, and the tyres tend to saturate. In such driving conditions, using the simple vehicle models as described above may yield unrealistic vehicle trajectories. Specifically, the planned vehicle sideslip angle and yaw rate might be either over- or under-estimated, as those simple models cannot represent well the true vehicle characteristics. This may lead to worsened control performance, and thus jeopardise vehicle safety. Moreover, yaw stability, which is especially important when planning trajectories in emergency conditions, is usually not considered directly in the previous motion planning studies, which may again compromise vehicle safety.

This study aims to evaluate the effect of model complexity on the trajectory planning performance of AVs in critical driving scenarios. Trajectory planners with vehicle and tyre models of various levels of complexity are designed and evaluated. Specifically, single-track, double-track, dynamic and kinematic vehicle models are assessed. Moreover, various tyre models are adopted in the planner design, e.g. a linear tyre model, the brush tyre model [5], and the Pacejka tyre model [6].

2 Vehicle dynamics modelling

Five sets of models are designed to represent the dynamics of the corresponding trajectory planners, including Planner STK (single-track kinematic model), Planner STDL (single-track dynamic vehicle model with a linear tyre model), Planner STD (single-track dynamic vehicle model with a simplified Pacejka tyre model), Planner DTB (double-track vehicle model with the brush tyre model), and Planner DTMlt (double-track vehicle model with load transfer consideration and the Pacejka tyre model).

2.1 Planner STK

With the additional air drag force consideration, Planner STK is modelled with the adapted kinematic equations from [7]:

$$m\dot{v} = F_{xy} - C_d A_f \frac{D_a v_x^2}{2} \quad (1)$$

$$\dot{\psi} = \frac{v \cos \beta}{l_f + l_r} \tan \delta_f \quad (2)$$

$$\dot{X} = v \cos(\psi + \beta) \quad (3)$$

$$\dot{Y} = v \sin(\psi + \beta), \quad (4)$$

where $v = \sqrt{v_x^2 + v_y^2}$ denotes the combined vehicle velocity at the centre of gravity (CoG), in which v_x and v_y are the longitudinal and lateral velocities at CoG, respectively. ψ is the yaw angle, X the longitudinal position, Y the lateral position, β the sideslip angle, δ_f the front steering angle at the wheel, and F_{xy} the combined actuator force. m represents the vehicle mass, and l_f and l_r the distance from CoG to the front and rear axles, respectively. C_d , A_f and D_a denote the drag coefficient, frontal area and air density, respectively.

2.2 Planners STDL and STD

Planner STDL is modelled with the following single-track vehicle model equations:

$$mv_x = F_{xf} \cos \delta_f + F_{xr} - F_{yf} \sin \delta_f + mv_y \omega_z - C_d A_f \frac{D_a v_x^2}{2} \quad (5)$$

$$mv_y = F_{xf} \sin \delta_f + F_{yf} \cos \delta_f + F_{yr} - mv_x \omega_z \quad (6)$$

$$I_z \dot{\omega}_z = l_f (F_{xf} \sin \delta_f + F_{yf} \cos \delta_f) - l_r F_{yr} \quad (7)$$

$$\dot{\psi} = \omega_z \quad (8)$$

$$\dot{X} = v_x \cos \psi - v_y \sin \psi \quad (9)$$

$$\dot{Y} = v_x \sin \psi + v_y \cos \psi, \quad (10)$$

where ω_z denotes the vehicle yaw rate; F_{xf}/F_{yf} and F_{xr}/F_{yr} the longitudinal/lateral force in the front and rear axles, respectively; and I_z is the vehicle yaw inertia.

In addition, a linear tyre model is used when modelling Planner STDL:

$$F_{yi} = C_{\alpha i} \alpha_i, \quad (11)$$

where $i \in \{f, r\}$ denotes the front/rear axle; $C_{\alpha i}$ the axle cornering stiffness; and α_i the tyre slip angle.

Planner STD is modelled in the same way as STDL, with the exception that the front and rear lateral tyre forces are modelled with [8, Eqs. (12)–(17)], where the lateral force saturation is considered.

2.3 Planners DTB and DTMlt

A planar double-track vehicle model and the brush tyre model are used to describe the dynamics for Planner DTB. Specifically, the longitudinal, lateral and yaw movement of the vehicle, and the rotational dynamics of the front and rear wheels are denoted with [9, Eqs. (1)–(10)], with the exception that the left and rear side of the front/rear wheels utilises the same amount of torque, i.e. $T_{fl} = T_{fr}$ and $T_{rl} = T_{rr}$. Moreover, the combined-slip longitudinal and lateral tyre forces are modelled with the brush tyre model as detailed in [9, Eq. (11)].

Planner DTMlt is modelled in the same manner as DTB, except that the brush tyre model is replaced with the Pacejka tyre equations [6, Eqs. (4.E1)–(4.E67)]. Specifically, the Pacejka tyre parameters and related modelling details are described in Section II-E of [9], and the vertical tyre forces with load transfer consideration are calculated with [9, Eq. (14)].

2.4 Model summary

Given the vehicle dynamics modelling described in Sections 2.1–2.3, the system state and input vectors for Planners STK, STDL/STD and DTB/DTMlt are respectively defined by Eqs. (12), (13) and (14) as follows:

$$x = [v \ \psi \ X \ Y]^T \quad (12a)$$

$$u = [\delta_f \ F_{xy}]^T, \quad (12b)$$

$$x = [v_x \ v_y \ \omega_z \ \psi \ X \ Y]^T \quad (13a)$$

$$u = [\delta_f \ F_{xf} \ F_{xr}]^T, \quad (13b)$$

$$x = [v_x \ v_y \ \omega_z \ \psi \ X \ Y \ \omega_{fl} \ \omega_{fr} \ \omega_{rl} \ \omega_{rr}]^T \quad (14a)$$

$$u = [\delta_f \ T_{fl} \ T_{rl}]^T. \quad (14b)$$

With the notation above and the same collocation technique as described in [9], the models for the five trajectory planners are represented in the following state-space form:

$$x_{k+1} = f(x_k, u_k). \quad (15)$$

3 Planner design

Due to its capability of explicitly including constraints in the problem formulation, the trajectory planning of the AV is formulated as an optimal control problem (OCP). Within the OCP formulation, constraints for handling obstacle, yaw stability and vehicle actuator capability are considered. The trajectory planners designed in the present study aim to generate reference trajectories that let the vehicle pass the test scenarios without causing instability or hitting any obstacle.

Inspired by [10], the OCP problem for the present trajectory planners in the double-lane change (DLC) manoeuvre for obstacle avoidance [11] is given as follows:

$$\min_{v_{x_0}, v_{x_f}} -0.05v_{x_0} - 0.05v_{x_f} \quad (16a)$$

$$\text{s. t. } x_{i+1} = f(x_i, u_i), i \in \{0, 1, \dots, N_t - 1\} \quad (16b)$$

$$g(x_i) \leq 0 \quad (16c)$$

$$x_0 = \tilde{x}_0 \quad x_f = \tilde{x}_f \quad (16d)$$

$$u_0 = \tilde{u}_0 \quad (16e)$$

$$u_{\min} \leq u_i \leq u_{\max} \quad (16f)$$

$$\Delta u_{\min} \leq \Delta u_i \leq \Delta u_{\max} \quad (16g)$$

where v_{x_0} and v_{x_f} are the initial and terminal longitudinal velocities, respectively, in which the subscripts 0 and f denote the initial and terminal time step within the horizon length, N_t , respectively. Eq. (16d) represents the initial and terminal constraints on the state variables. Specifically, in the DLC manoeuvre, the initial state variables are constrained as $[v_{y_0} \omega_{z_0} \psi_0 X_0 Y_0]^T = [0 \ 0 \ 0 \ 0 \ 0]^T$, and the final state variables as $X_f = 61$, where applicable, in which 61 is the track length. Eq. (16e) denotes the initial constraint, with all values being zero, on the control variables. Eqs. (16f) and (16g) are the constraints on the control variables and their variation, respectively.

Eq. (16c) denotes the limit on the state variables, including the yaw stability constraints. Specifically, the boundary $\pm \arctan(0.02\mu g)$ rad is applied to the sideslip angle, as suggested in [7]. Moreover, a yaw rate constraint considering the transient behaviour of the vehicle via the inclusion of a β term, i.e. [9, Eqs. (24) and (25)], is applied. It should be noted that, for Planner STK, the yaw rate constraint without the β term is used, as Planner STK generates the sideslip angle of opposite sign compared with other planners, which is discussed in detail in Section 4.1.

Similar to the case in the DLC manoeuvre, a second planner formulation with the cost function designed for a single-lane change (SLC) manoeuvre is given as follows:

$$\min_{v_{x_f, T}} -0.1v_{x_f} + T. \quad (17)$$

The SLC manoeuvre can be seen as the left half of the aforementioned DLC manoeuvre, with an extended end section and the total length being 40 m.

As can be seen from Eq. (16a), in the DLC manoeuvre, it is desired that both the entry and exit velocities are maximised. On the other hand, in the SLC manoeuvre, the exit velocity is maximised and the time to complete the manoeuvre is minimised, with the entry velocity being fixed, as described by Eq. (17).

Note that the coefficient -0.05 in Eq. (16a) is mainly applied to ensure that the value of the corresponding cost function is in the magnitude of 1. This way, it would be easier for the solver to find the solution to the resulted optimisation problem. For the same purpose, the coefficients -0.1 and 1 are applied to v_{x_f} and T , respectively, in Eq. (17).

The trajectory planners are implemented by using `rockit` [12], which is a toolkit for implementing OCPs and is built based on the opti functionality of `CasADi` [13]. The resulting optimisation problems from the planners are solved with the optimisation package `IPOPT` [14] and the solvers `MA27` [15] and `MUMPS` [16].

4 Results and discussion

This section presents an evaluation of the five trajectory planners, including Planners STK, STDL, STD, DTB and DTMlt. These planners are assessed with the following procedure:

1. Reference trajectories are generated from each planner in the same test manoeuvre, during which yaw stability should be maintained and any obstacle should be avoided.
2. The same MPC controller, i.e. the one-level controller with torque vectoring (OLTV) from [9], is used to track the generated reference trajectories from each planner, where the same vehicle plant from [9] is used in the present study for the trajectory tracking evaluation.
3. The trajectory generation and tracking performance corresponding to each planner is analysed and evaluated.

4.1 DLC manoeuvre

Fig. 1 presents the obtained vehicle trajectories from the five planners in the DLC manoeuvre. As can be seen from Fig. 1(d), all the five planners are able to successfully plan trajectories through the DLC manoeuvre without hitting any cone, considering the trajectories of the four corners of the vehicle (not plotted for clear comparison of planners). On the other hand, the five planners generate significantly different sideslip angle and obviously different yaw rate, path and velocity profiles, especially when the vehicle exits the middle section of the DLC track. Moreover, the vehicle yaw stability is ensured for the planners, due to the inclusion of yaw stability constraints in the planner formulation.

With the generated trajectories from Planners DTMlt and DTB, the vehicle is able to successfully pass the DLC manoeuvre with the help of Controller OLTV, as can be seen in Fig. 2. Specifically, with the trajectories from Planner DTMlt, the vehicle is able to pass the DLC manoeuvre with smaller peak sideslip angle and yaw rate while with higher velocity in general, compared with the trajectories from Planner DTB. This, in fact, is consistent with the trajectory planning results, as can be seen from Fig. 1(a) and (b).

In contrast, the vehicle fails to pass the DLC manoeuvre by tracking the trajectories from Planners STD, STDL and STK, which is contrary to the trajectory planning results as indicated in Fig. 1(e). (For this reason, the trajectory tracking results corresponding to these planners are not shown in Fig. 2.) The failed trajectory tracking of these planners can be explained by the fact that the simplification of vehicle dynamics details yields unrealistic

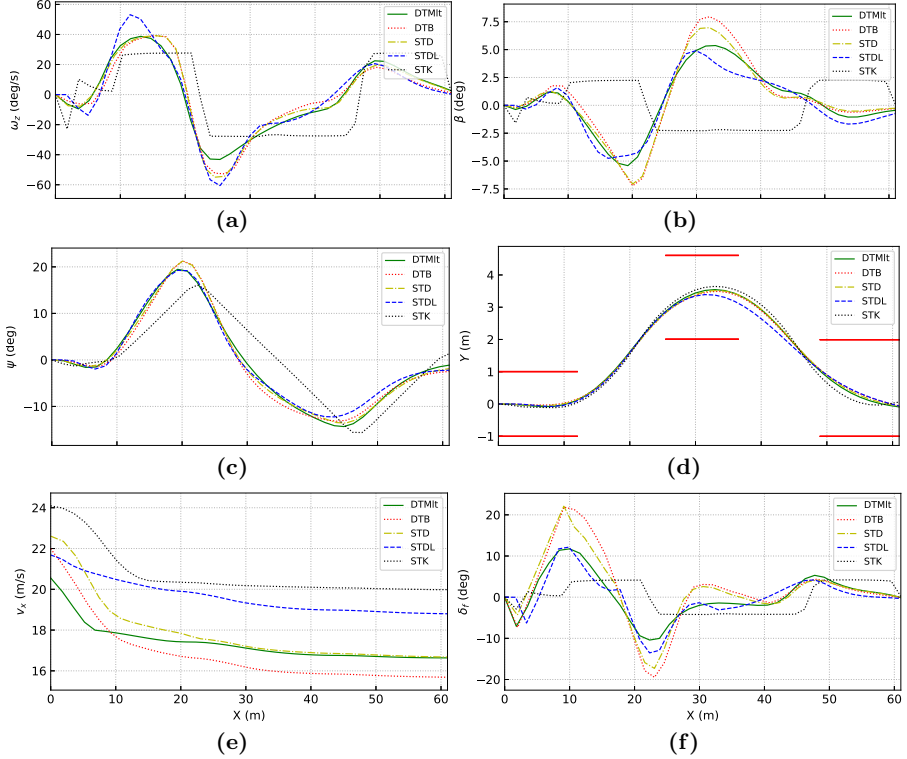


Fig. 1 Comparison of trajectory planning of planners with various levels of model complexity in the DLC manoeuvre. (a)–(f) show the planned yaw rate (ω_z), sideslip angle (β), yaw angle (ψ), lateral position (Y), longitudinal velocity (v_x) and steering angle (δ_f), respectively. In (d), the solid red lines denote the cones for the DLC track.

reference trajectories, e.g. the too high passing velocity and/or too large sideslip angle, which makes the successful trajectory tracking impossible to achieve.

One fact worth noting is that Planner STK generally yields the sideslip angle profile of opposite sign to other planners, as shown in Fig. 1(b). This is because, with the formulation from [7], the resulted sideslip angle from Planner STK will have the same sign as the resulted steering angle, which is obviously different from other planners with dynamic models. This can be easily seen after comparing Fig. 1(b) and 1(f). For this reason, the sideslip angle from Planner STK is replaced by calculating it with a single-track model when evaluating its trajectory tracking performance.

4.2 SLC manoeuvre

Table 1 and Figs. 3 and 4 show the trajectory planning and tracking results of the five planners in the SLC manoeuvre.

As shown in Table 1, Planner DTMlt yields the highest passing velocity during trajectory tracking while Planner STK the lowest. On the other hand, Planner STDL yields the highest

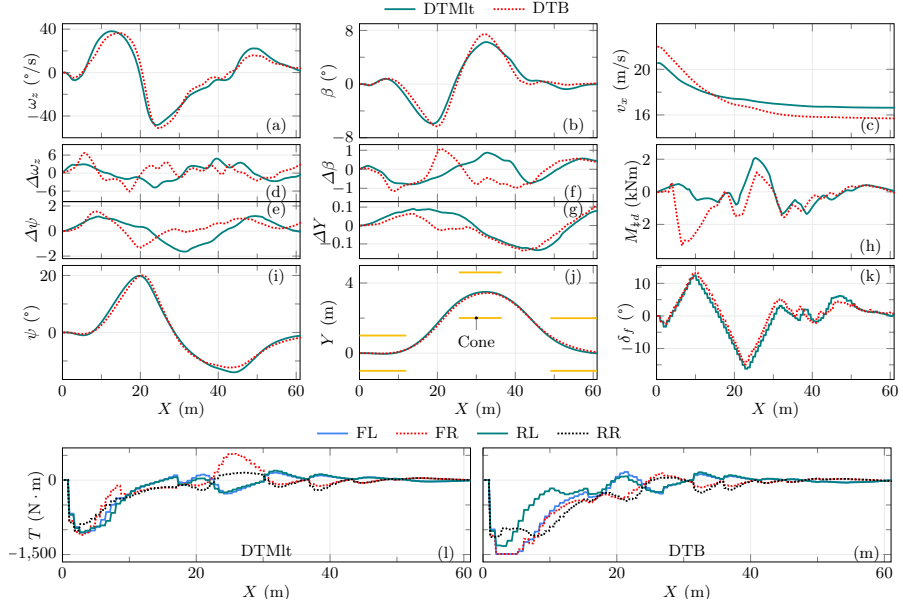


Fig. 2 Comparison of trajectory tracking of planners with various levels of model complexity in the DLC manoeuvre. (d)–(g) give the trajectory tracking errors corresponding to the yaw rate (ω_z), yaw angle (ψ), sideslip angle (β), and lateral position (Y), respectively. (l) and (m) display the commanded drive/braking torques at the wheel. In (h), M_{zd} denotes the required yaw moment for the yaw movement of the vehicle. In (j), “Cone” denotes the cones for the DLC track.

Table 1 Maximum passing (initial) velocity during trajectory planning and tracking of planners with various levels of model complexity in the SLC manoeuvre (km/h)

Planner	DTMlt	DTB	STD	STDL	STK
Planning	79	74	79	86	82
Tracking	76	74	74	67	65

passing velocity during trajectory planning but the second lowest passing velocity during trajectory tracking. Moreover, the maximum passing velocity corresponding to trajectory planning is in general lower than that corresponding to trajectory tracking. More specifically, the maximum passing velocity difference between trajectory tracking and planning is -3, 0, -5, -19, and -17 km/h for Planners DTMlt, DTB, STD, STDL and STK, respectively. This indicates that planners with more simplified models tend to over-estimate the passing velocity during trajectory planning, especially the planners with a single-track vehicle model and simple tyre models.

As indicated by Fig. 3, all the planners are able to successfully generate trajectories through the SLC manoeuvre. On the other hand, Fig. 4 presents the comparison of the trajectory tracking performance corresponding to the five planners. As can be seen, with the trajectories from Planner DTMlt, the vehicle is able to pass the SLC manoeuvre with intermediate magnitude of tracking errors and overall passing velocity, compared with other planners. Moreover, Planner DTMlt results in smaller peak yaw rate and sideslip angle than

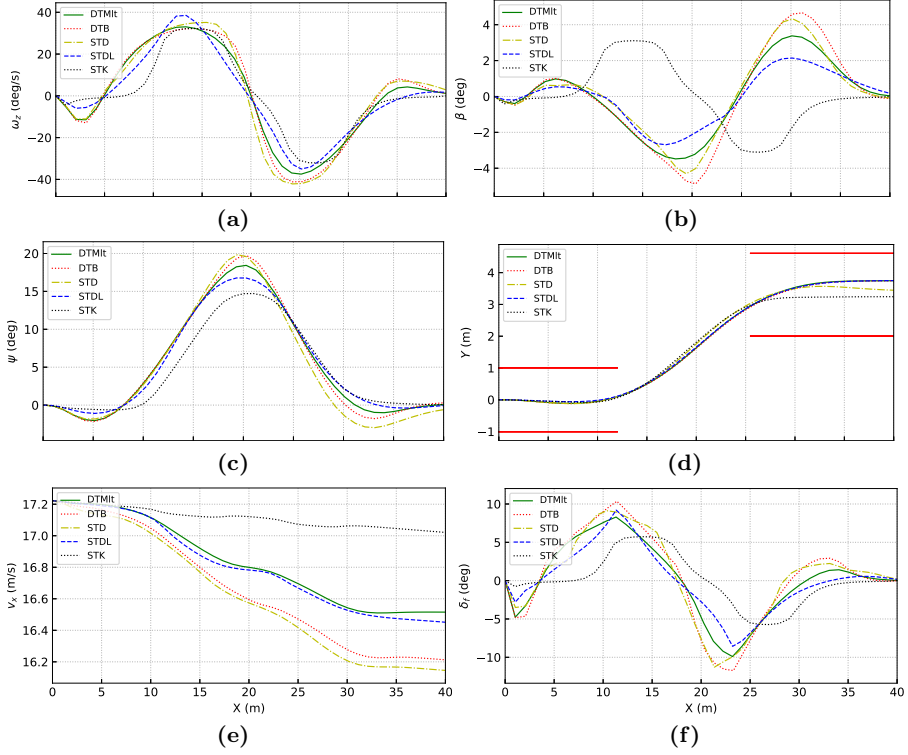


Fig. 3 Comparison of trajectory planning of planners with various levels of model complexity in the SLC manoeuvre with the initial velocity being 62 km/h. In (d), the solid red lines denote the cones for the SLC track.

DTB during both trajectory planning and tracking, which is similar to the observation in the DLC manoeuvre. Furthermore, Planner DTMIlt generally yields the smallest motor torque usage among all the planners.

5 Conclusions

This paper has presented five planners of different levels of model complexity, i.e. Planners STK, STDL, STD, DTB and DTMIlt, for trajectory planning in critical driving scenarios. The planners were formulated as OCPs with both safety- and actuator-related constraints explicitly considered and were evaluated in two severe driving manoeuvres. The main findings concerning the five trajectory planners are summarized as follows. Firstly, the vehicle was able to successfully pass the DLC manoeuvre by tracking the reference trajectories from Planners DTMIlt and DTB. In contrast, the vehicle failed to pass the DLC manoeuvre with the trajectories from Planners STD, STDL and STK, although the trajectory planning results indicated otherwise. Secondly, Planners DTMIlt and DTB resulted in consistently high passing velocity during both trajectory planning and tracking in the SLC manoeuvre. On the other hand, the passing velocities during trajectory tracking in the SLC manoeuvre

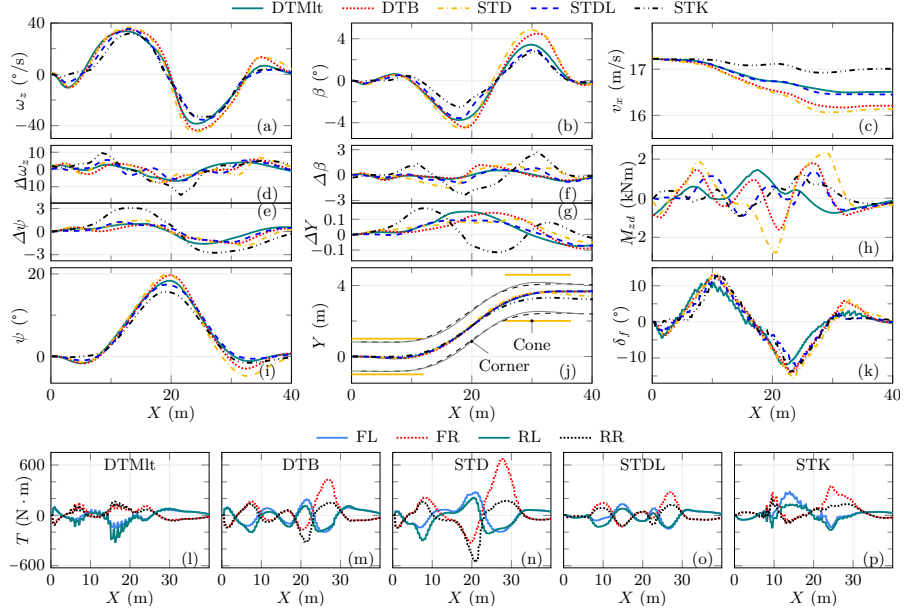


Fig. 4 Comparison of trajectory tracking of planners with various levels of model complexity in the SLC manoeuvre with the initial velocity being 62 km/h. In (j), “Corner” denotes the vehicle boundaries corresponding to Planner STK, and “Cone” the cones for the SLC track.

were over-estimated by 5, 19, and 17 km/h, respectively, for Planners STD, STDL and STK, compared with that during trajectory tracking. Thirdly, in both the DLC and SLC manoeuvres, Planner DTMlt yielded smaller peak yaw rate and sideslip angle than DTB during both trajectory planning and tracking. Finally, the poor performance indicated that the three single-track planners, i.e. Planners STD, STDL and STK, were not suitable for trajectory planning in the severe DLC and SLC manoeuvres. The trajectory planners will be further evaluated in different critical driving scenarios.

Acknowledgment

The authors would like to gratefully acknowledge the financial support from TRENOP (Transport Research Environment with Novel Perspectives) at KTH Royal Institute of Technology.

References

1. Delsart, V., Fraichard, T., Martinez, L.: Real-time trajectory generation for car-like vehicles navigating dynamic environments. In: 2009 IEEE International Conference on Robotics and Automation. IEEE (2009)
2. Lima, P.F.: Optimization-based motion planning and model predictive control for autonomous driving : With experimental evaluation on a heavy-duty construction truck. Ph.D. thesis, KTH, Automatic Control, Stockholm, Sweden (2018)

3. Rosolia, U., Bruyne, S.D., Alleyne, A.G.: Autonomous vehicle control: A nonconvex approach for obstacle avoidance. *IEEE Transactions on Control Systems Technology* **25**(2), 469–484 (2017)
4. Rasekhipour, Y., Khajepour, A., Chen, S.K., Litkouhi, B.: A potential field-based model predictive path-planning controller for autonomous road vehicles. *IEEE Transactions on Intelligent Transportation Systems* **18**(5), 1255–1267 (2017)
5. Dugoff, H., Fancher, P.S., Segel, L.: Tire performance characteristics affecting vehicle response to steering and braking control inputs. *Tech. Rep. Contract CST-460*, Washington, DC (1969)
6. Pacejka, H.: *Tire and Vehicle Dynamics*, third edn. Elsevier, Oxford, UK (2012)
7. Rajamani, R.: *Vehicle Dynamics and Control*, second edn. Springer, New York, NY, USA (2012)
8. Mårtensson, J., Nybacka, M., Jerrelind, J., Drugge, L.: Evaluation of safety distance in vehicle platoons by combined braking and steering. In: *Proceedings of 11th International Symposium on Advanced Vehicle Control*, Sept 9-12, 2012, Seoul, Korea .: Japan Society of Mechanical Engineers (JSAE) (2012)
9. Zhang, W., Wang, Z., Drugge, L., Nybacka, M.: Evaluating model predictive path following and yaw stability controllers for over-actuated autonomous electric vehicles. *IEEE Transactions on Vehicular Technology* **69**(11), 12,807–12,821 (2020)
10. Fors, V., Olofsson, B., Nielsen, L.: Formulation and interpretation of optimal braking and steering patterns towards autonomous safety-critical manoeuvres. *Vehicle System Dynamics* **57**(8), 1206–1223 (2018)
11. ISO: Road vehicles - passenger cars - test track for a severe lane-change manoeuvre - part 2: Obstacle avoidance. ISO Std. 3888-1:1999 (2011)
12. Gillis, J.: rockit (2020). URL <https://gitlab.kuleuven.be/meco-software/rockit>
13. Andersson, J.A.E., Gillis, J., Horn, G., Rawlings, J.B., Diehl, M.: CasADi – A software framework for nonlinear optimization and optimal control. *Mathematical Programming Computation* **11**(1), 1–36 (2019)
14. Wächter, A., Biegler, L.T.: On the implementation of an interior-point filter line-search algorithm for large-scale nonlinear programming. *Math. Program.* **106**(1), 25–57 (2005)
15. HSL: A collection of Fortran codes for large scale scientific computation (2014). URL <http://www.hsl.rl.ac.uk/>
16. Amestoy, P.R., Duff, I.S., L'Excellent, J.Y., Koster, J.: A fully asynchronous multifrontal solver using distributed dynamic scheduling. *SIAM J. Matrix Anal. & Appl.* **23**(1), 15–41 (2001)

Paper E

“Integrated control of motion actuators for enhancing path following and yaw stability of autonomous electric vehicles”,

Wenliang Zhang, Lars Drugge, Mikael Nybacka, Jenny Jerrelind and Zhenpo Wang,

Submitted for publication, 2022.

Paper E

Integrated Control of Motion Actuators for Enhancing Path Following and Yaw Stability of Autonomous Electric Vehicles

Wenliang Zhang, Lars Drugge, Mikael Nybacka, Jenny Jerrelind, and Zhenpo Wang, *Member, IEEE*

Abstract—Advanced active safety systems play a crucial role in the safe driving of vehicles in safety-critical conditions like an obstacle-avoidance manoeuvre. However, conventional systems that mainly rely on braking intervention may not result in the desired vehicle response in such conditions. Over-actuation through controlling individual motion actuators, on the other hand, can potentially improve the safety performance of the vehicles. This study evaluates various combinations of motion actuators for path following and yaw stability control in critical driving scenarios, including active front steering (AFS), AFS plus torque vectoring (TV), AFS plus active camber (AC), as well as AFS plus TV and AC. The evaluation is based on a model predictive control formulation, where constraints related to yaw stability and actuator physical limits are considered. In this problem formulation, a double-track vehicle model, combined with the Dugoff tyre model and its variant with camber effect, is used to model the vehicle dynamics. These motion actuator configurations are assessed in terms of passing velocity, tracking accuracy, safety distance, as well as robustness to reference trajectory variation. Results show that the integrated control of AFS plus TV and AC performs the best among all the four configurations while AFS the worst and that AFS plus AC is generally superior to AFS plus TV.

Index Terms—Integrated control, yaw stability, over-actuation, model predictive control, autonomous vehicles.

NOMENCLATURE AND NOTATION

General Symbols

\mathcal{A}	A set in which the elements denote the front left, front right, rear left and rear right wheels, respectively, $= \{fl, fr, rl, rr\}$.
\mathcal{B}	A set in which the elements denote the front and rear (left/right) wheels, respectively, $= \{f, r\}$.
XOY	Earth frame; for global positioning system.
x_{b0yb}	Vehicle body frame; for inertial measurement unit.
xyo	Vehicle frame; for describing vehicle motion.

The authors would like to gratefully acknowledge the financial support from TRENOP (Transport Research Environment with Novel Perspectives) at KTH Royal Institute of Technology.

Wenliang Zhang, Lars Drugge, Mikael Nybacka and Jenny Jerrelind are with Vehicle Dynamics, Department of Engineering Mechanics, KTH Royal Institute of Technology, SE-10044 Stockholm, Sweden. Wenliang Zhang is also with the National Engineering Laboratory for Electric Vehicles and the Collaborative Innovation Centre for Electric Vehicles in Beijing, Beijing Institute of Technology, Beijing 100081, China.

Zhenpo Wang is with the National Engineering Laboratory for Electric Vehicles and the Collaborative Innovation Centre for Electric Vehicles in Beijing, Beijing Institute of Technology, Beijing 100081, China.

$f(\cdot), h(\cdot)$	Discrete-time state, output equation.
<i>Model Variables</i>	
x, u, y	State, input, output vector.
v_x, v_y	Longitudinal, lateral velocity at centre of gravity (CoG) in frame xoy (m/s).
ω_z	Yaw rate around CoG in frame xoy (rad/s).
ψ	Yaw angle in frame XOY (rad).
X, Y	Longitudinal, lateral position in frame XOY (m).
ω_i	Angular velocity of the wheel (rad/s) ($i \in \mathcal{A}$).
ω	Angular velocity of one wheel (rad/s).
β	Sideslip angle (rad).
a_x, a_y	Longitudinal, lateral acceleration in frame x_{b0yb} (m/s ²).
α_i	Tyre slip angle (rad) ($i \in \mathcal{A}$).
κ_i	Tyre slip ratio ($i \in \mathcal{A}$).
δ_f	Steering angle, mean of two front wheels in frame xoy (rad).
γ_f, γ_r	Front, rear camber angle in frame xoy (rad).
T_i	Drive/braking torque on the wheel (N·m) ($i \in \mathcal{A}$).
T	Drive/braking torque on one wheel (N·m).
F_{xi}, F_{yi}	Longitudinal, lateral tyre force (N) ($i \in \mathcal{A}$).
F_x	Longitudinal tyre force at one wheel (N).
F_{zi}	Vertical tyre force (N) ($i \in \mathcal{A}$).
<i>Model Parameters</i>	
$C_{\alpha i}$	Tyre cornering stiffness (N/rad) ($i \in \mathcal{A}$).
$C_{\kappa i}$	Tyre longitudinal stiffness (N) ($i \in \mathcal{A}$).
$C_{\gamma j}$	Tyre camber stiffness (N/rad) ($i \in \mathcal{B}$).
$C_{\gamma 0j}$	Tyre camber stiffness when with zero slip angle (N/rad) ($j \in \mathcal{B}$).
$C_{\gamma f j}$	Tyre camber stiffness when slip angle reaches α_{lim} (N/rad) ($j \in \mathcal{B}$).
α_{lim}	Variation in camber stiffness with respect to slip angle (N/rad ²) ($j \in \mathcal{B}$).
I_{wi}	Limiting value (depending on tyre property) for determining tyre camber stiffness (rad).
I_w	Wheel rotational inertia (kg·m ²) ($i \in \mathcal{A}$).
r_e	Rotational inertia of one wheel (kg·m ²).
m	Tyre effective rolling radius (m).
	Vehicle mass (kg).

I_z	Vehicle yaw inertia ($\text{kg} \cdot \text{m}^2$).
B_f, B_r	Front, rear track width (m).
l_f, l_r	Distance from CoG to front, rear axle (m).
h_g	Height of CoG (m).
μ	Road friction coefficient.
g	Gravitational acceleration (m/s^2).

Controller Variables

x	Sequence of state vectors.
$u, \Delta u, s$	Sequence of vectors for control actions, change of control actions, slack variables.

Controller Parameters

N	Prediction horizon.
Q_y, Q_{yf}	Weight matrix for penalising stage, terminal output tracking.
R_u, R_{du}	Weight matrix for penalising control and change of control.
Q_s, Q_{sf}	Weight matrix for penalising stage, terminal slack.

I. INTRODUCTION

AUTONOMOUS vehicles (AVs) have been a hot topic in recent years, as they can potentially reduce fatality and improve efficiency in road transport. In the meanwhile, the driving environment is becoming increasingly complicated, as there exist mixed road traffic participants, e.g. road vehicles, e-scooter riders, cyclists and pedestrians. Therefore, to ensure the safe driving of vehicles, it is especially important to develop advanced active safety systems, e.g. those for path following and yaw stability control. Although extensive studies, e.g. [1]–[3], have been carried out for achieving yaw stability, purely utilising active steering and/or braking control for this purpose may not always yield the desired performance in critical driving scenarios, e.g. in an obstacle-avoidance manoeuvre, leading to jeopardised safety in such situations for AVs.

With the introduction of AVs there is a need for by-wire actuation, which has increased the interest in over-actuated vehicle platforms. Here over-actuation refers to vehicles with more actuators than the degrees of freedom (DoFs) to be controlled. For instance, the actuators in a vehicle with individual steering, traction and camber actuation outnumber its DoFs to be controlled, i.e. the longitudinal, lateral and yaw directions of the vehicle. This, compared with conventional vehicles, provides additional DoFs for controlling the vehicle, and thus can potentially improve driving safety in addition to other control objectives.

By generating a supplemental yaw moment through regulating the individual hub/in-wheel motors, torque vectoring has been studied in [4]–[7] to stabilise the vehicle. With the potential of increasing lateral tyre forces [8], camber control has been utilised to improve the trajectory tracking performance [9], increase the cornering margins [10] and enhance the path following and yaw stability performance [11]. When designing such active safety controllers, various types of methods have been adopted, e.g. linear quadratic

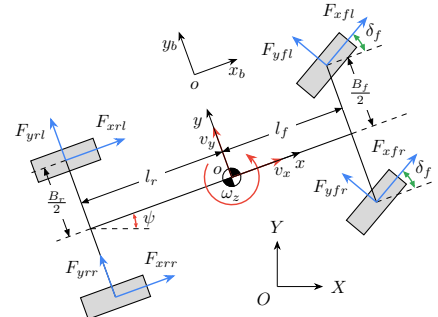


Fig. 1. Double-track planar vehicle model.

regulator (LQR) [12], sliding mode control (SMC) [13] and model predictive control (MPC) [14]–[16].

Although existing studies on exploiting over-actuation for achieving active safety have shown promising results, the following points can be further explored. Firstly, there is a lack in comparison of different combinations of over-actuation for path following and yaw stability control of AVs, especially when it involves active camber. Secondly, previous studies mainly determined the reference yaw rate and sideslip angle by using single-track models, which is a separate process to the path planning, which may compromise the path following and yaw stability performance. Thirdly, the robustness of controller performance to trajectory generation needs to be explored further.

This study aims to address the issues identified above by evaluating the effect of various over-actuation configurations on the path following and yaw stability performance of AVs in critical driving scenarios. Specifically, four motion actuator combinations, i.e. active front steering (AFS), AFS plus torque vectoring (TV), AFS plus active camber (AC), as well as AFS plus TV and AC, are investigated through the corresponding controllers. The controllers are designed in the framework of MPC, where constraints on yaw stability and actuator limits are explicitly considered in the controller formulation. Moreover, the evaluation is carried out based on reference signals obtained through concurrent yaw rate, sideslip angle and path planning. In addition, the robustness of the controllers to reference trajectory variation is studied.

II. VEHICLE DYNAMICS MODELLING

This section describes the modelling of vehicle movement and tyre forces for controllers corresponding to four means of over-actuation, i.e. Controllers S (AFS), ST (AFS and TV), SC (AFS and AC) and STC (AFS, TV and SC). The methods for modelling the vehicle dynamics are detailed in previous studies [7], [11]. For the sake of completeness, this section presents the modelling of a few key components.

A. Vehicle Model

A double-track planar vehicle model (see Fig. 1) is used to model the vehicle dynamics used in all the four controllers.

The model describes the movement of the vehicle in the longitudinal, lateral and yaw directions, and the rotational movement of the four wheels. This model can be represented by the following equations:

$$\begin{aligned} m\dot{v}_x &= -(F_{yfl} + F_{yfr}) \sin \delta_f + (F_{xfl} + F_{xfr}) \cos \delta_f \\ &\quad + F_{xrl} + F_{xrr} + mv_y \omega_z \end{aligned} \quad (1)$$

$$\begin{aligned} m\dot{v}_y &= (F_{yft} + F_{yfr}) \cos \delta_f + F_{yrl} + F_{yrr} \\ &\quad + (F_{xfl} + F_{xfr}) \sin \delta_f - mv_x \omega_z \end{aligned} \quad (2)$$

$$\begin{aligned} I_z \dot{\omega}_z &= l_f(F_{yfl} + F_{yfr}) \cos \delta_f - l_r(F_{yrl} + F_{yrr}) \\ &\quad + \frac{B_f}{2}(F_{yfl} - F_{yfr}) \sin \delta_f + \frac{B_f}{2}(F_{xfr} - F_{xfl}) \cos \delta_f \\ &\quad + \frac{B_r}{2}(F_{xrr} - F_{xrl}) + l_f(F_{xfl} + F_{xfr}) \sin \delta_f \end{aligned} \quad (3)$$

$$\dot{X} = v_x \cos \psi - v_y \sin \psi \quad (4)$$

$$\dot{Y} = v_x \sin \psi + v_y \cos \psi \quad (5)$$

$$\dot{\psi} = \omega_z \quad (6)$$

$$I_{wi} \dot{\omega}_i = T_i - r_e F_{xi} \quad (i \in \mathcal{A}). \quad (7)$$

In order to calculate the longitudinal and lateral tyre forces, the vertical wheel load is determined by considering the load transfer among the four wheels with the steady-state equations from [17]:

$$F_{zfl} = \frac{l_r mg}{2(l_f + l_r)} - \frac{h_g m a_x}{2(l_f + l_r)} - \frac{l_r h_g m a_y}{B_f(l_f + l_r)} \quad (8a)$$

$$F_{zfr} = \frac{l_r mg}{2(l_f + l_r)} - \frac{h_g m a_x}{2(l_f + l_r)} + \frac{l_r h_g m a_y}{B_f(l_f + l_r)} \quad (8b)$$

$$F_{zrl} = \frac{l_f mg}{2(l_f + l_r)} + \frac{h_g m a_x}{2(l_f + l_r)} - \frac{l_f h_g m a_y}{B_r(l_f + l_r)} \quad (8c)$$

$$F_{zrr} = \frac{l_f mg}{2(l_f + l_r)} + \frac{h_g m a_x}{2(l_f + l_r)} + \frac{l_f h_g m a_y}{B_r(l_f + l_r)}. \quad (8d)$$

B. Tyre Model

Required by the vehicle model equations, the Dugoff tyre model [18] is used for calculating the nonlinear, combined-slip longitudinal and lateral tyre forces for Controllers S and ST, with the equations detailed by

$$F_{xi} = C_{\kappa i} \frac{\kappa_i}{1 + \kappa_i} f(\lambda_i) \quad (9a)$$

$$F_{yi} = C_{\alpha i} \frac{\tan \alpha_i}{1 + \kappa_i} f(\lambda_i) \quad (9b)$$

$$\lambda_i = \frac{\mu F_{zi}(1 + \kappa_i)}{2((C_{\kappa i} \kappa_i)^2 + (C_{\alpha i} \tan \alpha_i)^2)^{1/2}} \quad (9c)$$

$$f(\lambda_i) = \begin{cases} (2 - \lambda_i)\lambda_i, & \text{if } \lambda_i < 1 \\ 1, & \text{if } \lambda_i \geq 1 \end{cases}. \quad (9d)$$

To utilise camber actuators for path following and yaw stability control, Controllers SC and STC consider the camber effect in tyre modelling. Therefore, besides the Dugoff tyre model denoted by Eq. (9), a linear equation (with respect to camber angle) is used to represent the extra lateral tyre force due to wheel camber:

$$F_{y\gamma j} = C_{\gamma j} \gamma_j \quad (10a)$$

$$C_{\gamma j} = \begin{cases} C_{\gamma 0j} + C_{\gamma \alpha j} |\alpha_j|, & \text{if } |\alpha_j| < \alpha_{lim} \\ C_{\gamma f j}, & \text{if } |\alpha_j| \geq \alpha_{lim} \end{cases}. \quad (10b)$$

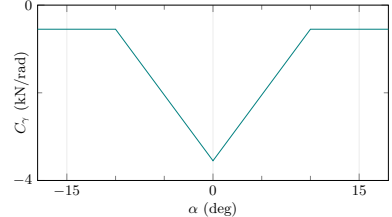


Fig. 2. Camber stiffness variation with respect to tyre slip angle.

$F_{y\gamma j}$ ($j \in \mathcal{B}$) denotes the extra lateral tyre force due to camber effect at the wheel (left/right); $C_{\gamma j}$ is the camber stiffness and γ_j the camber angle; $C_{\gamma 0j}$ and $C_{\gamma f j}$ are the camber stiffness when with zero tyre slip angle and when the tyre slip angle, α_j , reaches α_{lim} , respectively, where α_{lim} is a saturation value that depends on the tyre property; and $C_{\gamma \alpha j}$ is the variation in camber stiffness with regard to the tyre slip angle.

Note that the camber stiffness is defined as negative, to be consistent with the definition of cornering stiffness, and the variation in camber stiffness is defined as positive. This means that $|C_{\gamma j}|$ decreases as $|\alpha_j|$ increases until $|\alpha_j|$ reaches α_{lim} , as can be seen in Fig. 2. More details regarding camber effect modelling and its influence on lateral tyre forces can be found in [11].

C. Model Summary

Considering the vehicle and tyre modelling described in Sections II-A–II-B, the system state and output vectors, x and y , for Controllers S, ST, SC and STC are summarised as

$$x = [v_x \ v_y \ \omega_z \ \psi \ X \ Y \ \omega_{fl} \ \omega_{fr} \ \omega_{rl} \ \omega_{rr}]^T \quad (11a)$$

$$y = [\omega_z \ \beta \ \psi \ Y \ v_x]^T, \quad (11b)$$

where v_x and v_y are the longitudinal and lateral velocities at the centre of gravity (CoG) of the vehicle; ω_z denotes the vehicle yaw rate at the CoG and ψ the yaw angle; X and Y represent the longitudinal and lateral positions of the vehicle; and ω_i ($i \in \mathcal{A}$) denotes the angular velocity of the front left, front right, rear left and rear right wheels respectively. Additionally, $\beta = \arctan v_y/v_x \approx v_y/v_x$ is the vehicle sideslip angle.

Moreover, considering the fact that different combinations of actuators are utilised in the controllers, the system input vectors, u , for Controllers S, ST and SC are defined by Eqs. (12a), (12b) and (12c), respectively, as follows:

$$u = [\delta_f \ T]^T \quad (12a)$$

$$u = [\delta_f \ T_{fl} \ T_{fr} \ T_{rl} \ T_{rr}]^T \quad (12b)$$

$$u = [\delta_f \ T \ \gamma_f \ \gamma_r]^T, \quad (12c)$$

where δ_f is the steering angle at the front wheels, T and T_i ($i \in \mathcal{A}$) the torque at the four wheels, and γ_f and γ_r are the camber angle of the front and rear wheels, respectively.

It should be noted that Controller S would generate the same torque command to all four wheels, as it does not exploit the

capability of torque vectoring. This means that, for Controller S, Eq. (7) becomes

$$I_w \dot{\omega} = T - r_e F_x. \quad (13)$$

This is why merely one variable corresponding to wheel torque is included in Eq. (12a). The same applies to Controller SC, and thus Eq. (12c) is used.

To fully exploit the capability of vehicle actuators, Controller STC combines the features of ST and SC, i.e. using both torque vectoring and active camber for controlling the vehicle. To this end, the system input vector, u , for Controller STC is given by

$$u = [\delta_f \ T_{fl} \ T_{fr} \ T_{rl} \ T_{rr} \ \gamma_f \ \gamma_r]^T. \quad (14)$$

In summary, with the collocation method as described in [7] and [11], the modelling for Controllers S, ST, SC and STC can be denoted with the following state-space form:

$$x_{k+1} = f(x_k, u_k). \quad (15)$$

III. CONTROLLER DESIGN

This section presents the design of the four controllers, i.e. Controllers S, ST, SC and STC. The main purposes of these controllers are to follow the reference trajectories given by an upper-level planner while maintaining yaw stability in safety-critical driving conditions. To achieve this, MPC is used as the framework for designing the controllers, due to its capability of predicting future vehicle trajectories and explicitly considering constraints in its formulation.

When designing the MPC controllers, the tracking errors of the reference trajectories, as well as the magnitude of the control actions and their variation are included in the cost function. Additionally, constraints on the state and control variables are explicitly considered. The formulation of the MPC [19] controllers is summarised as follows:

$$\begin{aligned} & \min_{x, u, \Delta u, s} \underbrace{\sum_{p=0}^{N-1} \|y_{k+p|k} - y_{k+p|k}^{\text{ref}}\|_{Q_y}^2}_{\text{tracking error}} + \underbrace{\sum_{p=0}^{N-1} \|u_{k+p|k}\|_{R_u}^2}_{\text{control action}} \\ & + \underbrace{\sum_{p=0}^{N-1} \|\Delta u_{k+p|k}\|_{R_{du}}^2}_{\text{change of control action}} + \underbrace{\|y_{k+N|k} - y_{k+N|k}\|_{Q_{yf}}^2}_{\text{terminal cost of tracking error}} \\ & + \underbrace{\sum_{p=0}^{N-1} \|s_{k+p|k}\|_{Q_s}^2}_{\text{slack term}} + \underbrace{\|s_{k+N|k}\|_{Q_{sf}}^2}_{\text{terminal cost of slack variable}} \end{aligned} \quad (16a)$$

$$\text{s.t. } x_{k+p+1|k} = f(x_{k+p|k}, u_{k+p|k}) \quad (16b)$$

$$y_{k+p|k} = h(x_{k+p|k}), p \in \{0, 1, \dots, N\} \quad (16b)$$

$$u_{\min} \leq u_{k+p|k} \leq u_{\max} \quad (16c)$$

$$\Delta u_{\min} \leq \Delta u_{k+p|k} \leq \Delta u_{\max} \quad (16c)$$

$$x_{k|k} = \tilde{x}_k \quad g(x_{k+p|k}, s_{k+p|k}) \leq 0 \quad (16d)$$

where $x = [x_{k+1|k}, \dots, x_{k+N|k}]$, $u = [u_{k|k}, \dots, u_{k+N-1|k}]$, $\Delta u = [\Delta u_{k|k}, \dots, \Delta u_{k+N-1|k}]$ and $s = [s_{k|k}, \dots, s_{k+N|k}]$ are sequences of vectors for the state, control, variation of

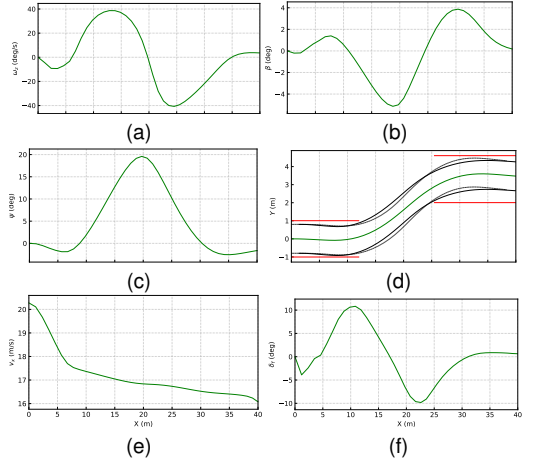


Fig. 3. Reference trajectories from the advanced planner in the SLC manoeuvre with the initial velocity being 73 km/h. (a)-(f) show the planned yaw rate (ω_z), sideslip angle (β), yaw angle (ψ), lateral position (Y), longitudinal velocity (v_x), and steering angle (δ_f), respectively. In (d), the solid red lines denote the cones for the SLC track, and the grey lines denote the trajectories of the four vehicle corners.

control and slack variables over the prediction horizon, N , respectively.

As can be seen from Eq. (16a), the cost function consists of six terms of L2-norm. For instance, $\|u_{k+p|k}\|_{R_u}^2$ can be expressed as $u_{k+p|k}^T R_u u_{k+p|k}$. The six terms penalise the trajectory tracking errors and the magnitude of control actions and their variation, with the corresponding weight matrices Q_y , R_u , R_{du} , Q_{yf} , Q_s and Q_{sf} , respectively.

The constraints in the MPC formulation account for the yaw stability, i.e. limits on the yaw rate and sideslip angle, and the physical limits of the vehicle actuators, which are defined by Eq. (16c) and (16d). It should be noted that the initial state over the prediction horizon, $x_{k|k}$, should be determined according to the current state of the vehicle, as shown in Eq. (16d). Moreover, this initial state is treated as a starting point for obtaining the final optimisation problem along the prediction horizon. More details on the controller formulation can be found in [7] and [11].

Reference trajectories denoting yaw stability, i.e. reference yaw rate and sideslip angle, are usually calculated by using a single-track model and actual steering angle, e.g. in [20], and/or determined separately from the reference path and steady-state steering angle, e.g. in [7]. In the present study, vehicle reference trajectories, including the reference yaw rate, sideslip angle and path, are provided concurrently by an optimisation-based trajectory planner, which is detailed in [21]. This alleviates the difficulties from deficient reference trajectories in controller evaluation.

IV. RESULTS AND DISCUSSION

This section presents an evaluation of four motion actuator combinations through the controllers designed in Sections

II and III, i.e. Controllers S, ST, SC and STC. The four controllers are designed by using **MPCTools** [22], which is an interface for implementing MPC problems. The designed MPC formulation in **MPCTools** is interpreted by **CasADi** [23] and transferred to **IPOPT** [24] as an optimisation problem, which is then solved by the solver **MA27** [25].

The four motion actuator configurations are evaluated with the following steps:

- 1) Reference trajectories are generated with various initial velocities in a single-lane change (SLC) manoeuvre [21] by using two trajectory planners, to test the robustness of the controllers. The advanced trajectory planner, which is Planner DTMLt in [21], is modelled by using a double-track vehicle model that considers load transfer and the Pacejka tyre model [26]; and the simplified planner adopts a single-track vehicle model and a linear tyre model, and it does not include the sideslip angle variation term in the yaw rate constraint as the advanced planner.
- 2) The four controllers are used to control the vehicle by following the reference trajectories, i.e. the reference yaw rate, sideslip angle, yaw angle, lateral position and longitudinal velocity, while complying with the yaw stability constraints, i.e. the constraints on the yaw rate and sideslip angle, at various initial velocities in the SLC manoeuvre. Both the reference trajectories and the yaw stability constraints directly come from the trajectory planners. The vehicle plant that is used to simulate the vehicle behaviour is detailed in [7].
- 3) The results from the four controllers are analysed and compared in terms of passing velocity and tracking accuracy, with the performance indicators RMS and maximum tracking errors detailed in [7].

As an example, Fig. 3 shows the generated reference trajectories from the advanced planner in the SLC manoeuvre with the initial velocity being 73 km/h. Similarly, reference trajectories are generated at various other initial velocities from both the advanced and simplified planners (results not shown to save space). Subsequently, these reference trajectories are used by the four controllers for trajectory tracking in the following discussions.

Considering their physical limits, the capability of the steering, torque and camber actuators of the vehicle are constrained to be within $\pm 25^\circ$, ± 1490.2 Nm and $\pm 15^\circ$, respectively. Accordingly, the rate of change of these actuators are defined as $\pm 37^\circ/\text{s}$, ± 2980.5 Nm/s and $\pm 45^\circ/\text{s}$, respectively.

As different combinations of actuators are considered in the four controllers, the weight matrices are set accordingly for each controller. Specifically, the same components in the weight matrices are used for all the controllers where applicable, for a fair comparison. To this end, the R_u , R_{du}

TABLE I
HIGHEST (MAXIMUM INITIAL) PASSING VELOCITY OF CONTROLLERS WITH TRAJECTORIES FROM THE ADVANCED PLANNER.

Controller	S	ST	SC	STC
Velocity (km/h)	73	76	76	79

TABLE II
TRAJECTORY TRACKING ERRORS OF CONTROLLERS WITH REFERENCE TRAJECTORIES FROM THE ADVANCED PLANNER.

v_{xi} (km/h)	Controller	ω_z ($^\circ/\text{s}$)		β ($^\circ$)		ψ ($^\circ$)	
		e_{rms}	e_{max}	e_{rms}	e_{max}	e_{rms}	e_{max}
73	S	3.2	7.7	0.6	1.0	0.9	1.9
	ST	2.9	7.7	0.5	0.9	0.8	1.7
	SC	2.0	6.0	0.3	0.7	0.6	1.5
	STC	2.0	6.9	0.2	0.4	0.5	1.2
76	ST	3.6	11.4	0.6	1.3	0.9	2.1
	SC	2.5	9.2	0.4	1.3	0.6	1.3
	STC	2.6	8.6	0.2	0.6	0.6	1.5
79	STC	3.3	9.6	0.5	1.2	0.8	2.5

^a The text colour red indicates the largest tracking error (at the same initial velocity) of each column, while the text colour blue the smallest tracking error.

and Q_y matrices are set for the four controllers as follows:

$$R_{u,s} = R_{du,s} = \text{diag}([10 \ 20 \cdot 10^{-6}]) \quad (17a)$$

$$R_{u,sc} = R_{du,sc} = \text{diag}([10 \ 20 \cdot 10^{-6} \ 10 \ 10]) \quad (17b)$$

$$\begin{aligned} R_{u,st} &= R_{du,st} \\ &= \text{diag}([10 \ 5 \cdot 10^{-6} \ 5 \cdot 10^{-6} \ 5 \cdot 10^{-6} \ 5 \cdot 10^{-6}]) \end{aligned} \quad (17c)$$

$$\begin{aligned} R_{u,stc} &= R_{du,stc} \\ &= \text{diag}([10 \ 5 \cdot 10^{-6} \ 5 \cdot 10^{-6} \ 5 \cdot 10^{-6} \ 5 \cdot 10^{-6} \ 10 \ 10]) \end{aligned} \quad (17d)$$

$$\begin{aligned} Q_{y,s} &= Q_{y,st} = Q_{y,sc} = Q_{y,stc} \\ &= \text{diag}([120 \ 30 \ 30 \ 100 \ 10]). \end{aligned} \quad (17e)$$

A. Velocity and Accuracy

Table I shows the highest passing velocity of the four controllers with the reference trajectories from the advanced planner. As can be seen, Controller S yields the lowest passing velocity among all the controllers, which is 3 km/h lower than that from ST and SC; on the other hand, STC has a 6 km/h higher passing velocity than Controller S.

Controller S produces in general the largest tracking errors for the yaw rate, sideslip angle and yaw angle at the initial velocity 73 km/h with the advanced planner, as shown in Table II and Fig. 4. It can also be seen that Controller ST results in a lower tracking accuracy than SC at the same initial velocity with the advanced planner. On the other hand, at the same initial velocity, Controller STC in general results in smaller tracking errors for the yaw rate, sideslip angle and yaw angle than the other controllers, as can be seen in Table II and Fig. 4. Moreover, when the initial velocity increases to 76 km/h, STC produces smaller peak sideslip angle than the

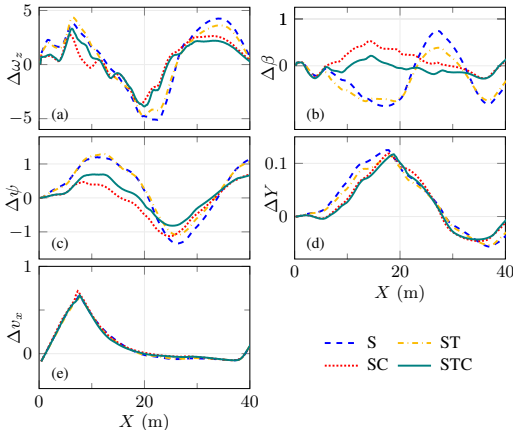


Fig. 4. Comparison of trajectory tracking errors of the four controllers with the trajectories from the advanced planner with the initial velocity being 73 km/h. (a)–(e) show the trajectory tracking errors corresponding to the yaw rate (ω_z), sideslip angle (β), yaw angle (ψ), lateral position (Y), and longitudinal velocity (v_x), respectively.

other controllers at the position around 20 m, as can be seen in Fig. 5(b).

The improved performance of Controller SC over ST can be due to the fact that active camber is more effective than torque vectoring in the present study, especially when the lateral tyre force is relatively large and the tyre slip angle is relatively small. Specifically, ST needs to produce proper amount of total longitudinal forces such that it satisfies the longitudinal movement requirement as indicated by Eq. (1). This, together with the combined-slip driving condition in the manoeuvre, limits the capability of ST in generating the required yaw moment. As a result, the build-up of critical vehicle states, e.g. sideslip angle, from ST is quicker than that from SC, as shown in Fig. 5(b). In contrast, the improved performance of Controller SC over ST can be attributed to the following two points. Firstly, the lateral tyre forces are much larger than the corresponding longitudinal tyre forces for the most of the time in the test scenarios, meaning that it can be more effective to control the lateral tyre forces than the longitudinal forces. Secondly, with different values of camber angle produced in the front and rear wheels, additional yaw moment can be generated by controlling the lateral tyre forces. For instance, at the beginning of the SLC manoeuvre, the generated yaw moment from Controller SC is more than twice the value from ST, as shown in Fig. 5(f).

The working principles of Controller SC can be further explained by examining Figs. 5–6. At the position around $X = 10$ m, the steering angle of the front wheels reaches 13.9° , as shown in Fig. 5(g); and the tyre slip angle of the four wheels are $\alpha_{fl} = -10.2^\circ$, $\alpha_{fr} = -11.4^\circ$, $\alpha_{rl} = -2.6^\circ$ and $\alpha_{rr} = -2.0^\circ$, respectively, as shown in Fig. 6(g). This means that, at this position, controlling the inclination angle of the two front wheels may not be as effective as controlling the

TABLE III
SAFETY DISTANCE OF CONTROLLERS AT FOUR CRITICAL LOCATIONS WITH TRAJECTORIES FROM THE ADVANCED PLANNER (m).

v_x (km/h)	Controller	PA (FR)		PB (FL)		PC (FR)		PD (RL)	
		min	X	min	X	min	X	min	X
73	S	0.12	7.6	0.09	11.9	0.14	25.5	0.18	32.1
	ST	0.12	7.6	0.09	12.1	0.14	25.5	0.18	32.1
	SC	0.10	7.8	0.11	12.0	0.15	25.5	0.18	32.4
	STC	0.09	8.0	0.12	11.9	0.15	25.5	0.18	32.4
76	ST	0.17	7.3	0.03	12.0	0.13	25.5	0.23	31.4
	SC	0.14	7.5	0.06	12.0	0.10	25.5	0.26	31.6
	STC	0.14	7.5	0.08	12.0	0.12	25.5	0.23	31.6
79	STC	0.15	6.7	0.04	12.0	0.10	25.4	0.10	33.0

^a The background colour green indicates the largest safety distance (at the same initial velocity) of each column, while the background colour yellow the shortest safety distance.

^b X indicates the global longitudinal position of the vehicle corner where there is the shortest safety distance with respect to the corresponding critical location, e.g. “PB”.

two rear wheels, considering the relationship between camber stiffness and slip angle, as illustrated in Fig. 2. This is why Controller SC produces the camber angle for the rear wheels (-12.2°) twice the value for the front wheels (-5.8°) at this position, as can be seen in Fig. 5(h). Moreover, the fact that the vehicle is decelerating while steering to the left at this position makes the rear right wheel have larger vertical load than the rear left, as shown in Figs. 5(c), 5(g), 6(j) and 6(k). This explains the higher tyre utilisation in the rear right wheel of Controller SC than that of ST at the position around $X = 10$ m, as can be observed in Fig. 6(b)–(c).

As for Controller STC, it combines the features of both ST and SC. Therefore, STC does not need to exploit as much torque vectoring as ST to rotate the vehicle at the position around $X = 10$ m, as shown in Fig. 5(k) and (m). Moreover, compared with SC, STC results in lower build-up and rate of change of sideslip angle, as well as smaller peak camber demand in the entire manoeuvre, as evident in Fig. 5(b), (h) and (i). In short, by exploiting the steering, torque and camber actuators in an integrated manner, Controller STC can regulate both the longitudinal and lateral forces of individual wheels when needed, and thus resulting in larger safety margin and improved performance.

B. Safety Distance

Although from Fig. 5(e) it can be seen that Controller S yields a rather smooth path through the SLC manoeuvre at the initial velocity 76 km/h, the front left corner of the vehicle in fact collides with the cone at the position around $X = 12$ m. Therefore, this section discusses the safety distance between vehicle corners and cones at four critical locations with the advanced planner.

Fig. 7 shows the position envelope of the four controllers with trajectories from the advanced planner. Specifically, Fig. 7(a)–(c) present results at the three highest possible initial velocities (see Table I). As can be seen, the vehicle tends to

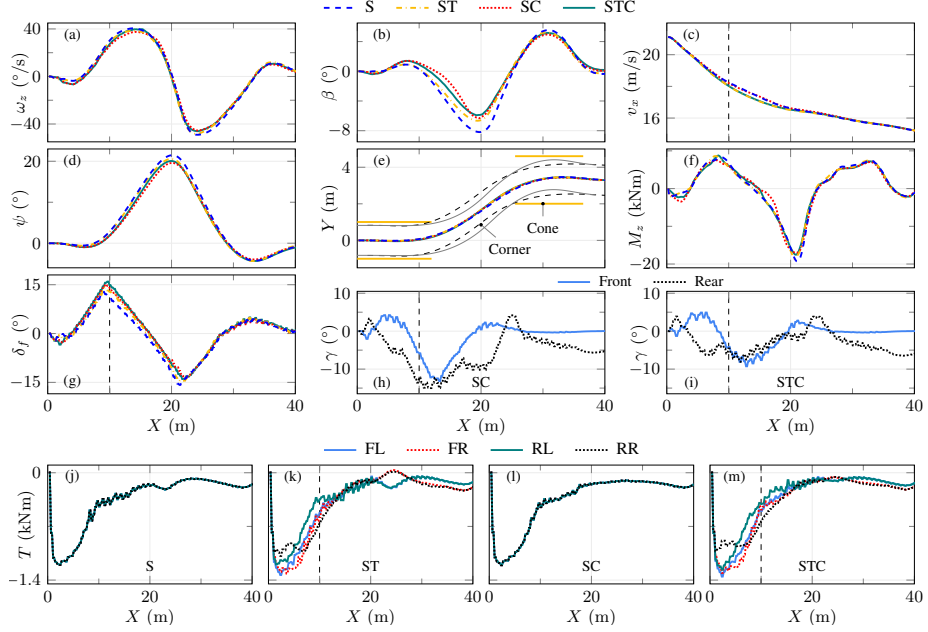


Fig. 5. Comparison of trajectory tracking of the four controllers with the trajectories from the advanced planner with the initial velocity being 76 km/h. (a)–(e) show the yaw rate ($\dot{\omega}_z$), sideslip angle (β), longitudinal velocity (v_x), yaw angle (ψ), and lateral position (Y), respectively, from the vehicle after trajectory tracking. In (f), M_z , which is expressed as the right-hand-side of Eq. (3), denotes the required yaw moment (from the contribution of both longitudinal and lateral tyre forces) for the yaw movement of the vehicle. (g) presents the commanded front steering angle at the wheel. (h) and (i) give the commanded camber angle of the front and rear wheels, and (j)–(m) display the commanded drive/braking torques at the wheel. In (e), “Cone” denotes the cones for the SLC track, and “Corner” the vehicle boundaries corresponding to Controller S, with the dashed lines showing the front corners and the solid lines the rear corners. In (e), it can be seen that the front left corner collides with the cone at around $X = 12$ m.

collide with the cones at four positions, which are indicated by “PA”, “PB”, “PC” and “PD”, respectively.

As shown in Table III, at locations “PA”, “PB”, “PC” and “PD”, the vehicle tends to collide with the cones by the front right, front left, front right and rear left corners, respectively. In general, the vehicle is most likely to collide with the cone at location “PB” for all the controllers. Moreover, at this location, the safety distance from Controller STC increases by 33% (3 cm), compared with that from S and ST, when tested with the initial velocity 73 km/h. Further, when the velocity increases to 76 km/h, the safety distance (at “PB”) from STC is 166% (5 cm) larger than that from ST. It should be noted that this 5 cm increase in safety distance can be of significant importance in a near crash scenario.

The increased safety distance of Controller STC over ST at “PB” can be explained after examining their location envelopes formed from the four critical locations, e.g. with the initial velocity 73 km/h. As indicated by Table III, the resulted overall position envelope (especially the first half of the manoeuvre) from STC shifts closer to the cones on the right side of the vehicle, compared with that from ST. By using this strategy, Controller STC succeeds in manoeuvring the vehicle further away from the cone at the most critical location “PB” and at a higher velocity.

When the initial velocity increases from 73 to 79 km/h,

TABLE IV
HIGHEST (MAXIMUM INITIAL) PASSING VELOCITY OF CONTROLLERS
WITH TRAJECTORIES FROM THE SIMPLIFIED PLANNER.

Controller	S	ST	SC	STC
Velocity (km/h)	67	67	77	79

the safety distance of Controller STC at locations “PA”, “PB”, “PC” and “PD” change by 6, -8, -5 and -8 cm, respectively, as shown in Table III. Take the right-side corners of the vehicle as an example, this means that the position envelope at “PA” moves leftwards while at “PC” it moves rightwards. Similarly, it can be seen that the position envelope at “PA” moves backwards along the X axis while at “PD” it shifts forwards. This means that the envelope tube formed from the trajectories of the vehicle corners is somewhat stretched along the X direction. In other words, when the initial velocity increases, STC tends to produce a smoother position envelope.

C. Robustness Test

To assess the robustness of the controllers, tests are carried out by using reference trajectories from the simplified planner. As can be seen from Table IV, compared with Controller S, ST

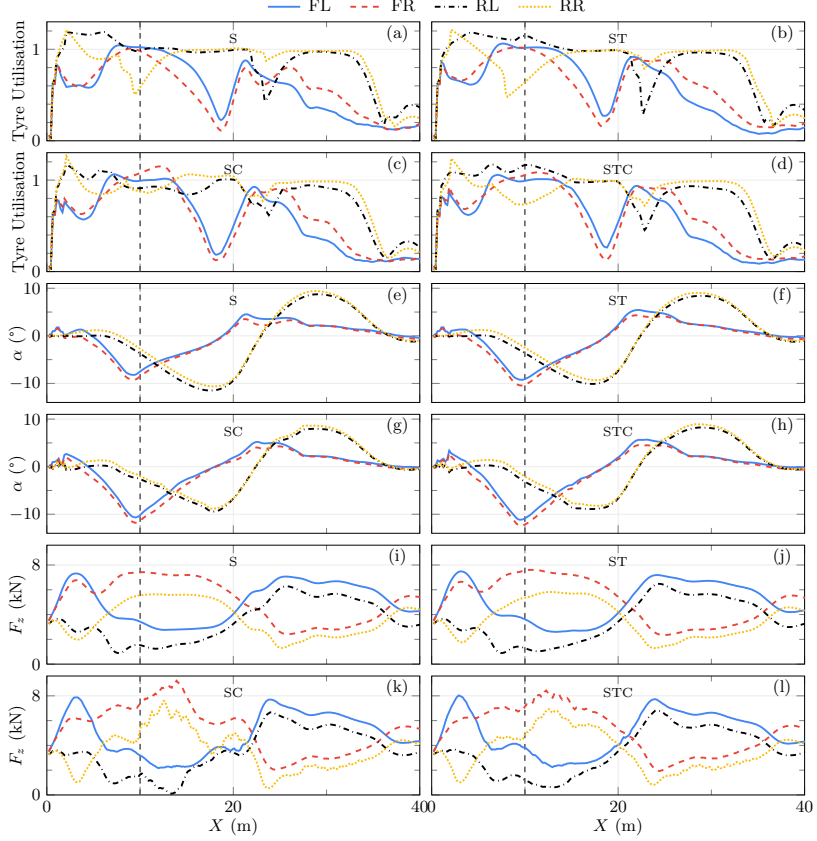


Fig. 6. Tyre utilisation, slip angle and vertical load of the four controllers with the trajectories from the advanced planner with the initial velocity being 76 km/h. [(a), (e), (i)], [(b), (f), (j)], [(c), (g), (k)] and [(d), (h), (l)] show the results obtained from Controllers S, ST, SC and STC, respectively. The tyre utilisation is calculated by dividing the combined longitudinal and lateral tyre forces with the vertical wheel load and is detailed in [11]. It should be noted that, for Controller S, the vehicle fails to pass the manoeuvre, as explained in Fig. 5.

TABLE V
TRAJECTORY TRACKING ERRORS OF CONTROLLERS WITH REFERENCE TRAJECTORIES FROM THE SIMPLIFIED PLANNER.

v_{xi} (km/h)	Controller	ω_z (°/s)		β (°)		ψ (°)	
		e_{rms}	e_{max}	e_{rms}	e_{max}	e_{rms}	e_{max}
67	S	4.0	9.3	0.7	1.8	1.1	2.2
	ST	3.3	8.3	0.5	1.3	0.9	1.8
	SC	2.1	5.2	0.3	0.6	0.6	1.4
	STC	2.0	5.4	0.3	0.7	0.5	1.2
77	SC	3.3	11.7	0.5	1.2	0.6	1.7
	STC	3.0	10.5	0.4	0.9	0.6	1.5
79	STC	4.0	12.0	0.6	1.6	0.8	1.8

TABLE VI
SAFETY DISTANCE OF CONTROLLERS AT FOUR CRITICAL LOCATIONS WITH TRAJECTORIES FROM THE SIMPLIFIED PLANNER (m).

v_x (km/h)	Controller	PA (FR)		PB (FL)		PC (FR)		PD (RL)	
		min	X	min	X	min	X	min	X
67	S	0.12	7.5	0.08	11.9	0.21	25.5	0.25	31.7
	ST	0.12	7.7	0.09	11.9	0.21	25.5	0.25	32.0
	SC	0.10	8.1	0.10	11.9	0.19	25.5	0.24	32.7
	STC	0.10	8.1	0.10	11.9	0.20	25.5	0.23	32.8
77	SC	0.14	7.0	0.04	12.0	0.12	25.5	0.08	33.7
	STC	0.13	7.2	0.07	11.9	0.14	25.6	0.07	33.7
79	STC	0.15	6.7	0.02	12.0	0.14	25.5	0.07	33.0

does not gain in passing velocity with the simplified planner, which is worse than the case with the advanced planner where

there is a 3 km/h gain. On the other hand, the passing velocity difference between SC and ST increases from 0 in the case

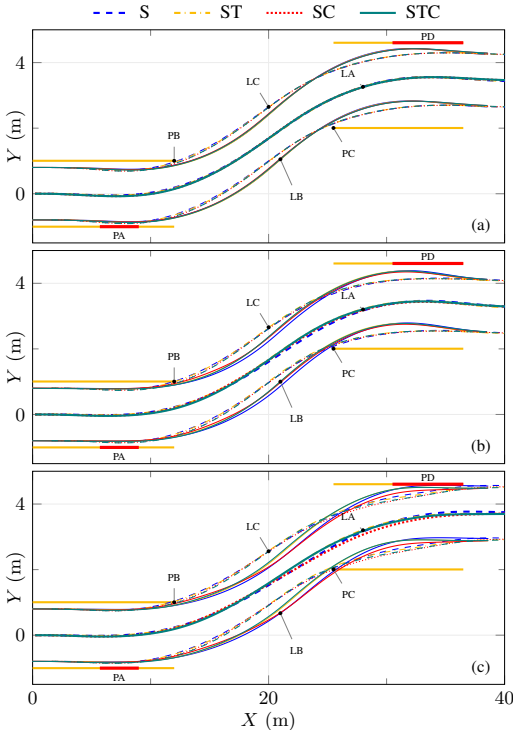


Fig. 7. Position envelope of the four controllers with trajectories from the advanced planner. (a)–(c) show the results with the initial velocities being 73, 76 and 79 km/h, respectively. “PA”, “PB”, “PC” and “PD” denote four critical positions where the vehicle tends to collide with the cones. “LA” denotes the position of vehicle centre of gravity with the legend entries as shown above this figure. “LB” and “LC” denote vehicle boundaries of the left and right corners, respectively, where the colours indicate controllers as defined in the legend entries above this figure.

with the advanced planner to 10 km/h with the simplified planner. Moreover, the passing velocity difference between STC and SC with the simplified planner is 2 km/h, which is similar to the case with the advanced planner. Furthermore, the passing velocity gap between Controllers STC and S increases to 12 km/h when using the reference trajectories from the simplified planner; in contrast, the passing velocity difference between these two controllers is merely 6 km/h with the advanced planner.

Table V and Figs. 8–9 show the tracking performance of the four controllers with the simplified planner. As can be seen, Controller S performs the worst among all the four controllers in terms of tracking accuracy and the magnitude of the resulted critical vehicle states, e.g. sideslip angle, which is similar to the case with the advanced planner. Moreover, ST again is inferior to SC with the simplified planner, with respect to tracking accuracy, as well as the resulted peak sideslip angle.

Controller STC yields similar tracking accuracy to SC with the simplified planner at the initial velocity 67 km/h, as can be seen from Table V and Figs. 8–9. This can be due to the

fact that, at this relatively low velocity, STC does not need to utilise the full potential of the available actuators. When the initial velocity increases to 77 km/h, STC yields higher accuracy than SC, as shown in Table V. Moreover, at this higher velocity, both SC and STC request more actuator usage than the case at 67 km/h, which can be observed in Fig. 10(a)–(b), as a result of the more severe driving condition. Still, at 77 km/h, the peak camber angle in both the front and rear wheels from Controller STC is lower than that from SC, due to its integrated usage of camber and torque actuators.

The safety distance of the controllers at the four critical positions with the simplified planner can be seen in Table VI. “PB” is again the most critical position where the vehicle is likely to collide with the cone for all the controllers. Moreover, the safety distance from Controller STC is 75% larger (3 cm) than that from SC at this location with the initial velocity 77 km/h. Furthermore, when the initial velocity increases from 67 to 79 km/h, STC also generates a smoother position envelope (figure for 79 km/h not shown to save space), which is similar to the observation with the advanced planner.

V. CONCLUSIONS

This paper has presented an evaluation of four motion actuator combinations for path following and yaw stability control in critical driving scenarios, including active front steering (AFS), AFS plus torque vectoring (TV), AFS plus active camber (AC), as well as the integrated control of AFS plus TV and AC. These over-actuation configurations were examined through the design of four controllers, i.e. Controllers S, ST, SC and STC. The controllers were designed by using a double-track vehicle model, coupled with the Dugoff tyre model and its variant that includes camber effect. Based on these vehicle and tyre models, the controllers were formulated in the MPC framework with constraints related to yaw stability and actuator limits considered. The four motion actuator configurations were evaluated in the SLC manoeuvre at various initial velocities, with respect to passing velocity, tracking accuracy, safety distance, and robustness to trajectory generation. The main findings regarding the performance of these over-actuation combinations are summarised as follows:

- The integrated control of AFS plus TV and AC yielded the highest passing velocity, i.e. 79 km/h, among all the over-actuation configurations with the reference trajectories from both the advanced and simplified planners. In general, this configuration produced consistently smaller peak values and tracking errors for critical vehicle states, e.g. sideslip angle, than the other configurations, with these two types of reference trajectories. Moreover, this configuration generated in general larger safety distance in the most critical position “PB” than the other configurations, which is crucial in near-crash scenarios.
- AFS plus AC was in general superior to AFS plus TV in terms of passing velocity, tracking accuracy, as well as safety distance at location “PB”, with the two types of reference trajectories, indicating that active camber was more effective than torque vectoring in the tested scenarios.

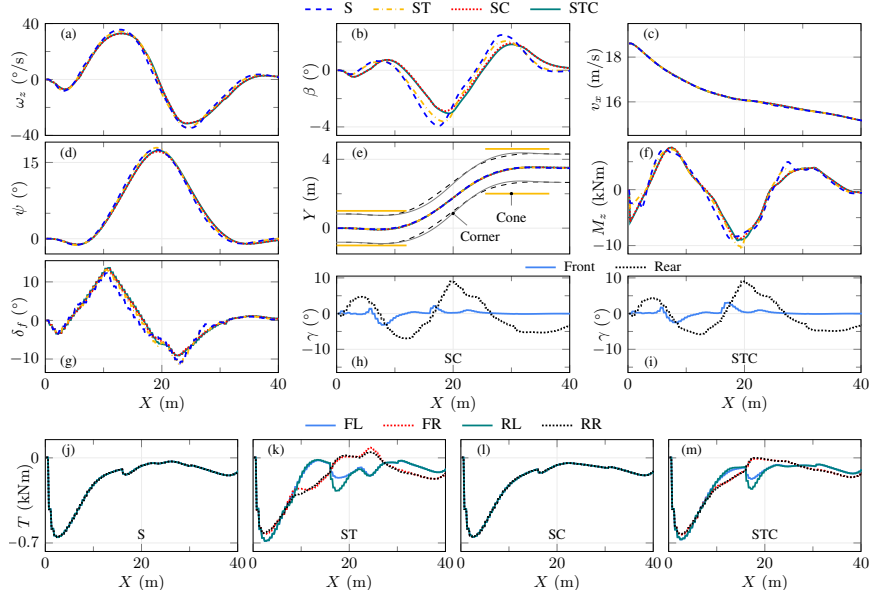


Fig. 8. Comparison of trajectory tracking of the four controllers with the trajectories from the simplified planner with the initial velocity being 67 km/h.

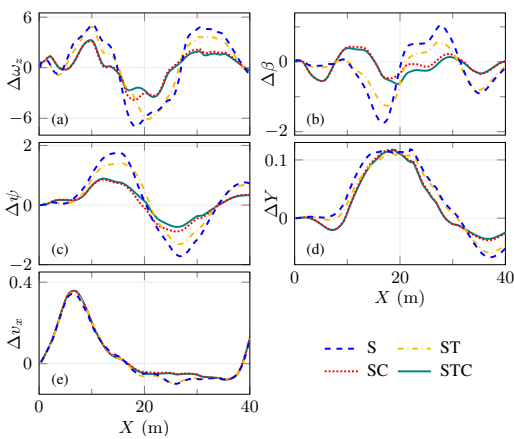


Fig. 9. Comparison of trajectory tracking errors of the four controllers with the trajectories from the simplified planner and the initial velocity 67 km/h.

- AFS performed in general the worst among all the motion actuator combinations, due to its lack of access to overactuation.
- AFS and AFS plus TV gained 6 and 9 km/h, respectively, in passing velocity when tested with the advanced planner, compared to the case with the simplified planner. On the other hand, the passing velocity gap between AFS and the integrated control of AFS plus TV and

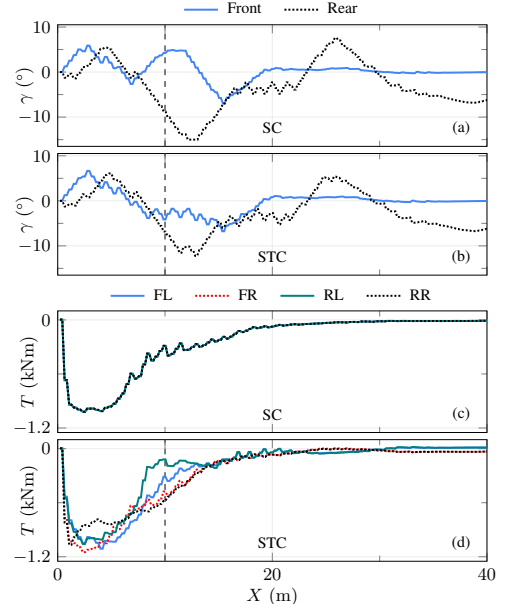


Fig. 10. Comparison of control actions of Controllers SC and STC with the trajectories from the simplified planner and the initial velocity 77 km/h.

AC increased from 6 km/h with the advanced planner to 12 km/h with the simplified planner. This, in the

presented test scenarios, indicates that a simpler motion actuator configuration could benefit more from accurate reference trajectories and that a more advanced configuration could to a certain degree compensate for the deficiencies caused by the less accurate trajectories.

In the future, it is planned to further evaluate the proposed controllers with more test manoeuvres and with reference trajectories from more advanced planners.

REFERENCES

- [1] P. Falcone, F. Borrelli, J. Asgari, H. E. Tseng, and D. Hrovat, "Predictive active steering control for autonomous vehicle systems," *IEEE Transactions on Control Systems Technology*, vol. 15, no. 3, pp. 566–580, May 2007.
- [2] E. K. Liebemann, K. Meder, J. Schuh, and G. Nenninger, "Safety and performance enhancement: The Bosch electronic stability control (ESP)," in *Proc. SAE Convergence*, 2004, pp. 421–428.
- [3] T. Tjonnas and T. A. Johansen, "Stabilization of automotive vehicles using active steering and adaptive brake control allocation," *IEEE Transactions on Control Systems Technology*, vol. 18, no. 3, pp. 545–558, May 2010.
- [4] M. Jonasson, J. Andreasson, S. Solyom, B. Jacobson, and A. S. Trigell, "Utilization of actuators to improve vehicle stability at the limit: From hydraulic brakes toward electric propulsion," *Journal of Dynamic Systems, Measurement, and Control*, vol. 133, no. 5, p. 051003, 2011.
- [5] K. Nam, H. Fujimoto, and Y. Hori, "Lateral stability control of in-wheel-motor-driven electric vehicles based on sideslip angle estimation using lateral tire force sensors," *IEEE Transactions on Vehicular Technology*, vol. 61, no. 5, pp. 1972–1985, 2012.
- [6] L. D. Novellis, A. Sorniotti, P. Gruber, J. Orus, J.-M. R. Fortun, J. Theunissen, and J. D. Smet, "Direct yaw moment control actuated through electric drivetrains and friction brakes: Theoretical design and experimental assessment," *Mechatronics*, vol. 26, pp. 1–15, Mar. 2015.
- [7] W. Zhang, Z. Wang, L. Drugge, and M. Nybacka, "Evaluating model predictive path following and yaw stability controllers for over-actuated autonomous electric vehicles," *IEEE Transactions on Vehicular Technology*, vol. 69, no. 11, pp. 12 807–12 821, Nov. 2020.
- [8] D. Ammon, "Vehicle dynamics analysis tasks and related tyre simulation challenges," *Vehicle System Dynamics*, vol. 43, no. sup1, pp. 30–47, Jan. 2005.
- [9] P. Gáspár and B. Németh, "Integrated control design for driver assistance systems based on LPV methods," *Int. J. Control.*, vol. 89, no. 12, pp. 2420–2433, Mar. 2016.
- [18] H. Dugoff, P. S. Fancher, and L. Segel, "Tire performance characteristics affecting vehicle response to steering and braking control inputs," Washington, DC, Tech. Rep. Contract CST-460, Aug. 1969.
- [10] T. Yoshino and H. Nozaki, "Effect of direct yaw moment control based on steering angle velocity and camber angle control," in *SAE Technical Paper Series*. SAE International, Sep. 2014.
- [11] W. Zhang, L. Drugge, M. Nybacka, and Z. Wang, "Active camber for enhancing path following and yaw stability of over-actuated autonomous electric vehicles," *Vehicle System Dynamics*, pp. 1–22, Feb. 2020.
- [12] Z. Shuai, H. Zhang, J. Wang, J. Li, and M. Ouyang, "Combined AFS and DYC control of four-wheel-independent-drive electric vehicles over CAN network with time-varying delays," *IEEE Transactions on Vehicular Technology*, vol. 63, no. 2, pp. 591–602, Feb. 2014.
- [13] H. Alipour, M. Sabahi, and M. B. B. Sharifian, "Lateral stabilization of a four wheel independent drive electric vehicle on slippery roads," *Mechatronics*, vol. 30, pp. 275–285, Sep. 2015.
- [14] P. Falcone, H. E. Tseng, J. Asgari, F. Borrelli, and D. Hrovat, "Integrated braking and steering model predictive control approach in autonomous vehicles," *IFAC Proceedings Volumes*, vol. 40, no. 10, pp. 273–278, 2007.
- [15] B. Ren, H. Chen, H. Zhao, and L. Yuan, "MPC-based yaw stability control in in-wheel-motored EV via active front steering and motor torque distribution," *Mechatronics*, vol. 38, pp. 103–114, Sep. 2016.
- [16] M. Jalali, A. Khajepour, S. ken Chen, and B. Litkouhi, "Integrated stability and traction control for electric vehicles using model predictive control," *Control Engineering Practice*, vol. 54, pp. 256–266, Sep. 2016.
- [17] M. Doumiati, A. Charara, and A. Victorino, *Vehicle Dynamics Estimation Using Kalman Filtering: Experimental Validation*. ISTE LTD, Dec. 2012.
- [19] J. B. Rawlings, D. Q. Mayne, and M. M. Diehl, *Model Predictive Control: Theory, Computation, and Design*, 2nd ed. Madison, WI, USA: Nob Hill Publishing, 2017.
- [20] R. Rajamani, *Vehicle Dynamics and Control*, 2nd ed. New York, NY, USA: Springer, 2012.
- [21] W. Zhang, L. Drugge, M. Nybacka, J. Jerrelind, Z. Wang, and J. Zhu, "Exploring model complexity for trajectory planning of autonomous vehicles in critical driving scenarios," in *Advances in Dynamics of Vehicles on Roads and Tracks (IVSVD 2021)*, 2021.
- [22] M. J. Risbeck and J. B. Rawlings. (2015) MPCTools: Nonlinear model predictive control tools for CasADi (Python interface). [Online]. Available: <https://bitbucket.org/rawlings-group/mpc-tools-casadi>
- [23] J. A. E. Andersson, J. Gillis, G. Horn, J. B. Rawlings, and M. Diehl, "CasADi – A software framework for nonlinear optimization and optimal control," *Mathematical Programming Computation*, vol. 11, no. 1, pp. 1–36, Jul. 2019.
- [24] A. Wächter and L. T. Biegler, "On the implementation of an interior-point filter line-search algorithm for large-scale nonlinear programming," *Math. Program.*, vol. 106, no. 1, pp. 25–57, Apr. 2005.
- [25] HSL. (2014) A collection of Fortran codes for large scale scientific computation. [Online]. Available: <http://www.hsl.rl.ac.uk/>
- [26] H. Pacejka, *Tire and Vehicle Dynamics*, 3rd ed. Oxford, UK: Elsevier, 2012.